Title	Mechanobiological origins of osteolysis during bone metastasis
Author(s)	Verbruggen, Anneke
Publication Date	2023-03-28
Publisher	NUI Galway
Item record	http://hdl.handle.net/10379/17716

Mechanobiological Origins of Osteolysis during Bone Metastasis

---

Anneke Verbruggen, M.E. (2017)

A thesis submitted to the University of Galway as fulfilment of the
requirements for the degree of Doctor of Philosophy

December 2022

Department of Biomedical Engineering
College of Science and Engineering
University of Galway, Ireland

Supervisor of Research: Prof. Laoise M. McNamara

Abstract

Metastasis is the final, lethal stage of cancer where cells migrate from a primary tumour site to colonise a secondary organ and is the primary cause of mortality in cancer patients. Breast cancer is the leading cause of cancer death in women in the world, with a recorded 627,000 deaths in 2018, and projected to reach 800,000 by 2030. In advanced breast cancer patients, cancer cells favour metastasis to bone tissue 70-80% of the time, primarily leading to osteolysis (bone destruction) and sometimes unwanted tissue formation. The evolving mechanical environment during tumour invasion might play an important role in these processes, as the activity of both bone and cancer cells is regulated by mechanical cues. However, it is not yet known how specific bone tissue composition is associated with tumour invasion. In particular, how compositional and nano-mechanical properties of bone tissue evolve during metastasis, where in the bone they arise, and how they influence the overall aggressiveness of tumour invasion, are not well understood.

The first study of this thesis sought to develop an advanced understanding of temporal and spatial changes in nano-mechanical properties and composition of bone tissue during metastasis. Primary mammary tumours were induced by inoculation of immune-competent BALB/c mice with 4T1 breast cancer cells, and microcomputed tomography and nanoindentation were conducted to quantify cortical and trabecular bone matrix mineralisation and nano-mechanical properties, respectively. Spatial analysis was performed in proximal and distal femur regions of tumour-adjacent (ipsilateral) and contralateral femurs after 3 weeks and 6 weeks of tumour and metastasis development. By 3 weeks post-inoculation there was no significant difference in bone volume fraction or nano-mechanical properties of bone tissue between the metastatic femora and healthy controls. However, early osteolysis was indicated by trabecular thinning in the distal and proximal trabecular compartment of tumour-bearing femora. Moreover, cortical thickness was significantly increased in the distal region, and the mean mineral density was significantly higher in cortical and trabecular bone tissue in both proximal and distal regions, of ipsilateral (tumour-bearing) femurs compared to healthy controls. By 6 weeks post-inoculation, overt osteolysis, decreased bone volume fraction, cortical area, cortical and trabecular thickness were reported in metastatic femora. Trabecular bone tissue stiffness in the

proximal femur decreased in the ipsilateral metastatic femurs compared to contralateral and control sites. This study uncovered changes in bone tissue composition prior to and following overt metastatic osteolysis, local and distant from the primary tumour site. On the basis of these findings, it was proposed that changes in tissue composition may alter the mechanical environment of both the bone and tumour cells, and thereby perpetuate the cancer vicious cycle during breast cancer metastasis to bone tissue.

The objective of the second study was to quantify changes in the mechanical environment within bone tissue, during bone metastasis and osteolytic resorption. This study used finite element (FE) models reconstructed from micro-CT images obtained during the first study of this thesis. In particular, the time-dependent changes in the mechanical environment, local to and distant from an invading tumour mass, were quantified to investigate putative mechanobiological cues for osteolysis during bone metastasis. This study reported a decrease in strain distribution within the proximal femur trabecular and distal cortical bone tissue in early metastasis (3 weeks after tumour inoculation). These changes in the mechanical environment preceded extensive osteolytic destruction, but coincided with the onset of early trabecular thinning, cortical thickening and mineralisation of proximal and distal femur bone, which were reported in the first study of this thesis. From these findings, it was proposed that early changes in the mechanical environment within bone tissue may activate resorption by osteoclast cells and thereby contribute to the extensive osteolytic bone loss at later stage (6 weeks) bone metastasis.

To investigate this proposed adaptation of bone tissue upon breast cancer metastatic invasion, the third and final study of this thesis sought to apply the mechanoregulation theory, which predicts tissue adaptation on the basis of changes within the mechanical environment. This was performed using a bone remodelling algorithm driven by changes in mechanical strain. A user-defined field (USDFLD) subroutine was applied to murine proximal femur models, with material properties obtained from the first study, such that each individual element within an FE model adapted material density and stiffness according to pre-defined strain stimuli criteria. In this way, this model generated an iterative mechanoregulatory response to changes in strain distribution throughout the bone mechanical environment, over a period of 3 weeks. This study

predicted that bone tissue would undergo resorption in regions which corresponded to those in the first study of this thesis upon overt osteolysis by 6 weeks of bone metastasis. These findings further support the proposal that mechanobiology may play a role in breast cancer bone osteolysis.

Together, the studies in this thesis report, for the first time, changes in bone mineral content and mechanical properties prior to overt osteolytic destruction in an *in vivo* animal model of breast cancer metastasis. Computational analysis revealed decreased strain distribution at this early time point, prior to osteolysis, and on this basis it was proposed that a mechanoregulatory response may contribute to subsequent osteolytic destruction.

Publications

Journal Articles

The following publications have arisen from the work presented in this thesis:

- A.S.K. Verbruggen, E.C. McCarthy, R.M. Dwyer, L.M. McNamara "Temporal and spatial changes in bone mineral content and mechanical properties during breast-cancer bone metastases." (2022) *Bone Reports*, 17, p.101597.

- A.S.K. Verbruggen, L.M. McNamara "Mechanoregulation may drive osteolysis during bone metastasis: A Finite Element Analysis of the mechanical environment within bone tissue during bone metastasis and osteolytic resorption" *Journal of Mechanical Behaviour of Biomedical Materials*

The following publications have been generated separate to this thesis:

- S.M. Naqvi, J.A. Panadero Pérez, V. Kumar, A.S.K. Verbruggen, L.M. McNamara, "A novel 3D osteoblast and osteocyte model revealing changes in mineralization and pro-osteoclastogenic paracrine signalling during estrogen deficiency." (2020) *Frontiers in bioengineering and biotechnology* 8:601.

Under review:

- V. Kumar, S.M. Naqvi, A.S.K. Verbruggen, E. McEvoy, and L.M. McNamara "A novel mechanobiological model of bone metastasis reveals that mechanical stimulation inhibits the pro-osteoclastogenic effects of breast cancer cells." (2022) bioRxiv.

Conference presentations

Peer Reviewed International Conferences

- Podium presentation at the annual ‘Modelathon’ Symposium Sheffield University, UK. January 2020
- Podium presentation at the Annual meeting of the Orthopaedic Research Society (ORS), Virtual, USA. February 2021
- Poster presentation at the Annual meeting of the Orthopaedic Research Society (ORS), Tampa, Florida, USA. February 2022.
- Podium presentation at the European Society of Biomechanics (ESB), Porto, Portugal, June 2022

Peer Reviewed National Conferences

- Podium presentations at 25th, 26th and 27th Annual conference of the Section of Bioengineering of the Royal Academy of Medicine in Ireland (BINI), Limerick (2019), Dublin (2020) and Galway (2022).

Acknowledgements

First and foremost, I would like to express my deepest gratitude to my supervisor, Prof. Laoise McNamara, for her hard work, patience, support and invaluable guidance throughout this project. With such dedication to the field of biomedical engineering and enthusiasm for all things mechanobiology, she holds the highest possible standard of research and ‘wordsmith’ writing that will forever be an inspiration to me. Thank you, Laoise.

I would also like to thank Dr. Róisín Dwyer, our fantastic collaborator at the Lambe Institute. This thesis would not have been possible without the amazing animal model design and detailed organising required for me to collect the perfect bone samples. I would also like to send a big thank you to Katie Gilligan and Elan McCarthy for providing me with the extra measurements and data that provided a full picture of the study, I wish the very best to all of you in your future endeavours! Also, a big thanks goes to our lab staff members David Connolly and Maja Drapiewska, for patiently helping with every micro-CT archiving problem and nanoindenter issue. You both showed me how to be a competent researcher.

Of course, a massive thank you goes to the McNamara research group, past and present. Thank you, Vatsal, the best right-hand man I could ever ask for. You deserve every good thing you ‘manifest’! Jessica and Masooma, you are the best lab moms I never knew I needed. Juan, Vinnie, Marissa, Dave, Ela, Genna, Ryan, Tanya, Ruchika, Sarah, Mostafa, Munam, thank you all for fighting in the trenches with me. Even when life became virtual, I never felt alone. And thank you, Sam, for reading every last word, except this page!

A special thank you to my family for being the best support I could ask for and checking in when I needed it most. A big thank you to my extended Mayo family and the ‘Backa This’ friends for asking ‘how’s the PhD going?’ despite the impending rant. It really did mean a lot to me. Last but certainly not least, thank you Laura Cuffe. From the shaky tears, to the 30-second dance-parties to the big wins, there is no way I could have done this without you. Thank you for believing in me, even when I didn’t. We finally reached the end of the tunnel!

Acronyms & Nomenclature

Acronyms

BMD	Bone Mineral Density
BMDD	Bone Mineral Density Distribution
BV	Bone Volume
BV/TV	Bone Volume fraction
Ca^{2+}	Calcium ion
Conn.D	Connectivity Density
MET-CONTRA	Contralateral side of tumour inoculated mouse
Ct. Th	Cortical bone tissue thickness
Ct.Ar	Cortical bone tissue cross-sectional area
Ct.Ar/Tt.Ar	Cortical bone area fraction
CTRL	Control group
DICOM	Digital Imaging and Communications in Medicine (scan)
DTCs	Disseminated Tumour Cells
ECM	Extracellular Matrix
FEA	Finite Element Analysis
FWHM	Full Width at Half Maximum
HA	Hydroxyapatite
HU	Hounsfield Units
IPL	Image Processing Language (Scanco Medical)
MET-IPS	Ipsilateral side of tumour inoculated mouse
kVp	Peak kilovoltage
MET	Metastatic disease group
M_{high}	High Mineral Density Region
Micro-CT	Micro-Computed Tomography
M_{low}	Low Mineral Density Region
M_{mean}	Mean Mineral Density
M_{mid}	Middle Mineral Density Region
M_{peak}	Peak Mineral Density

PTHrP	Parathyroid Hormone-related Protein
SMI	Structural Model Index
Tb. N	Trabecular Number
Tb.Sp	Trabecular bone tissue Spacing
Tb.Th	Trabecular bone tissue Thickness
TGF-β	Transforming Growth Factor β
Tt.Ar	Total cortical bone tissue cross-sectional area
TV	Total Bone Volume
VOI	Volume of Interest

Nomenclature

A	Area of Indentation
C_1	Indenter tip shape constant
C_2	Indenter tip apical radius constant
E	Young’s modulus
f	Function of Area
H	Material hardness
h_c	Contact depth
P	Maximum applied load
S	Material stiffness
ϵ	Berkovich tip constant
μA	Microampere
$\mu\varepsilon$	Microstrain
v	Poisson’s ratio
v_i	Indenter Poisson’s ratio
ρ_{Ash}	Ash density
ρ_{CT}	Computed Tomography measured density

Table of Contents

List of Figures

List of Tables

Chapter 1: Introduction

1.1 Bone and Bone Tissue Metastasis

Metastasis is the final, often lethal, stage of cancer that occurs when tumour cells migrate from a malignant primary mass to target a secondary site for tumour proliferation. In approximately 70-80% of advanced breast cancer patients, tumour cells metastasise to bone tissue (Coleman and Rubens, 1987, Plunkett and Rubens, 1999). Metastasis leads to bone destruction (osteolysis), inferior quality bone tissue formation (osteoblastic metastasis) or a mixture of these metastases (Mundy, 2002, Clines and Guise, 2005, Kozlow and Guise, 2005). While the 5-year survival rate for patients with localised breast cancer is approximately 99%, this is reduced to just 27% upon metastasis (Siegel et al., 2019). Current treatments for advanced bone metastasis include surgical intervention, radiotherapy, chemotherapy, drug therapies (bisphosphonates, denosumab), but treatment effectiveness is patient-specific and have harmful side-effects such as kidney infection and osteonecrosis of the jaw (Baron et al., 2011). Mechanical stimulation of metastatic long bones via exercise inhibits breast cancer cell extravasation (Jones et al., 2010, Zhou et al., 2016, Regmi et al., 2017). However, a greater understanding of the precise mechanical mechanisms that govern osteolytic metastasis is imperative for the discovery of more promising treatment options.

Bone tissue is a naturally adaptive composite material, which supports mobility and physiological loading demanded of the human body during everyday locomotion. Bone is composed of two macroscale components; sponge-like and highly porous trabecular bone tissue extends throughout the bone marrow niche, while dense, compact cortical bone tissue forms a surrounding shell. Bone tissue is predominantly composed of collagen (primarily type I), an abundant protein that is specifically organised into fibres and fibrils to provide structural support to the extracellular matrix, and mineral, whereby hydroxyapatite crystals formed from calcium and phosphorus are bound between collagen fibrils in the presence of non-collagenous proteins. Together these components are hierarchically organised to provide a strong, dense, and lightweight connective material capable of withstanding high mechanical loads. Bone tissue is produced by osteoblasts, which first produce the osteoid collagenous matrix and then deposit non-collagenous proteins and minerals over time.

Non-collagenous proteins (TGF-β, sclerostin, osteocalcin, osteopontin, osteonectin, bone sialoprotein) regulate bone cell migration, proliferation and differentiation (Poundarik et al., 2018, Licini et al., 2019).

Throughout life, bone tissue is renewed and replaced through the action of osteoclasts, which resorb aged and damaged tissue, and osteoblasts which replace this with new bone. This continuous process of bone renewal and repair is known as bone remodelling. Osteocytes can detect changes in their mechanical microenvironment (mechanosensation) and communicate these changes, via biochemical signalling, to osteoblasts and osteoclasts (mechanotransduction) to regulate bone remodelling. In this way, bone tissue is extraordinary in that it is continuously resorbed and formed in an adaptive response to changes in external mechanical stimuli (mechanoregulation).

According to mechanoregulation theory, bone remodelling cells actively undergo new bone formation when physical loading elicits mechanical stimulation beyond a specific threshold (Frost, 1996, McNamara and Prendergast, 2007, Smotrova et al., 2022), whereas insufficient mechanical stimulation results in bone tissue resorption. Mechanosensitive osteocytes produce factors that manipulate biochemical signalling (in particular the Wnt signalling pathway) to either activate bone formation by osteoblasts or osteoclast resorption in response to changes in mechanical strain, thereby counteracting such mechanical changes, in constant pursuit of a homeostatic physical environment. In this way, alterations in the mechanical environment as bone diseases progress (osteoporosis, bone metastasis) may also elicit changes in the mechanical signals received by osteocytes and contribute to disease progression. While it has been established that bone tissue is an attractive physical environment for breast cancer metastasis, how the process of mechanoregulation may contribute to tumour cell affinity is not yet understood.

1.2 Changes in the Bone Microenvironment during Metastatic Invasion

While breast cancer may result in increased formation (osteoblastic) at the target bone site, 80% of metastatic invasion within bone tissue results in devastating bone destruction, known as osteolysis. During osteolytic bone metastasis, tumour cells disrupt the remodelling process by adhering, invading, and proliferating within the bone tissue microenvironment. In brief, cancer cells release growth factors (OPN, BSP, OCN, IL-8, PTHrP) that manipulate resident bone cells, in particular osteoclasts to drive bone resorption (Langley and Fidler, 2007, Zheng et al., 2013). Bone tissue is an abundant source of growth factors (IGF-1, BMPs, VEGF, TGF-β) and osteolysis releases these, which promote the further infiltration and proliferation of metastatic cancer cells (Chen et al., 2010). This process, whereby cancer cells invade, manipulate, and perpetuate bone tissue resorption, is known as the cancer vicious cycle (Guise and Mundy, 1998). According to Paget's 'Seed and Soil Theory', bone tissue provides a particularly attractive substrate ('soil') for circulating metastatic cancer cells ('seed') to invade and proliferate (Paget, 1889). Over time, this cancer vicious cycle results in extensive osteolytic lesions in advanced metastatic patients, which results in severe bone pain, hypercalcemia, and an increased risk of fracture (Clines and Guise, 2005). Studies of human metastatic bone tissue from patients with a variety of cancer types (lung, breast, prostate, ovarian, colon) have reported that bone tissue density, mineral content, stiffness and strength significantly reduced when compared to site-matched healthy bone tissue (Kaneko et al., 2003, Nazarian et al., 2008). Animal models of bone metastasis, in which tumour cells are inoculated into the vascular system to induce metastatic spread, have enabled the study of bone tissue *in vivo*. These pre-clinical studies report decreased bone mineral density, tissue crystallinity, collagen quality, crystal width, trabecular tissue thickness and overall bone volume in osteolytic bone tissue (Richert et al., 2015, Wang et al., 2015, Burke et al., 2016, Burke et al., 2017, He et al., 2017, Sekita et al., 2017, Burke et al., 2018). In particular, in a study of female NCr mice inoculated with breast cancer cells (MDA-MB-231) into the distal femur, osteolytic lesions had formed in 58% of femurs by 3 weeks post-inoculation, but no change in bone strength was reported and bone mineral density (BMD) had in fact increased in both inoculated and contralateral femurs (Arrington et al., 2006). By 6 weeks, tumour-injected femora had significantly lower stiffness and BMD, while 56% of the mice were removed from the study by 9 weeks due to high risk of fracture failure. This study suggests the microenvironment of bone tissue undergoes significant changes over the time course of metastasis. However, how these changes in bone metastasis correlate with the physical properties of bone tissue is not fully understood. Therefore, the first hypothesis of this thesis was "***Bone mineral content and mechanical properties are altered during breast cancer bone metastasis".***

1.3 Impact of Metastasis on the Mechanical Environment of Bone Tissue

The finite element method (FE) is a numerical method of solving boundary value problems. This is conducted first by converting these boundary value problems into a discrete system of equations, then discretized by approximating the integrals within this system. The equations are solved in either a linear or nonlinear fashion, in accordance with assigned boundary conditions and within a pre-defined domain. Numerous FE studies have been conducted, via computational means, to investigate how the mechanical environment of bone tissue is altered during metastasis. Bone mineral content and mechanical properties are consistently reported to be greatly diminished upon metastatic osteolysis. Computational FE studies have identified the risk of bone fracture increases substantially with the introduction of osteolytic lesions, reportedly inferred by decreased bone tissue strength (Keyak et al., 2005), rigidity (Anez-Bustillos et al., 2014) and stiffness (Benca et al., 2017), or to corresponding increases in local bone tissue strain (Palanca et al., 2018), vertebral bulge (Salvatore et al., 2018) and microdamage (Choudhari et al., 2016, Atkins et al., 2019). A number of these studies analysed bone tissue samples where lytic lesions were introduced artificially (Keyak et al., 2005, Anez-Bustillos et al., 2014, Benca et al., 2017, Palanca et al., 2018, Salvatore et al., 2018). In other studies, bone samples with naturally formed metastatic osteolytic lesions were imaged using computed tomography (CT) and 3D reconstructed to develop the FE models (Choudhari et al., 2016, Atkins et al., 2019, Costa et al., 2019). These studies revealed that principal strain was elevated in regions of osteolytic lesions (Choudhari et al., 2016), which correlated with locations of microdamage (Atkins et al., 2019) and bone tissue of low mineral density in both osteolytic and non-lesion metastatic vertebrae (Costa et al., 2019). However, the changes in mechanical strain stimuli that arise as a consequence of osteolytic lesion formation during bone metastasis are not fully understood. The above studies highlight a need to characterise how the bone tissue mechanical microenvironment evolves *in vivo* as bone metastasis progresses.

In addition to evolving changes in bone tissue physical properties, the presence of a developing primary tumour mass may also contribute to changes in the bone tissue mechanical environment (see Figure 1). As a solid primary tumour mass grows and stiffens over time, physiological forces such as surface traction, solid stress and interstitial fluid pressure may be exerted on its surrounding physical environment

(Ambrosi and Mollica, 2002, Jain et al., 2014). Thus, knowledge of how mechanical stimuli may affect the evolution of the bone tissue mechanical environment, and ensuing mechanobiological responses by bone cells, during osteolytic metastasis, is imperative to understanding the bone metastatic process. The second hypothesis of this thesis is "***Mechanical stimuli within the bone tissue microenvironment are altered during breast cancer bone metastasis and osteolysis".***

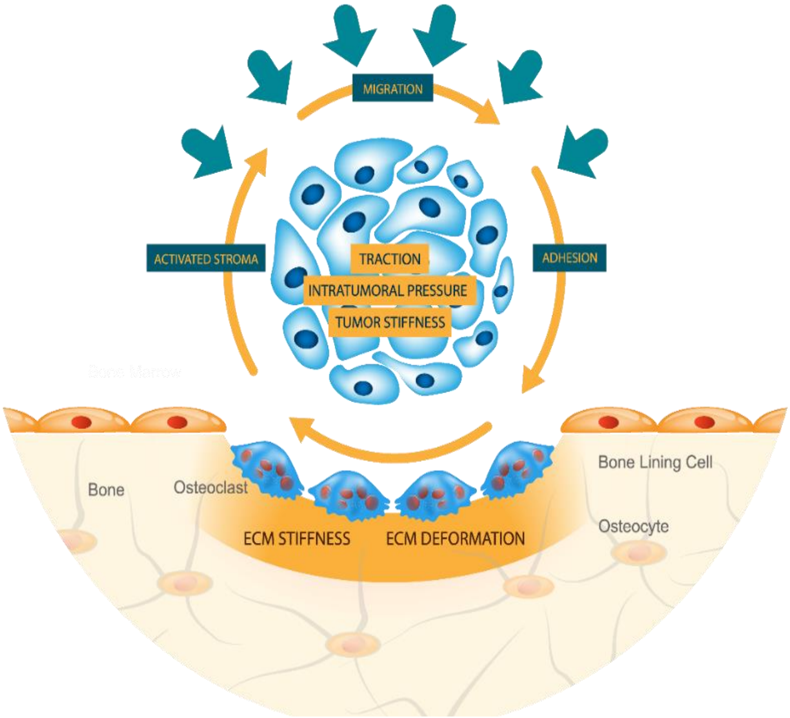

Figure 1.1: Metastatic invasion of the bone tissue extracellular matrix. Invading metastatic cells adhere to the bone tissue surface, activating resorption by osteoclasts, reducing stiffness and bone mineral density as a response. Such bone tissue resorption subsequently results in the release of growth factors, which activate metastatic cells within the tumour stroma to undergo further proliferation and thereby perpetuate the cancer vicious cycle.

If the second hypothesis of this thesis is true, a significantly altered mechanical environment may influence the remodelling behaviour of resident bone cells (osteoblasts, osteoclasts, osteocytes) during osteolytic bone tissue metastasis. This would, in turn, effect the release of growth factors during bone tissue resorption, and therefore potentially play a role in the cancer vicious cycle. Returning to mechanoregulation theory, changes in mechanical strain may induce increased osteoblast activity (increased strain beyond a threshold) or upregulate osteoclastogenesis (decreased strain below a threshold) (Frost, 1996, McNamara and Prendergast, 2007). Therefore, alterations in mechanical strain stimuli during early bone metastasis may induce increased osteoclast activity and bone tissue resorption, manifested as the subsequent development of osteolytic lesions reported in late metastasis.

Mechanoregulation theory has been applied to *in silico* models, via the coupling of finite element analysis and computational algorithms, to predict the adaptation of bone tissue to changes due to mechanical stimuli within the local environment. This methodology involves defining the material properties of each element within a model mesh according to a predefined mechanical stimulus and mathematical expressions that describe the evolution of these properties to achieve homeostasis over multiple iterations to account for time dependence. In this way, mechanoregulation theory has been used to predict bone formation and resorption in healthy bone (Schulte et al., 2011, Schulte et al., 2013, Pereira et al., 2015, Cheong et al., 2020a), tissue undergoing repair (McNamara and Prendergast, 2007) and osteoporotic bone (Mulvihill et al., 2008, Schulte et al., 2013, Cheong et al., 2020b). In many of the above studies, the bone regions of interest were imaged using computed tomography (CT) and these scans 3D reconstructed for FE simulations, to ensure *in vivo*-specific bone geometry, density and stiffness, and most often introduced strain or strain energy density as the driving mechanical stimuli. In one recent study, strain energy density driven mechanoregulation was simulated in high resolution µCT-FE models of murine tibiae, and accurately predicted regions of bone tissue apposition in both healthy and osteoporotic bone tissues (Cheong et al., 2020b). Notably, however, this algorithm did not succeed in accurately predicting bone tissue resorption (Cheong et al., 2020b), thus there remains a need to predict the development of osteolytic lesions, guided by experimental analysis at time points before and after their development. Taking together hypothesis 1 and hypothesis 2 above, if changes occur within the bone tissue microenvironment upon metastasis and these changes alter the mechanical stimuli within this environment, simulations of mechanoregulation theory could provide new insights into the potential impact of such altered bone tissue on osteoclast activity and subsequent osteolysis during the cancer vicious cycle. Notably, while this study focuses on osteolytic breast cancer metastasis, this computational model and coupled algorithm could be later adapted for predicting metastatic progression in alternative models of osteoblastic metastases and varied cancer types. Thus, the final hypothesis of this thesis is "***Changes in mechanical strain of bone tissue during metastasis may***

drive bone cell activity and subsequent bone tissue resorption, thereby contributing to osteolysis and the cancer vicious cycle."

1.4 Objective and Hypotheses

The global objective of this PhD thesis is to investigate the mechanobiological origins of osteolysis during breast cancer metastatic invasion into bone tissue. The primary objective of this PhD thesis is to investigate whether the physical properties of bone tissue extracellular matrix are altered during early metastasis, prior to overt osteolytic destruction. The second objective is to establish whether these changes significantly alter the mechanical environment of bone tissue at this early stage of metastasis. The final objective is to predict, using computational modelling and mechanoregulation theory, the impact of changes in the mechanical environment on bone tissue adaption during early metastasis, and investigate whether mechanobiological cues contribute to later stage metastatic osteolysis and the cancer vicious cycle. Three hypotheses have been defined to address these three objectives, each of which will underpin the research of chapters 3-5 of this thesis.

- **Hypothesis 1:** Bone mineral content and mechanical properties are altered during breast cancer bone metastasis
- **Hypothesis 2:** Mechanical stimuli within the bone tissue microenvironment are altered during breast cancer bone metastasis and osteolysis
- **Hypothesis 3:** Changes in mechanical strain of bone tissue during metastasis may drive bone cell activity and subsequent bone tissue resorption, thereby contributing to osteolysis and the cancer vicious cycle

1.5 Thesis Structure

This thesis comprises the work completed for the duration of the candidate's PhD studies. A review of the current literature is presented in chapter 2, detailing bone metastasis, the cancer vicious cycle, bone hierarchical structure, bone cells, remodelling, mechanobiology, mechanoregulation theory, and the known impact of bone metastasis on bone physical properties. Chapter 3 investigates how the microenvironment and mechanical properties of bone tissue are altered during metastasis, testing hypothesis 1 of this thesis. Chapter 4 tests hypothesis 2 by investigating (a) whether mechanical stimuli within the bone microenvironment are significantly altered during metastasis and (b) whether the presence of a primary tumour mass could contribute to these changes. Chapter 5 investigates whether mechanobiological cues contribute to later stage metastatic osteolysis and the cancer vicious cycle, by applying mechanoregulation theory to predict bone tissue adaptation during metastasis. Finally, chapter 6 summarises the main findings of this thesis, placing them in the context of current understanding of bone mechanoregulation during breast cancer bone metastasis and osteolysis, and outlines recommendations for future research in the field.

Chapter 2: Literature Review

2.1 Breast Cancer Bone Metastasis

Breast cancer is the leading cause of cancer death in women in the world, with a recorded 627,000 deaths in 2018 (Bray et al., 2018), and projected to reach 800,000 by 2030 (Cardoso et al., 2018). While patients diagnosed with early stage breast cancer (stages I to III) have an optimistic chance of 5-year survival (99%), survival rate in the final stage of cancer (IV, metastatic) decreases to approximately 27% (Siegel et al., 2019). Currently, there is no definitive cure for metastasis. Surgical intervention, radiotherapy and chemotherapy are all mitigating treatments with patient-specific results. More recently, a variety of chemical drug treatments have shown potential in impeding metastasis but come with considerable side-effects. Bisphosphonates, shown to secrete cancer-inhibitory epidermal growth factor receptor (EGFR) (Robert and Reinhold, 2015), come with increased risk of mandibular osteonecrosis (Woo and Solomon, 2007), while denosumab, an antibody to RANKL, reportedly causes skin infections which require hospitalization (Jie et al., 2019). Therefore, a greater understanding of the precise mechanisms which govern metastasis is imperative for the discovery of more promising treatment options.

When breast cancer cells migrate from a primary tumour, the target site for metastatic development is bone tissue in 70-80% of reported cases (Coleman and Rubens, 1987, Kretschmann and Welm, 2012). A long-standing theory proposed by Paget (1889), suggests bone tissue is a particularly attractive ‘soil’ for a metastatic cell (‘seed’) to occupy and proliferate. Healthy bone tissue undergoes constant regulation by continuously resorbing old, damaged tissue and replacing this with new, strong tissue in a process known as bone remodelling. The effect of the external tissue mechanical environment on cellular behaviour (‘mechanobiology’) influences osteocyte cells to continuously regulate this process. Breast cancer bone metastasis most often results in excess bone tissue resorption, known as osteolysis (Kozlow and Guise, 2005) and is reported to coincide with reduced bone tissue strength, density and mineral content (Kaneko et al., 2003, Arrington et al., 2008, Nazarian et al., 2008, Palanca et al., 2021a). Given the mechano-sensitive nature of osteocytes, such changes within the mechanical environment of bone tissue are proposed to influence the cancer vicious cycle (Zheng et al., 2013). Indeed, mechanical stimulation of long bones, either via direct loading mechanisms or with the introduction of exercise regimes, has reported to increase interstitial fluid flow, hydrostatic pressure and tissue strain within the bone marrow and subsequently inhibit breast cancer cell extravasation (Lynch et al., 2020). However, the precise role of mechanobiology during the cancer vicious cycle is not fully understood. Furthermore, how the microenvironment of bone tissue is altered prior to the development of osteolysis, and how these early changes in bone tissue composition and mechanical properties could influence later osteolytic destruction, have not yet been explored. This thesis seeks to characterise changes in the bone extracellular matrix as breast cancer metastasis invades, to provide important insights into the key mechanisms which may play a role in bone tissue osteolysis.

2.1.1 The Metastatic Pathway

Metastasis occurs when cancer cells migrate from a primary tumour site and colonise a secondary organ, and is the primary cause of mortality in cancer patients (Weigelt et al., 2005, Langley and Fidler, 2007). The journey of breast cancer cells from the primary tumour mass to secondary sites within the skeletal system involves direct interaction between cancer cells and homeostatic factors of the host immune system, which work to inhibit tumour migration.

Individual tumour cells undergo each of the following stages to successfully metastasise, or otherwise face termination (see Figure 2.1). **Transformation:** Healthy cells within the human body undergo abnormal proliferation, becoming neoplastic and forming a tumour mass which initially remains within confined borders (benign), categorised as stage I cancer. As this can stem from any cell type, over one hundred different variations of cancer can form (Cooper and Hausman, 2000). **Angiogenesis:** Chemokines (CXCL1-3 and CXCL8) released from tumour cells act as autocrine growth factors to induce vascular growth (Kakinuma and Hwang, 2006). This enables further cancer cell proliferation, thus forming a now malignant tumour mass and moving into stage II of cancer development. **Motility and Intravasation:** At the penultimate stage of cancer the primary tumour cells, now supported by a new capillary network, penetrate the surrounding endothelial barrier, with the possibility of also entering the lymphatic system (Cooper and Hausman, 2000). **Transport:** Once within the circulatory system, either through direct penetration or via the lymph nodes, cancer cells rapidly migrate to the distant target organ. According to Paget’s “Seed and Soil theory” the precise destination (‘soil’) must be suitable for the invading tumour type (‘seed’) or subsequent metastatic development will not be successful (Paget, 1889). During their travel to a secondary organ, the majority of circulating tumour cells are destroyed by the host concomitant immune response. For example, anti-tumour associated macrophages within the circulatory system release glycoproteins (IL-2, IL-6) and cytokines (CKCL9) to not only promote immunity but also elicit increased iNOS expression, directly killing tumour cells via nitric oxide (Janssen et al., 2017). **Arrest:** What remains of the cancer cell population finally attaches to the capillary bed and the endothelial layer of the new target organ, located far from the primary tumour site (Langley and Fidler, 2007). **Extravasation:** Tumour cells work to infiltrate the parenchyma of this secondary site and emerge within the target secondary organ. Notably, for bone tissue metastasis, the bone marrow niche is a reported site for metastatic extravasation to bone (Allocca et al., 2019) and is also where dormant tumour cells are reportedly located (Jinnah et al., 2018)**. Response to microenvironment:** Tumour cell interactions with bone cells (osteoblasts, osteoclasts, osteocytes), interactions with the mechanical microenvironment and biochemical factors (growth factors, chemokines) all influence the rate and impact of metastatic invasion within the secondary site (Kakinuma and Hwang, 2006). **Tumour cell proliferation and angiogenesis:** Following all of the above stages, and having overcome numerous obstacles presented by the host immune system, surviving tumour cells within the bone extracellular matrix must continue to proliferate and build a vascular network to facilitate the final phase, known as **metastasis** (Langley and Fidler, 2007). Inefficient angiogenesis by tumour cells within their new environment is reportedly a key cause of cancer cell dormancy (Gimbrone Jr et al., 1972).

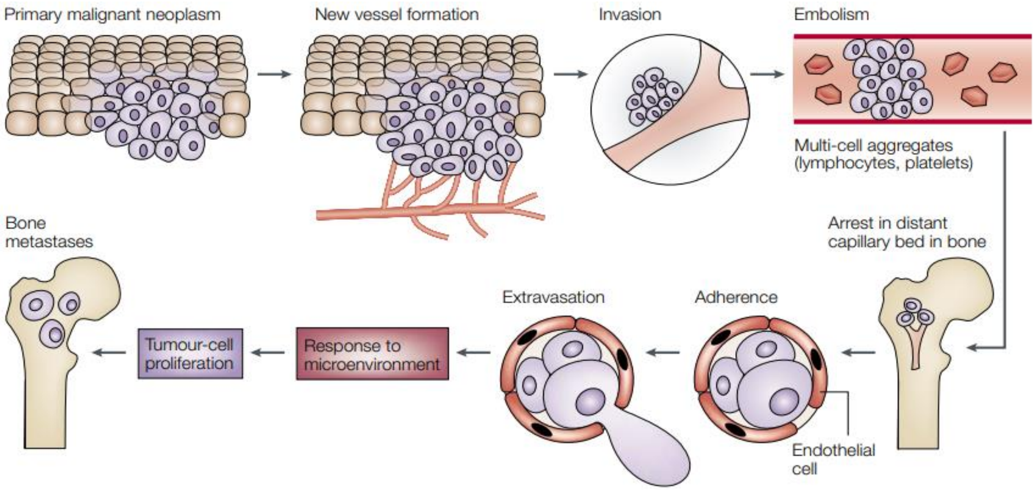

Figure 2.1: Flowchart of the Cancer Metastatic Pathway (Mundy, 2002). Cancer cells migrate from the primary tumour mass undergo angiogenesis to form a new vascular system, then infiltrate the capillary network and migrate to a distant organ such as bone tissue, evading host immunity along the way. Once at the distant organ, the surviving metastatic cells adhere to the capillary bed and extravasate to the target site, responding to stimulatory factors, such as mechanobiological cues, within the microenvrionment. These factors influence further tumour proliferation within the new metastatic cite and thereby perpetuate metastatic invasion.

2.1.2 Bone Tissue as an Attractive Environment for Metastasis

Upon arrival of metastatic cells within the bone extracellular matrix, a perpetuated system known as the cancer ‘Vicious Cycle’ begins (Paget, 1889). This process is composed of three phases, described further below in detail (see section 2.1.4). Interestingly, genes expressed from metastatic breast cancer tumour cells (MDA-MB-231) differ from those expressed by these same cancer cells, which remained within the primary tumour site. Specifically, upregulation of MMP-1, IL-11 and CXCR-4 were expressed by these metastatic cells, promoting bone-resorbing enzyme secretion (proteolysis), osteoclastogenesis and homing to bone tissue, respectively (Langley and Fidler, 2007). Metastasis leads to bone tissue destruction (osteolysis), the formation of new bone tissue (osteoblastic metastasis) or a combination of osteoblastic and osteolytic metastases (Mundy, 2002, Clines and Guise, 2005, Kozlow and Guise, 2005). Metastatic invasion of the skeletal environment leads to severe pain, increased fracture risk, nerve compression and hypercalcemia (Clines and Guise, 2005, Kozlow and Guise, 2005).

2.1.3 Osteoblastic and osteolytic Metastasis

Osteoblastic metastasis is recognised as new, high density bone formation and has the opposite resulting effects as osteolytic metastasis, in that the bone tissue is formed rather than resorbed. 20% of advanced cancer patients experience mixed osteoblastic-osteolytic bone tissue (Kozlow and Guise, 2005). While the precise mechanisms by which osteoblastic lesions develop are not well understood, TGF-β and VEGF release by invading tumour cells may upregulate the Wnt pathway and downregulate dikkopf-1, a Wnt pathway antagonist, to thereby encourage osteoblastogenesis (Jinnah et al., 2018) (see Figure 2.2A). An *in vitro* study of the effects of prostate-specific antigen (PSA), this antigen cleaves PTHrP and would, theoretically, inhibit the bone resorption process *in vivo* and allow for osteoblast formation of new lesions (Iwamura et al., 1996). Prostate cancer cell lines are most commonly used to study osteoblastic metastasis in murine studies (Dai et al., 2016). Carcinoid, lung cancer, Hodgkin lymphoma and medulloblastoma have also reportedly formed osteoblastic lesions (Macedo et al., 2017). Osteoblastic metastasis is directly influenced by inflammatory cytokines such as TNFα (Ganguly et al., 2014), growth factors such as TGF-β (Logothetis and Lin, 2005), and bone morphogenic proteins (BMPs) (Masuda et al., 2004). When compared to healthy bone formation, the resulting osteoblastic tissue is reportedly higher in bone mineral density (Kozlow and Guise, 2005), but also greater in material homogeneity (Burke et al., 2017) which is previously theorised to lead to increased bone brittleness and fracture risk (Boskey et al., 2009, Renders et al., 2011).

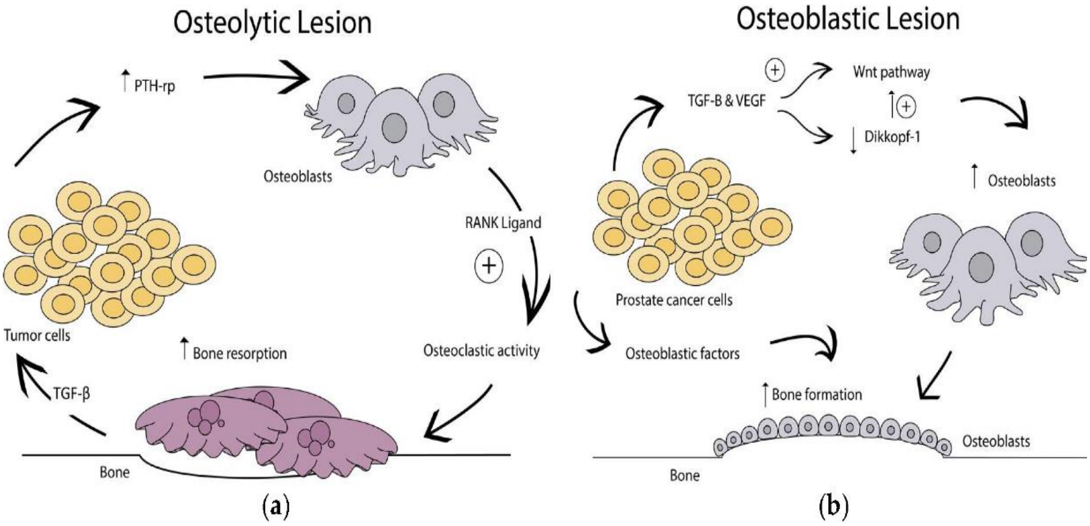

Figure 2.2: Schematics of key biological cells and processes involved in (a) osteolytic and (b) osteoblastic metastasis. a) Osteolytic lesion development is perpetuated by the release of PTHrP from invading metastatic cells, triggering an imbalance in the RANKL/OPG ratio and an increase in osteoclastic activity and bone resorption, subsequently eliciting the release of TGF-β and PTHrP and further tumour

cell invasion proliferation and invasion. b) During osteoblastic lesion development, growth factors (TGF-β, VEGF) released by invading tumour cells upregulate the Wnt pathway while downregulating dikkopf-1, triggering osteoblastogenesis and the formation of new bone tissue of higher density (Jinnah et al., 2018).

While approximately 20% of breast cancer metastatic invasion results in osteoblastic metastasis, the remaining 80% of advanced patients undergo osteolytic metastasis (Kozlow and Guise, 2005). Osteolytic metastasis is the loss of bone extracellular matrix due to the interference of invading tumour cells and their manipulation of osteoclast cells (Taube et al., 1994, Selvaggi and Scagliotti, 2005). Such resorption stems from the release of PTHrP from invading tumour cells, overactivity of osteoclasts, inhibition of osteoblasts, and the subsequent release of TGF-β from resorbed bone tissue, in a process known as the cancer 'vicious cycle' (see section 2.1.4 below). Ultimately, osteolytic metastasis results in net bone tissue resorption, where little or no repair occurs (Zheng et al., 2013).

Osteolytic metastasis can be exacerbated by multiple factors. Firstly, metabolism appears to play a key factor in metastatic activity. In a study of BALB/c mice of 6 week old and 12 week old cohorts inoculated with cancer cells via intracardiac injection, the frequency of both breast cancer (MDA-MB-231 cell line) and prostate cancer (PC3 cell line) metastatic tumours had significantly increased in younger models, correlating with higher metabolic activity and greater bone turnover rate (Wang et al., 2015). This was despite no change in metastatic cell number (Wang et al., 2015). Secondly, oestrogen deficiency, a key ailment of post-menopausal women which elicits subsequent osteoporosis, is also indicated to accelerate osteolytic destruction in patients with advanced breast cancer metastasis. Specifically, oestrogen receptor α (ERα) and oestrogen receptor β (ERβ) are expressed by both osteoblasts and invading breast cancer cells. While ERα tumours have been associated with a threefold increase in the occurrence of bone metastasis compared to oestrogen-negative tumours (Koenders et al., 1991), the specific role of Erβ is not yet known (Farach-Carson et al., 2017). Finally, insufficient calcium and vitamin D levels have also been linked to more progressive osteolytic metastasis (Chen et al., 2010).

2.1.4 The Cancer Vicious Cycle

Phase 1 – Secretion of osteolytic factors: Upon arrival within the bone marrow niche, cancer cells have the ability to undergo osteomimicry; invading tumour cells express genes normally recognised within the bone extracellular matrix, which allows them to invade, adhere, survive and proliferate relatively undisturbed (see Figure 2.3) (Chen et al., 2010). The most important of these factors is PTHrP, which initiates bone tissue resorption by binding to the G protein-coupled PTH receptor that is present on osteoblasts (Langley and Fidler, 2007). In this way, PTHrP upregulates the expression of RANKL and downregulates OPG on osteoblast precursors, osteoblasts and osteocytes (Zheng et al., 2013). An imbalance in the RANKL/OPG ratio elicits bone formation in mature osteoblasts while also triggering the differentiation of osteoclast precursors. PTHrP also stimulates vascular endothelial growth factor (VEGF), the interleukin-11 cytokine (IL-11) and macrophage colony stimulating factor (MCSF), which induce osteoclast formation, activity and proliferation, respectively (Clezardin and Teti, 2007). In addition, metastatic cells secrete factors such as osteopontin (OPN), bone sialoprotein (BSP), matrix metalloproteinase (MMP-1), more cytokines from the interleukin family (IL-1, -6, -8), and chemokine receptor CXCR-4. Specifically, OPN promotes osteoclast adhesion to the bone surface (Clezardin and Teti, 2007), BSP has been shown to act as a chemo-attractant for breast cancer cells (Langley and Fidler, 2007), MMP-1 promotes bone-resorbing enzyme secretion (proteolysis), ILs contribute to osteoclast activation, and CXCR-4 promotes homing of metastatic cells to bone(Langley and Fidler, 2007). It is important to note that osteoblast, osteoclast and osteocyte behaviours have otherwise not been altered. Instead, the release of the above biochemical factors have been shown to upregulate osteoclastogenesis while downregulating osteogenesis, in an effort to subvert the healthy bone remodelling process.

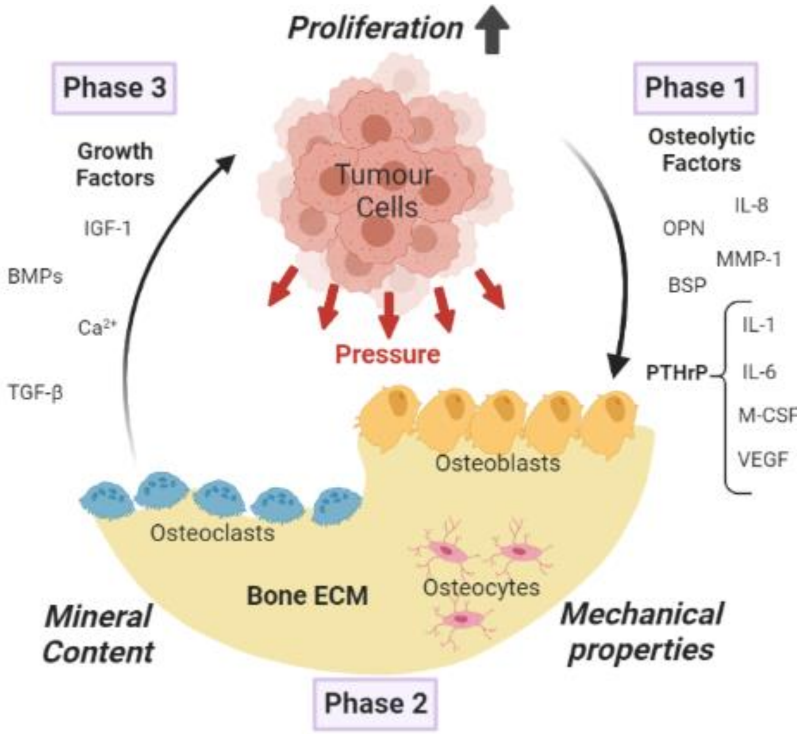

Figure 2.3: The Cancer Vicious Cycle: Phase 1: Invading tumour cells produce osteolytic factors that influence the behaviour of resident bone tissue osteoblasts and osteoclasts. Phase 2: In turn, mechanical properties and mineral content of bone tissue are altered, potentially eliciting a stimulatory response in mechanosensitive osteocytes within the bone ECM. Phase 3: Bone tissue resorption results in the release of growth factors**,** which are redirected to invading tumour cells to induce further tumour proliferation and the continuous release of PTHrP, thereby perpetuating the vicious cycle. (Created using BioRender.com)

Phase 2 – Lesion development: Factors released by the invading metastatic cells permanently alter local bone tissue quality, morphology, mineral content, and mechanical properties. Upon increased osteoclast activity due to the upregulation of RANKL, in approximately 80% of advanced breast cancer patients, the microenvironment undergoes excessive bone tissue resorption, known as ‘osteolytic metastases’. The remaining 20% also present regions of ‘osteoblastic metastasis’, where bone tissue of inferior quality and physical properties has formed (Mundy, 2002, Clines and Guise, 2005, Kozlow and Guise, 2005). Table 2.2-2.4 later demonstrate the specific changes in bone tissue morphology, mineral content and mechanical properties which have been reported in bone tissue of overt osteolytic lesions (see section 2.5.2).

Phase 3 – Further growth factor release: The bone extracellular matrix is a rich source of growth factors. These factors, which would aid in bone mineralisation and repair in healthy tissue, are instead redirected for tumour cell development upon lesion formation during the cancer vicious cycle (see Figure 2.3). Known factors include insulin-like growth factor 1 (IGF-1**)**, bone morphogenic proteins (BMPs), fibroblast-derived factors and calcium (Ca^{2+}) and transforming growth factor-beta (TGF-β) (Chen et al., 2010). The most notable of these factors, TGF-β, binds to its corresponding receptor on the surface of invading tumour cells, rather than promoting osteoblastogenesis as would occur during regular bone remodelling. In this way, activity and proliferation of bone-forming osteoblasts is inhibited, while TGF-β simultaneously promotes the growth and proliferation of invading metastatic cells (Langley and Fidler, 2007). In this final phase, the increased growth and activity of metastatic cells leads to further release of osteolytic factors, thereby returning to phase 1 of this process and the vicious cycle is perpetuated. The cancer vicious cycle, and the osteolytic lesions which form as a result, lead to bone pain, increased risk of fracture failure and hypercalcemia (Clines and Guise, 2005, Kozlow and Guise, 2005).

2.2 Bone Tissue Composition and Biomechanics

The skeletal system is vital for structural support, movement, protection of organs, calcium storage and houses the bone marrow within the human body. Bone is composed of haematopoietic stems cells, mesenchymal stems cells (MSCs), a vascular system, bone marrow stroma and the bone extracellular matrix. Bone tissue is composed of a complex hierarchical structure, which stems from the macroscale (cortical and trabecular bone regions) to the cellular level (osteoblasts, osteoclasts, osteocytes). Knowledge of bone tissue modelling and remodelling processes is vital for understanding the behavioural abnormalities that occur during breast cancer metastatic invasion.

2.2.1 Bone tissue hierarchical structure

Bone tissue is a natural composite material composed of a hierarchy of layered components, as in Figure 2.4, forming an anisotropic, viscoelastic tissue capable of withstanding high loads (Rubin and Jasiuk, 2005). One third of bone matrix is comprised of organic compounds categorised as either collagenous or non-collagenous proteins (NCPs) such as osteocalcin, osteopontin, osteonectin and bone sialoprotein. Ninety percent of the organic matrix contains Type I collagen, a fibrous tissue that provides tensile strength and ductility. When mineralised collagen fibrils are uniformly oriented, they combine to form lamellae, which in turn form concentric layers until long tube-like structures called osteons are formed. Osteons are the primary structural unit of bone, providing a suitable internal longitudinal space, known as the Haversian Canal, for blood vessels (Figure 2.4) (Vaughan et al., 2012)**.** Collagen fibril quality and orientation are therefore key contributors to bone stress, while bone density and mineral content are associated with bone tissue stiffness (Augat and Schorlemmer, 2006). Collagen cross-linking behaviour has proven to directly facilitate the bone mineralisation process via deposition of carbon hydroxyapatite (HA) crystals (Hunter and Goldberg, 1993, Saito and Marumo, 2010).

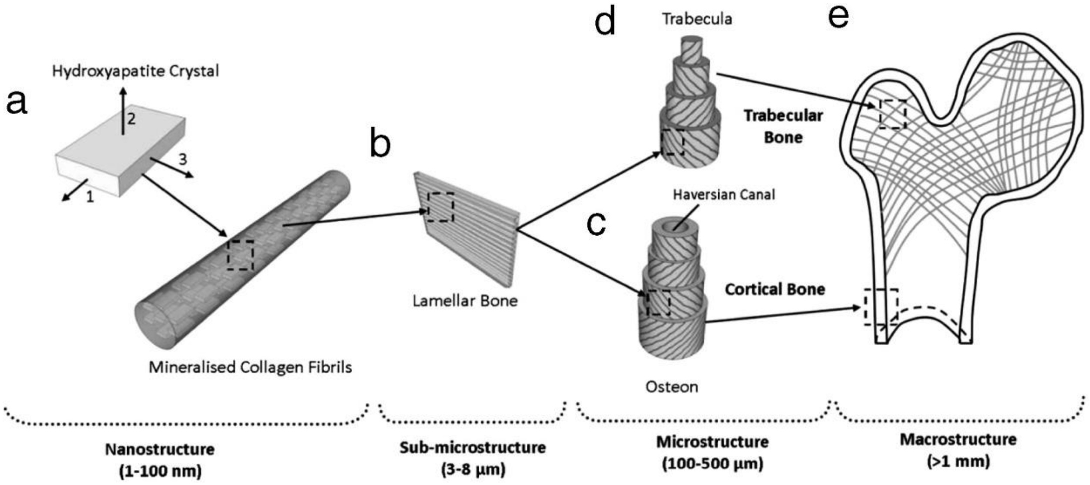

Figure 2.4: Illustration of bone tissue structural hierarchy. Diagram of the layered components of bone tissue from nanoscale to macroscale. Clustered hydroxyapetite crystals adhere to collagen fibrils, which combine to form a single lamellae. These lamellar in turn form osteons, the primary structural unit of bone tissue. An abundance of osteons and lamellae make up the bone tissue structure, divided into cortical and trabecular sub-regions (Vaughan et al., 2012).

2.2.2 Cortical and Trabecular Bone Tissue

The bone macroscale structure is divided into two key regions; a cortical bone tissue layer, and ‘spongy’ trabecular bone tissue which lies within the cortical bone shell. This configuration of an outer, densely packed bone tissue shell and porous internal bone tissue region is ideal in vertebrates, withstanding high functional loads while reducing stress and strain in skeletal joints (Hamed et al., 2010). Cortical bone tissue makes up 85% of total bone mass within the musculoskeletal system and is compact due to its highly mineralised condition, providing support and structure to the human body to undergo everyday activities (Clines and Guise, 2005). Within compact cortical bone tissue lie lacunae, crevices between layers of collagen fibrils that house mechanosensitive osteocytes (Ashique et al., 2017). These collagen fibrils run longitudinally within the dense cortical tissue, allowing for dense cortical bone to withstand high stresses in this direction. Canaliculi, small openings between each lacunae, form the lacunar-canalicular network (LCN), which allows for cellular communication vital for bone modelling and remodelling processes (Ashique et al., 2017), and has a magnitude of complex branches comparable to the neural network of the human brain (Buenzli and Sims, 2015). Cortical bone tissue has a relatively low bone turnover rate of 2-3% per year in human adults (Clarke, 2008).

Trabecular bone tissue lies internal to cortical bone and is described as ‘spongy’ due to its approximately mesh-like features and 80% porosity (Fratzl and Weinkamer, 2007). Trabecular struts function to evenly distribute and reduce strains throughout the bone connective tissue upon mechanical loading. Indeed, results from high-resolution computational models mimicking weight-bearing loads in a human ankle bone suggest the arrangement of trabeculae is imperative for the even dispersal of loads applied to the cortical bone surface (Parr et al., 2013). Notably, trabecular bone has a higher rate of bone turnover and metabolic activity compared to cortical bone tissue in human patients (Clarke, 2008). Collectively, these micro and macroscale components of bone form a structure of great stiffness, density, and strength to counteract high loading and unloading cycles expected during regular activity in vertebrates.

2.2.3 The Bone Extracellular Matrix

The extracellular matrix (ECM) resides within the bone microenvironment and is composed of functional proteins (primarily collagen), proteoglycans (GAG) and adhesive glycoproteins (fibronectin, laminin) (Wang and Thampatty, 2006). As a mechanosensitive biological material, bone ECM is a source of mechanobiological cues for regular bone remodelling (Lynch et al., 2020) and its material properties dictate bone fragility and mechanical strength. This connective tissue is the site for bone cellular interactions and provides exposed surfaces for the adhesion of cell receptors, facilitating cell migration, growth and differentiation (Wang and Thampatty, 2006). Importantly, bone ECM is an abundant source of growth factors including vascular endothelial growth factor (VEGF), insulin-like growth factor I (IGF), bone morphogenic proteins (BMPs) and, most notably, transforming growth factor beta (TGF-β) (Chen et al., 2010).

2.2.4 Collagen and Bone Mineral

Biomineralization is the process by which hard tissues are biologically produced. Thirty-five percent of mature bone tissue is organic in nature, containing approximately 90% collagen, 10% non-collagenous proteins (NCPs), water, lipids and cells (McNamara, 2011). Collagen is a constitutive protein, which is the key component of matrix formation, and thereby a fundamental building block of all connective tissue throughout the human body. The basic structural unit of collagen, tropocollagen, is rod-like in structure, 280-300 nm in length and 1.5 nm in diameter, and is formed from three polypeptide strands (α-chains) twisted to form a triple-helix configuration (McNamara, 2011, Bonucci, 2012), see Figure 2.5. A whole collagen fibre structure is thereby formed in a staggered arrangement of cross-linked tropocollagen molecules, aligned in parallel to form 'lamellae'. The most abundant collagen type in bone tissue extracellular matrix, at approximately 95%, is collagen type I (Niyibizi and Eyre, 1994), with type III, IV and VI also present. The precise organising of collagen molecules and collagen fibrils provide bone tissue with strength, elasticity and toughness (McNamara, 2011). The vital role of collagen is demonstrated in bone clinical disorders such as in osteogenesis imperfecta (mutations within the triple helix), Paget's disease (misaligned collagen fibres), lathyrism (cross-linking is impaired) and osteoporosis (genetic abnormalities leading to irregular collagen production) (Viguet-Carrin et al., 2006).

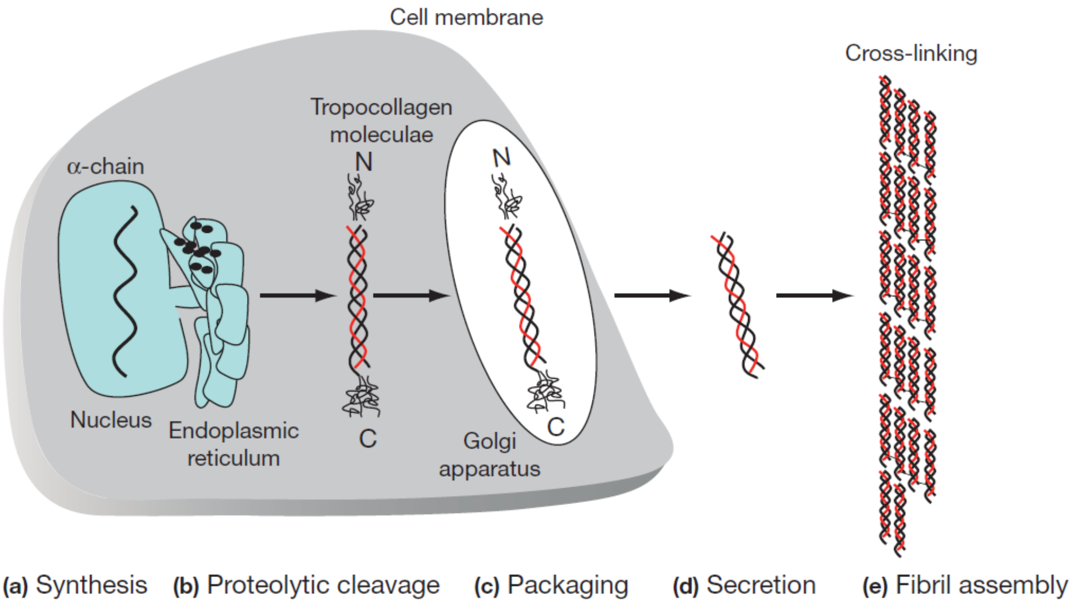

Figure 2.5: Intracellular synthesis and assembly of type I collagen in the osteoblast (a–c) and extracellular formation of collagen fibrils (d–e) (McNamara, 2011).

While 35% of bone tissue is ‘organic’ in nature, the remaining 65% of tissue content is ‘mineral’, a complex inorganic system comprised of calcium and phosphorus, which form hydroxyapatite crystals. Collagen molecules form natural gaps between which water is distributed and hydroxyapatite crystals become nucleated (Hamed et al., 2010). The diamond-shaped hydroxyapatite molecular structures then adhere in a uniform distribution around the collagen fibrils and orientate themselves in line with the fibril structure. Although the specific mechanisms of hydroxyapatite crystal formation are not fully understood, it is theorized that amorphous calcium phosphate (ACP), composed of closely packed Posner's ion clusters, undergoes autocatalytic transformation to form these stable crystalline constructs (Posner and Betts, 1975, Roohani et al., 2021). The inorganic bone material appears to undergo the following sequence of steps to establish calcification: 1) Osteoblasts generate matrix vesicles, 2) within these vesicles, calcium nodules and islands are formed, grow in size and merge to become crystalline in structure, 3) collagen fibrils aggregate and 4) calcified crystals propagate and orient themselves in alignment with their surrounding collagen fibril structures (Bonucci, 2012). Polycrystalline hydroxyapatite (HA) formation initiates at relatively low densities and gradually increases with bone tissue maturation (Wergedal and Baylink, 1974). The inorganic phase of bone tissue is the primary contributor to bone physical properties, including bone strength, elasticity, toughness, and hardness.

2.2.5 Analysis of Bone Tissue Composition and Mineral Content

A key method for establishing the health of bone tissue is by evaluating its tissue mineral content and microarchitecture. A variety of popular techniques are currently utilised to perform detailed analysis of bone tissue composition and mineral quality, including computed tomography (CT), qualitative backscatter emission microscopy (qBSEM), dual energy X-ray absorptiometry (DEXA), Raman spectroscopy and Fourier transform infrared spectroscopy (FTIR). Of these techniques, CT is the only methodology that combines non-destructive analysis with visualisation and detailed bone mineral density distribution (BMDD) analysis throughout a three-dimensional region of interest. For analysis of changes in patient bone mineralisation, quantitative computed tomography (QCT) is most often performed to analyse these large human bone tissue samples requiring lower image resolution, a measurement inversely related to image pixel size. In contrast, micro-computed tomography (micro-CT) must be used for analysis of murine bone samples which are far smaller in scale and therefore require higher resolutions for precise measurement of cortical and trabecular content. While standard desktop micro-CT imaging is a highly efficient process for bone tissue analysis, it must be noted that limited resolutions and image artefacts, discussed in detail below, constrain the ability to analyse local bone tissue mineralisation at this scale. An alternative method, synchrotron (SR) micro-CT, reduces the incidence of such artefacts by emitting a high-flux, high-intensity and monochromatic X-ray beam, resulting in high-resolution images at a high signal-to-noise ratio. However, the relative inaccessibility of synchrotron facilities limits the widespread use of this technique. Of the techniques above, in the past four decades, micro-CT analysis has become the ‘gold standard’ for analysing bone tissue morphology and microarchitecture, especially in rodent models (Bouxsein et al., 2010). While *in vivo* micro-CT imaging allows for longitudinal analysis of the same animal models throughout a study, *ex vivo* micro-CT allows for higher resolution images, with voxel sizes as low as 5μm, and therefore was the chosen method used for the purposes of this thesis.

Within a CT machine lies a microfocus x-ray tube, which must first pass through a collimator to concentrate the emitted photons into a beam, and through an aluminium filter to reduce hardening effects (see Figure 2.6). This beam then permeates the sample before reaching a detector for measurement of hydroxyapatite densities. Once emission and detection are complete, the sample is then rotated approximately 0.5 degrees and the process repeated. Upon complete rotation of a single sample, the resulting images are reconstructed into a 3D representation of the scanned region of interest. Prior to new sample imaging, micro-CT scans are performed in a similar manner on phantom samples of five different known hydroxyapatite densities (0, 100, 200, 400 and 800 mg HA/cm^3), daily and weekly, to ensure the machine is continuously calibrated. Higher bone mineral density (BMD) regions imply increased calcium content, collagen concentration and overall greater mineralisation of bone tissue due to heightened activity of osteoblasts in the analysed region. In contrast, lower BMD indicates a loss of bone tissue quality and lower mineralisation.

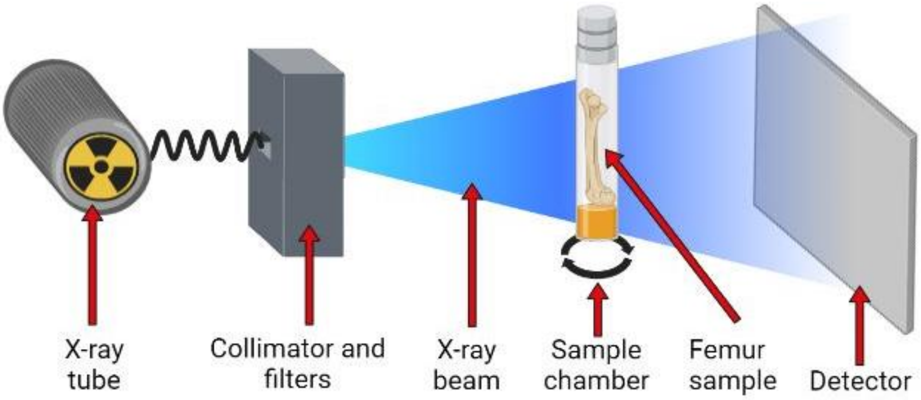

Figure 2.6: Components of a standard micro-CT scanner. Photons emitted from a microfocus x-ray tube are concentrated and filtered before the sample within a transparent chamber is exposed to the x-ray beam. The resultant image is captured on a detector. For each image captured, the sample is rotated by 0.5˚ and emission repeated. (Illustration created with BioRender.com)

Micro-CT imaging requires precise parameter adjustments to obtain the clearest visible scan resolutions, defined by its signal-to-noise ratio and whether impeding image artefacts are present. Beam hardening artefacts are generated when low energy photons are attenuated as the x-ray beam passes through the object of interest. This first issue is mitigated via both the application of an aluminium filter and also by integrating trinomial functions upon image reconstruction. Micro-CT images may also form ring artefacts, appearing as concentric circles, but these are removed by using a Gaussian filter of specified kernel and standard deviation (relating to filter thickness), and by an additional support of 1 or 2 voxels (Bouxsein et al., 2010).

Hydroxyapatite (HA) densities within a sample are measured in interchangeable units of HA mg/cm^3, Hounsfield units (HU) or grey values, with mg HA/cm^3 being the preferred unit for universal repeatability (Bouxsein et al., 2010). Connective tissues of a lower density, such as adipose and cartilage tissues, are eliminated by defining a density threshold value, below which is not considered to be bone tissue. It is vitally important that the chosen threshold level remains consistent throughout the study (Bouxsein et al., 2010). A variety of density thresholds for the analysis of murine bone tissue have been reported, from 247 mg HA/cm^3 to 513.7 mg HA/cm^3 (Ravoori et al., 2010, Wernle et al., 2010, Lynch et al., 2013, Cheong et al., 2020b), and this value commonly determined by finding a midpoint between the scanning background and peak bone density (Arrington et al., 2008, Willinghamm et al., 2010, Cheong et al., 2020b). While a variety of parameters may be measured using micro-computed tomography technique, the precise values of interest for quantifying changes in bone mineral content are outlined Table 2.1 below.

2.2.5.1 Bone Mineral Density Distribution Analysis

Bone mineral density distribution (BMDD) is a precise analytical technique which utilises histograms of tissue density to calculate changes in bone tissue mineralisation and uniformity. Previously detailed in the analysis of calcium content in human bone biopsies using quantitative backscatter electron imaging (qBEI) (Roschger et al., 2003, Ruffoni et al., 2007), this methodology has also been adapted for various imaging techniques of human bone tissue such as quantitative microradiography (Boivin and Meunier, 2002) and synchrotron radiation microtomography (Nuzzo et al., 2002). More recently, BMDD analysis has been a useful tool for assessing hydroxyapatite distribution in micro-CT scans of rodent bone tissue (Mashiatulla et al., 2017, O'Sullivan et al., 2020). This technique includes calculating the most frequent density value present within a VOI (M_{mode}), and categorising bone tissue mineral as low, normative, or especially high in hydroxyapatite density (M_{low}, M_{medium}, M_{high}, respectively) according to the 25th and 75th percentiles of density distribution. Finally, and arguably the most important value of BMDD, the Full Width at Half Maximum (FWHM) is a measure of bone tissue heterogeneity. FWHM is calculated by halving the M_{mode} and subtracting the corresponding upper and lower density values (Roschger et al., 2003). A detailed table describing each micro-CT output used in this thesis is presented below (Table 2.1). While micro-CT analysis is effective in measuring changes in bone mineral content, mechanical properties must also be measured to fully establish how the bone tissue microenvironment is altered during breast cancer metastatic invasion.

Table 2.1: Micro-CT and BMDD analysis parameters, standard acronyms, units and description (Ruffoni et al., 2007, Bouxsein et al., 2010)

Micro-CT parameter	Acronym	Units	Description
Cortical bone tissue			
Total bone surface area	Tt. Ar.	mm^2	Total surface area as outlined via micro-CT contouring
Cortical bone area	Ct. Ar	mm^2	Tissue area, within the total surface area, which exceeds the specific density threshold
Cortical bone fraction	Ct. Ar/ Tt. Ar.	%	Cortical bone surface area as a ratio of isolated tissue
Cortical thickness	Ct. Th	mm	Thickness of cortical tissue regions which reside above the specified density threshold
Trabecular bone tissue			
Total volume	TV	mm^3	Total VOI as outlined via micro-CT contouring
Bone volume	BV	mm^3	Bone volume, within the VOI, which exceeds the specific density threshold
Bone volume fraction	BV/TV	%	Trabecular bone tissue volume as a ratio of isolated tissue
Connectivity Density	Conn.D.	$mg\ HA/cm^3$	Measure of connectivity of trabeculae, normalised by TV
Structure model index	SMI	–	Measure of tendency of a trabecular strut to form cylindrical morphology (0-3)
Trabecular number	Tb. N.	1/mm	The average number of trabeculae, as a unit of trabecular length
Trabecular thickness	Tb. Th.	mm	Space, within the trabecular regions, which resides above the specified density threshold
Trabecular spacing	Tb. Sp.	mm	Space, between trabecular regions, which resides below the specified density threshold
Cortical and trabecular bone tissue			
Mean bone mineral density	M_{mean}	$mg\ HA/cm^3$	Average BMD value within the volume of interest
Mode bone mineral density	M_{mode}	$mg\ HA/cm^3$	Most frequent BMD value within the volume of interest
Low bone mineral density	M_{low}	%	BMD which has mineralised below the 25th percentile of the distribution
Medium bone mineral density	M_{medium}	%	BMD which has mineralised within a normative range of distribution
High bone mineral density	M_{high}	%	BMD which has mineralised above the 75th percentile of the distribution
Full Width Half Maximum	FWHM	$mg\ HA/cm^3$	Range of BMD within the M_{mode} half-height range, indicates tissue heterogeneity

2.2.6 Bone Mechanical Behaviour

Bone tissue physical structure, integrity and mechanical behaviour are governed by the organic and inorganic (mineral) phases of bone. In particular, the mechanical properties of cortical bone tissue (tissue stiffness, hardness, toughness, strength) are determined by collagen and hydroxyapatite alignment and orientation within the extracellular matrix. Bone tissue is generally described as having the following physical properties. **Heterogeneous:** It does not have uniformly distributed material properties, therefore, density and stiffness are unique to each location at a micro-scale. **Anisotropic:** As a consequence of unidirectionally aligned collagen fibrils, the mechanical properties measured are dependent on loading direction. **Poroelastic:** Bone tissue has both a solid and fluid phase, in that the presence of osteons make this material porous in structure, while also saturated by a vascular system. **Plastic:** The stress-strain curve of bone tissue is only uniform up to a yield point, beyond which its material behaviour is permanently altered. **Geometrically unique:** Due to changing physiological loads of daily activity and the constant bone remodelling process, bone tissue morphology is unique, even when comparing contralateral bones within the same host (McNamara, 2011).

Bone tissue differs in these mechanical properties between species, anatomical location, and between cortical and trabecular bone tissues. Bone tissue biomechanical behaviour also differs depending on the length scale at which its physical properties are measured. Macro-scale test methods such as 3-point bending, compression and tensile tests are common techniques for analysing the mechanical behaviour of bone tissue with natural or simulated lytic lesions. Young’s modulus, yield stress, strength, and strain energy density distribution can be obtained from these techniques, while also revealing regions of fracture failure in specimens with osteolytic lesions (Kaneko et al., 2003, Kaneko et al., 2004, Spruijt et al., 2006, Nazarian et al., 2008, Rennick et al., 2013, Cheong et al., 2020b). However, 3-point bending of murine femurs reportedly leads to underestimation of Young’s moduli because this method assumes perfect beam-like geometries and does not account for complex morphologies inherent in anatomical bone regions (van Lenthe et al., 2008), while compression and tensile tests are susceptible to loading misalignment and inaccurate estimation of the size of the contact surfaces (Wu et al., 2018). Importantly, given the hierarchical nature of bone tissue, bone stiffness (measured as Young’s modulus) and hardness of bone tissue differ between micro- and nano-scales (Chen et al., 2003). As such, nano-scale mechanical tests such as atomic force microscopy (AFM), ultrasonic acoustic methods and nanoindentation mechanical testing techniques may be used to measure changes in bone tissue stiffness at the sub-micron level. This thesis uses nanoindentation to determine the Young's modulus and hardness of bone tissue, an efficient and precise mechanical test method which is not effected by bone tissue size, shape or porosity (Rodriguez-Florez et al., 2013).

2.2.7 Characterising Bone Nano-Mechanical Properties

Nanoindentation involves applying a predetermined force or depth through an electromagnetic actuator mechanism, driving the tip of an indenter of especially high stiffness and hardness into the substrate surface. A high-resolution sensor then continuously measures the resulting penetration force. The G200 Nano Indenter (Keysight Technologies, USA), which was utilised for the purposes of this thesis, can test substrate at depths as low as 0.01nm, (0.0002nm tolerance), and a maximum load of 500 mN, (Keysight Technologies Inc., 2017) (Figure 2.7).

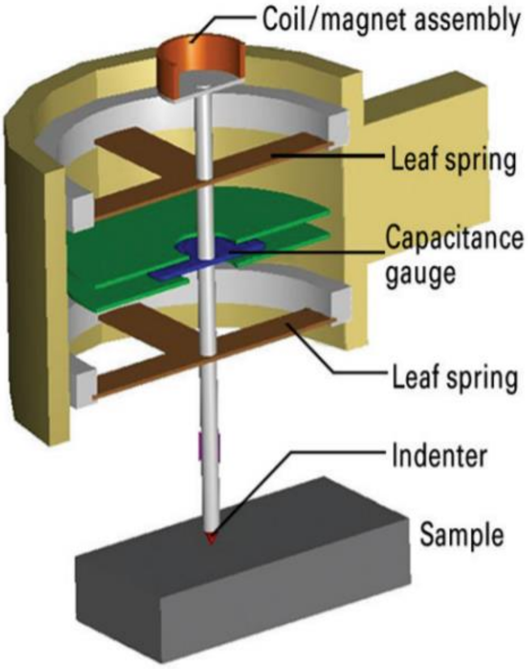

Figure 2.7: Nanoindenter assembly schematic. The Keysight G200 includes a coil/magnet assembly, directly manipulated via Keysight interactive software, to apply a predetermined load supported by a leaf spring mechanism. Displacement of the long indenter column throughout the structure is constantly measured using a capacitance gauge. A final leaf spring completes the overall indenter upper section or 'frame' (Keysight Technologies Inc., 2017).

Each nanoindentation mechanical test involves the loading and subsequent unloading of the Berkovich indenter into a substrate surface. According to nanoindentation pioneers Oliver and Pharr (1992), for any axisymmetric indenter such as the Berkovich, the slope of maximum load, P, and penetration depth, h, from the upper 25% of the resulting unloading curve are used to calculate the contact stiffness S (Figure 2.8). Contact stiffness was specifically calculated from the unloading curve because the loading curve would have included both plastic and elastic material deformation while the unloading curve reflects only elastic deformation recovery and therefore the elastic modulus can be calculated.

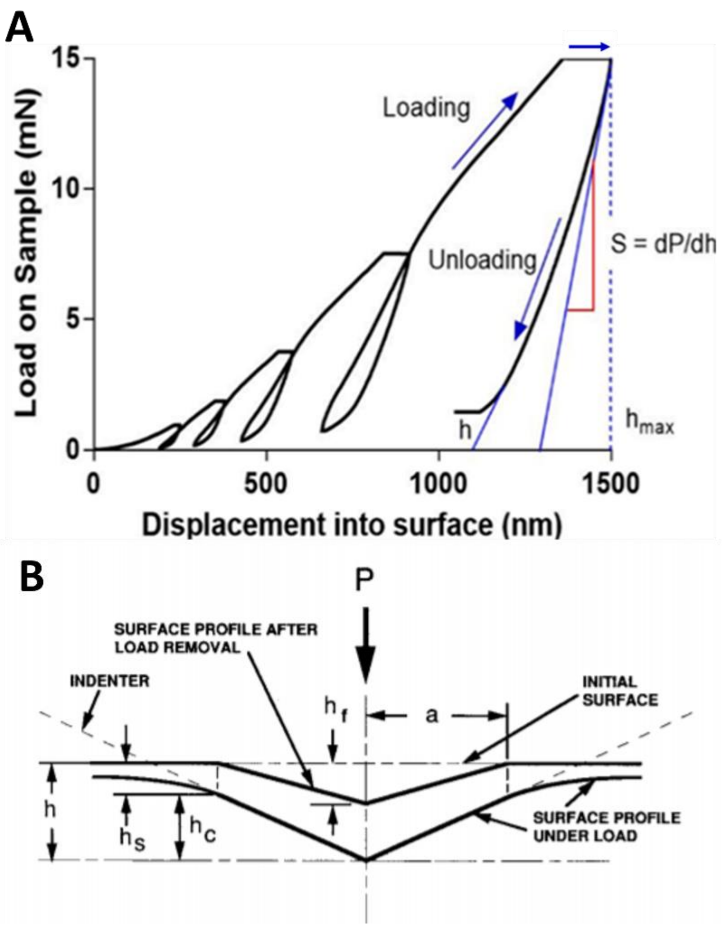

Figure 2.8: Nanoindentation loading curves and indentation heights. (A) Five-cycle nanoindentation regime, where the slope of the final unloading curve used to calculate contact stress of the indented bone tissue surface. (B) Profiles of a solid substrate surface following an indenter load and unload cycle, including the altered tip heights, h, and indented surface area, a (Oliver and Pharr, 1992).

This stiffness is also used to calculate the reduced modulus, E_r, where A_c is the contact depth. Despite the high stiffness and strength of a Berkovich indenter, the tip is still susceptible to blunting over time, resulting in gradual rounding of the diamond at point of contact and therefore a gradual change in tip area. The contact area of this complex geometry must therefore be calculated from established constants m, calculated as part of Keysight calibrations of the nanoindenter machine upon assembly, and with known contact depth h_c.

$$\frac{dP}{dh} = S = \frac{2}{\sqrt{\pi}} E_r \sqrt{A_c} \tag{2.1}$$

$$A_C = m_1 {h_c}^2 + m_2 {h_c}^1 + m_3 {h_c}^{1/2} + m_4 {h_c}^{1/4} + \ldots \, m_8 {h_c}^{1/128} \tag{2.2}$$

where the Berkovich indenter has a known and consistent Young's modulus, E_i (1141 GPa) and Poisson's ratio, ν_i, 0.07. Young's modulus of the indented material, E, is calculated using Equation 2.3 under the assumption that the indented tissue is isotropic, and utilises Poisson's ratio, ν. Finally, bone tissue hardness is calculated using with Equation 4, where P_{max} is the maximum load applied on a specimen surface (Pharr et al., 1992a).

$$\frac{1}{E_r} = \frac{(1 - v^2)}{E} - \frac{(1 - {v_i}^2)}{E_i} \tag{2.3}$$

$$H = \frac{P_{max}}{A} \tag{2.4}$$

The reduced Young's modulus and hardness of healthy C57BL/6 mouse femurs have previously been investigated via nanoindentation to investigate the anisotropy of cortical bone (Casanova et al., 2017). This study found a wide range of modulus values depending on loading direction and test location (minimum mean: 6.75 ± 0.50 GPa, maximum mean: 23.81 ± 2.47 GPa), and that both modulus and hardness were higher in the longitudinal direction compared to transverse tests and also found a low correlation in these properties between these two testing directions, suggesting independent testing should be conducted for murine bone nanoindentation, where available (Casanova et al., 2017). A later study conducted nanoindentation in the bone tissue in BALB/c mouse tibiae, in cortical (E = 24.3 ± 5.2 GPa, H = 0.9 ± 0.2 GPa) and trabecular bone tissue tests (E = 20.8 ± 4.1 GPa, H = 0.85 ± 0.2 GPa) (Pepe et al., 2020). Interestingly, this study found such mechanical properties differ significantly between mouse strains, and bone tissue on the medial side had higher stiffness (up to 13.2%) and hardness (up to 14.4%) than tissue tested in the anterior or posterior regions (Pepe et al., 2020).

2.2.7.1 Factors Affecting Nanoindentation Testing

In preparation for mechanical testing, bone samples are commonly fixed in hardened epoxy resin such as Polymethyl methacrylate (PMMA) and placed in a vacuum chamber such that all trapped air or micro-voids are filled (Shen et al. 2006). Sample dehydration has previously been reported to increase bone tissue stiffness in mouse tibiae (Rodriguez-Florez et al., 2013), theorised to be the result of an overall increase in collagen compliance of the bone composite (Hoffler et al., 2005). Specifically, water may behave as a plasticizer on collagen fibrils (Bembey et al., 2006). However, nanoindentation of dry bone tissue is deemed suitable for Oliver and Pharr calculations in comparative studies (Rho and Pharr, 1999), and gradual dehydration within the chamber during mechanical testing is a concerning additional factor that is best avoided by testing consistently dry samples. Bone tissue has viscoelastic properties, attributed to the presence of collagen fibrils. While spherical and cylindrical indenter tip shapes have been used in literature to indent soft and hydrated substrates, a sharp Berkovich diamond avoids buckling of bone tissue as the tip penetrates the surface (‘pile up’) or for local regions to collectively move in the direction of the indentation (‘sink in’), as in Figure 2.9A. This was avoided by utilising a brand new, and therefore very sharp, Berkovich indenter for mechanical testing and analysing trial indents within a fused silica sample to confirm no visual abnormalities in the indents, or irregular spikes in load and unload curves. Changes in the resultant contact area, in comparison to the nominal area, may lead to over- or underestimation of the elastic modulus and hardness (Bolshakov and Pharr, 1998). Bone tissue is also susceptible to creep due to its viscoelastic properties. Creep is best avoided by adding a ‘hold time’ such that the indenter tip remains at the peak loading depth for a predefined time period before measurements are taken, recommended as 15 seconds or higher per indentation (Wu et al., 2011). Local mechanical vibrations and thermal drift are two environmental factors to which the nanoindenter is especially sensitive (see Figure 2.9B) (Kuhn, 2000). As such, samples are housed within a suspended table that minimises the impact of external vibrations during testing, while a sealed thermal cabinet surrounding the entire machine setup reduces changes in environmental temperature. In addition, before each nanoindentation test commences, each new mechanical test is postponed until thermal drift remains below a predefined value of 0.001 mm/s. Finally, spacing between test sites must be at least 20 to 30 times the maximum depth applied to avoid edge effect influences between indents (Keysight Technologies Inc., 2017).

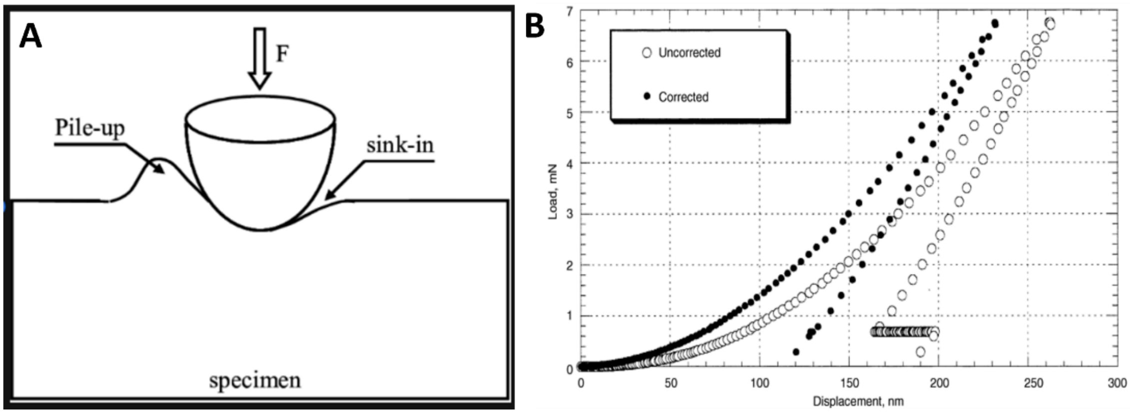

Figure 2.9 Factors effecting nanoindentaion mechanical testing. (A) Illustration of substrate 'pile up' and 'sink-in' effects upon loading into a specimen with force, *F*, with an insufficiently sharpened nanoindenter (Oumarou et al., 2010), (B) Two load-unload curves illustrating the importance of thermal drift, where the loading curve which has not been corrected for changes in environmental temperature (white datapoints) reaches greater maximum depth under the same applied force (black datapoints) (Kuhn, 2000).

2.3 Bone Biology and Mechanoregulation

Bone cell types reside within the bone tissue extracellular matrix and marrow, and dictate bone tissue formation and regulation, which specifically are osteoblasts, osteoclasts, osteocytes and bone-lining cells (Kenkre and Bassett, 2018). These cells are collectively described as the bone multicellular unit (BMU) and govern bone formation and resorption within the skeletal system.

2.3.1 Osteoblasts, osteoclasts, and osteocytes

Osteoblasts are cuboid-shaped cells that excrete bone osteoid, via the secretion of type I collagen and non-collagenous proteins (TGF-β, osteoprotogerin, osteonectin, osteocalcin) upon the surface of the extracellular matrix. This osteoid is later mineralised to form new bone tissue, firstly by forming hydroxyapatite (HA) crystals and subsequently elongating these crystals to occupy gaps between collagen fibrils (Del Fattore et al., 2012). This process of osteoid secretion and mineralisation is imperative for skeletal growth. Mesenchymal stems cells (MSCs), originating from the bone marrow, differentiate to form osteoblasts via osteoprogenitor cells and the Wnt pathway (Del Fattore et al., 2012). Osteoblasts not only elicit bone tissue formation, but also directly influence osteoclast activity and subsequent bone tissue resorption. Receptor activator of nuclear factor kappa-B ligand (RANKL) is a protein which, upon binding with its receptor (RANK), promotes osteoclast activity and differentiation (Langley and Fidler, 2007) (Figure 2.10). Upon sufficient osteoid production and mineralisation, however, osteoblasts upregulate the expression of osteoprotogerin (OPG), a non-collagenous protein that acts as a decoy receptor by binding to RANKL and inhibiting the RANK-RANKL pathway, consequently reducing bone resorption (Zheng et al., 2013). RANKL:OPG ratio is a key indicator of osteoclastogenesis and impending osteolysis. Interestingly, increased mechanical stimulation of the bone microenvironment reduces osteocyte expression of sclerostin and RANKL, thus leading to bone formation (Sarazin et al., 2021).

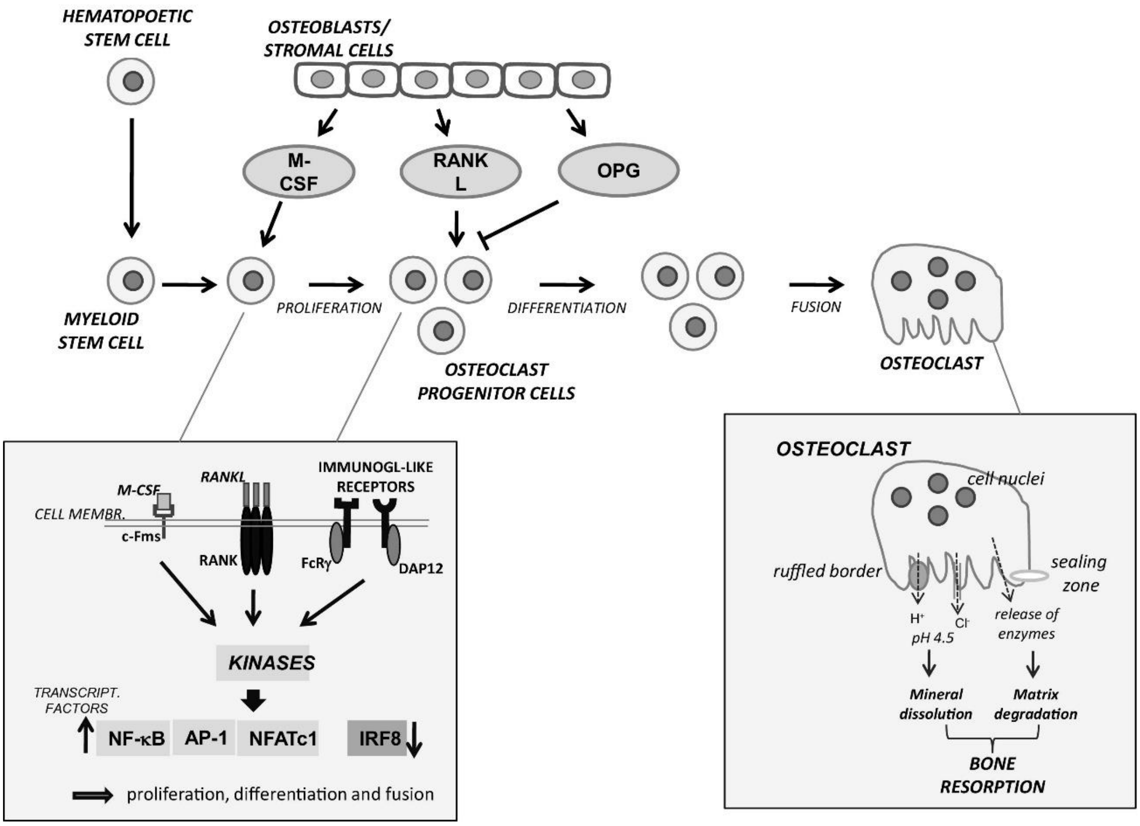

Figure 2.10: Osteoclast lineage, primary components and bone resorptive behaviour of an osteoclast cell. Proliferation and differentation, as well as upregulation of RANKL by osteoblasts, lead to the formation of osteoclast cells. Each osteoclast, composed of multiple nuceli, and a sealing zone, secretes enzymes from their ruffled boarder to induce to elicit mineral dissolution and matrix degradation, ultimately inducing bone tissue resorption (Lerner, 2012).

Osteoclasts are multinucleated cells, differentiated from osteoclast progenitor cells, which had previously proliferated from haematopoietic cells of the myeloid lineage (Lerner, 2012). Specifically, osteoclasts are formed when increased expression of

RANKL, as produced by osteoblasts, elicits osteoclast precursors to differentiate within the bone extracellular matrix (Figure 2.10). Osteoclasts function to actively resorb old and damaged bone residue from the tissue surface, providing a cavity in which new bone osteoid may be deposited as part of bone tissue repair. Within the osteoclast membrane lies multiple nuclei, gogli stacks, lysosomes and a rough endoplasmic reticulum, with one side of the osteoclast presenting a ruffled border membrane (Cappariello et al., 2014). Osteoclasts resorb bone by producing protons (Carbonic Anhydrase II), housed within this ruffled border, which dissolve the mineral content. Osteoclasts subsequently release enzymes (cathepsin K) that remove the organic matrix (Szewczyk et al., 2013). Osteoclast activity is influenced by the expression of parathyroid hormone-related protein (PTHrP), which upregulates RANKL expression and decreases OPG, in turn leading to differentiation of osteoclast precursors and bone tissue resorption (Kozlow and Guise, 2005).

Osteocytes, which account for 90-95% of all bone cells in the human skeleton (Tresguerres et al., 2020), are mechanosensitive bone cells that reside within the lacunae of cortical and trabecular bone tissue and regulate skeletal structure (Ashique et al., 2017). When osteoblasts cease forming new bone matrix, they either embed themselves within the newly formed osteoid matrix and mature into osteocytes, or alternatively undergo apoptosis (Bonewald, 2011). A typical human adult skeleton is comprised of approximately 42 billion osteocytes, which form an estimated 23 trillion intercellular connections within the lacunar-canalicular system (Buenzli and Sims, 2015). Osteocytes are star-shaped in their morphology, composed of 40-100 cilia that protrude from the cell through narrow passageways of the bone extracellular matrix (canaliculi). These dendritic extensions enable communication with other osteocytes, bone lining cells and osteoblasts, and contain mechanosensitive β_3 integrin (Chen et al., 2015). Osteocytes play a major role in the bone remodelling process by (a) Signalling for the initiation of bone remodelling upon sensing changes in loading within the extracellular matrix of bone, (b) regulating the activation of osteoclasts to initiate bone tissue resorption, (c) regulating calcium and phosphorus release from bone tissue stores, and (d) signalling the end of the bone remodelling process, via the secretion of antagonists to osteogenesis, including sclerostin (Kenkre and Bassett, 2018). Details of how osteocyte behaviour governs bone cellular responses to changes within the extracellular matrix (i.e., mechanoregulation) are described below.

2.3.2 Bone Modelling and Remodelling

Throughout childhood and adolescence, bone tissue primarily undergoes a large amount of growth and development, continuously changing and adapting the skeletal morphology into adulthood. During bone modelling, osteoblasts undergo bone formation and osteoclasts undergo bone resorption, not necessarily in a coordinated or simultaneous manner. Once vertebrates have reached adulthood, the rate of bone development slows considerably. Bone remodelling is a process that continues throughout life to continuously adapt to changes within its microenvironment, in the form of growth, reinforcement and resorption. As skeletal growth slows in the transition into adulthood, the role of osteocytes becomes more important as most bone tissue adaption stems from changes in the mechanical environment due to damage or loading.

The coordinated activities of osteocytes, osteoblasts, and osteoclasts govern bone tissue structure and composition, and ensure a constant remodelling process. In this way, bone remodelling works to repair tissue damage, prevent the development of hyper-mineralised bone tissue and maintain homeostasis by regulating the release of calcium and phosphorus. The remodelling process is divided into two categories; **Targeted remodelling** is more common and refers to the initiation of bone repair as a result of osteocyte signalling, via their dendritic network, when bone tissue is damaged (such as micro-fractures) or there is a change in mechanical loading. **Non-targeted remodelling** occurs systemically, whereby a change in hormones such as parathyroid hormone (PTH) regulates the release of calcium from storage in the bone extracellular matrix (Kenkre and Bassett, 2018).

Bone remodelling consists of five sequential stages (see Figure 2.11). In humans, though not in small animals, over 80% of the bone surface is quiescent (dormant) at any one time, and therefore is not undergoing active bone remodelling (Kenkre and Bassett, 2018). **Activation:** In this first stage, circulating osteoclast precursor cells differentiate in a process regulated by osteocytes. Bone lining cells detach from the substrate surface and form a canopy, isolating the bone remodelling units to a designated area of necessary remodelling. **Resorption:** Once formed, osteoclasts undergo extensive bone tissue resorption, consuming damaged or aged bone tissue of inferior quality. **Reversal:** Between bone resorption and formation, macrophages are formed from the differentiation of mononuclear cells, and work to remove the debris formed from prior resorption. **Formation:** Once the macrophages are finished cleaning up the resorbed tissue space, osteoblasts, which have been recruited and differentiated throughout the previous stages, arrive at the resorbed bone tissue cavity. Osteoblasts deposit osteoid, a bone matrix formed from protein, and work to mineralise this material to form new, healthy bone. **Termination:** Once sufficient osteoid has been deposited, osteocytes cease signalling for osteoblastogenesis. Osteoblasts either undergo apoptosis or reside within the bone extracellular matrix to become osteocytes (Kohli et al., 2018).

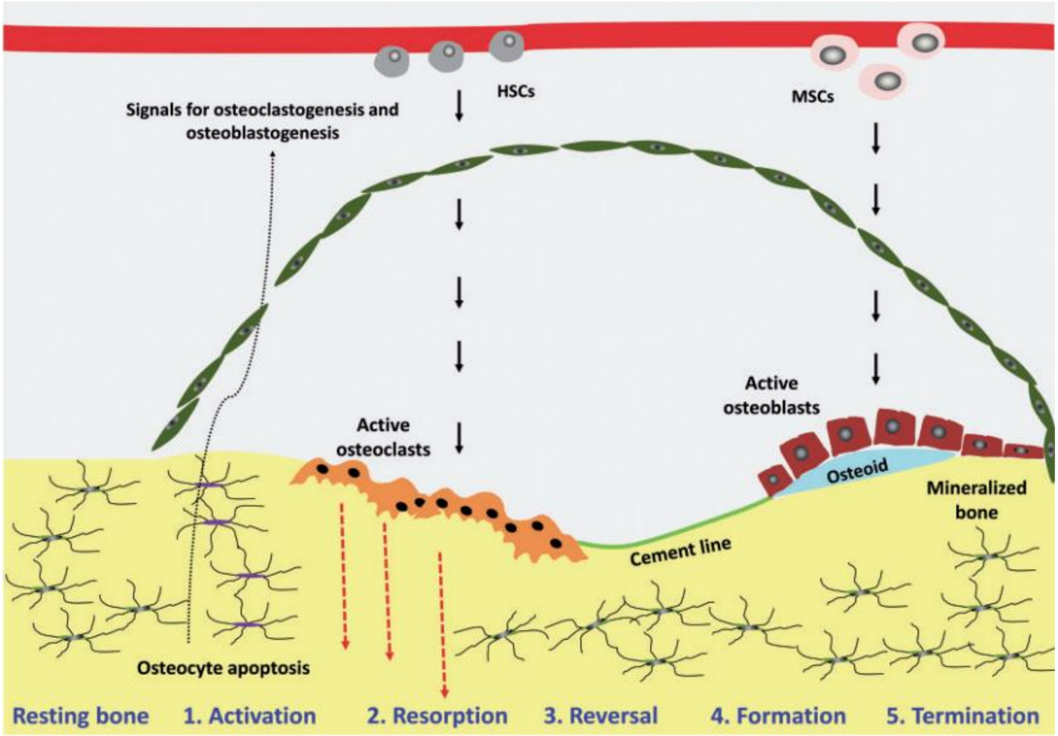

Figure 2.11: The five stages of bone remodelling. This illustration demonstrates the sequential progress as 1) osteocytes upregulate osteoclast activity leading to 2) bone tissue resortion until such time as 3) the process is reversed along the cavity cement line and 4) osteoblasts secrete osteoid within this cavity to 5) generate new bone tissue formation, until such time as osteocytes influence 6) termination of the remodelling process (Kenkre and Bassett, 2018).

Mechanobiology is the study of the effect of physical forces on cells residing within the bone microenvironment and their ability to convert these forces into biochemical signals (Liedert et al., 2005). Forces within the environment of bone tissue are altered upon changes such as fracture, underuse, damage, or disease, thus altering skeletal loading and triggering new mechanical cues (Del Fattore et al., 2012, Kenkre and Bassett, 2018). In response to these mechanical cues, resident bone cells are recruited for the resorption of degraded tissue (osteoclasts), new tissue formation (osteoblasts) and regulation of these processes (osteocytes) to maintain homeostasis and mitigate bone loss.

2.3.3 Mechanoregulation Theory

Given the complexity of bone remodelling processes, defining and predicting the adaptive behaviour of bone tissue has proven challenging. A foundation of biomedical research in bone tissue, Wolff's law (1893) states, in brief, that the internal microarchitecture of bone tissue adapts to changes in morphology and function, and is dictated by external forces in accordance with mathematical laws. From this theory stemmed the study of mechanobiology, whereby the mechanical environment of bone tissue influences the behaviour of mechanosensitive bone cells which it surrounds. Wolff's law was then implemented in numerous studies to form a clearer understanding of the adaptive behaviour of bone remodelling. Two categories of remodelling were distinguished, where resorption and deposition of osteoid is performed externally (surface remodelling) or within the lamellar bone structure (internal remodelling) (Frost, 1964). 'Adaptive elasticity theory' was applied in a porous elastic bone model, which continuously adapted to changes in mechanical strain in an effort to re-establish equilibrium by way of altered bone mass, density and stiffness, and had successfully correlated with clinical outcomes (Cowin and Hegedus, 1976). A further adaption was biphasic theory whereby constitutive equations, used to describe both solid tissue matrix and interstitial fluid components, predict creep and stress relaxation in articular cartilage and bone tissue under compression (Mow et al., 1980). Importantly, Frost's Mechanostat Theory (Frost, 1987) specified a mechanical strain range of 200 – 1,500με ('microstrains'), below which bone tissue would undergo tissue resorption, beyond which bone would undergo bone formation and between these strain thresholds lies a 'lazy zone' in which bone activity is minimal and no substantial bone tissue formation or resorption occurs (see Figure 2.12). By implementing the above theories of Wolff, Frost and Cowin, a two-dimensional mathematical FE model of a human proximal femur under physiological loading successfully demonstrated 'stress shielding' (Huiskes et al., 1987). This process is where bone tissue shares mechanical loads with a local prosthetic implant and, upon this reduced mechanical stimulation, undergoes excess tissue resorption to re-establish mechanical homeostasis.

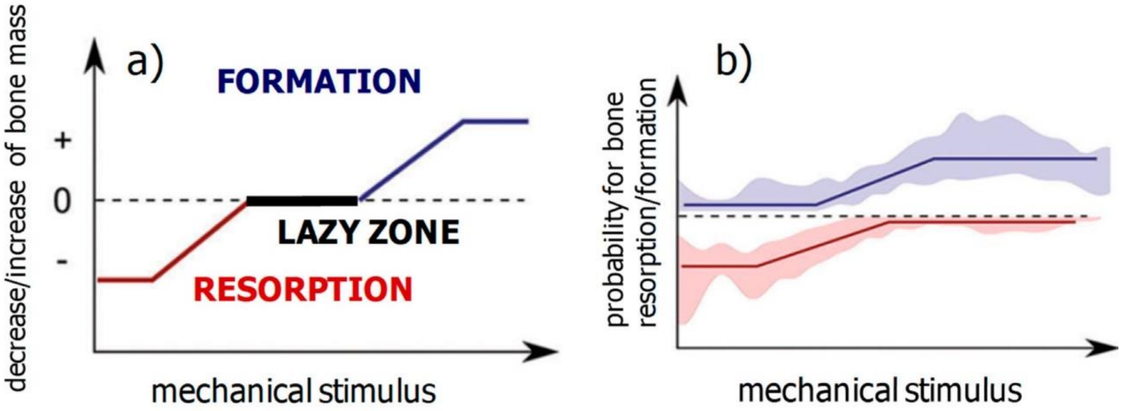

Figure 2.12: Bone mechanical stimulus and the Lazy Zone. Schematics demonstrating the a) criterion of bone formation and resorption according to Frost's Mechanostat Theory (Frost, 1996) and b) a more recent study of adult mouse bone tissue, where the Lazy Zone is not as clearly defined, and instead relates to a probability of bone resorption or formation with changes in mechnical stimulus (Razi et al., 2015), adapted by (Weinkamer et al., 2019).

Building on the above theories, the ability of resident mesenchymal stem cells (MSCs) to alter differentiation and expression in response to biophysical stimuli was explored (Prendergast et al., 1997). A linear, isotropic, biphasic FE model comprised of four separate tissues (connective, fibrocartilage, fibrous tissue with minimal bone, fibrous tissue with greater bone quantity) was developed to reflect a prior study (Søballe, 1993) in which bone tissue at the interface of a canine femur and tibia was mechanically stimulated via the micromotions of a piston-driven implant. Prendergast *et al*. (1997) outlines how two biophysical stimuli, such as fluid flow and shear strain, could mechanically stimulate MSCs residing within the bone extracellular matrix to undergo differentiation and collagen synthesis, deemed 'motion control', due to its continuous displacement under these conditions. New collagen formation would, in turn, increase bone tissue stiffness and reduce matrix porosity in an effort to re-establish a regulated mechanical environment. Stimulation of such stiff, unmoving bone tissue would therefore have graduated to the influence of 'force-control' stimuli as illustrated below (see Figure 2.13) (Prendergast et al., 1997). The stimulation and response of mechanosensitive cells within the bone microenvironment is now known as 'mechanoregulation', and involves active bone remodelling and regulation of bone cell differentiation in response to changes in the mechanical environment (McNamara, 2010).

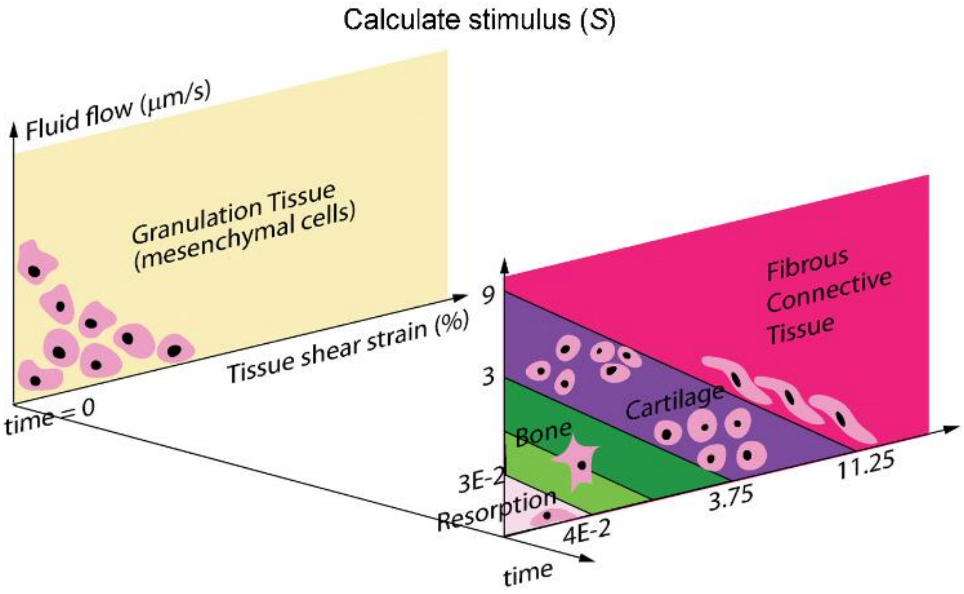

Figure 2.13: The 'mechano-regulatory pathway'. Illustration of two biophysical stimuli, fluid flow and shear strain, mechanically stimulating resident MSCs to undergo differentiation and collagen synthesis, thereby increasing tissue stiffness and reducing matrix porosity in a time-dependent process, to regulate their mechanical environment (Prendergast et al., 1997).

2.3.3.1 Stimuli Which Drive Mechanoregulation

Mechanical stimuli arising in the surrounding bone microenvironment regulate proliferation, differentiation, gene expression, protein synthesis, matrix production, apoptosis and necrosis of the resident bone cells (Wang and Thampatty, 2006) and is crucial for organ homeostasis. Cellular mechanosensing mechanisms include ion channels, gap junctions, integrins, primary cilia and the actin cytoskeleton (Yavropoulou and Yovos, 2016, Stewart et al., 2020). When the bone mechanical environment does not experience sufficient mechanical stimulation to meet the lazy zone criteria (e.g., immobility), osteocytes express catabolic factors (sclerostin, DKK1) to reduce osteoblast differentiation, thereby inhibiting bone formation. In the absence of mechanical loading, osteocytes undergo cell death. Correspondingly, in the absence of osteocytes, the process of mechanotransduction is severely impaired (Sarazin et al., 2021). In contrast, when bone tissue is subjected to loads exceeding an upper strain threshold, this is reported to induce fluid flow in the bone fluid that fills the lacunae of which osteocytes reside (Ashique et al., 2017). Increased fluid flow in turn elicits shear stresses upon the mechanosensitive osteocyte membrane, resulting in the upregulation of biochemical signalling and ultimately resulting in increased bone formation, explained in further detail below. In this way, there is an inextricable link between mechanical stimulation and the behaviour of osteoblasts, osteoclasts and osteocytes within the bone tissue microenvironment.

While mechanical strain is a key stimulus theorised to drive the mechanoregulatory behaviour of the bone remodelling unit, alternative stimuli have been investigated in an attempt to further understand bone adaption. The first of these stimuli to consider is microdamage, which initiates upon the introduction of fatigue-induced microcracks in the bone extracellular matrix. Such damage can be induced by excessive loading of bone tissue, and results in the disruption and perhaps apoptosis of resident osteocytes, which in turn signal for greater osteoclastogenic activity and therefore results in net bone tissue resorption (Lee et al., 2002). By utilising a bone remodelling algorithm, a methodology explained in further detail below (section 2.4.1), this stimuli has previously been investigated, in conjunction with strain stimuli, in a simplified FE model of bone tissue (McNamara and Prendergast, 2007) (see Figure 2.14). This study accurately predicted strain stimuli driving the remodelling process up to a specific threshold, beyond which microdamage stimuli overrides strain formation response, resulting in net bone resorption (McNamara and Prendergast, 2007). In a recent study, microdamage stimuli (as a function of accumulated plastic strain) has been predicted in micro-CT derived FE models of healthy ovine femurs under physiological loads with simulated defects (Fernández et al., 2022). This study found that microdamage accumulates in regions of trabecular thinning or large bone cavities, and that even at relatively low strains microdamage may still be an active stimulus for bone remodelling (Fernández et al., 2022).

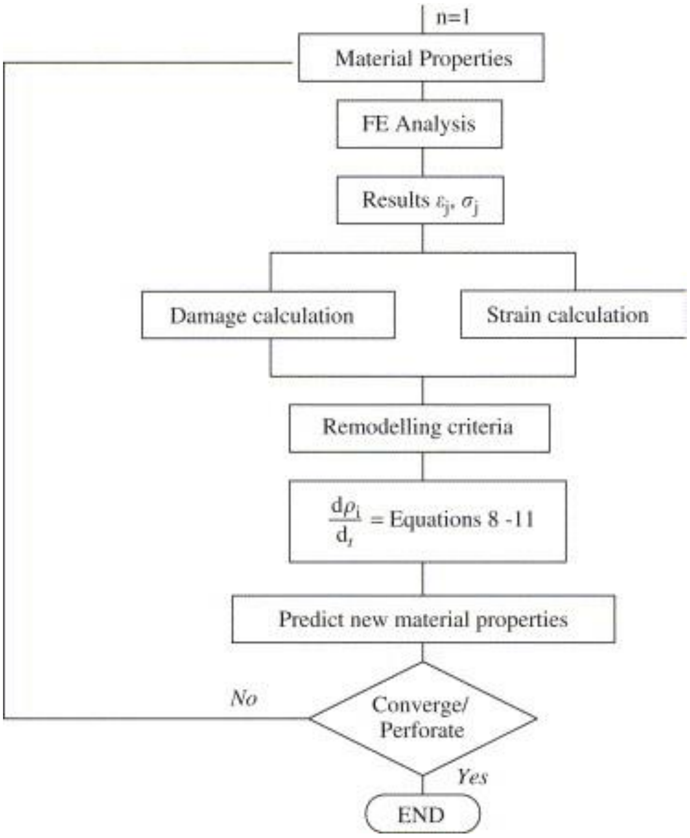

Figure 2.14: Flowchart of mechanoregulation subroutine For each simulated iteration, the material properties of a model are updated depending on calculated strain stimuli, microdamage stimuli, the rate of change of density *(dρi/dt)* and how mechanoregualtory response is catagorised according to remodelling criteria to induce net bone tissue resorption, formation or acquiescence. Each iteration of the algorithm brings a new, element-specific stress (σ_j) and strain response (ε_j) from the model, which is then reintroduced into the equations in a cyclical process. The mesh is then updated with new material properties to reflect these changes, and the algorithm iteratively repeated until the model converges or is perforated (McNamara and Prendergast, 2007).

Another stimulus reported to encourage mechanoregulation is fluid flow. This is theorised to be induced by a pressure differential brought about during physiological loading, manifested as shear stress, and experienced by osteocyte cells within the lacunar-canalicular network (LCN) which they inhabit (Fritton and Weinbaum, 2009). However, a paradox was found, in that strains induced by typical locomotion *in vivo* would not introduce the levels required to induce mechanoregulatory responses reported *in vitro* (You et al., 2000). From this paradoxical finding stemmed a more recent theory that mechanical strains are amplified by osteocytes cells, supported by simulation of an FE models of an idealised osteocyte cell, which found confocal protrusions within the bone tissue extracellular matrix to amplify applied strains by up to 50-420% at the cellular level (Verbruggen et al., 2012). More recently, changes in fluid flow were simulated via micro-CT derived poroelastic FE models of cortical bone within the tibiae of ovariectomised rats (Gatti et al., 2018). This study concluded increased porosity within the vascular system negatively impacts interstitial fluid flow (Gatti et al., 2018), and therefore may significantly impact the bone remodelling process. The need to include precise lacunar morphology as an additional factor, when predicting bone remodelling, was further supported in a study which applied axial compressive loads on murine tibiae and performed in vivo micro-CT over a 2 week period (van Tol et al., 2020). This study demonstrated that, when compared to remodelling predictions based on mechanical strain alone, the inclusion of LCN morphology allowed for precise calculations of strains derived from fluid flow within these structures, thereby significantly improving FE model predictions of bone tissue formation, resorption or quiescence (van Tol et al., 2020).

Two additional stimuli, though not as commonly reported in this research field, have been investigated via the use of bone remodelling algorithms and are briefly described here. Firstly, stress nonuniformity stimulation describes how bone remodelling is driven by disparities in Von Mises stress between local cells compared to neighbouring cellular units, assuming remodelling only occurred on the trabecular bone surface, and is reduced upon remodelling (Adachi et al., 2001). Secondly, daily stress describes the loading regime, which is cyclical, depends on load frequency, generates dynamic strain and reportedly predicts increases in bone volume fraction and strength that static loading simulations would not otherwise have achieved (Scheuren et al., 2020, Smotrova et al., 2022). The above computational studies of various mechanical stimuli within the bone microenvironment have demonstrated finite element analysis as an ideal method for investigating and predicting mechanoregulation theory.

2.4 Computational modelling of bone tissue

The Finite element (FE) method is an automated approach for solving partial differential equations in models of complex boundary conditions, geometries and applied loads. In computational studies, this methodology involves the isolation of individual sub-divisions within a 3D model, known as elements, further divided into individual nodal points such that complex polynomial functions are calculated across each element according to nodal forces and matrix stiffnesses. Further discretisation of a model mesh, by introducing a larger quantity of elements or nodal points (known as 'second order' elements) enables increased accuracy such that the physical problem under investigation can be precisely identified and calculated. Additionally, material properties may be simply defined as fundamentally elastic in nature, and therefore not undergoing plastic deformation, or alternatively involve more complex material behaviours such as fluid-solid interactions within a poroelastic model. In this way, FE analysis (FEA) allows for the inexpensive and efficient prediction of intricate changes in stress and strain states upon the application of specific forces and clearly defined materials. In particular, the non-invasive nature of FEA allows for the prediction of changes in mechanical quantities (such as tissue stress and strain) at the microscale, where conventional measurements may otherwise not be possible to acquire *in vivo*. For this reason, FEA has become a standard methodology for investigating changes within the mechanical microenvironment of biological tissues.

Early application of finite element analysis to study bone tissue behaviour and adaption sought to understand bone loss (Reinhardt et al., 1983), the remodelling process (Hart et al., 1991), fracture development (Rybicki et al., 1974) and post-fracture bone tissue repair (Meroi and Natali, 1989). However, these early studies relied on cumbersome manual measurements of irregular tissue geometries, which require a more precise approach for accurate simulations of *in vivo* processes. The computed tomography (CT) scanning technique, which is traditionally used to visualise patient connective tissues in clinical and experimental settings, has since been adapted for use in FE modelling by generating 3D reconstructed models from these scans. MRI and DXA scans have also been adapted for finite element analysis, but CT reportedly demonstrates fewer average errors and superior failure prediction capabilities based on bone strength (Keyak et al., 1990, Rathnayaka et al., 2012, Viceconti et al., 2018). Thus, CT scans have become a standard method for converting *in vivo* and *in vitro* scans of skeletal components to develop patient-specific FEA simulations, with predictions of clinical outcomes from patient-specific scans reaching accuracies comparable to current standards (Silva et al., 1998, MacNeil and Boyd, 2007).

Image processing software, for example Materialise MIMICS software (Belgium), can be used to 3D reconstruct CT scans, providing *in vivo*-specific geometries of long bones. Each CT scan slice, stored as a Digital Imaging and Communications in Medicine file (DICOM), includes a complete density distribution of the bone tissue region of interest. For use in clinical CT, densities have been converted from measured grey values to CT-derived density units, via a ratio comparing this value to ash density, which is in turn measured as the weight of bone tissue burned to 650˚C as a ratio over its volume (Schileo et al., 2008). Such a correction has been deemed necessary in the use of clinical CT analysis, as the phantoms required for calibration are homogeneous and this ratio accounts for the heterogeneous nature of the bone hierarchical structure. As calibrations phantoms are also typically used in micro-CT analysis, such a correction may also be necessary for this higher resolution methodology. The relationship between bone tissue density and Young’s modulus can be defined by a power-law equation, which varies in studies involving bone tissue of differing species, age and sex. In this way, material properties according to CT scans can be mapped onto a reconstructed model, such that it is not only geometrically accurate but also has voxel-specific physical properties. Reconstructed models are applied a threshold to eliminate lower density tissues, fixed for misaligned elements and imported into Abaqus as an orphan mesh. Notably, in simplified FE models of human proximal femora, tetrahedral elements were reportedly more representative of proximal femur mechanical environments than hexahedral elements, but were sensitive to the mesh degree or refinement (Ramos and Simoes, 2006) and therefore mesh convergence analysis is necessary in such models. While the above methodology is suitable for predicting instantaneous changes in bone tissue under precise loads and within *in vivo* specific geometries, FEA can also be utilised to accurately predict changes in bone tissue over time.

2.4.1 Predicting A Changing Mechanical Environment Over Time

An additional feature of Abaqus software is the use of subroutines, which allow a user to export outputs from a model, pass these outputs through a pre-scripted algorithm of calculations and then reintroduce these updated parameters into the FE model mesh. This can be conducted for each individual element of a mesh, and continuously iterated such that the mesh is updated with new parameters for each increment of a running simulation. Subroutines have the capacity to iteratively update the material properties of a mesh, over multiple iterations and according to established equations. Subroutine methodology has been used in a variety of published computational modelling studies to simulate the bone remodelling process, specifically applying the mechanoregulation criteria to each individual element within an FE model mesh to predict bone tissue adaption (Schulte et al., 2013, Phillips et al., 2015, Cheong et al., 2020a, Cheong et al., 2020b).

Computational subroutines, such as User-Defined Field (USDFLD) or user material (UMAT), define solution-dependent variables, such as density or Young's modulus at every element-integration point. A USDFLD subroutine can be introduced to an FE model with established geometry, mesh, boundary conditions and loading conditions, to simulate how properties within each element of the model mesh are gradually altered over time. Subroutine implementation to demonstrate bone mechanoregulation has previously been utilised for predicting longitudinal changes microenvironment of healthy (Garcia-Aznar et al., 2005, Schulte et al., 2011, Pereira et al., 2015, Costa et al., 2017, Cheong et al., 2020a), damaged (McNamara and Prendergast, 2007, Penninger et al., 2008, Isaksson et al., 2009) and osteoporotic bone tissue (Mulvihill et al., 2008, Schulte et al., 2013, Badilatti et al., 2016, Cheong et al., 2020b).

By implementing a bone remodelling algorithm, one can predict changes in the mechanical environment of bone tissue during disease, ageing or as a result of tissue damage, as demonstrated in a model of fracture repair below (Figure 2.15). With this incremental approach, simulations of bone adaption could predict how breast cancer metastatic invasion, and in particular their altered mechanical stimuli, may affect osteoblast, osteoclast and osteocyte bone remodelling behaviours and therefore could provide insight into how such changes may contribute to the cancer vicious cycle.

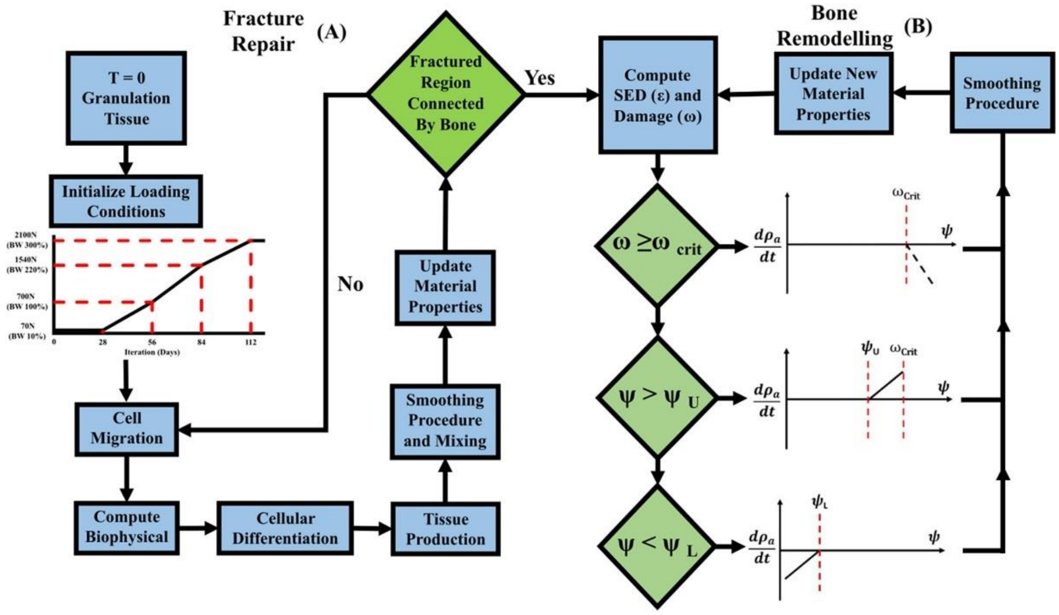

Figure 2.15: Flowchart of sequences involved in a bone remodelling algorithm, incorporating Mechanostat theory, and applying strain energy density and microdamage as two stimuli which influence the remodelling behaviour of bone tissue, in a model undergoing fracture healing (Quinn et al., 2022).

Aside from the above implementation of mechanoregulation theory, it must also be noted that alternative methods for predicting changes in the mechanical environment have been applied to replicate tissue adaption *in vivo*. The first of these studies developed micro-CT-derived FE models of human vertebral trabecular bone tissue and applied compressive strain to simulate physiological loading (Mc Donnell et al., 2009). This study utilised element deletion to remove voxel regions with the lowest principal strains, incrementally eliminating these trabecular regions until a bone loss of 5% was reached (Mc Donnell et al., 2009). Models were either a) strain-dependent b) strain and microdamage-dependent or c) strain-damage dependent but the damage threshold gradually increases during bone resorption, with the latter model version reportedly providing the most accurate apparent modulus values when compared to experimental results (Mc Donnell et al., 2009). Another study investigated the precise influences of autocrine and paracrine signalling of osteoblast and osteoclast cells, respectively, on FE bone remodelling predictions (Hambli, 2014). Bone cell density was determined by osteoblast and osteoclast populations, in turn driven by strain energy density and fatigue damage accumulation stimuli, and also incorporating a spatial influence function to determine the radius about which an osteocyte may elicit bone mineralisation, in a 3D human proximal femur model over 4-5 years of physiological loading (Hambli, 2014). A more recent study utilised micro-CT images of human trabecular bone tissue, and a machine-learning algorithm, to determine via the CT-derived changes in stiffness what key stimuli drive trabecular bone tissue resorption in osteoporotic tissue, concluded as yield stress and yield strain (Sohail et al., 2019). The machine-learning generated algorithm was then applied to a simplified trabecular strut model, whereby bone was considered resorbed when it had reached the tissue stiffness of surrounding bone marrow. It was reported that the resulting changes in trabecular bone morphology closely matched those reported in experimental findings (Sohail et al., 2019). While these studies have demonstrated successful alternative approaches for predicting bone tissue adaption to changes in the mechanical environment, these methods are not as widely reported and further validation against experimental data is needed.

2.5 Analysing Bone Metastasis

2.5.1 Pre-Clinical Models of Bone Metastasis

Extensive analysis of cadaveric bone from patients with metastatic cancers (Kaneko et al., 2003, Nazarian et al., 2008) have revealed reduced bone mineral density (BMD), bone tissue stiffness, yield strength and ultimate strength upon osteolysis. However, these results are limited in that inter-patient variability arises due to multiple conditions inherent for patient studies (age, lesion type, underlying conditions such as osteoporosis, treatment regimen) (Yao et al., 2020). Such variation between patients limits the comprehensive analysis of changes in bone tissue upon metastasis. As an alternative, *in vitro* analysis of metastasis is a promising method of analysing metastatic behaviours with highly controlled input factors. For example, a recent study utilised a novel *in vitro* MIMETIC construct involving osteoblasts, osteoclasts, osteocytes and 4T1 breast cancer cells included mechanical compression stimuli replicating *in vivo* conditions (Kumar et al., 2022). This study found tumour spheroid growth is influenced by bone cell signalling and matrix stiffness (Kumar et al., 2022), and further highlights the importance of mechanobiology during metastatic invasion. While a very promising alternative, *in vitro* constructs are currently limited in their ability to replicate the native mechanical environment that exists *in vivo* (Fan et al., 2020).

Pre-clinical models of metastasis provide controllable factors (age, sex, cancer type) while demonstrating metastatic spread *in vivo*. Though anatomical and musculoskeletal variation in mouse models may present different skeletal responses to metastatic invasion from those of human patients, bone morphological changes in mice are similar to those in humans upon aging (Jilka, 2013) and, importantly, the RANKL/RANK/OPG pathway is present in both species (Zheng et al., 2013). Published studies have utilised pre-clinical models of metastasis to assess changes in bone tissue physical properties following the development of overt lesions. These models often involve inoculation of cancer cells via intracardiac (Yoneda et al., 1997, Li et al., 2006, Wang et al., 2015, Burke et al., 2016, Burke et al., 2017, Sekita et al., 2017, Burke et al., 2018), intraperitoneal (Chiou et al., 2021), and intravenous means (Li et al., 2006, Richert et al., 2015, Allocca et al., 2019), or even via direct inoculation of cancer cells into the target bone region of interest (Arrington et al., 2006, Arrington et al., 2008, Nickerson et al., 2012, Sottnik et al., 2015). The time taken for breast cancer cells to traverse the metastatic pathway, from initial desertion of the primary tumour to the subsequent formation of metastatic lesions, can vary from 1 - 14 weeks (Wright et al., 2016). These temporal differences may be due to factors such as the chosen inoculation site, breast cancer cell line, mouse strain and which metastatic bone site is assessed (Wright et al., 2016). While such studies produce *in vivo* metastatic lesions, these methods of cancer inoculation bypass steps in the metastatic pathway from primary tumour site to bone tissue, which may furthermore alter the temporal progression of metastatic cellular adhesion and proliferation within bone.

An animal model developed by Lelekakis et al. (1999), was designed to generate particularly aggressive breast cancer metastasis *in vivo*, whereby 4T1 breast cancer cells are inoculated subcutaneously at the mammary fat pad to simulate metastatic spread from the primary tumour mass. 4T1 breast cancer cells are highly invasive, specifically when inoculated within the BALB/c mouse species, and recapitulates key steps of the *in vivo* metastatic pathway from a primary tumour site to bone, described previously (section 2.1.1). This 4T1-BALB/c mouse model has a reported 100% incidence of metastatic spread (Yoneda et al., 2000). In terms of rate of metastatic spread, tumour cells were consistently found within the proximal femur of BALB/c mice within 19 days of inoculation at the mammary fat pad, visualised using haematoxylin and eosin (H&E) staining of bone tissue cross-sections (Lelekakis et al., 1999). Another study which utilised this precise design of 4T1 breast cancer cells with BALB/c mice reported lethal metastatic spread established as early as 2 week post-inoculation, and life expectancy in an untreated mouse spans 5-9 weeks following cancer injection (Pulaski et al., 2000). It is important to note the 4T1-BALB/c model does not require the elimination of the murine immune system for metastasis to consistently occur, which further optimises the accuracy of this pre-clinical model compared to other metastatic studies which utilise nude mice, in which the thymus is removed to inhibit immune response (Arrington et al., 2006, Wang et al., 2015, He et al., 2017, Allocca et al., 2019, Chiou et al., 2021).

2.5.2 Comparisons of femoral bone development in mice and humans

The murine femur differs morphologically from a human femur (see Figure 2.16), as well as the weight-bearing load distribution and corresponding loading angle on the femoral head. In particular, the mouse proximal femur includes three trochanter regions (greater, lesser, third) (Figure 2.16) to support typical locomotion in this quadrupedal mammal, as opposed to bipedal human femurs with only the greater and lesser trochanters. The greater trochanter of the mouse femur extends proximally in line with the top of the femoral head, while a human greater trochanter is located far more distal in location along the femoral shaft (Figure 2.16A). Metastatic cells have an apparent preference for regions abundant in bone marrow, theorised to result from high vascularisation and metabolic activity in these regions (Rosol et al., 2003), thus long bones and lumbar vertebrae are standard sites of analysis for metastatic studies assessing lesion development (Wright et al., 2016). In the murine proximal femur, similar to human bones of the same tissue region, thin growth plates lie at between each trochanter and the intra-trabecular space, while a larger growth plate is located close to the distal femoral epiphysis, adjacent to the medial and lateral condyles (Cole et al., 2013) (Figure 2.16A, B). Notably, murine femurs contain three trochanters in the proximal region (greater, lesser, third), while humans possess only two and therefore do not present as many growth plate regions for tissue mineralisation during development. In addition, humans and mice similarly contain a growth plate at the threshold between the femoral head and femoral neck (Cole et al., 2013) (Figure 2.16A, B).

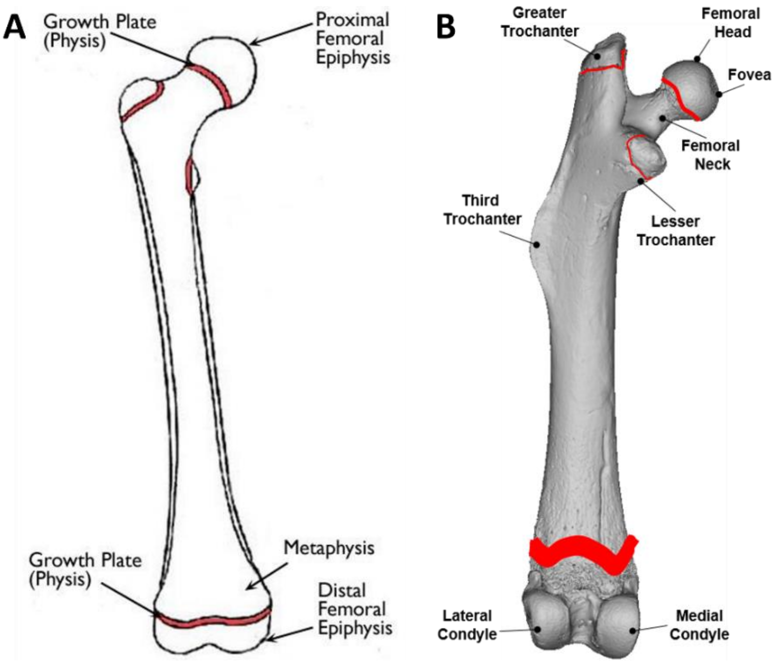

Figure 2.16: Comparison of femoral morphologies. Schematics of A) human (Sullivan and Anderson, 2000) and B) murine whole femur anatomies, with growth plates indicated in red.

It must be noted that murine growth plates do not fuse directly upon adulthood and are not sealed until elderly, in contrast to human growth plates which close once skeletally mature, however the growth rate of murine long bones slows considerably once mice have reached adulthood (Börjesson et al., 2012) and therefore adult mice are still considered a suitable model for analysing changes in mineral content during bone metastasis (Arrington et al., 2006, Richert et al., 2015, Burke et al., 2017, He et al., 2017, Sekita et al., 2017). Importantly, and similar to human femurs, trabecular bone tissue is present throughout the internal space of the murine proximal and distal femurs (Cole et al., 2013), while the femoral midshaft is almost entirely cortical tissue (Judex et al., 2004). Taking all of the above factors into consideration, the whole proximal femur which lies adjacent to the primary tumour inoculation site was chosen as the first region of interest. To investigate changes in the bone tissue microenvironment in the metastatic femur not directly adjacent to the primary tumour, a distal region of interest was also chosen. In micro-CT analysis, scanning of the large distal growth plate regions is discouraged, as large variations are present in bone tissue mineralisation at this region, avoided by setting the region of interest at least 0.25mm proximally away from this area (Bouxsein et al., 2010). As a consequence, a region closer to the midshaft but still abundant in trabecular and cortical bone tissue is ideal for capturing changes in bone mineral content and mechanical properties which is both far from the primary tumour site and yet not impacted by the most active site of mineralisation. These regions were therefore chosen for this thesis to fully characterise the changes which evolve during breast cancer metastatic invasion, in both cortical and trabecular bone tissues.

Although abundant in human cortical tissue, it should be noted that mice lack osteons and Haversian canals within their cortical bone structures (Hemmatian et al., 2018), however these are a standard pre-clinical model for bone tissue analysis due to their similarity in gene sequences to humans (at approximately 90%) (Birney et al., 2002) and exhibit similar bone morphological changes during ageing to humans (Jilka and Sciences, 2013). A key benefit of utilising murine models is their fast bone turnover rate, reported at 10-20% per year in the cortical bone of adult mice (Thudium et al., 2014), compared to 2-3% in human studies (Clarke, 2008), therefore providing significant changes in bone tissue morphology studies in a timely manner.

2.5.3 Impact of Osteolysis on the Bone Microenvironment

In the analysis of changes in bone mineral content and mechanical properties, pre-clinical studies of metastatic osteolysis vary wildly between species, cancer cell line, inoculation site, bone location of analysis, analysis methodology used and, importantly, the duration of disease progression when analysis was conducted. As such, the below tables were created to visualise trends in bone mineral parameters (volume, density, tissue thickness, lacunar orientation) and mechanical properties (elastic modulus, hardness, tissue strength) upon metastatic osteolytic destruction (Table 2.2-2.4). These analyses were conducted using a variety of imaging modalities, including micro-CT, nano-CT, DEXA, Goldner’s trichome staining and mechanical tests (compression, tension, nanoindentation, atomic force microscopy). Only findings from the below studies which had statistical significance ($p<0.05$) are included in these tables.

From cortical bone mineral analysis upon osteolysis (Table 2.2), a variety of bone mineral parameters (BV/TV, BMD, alignment of cortical lacunae) are degraded in the presence of osteolytic lesions when compared to healthy bone. This is similarly observed in metastatic trabecular tissue (Table 2.3), where all parameters had decreased upon osteolysis compared to controls, aside from trabecular spacing (Tb.Sp) which increases as surrounding trabeculae undergo thinning. The only exception to the above observations are the findings of Chiou et al., (2021) which, upon inoculation of breast cancer cells into the mammary fat pad of nude-Foxn1^{nu} mice, report increased bone volume, density and trabecular thickness, 3 weeks following the inoculation of tumour conditioned media into the mammary fat pad with tumour conditioned media. Such findings suggest metastatic invasion and subsequent osteolytic destruction may be sensitive to inoculation sites and the lapse of time between tumour cell extravasation and osteolytic destruction. Meanwhile, mechanical properties (Young's modulus, hardness, bone tissue strength) consistently decrease in osteolytic bone tissue when compared to healthy controls, for both cortical and trabecular regions, as in Table 2.4. While the below results have shed light on the impact of osteolytic metastasis on bone tissue physical environment following overt destruction, it is yet unclear how these changes have evolved over time, and therefore must be addressed to provide a more complete comprehension of the cancer vicious cycle, bone metastasis, and the factors which may be involved in its perpetuation.

Table 2.2: Reported significant changes in bone mineral properties upon overt metastatic osteolysis in **cortical bone** tissue (mean ± standard deviation). Abbreviations used: wo = weeks old, M = male, F = female, M/F = mixed sex, n.d. = data values not disclosed. New Parameters: BMC: bone mineral content, f_{θ} : degree of preferential alignment of lacunae along the bone longitudinal direction, Dist. Lc.V: Distribution entropy of lacunar density.

Study	**Cohort**	**Cancer**	**Inoculation site**	**Bone location**	**Disease duration**	**Imaging Method**	**Parameter**	**CTRL**	**MET**
(Kaneko et al., 2003)	Human, 36-75yo, M/F	Mixed (breast, prostate, lung)	N/A	Femoral diaphysis	N/A	Micro-CT of dumbbell-shaped cores	BMD$_{ash}$ (g/cm^3)	1.145 ± 0.02	1.011 ± 0.14
						Micro-CT OF Cubed cores	BMD (g/cm^3)	1.233 ± 0.03	1.096 ± 0.19
(Arrington et al., 2006)	Murine (NCr), 8-9wo, F	MDA-MB231 (F10)	Bone marrow	Distal femur	6 weeks	Micro-CT	BV/TV (%)	6.83 ± 1.75	0.77 ± 1.07
(Mann et al., 2008)	Murine (NCr), F, 8wo	MDA-MB231 (F10)	Bone marrow	Femoral Metaphysis	Lysis dependent	Micro-CT	BV (mm^3)	9.01 ± 0.94	8.97 ± 1.43
							BMC (mg)	8.96 ± 0.96	8.99 ± 1.54
						DEXA	Normalised BMD ratio	1.15 ± 0.09	1.21 ± 0.15
(Richert et al., 2015)	Murine (BALB/c), 4wo, F	MDA-MB-231	Intravenous	Tibial Metaphysis	32 days	Goldner's trichrome staining	BV/TV (%)	22.7 ± 1.8	9.5 ± 2.6
(Sekita et al., 2017)	Murine (C57Bl/6), 5wo, F	Melanoma (B16F10)	Intracardiac	Femoral diaphysis	14 days	Micro-CT	BV (mm^3)		CTRL > MET (n.d.)
							TV (mm^3)		CTRL > MET (n.d.)
						Nano-CT	f_{θ}	0.89 ± 0.03	0.81 ± 0.06
							Dist. Lc.V.	1.69 ± 0.15	2.02 ± 0.08

Table 2.3: Reported changes in bone mineral properties upon overt metastatic osteolysis in **trabecular bone** tissue. New parameters: BSE-WA: weighted average grey value measured via Backscatter Emission analysis, SAXS: Small-angle X-ray scattering, T-parameter: HA mineral crystal thickness, ρ-parameter: HA mineral crystal origentation (mean ± standard deviation).

Study	**Species**	**Cancer type**	**Inoculation site**	**Disease duration**	**Bone location**	**Imaging Method**	**Parameter**	**CTRL**	**MET**
(Arrington et al., 2006)	Murine (NCr) 8-9wo, female	MDA-MB231 (human breast)	Distal femur	6 weeks	Distal femur	Micro-CT	BV/TV (%)	3.55 ± 9.88	1.1 ± 1.91
(Nazarian et al., 2008)	Human, 36-75yo, M/F	Mixed (breast, lung, colon)	N/A	N/A	Spine and Femur	Micro-CT of bone cubes	BV/TV (%)	36.46 ± 15.38	24.29 ± 12.26
							BMD (g/cm^3)	1.82 ± 0.12	1.68 ± 0.22
							BSE-WA	142.91 ± 13.84	114.82 ± 15.75
(Burke et al., 2018)	Rat (Foxn1), female, 5-6wo	HeLa (human cervical)	Intracardiac injection	3 weeks	Spine (L1-L3)	Micro-CT	BV/TV (%)	46.5 ± 1.4	41.6 ± 1.3
							BMD (g/cm^3)	0.58 ± 0.025	0.481 ± 0.024
							Tb.Th (µm)	74.9 ± 1.6	71.4 ± 1.2
							Tb.N (#/mm^2)	6.2 ± 0.1	5.8 ± 0.1
							Tb.Sp (µm)	86.2 ± 3.5	100.4 ± 4.0
(Chiou et al., 2021)	Murine (BALB/c), female	MDA-MB-231	Intraperitoneal (daily)	3 weeks	Proximal tibiae	Micro-CT	BV/TV		CTRL < MET (n.d.)
							Tb.Th		CTRL < MET (n.d.)
							Tb.Sp		CTRL < MET (n.d.)
							Tb.N		CTRL > MET (n.d.)

Table 2.4: Reported changes in bone mechanical properties upon overt metastatic osteolysis in cortical and trabecular bone tissue. M = Male pateints, F = female patients; M/F = mixed sex, i.c. = intracardiac inoculation, i.v. = intraveneous inoculation, d.m.j: direct marrow injection, Cort. = cortical bone, Trab. = Trabecular bone, S_Y = Yield strength, S_U = Utlimate strength.

Study	**Species**	**Cancer Type**	**Bone location**	**Mechanical Test**	**Bone type**	**Parameter**	**CTRL**	**MET**
(Kaneko et al., 2003)	Human, 36-75yo, M/F	Mixed (breast, prostate, lung)	Femoral diaphysis, dumbbell-shaped cores	Compress to failure	Cort.	E (GPa)	23.0 ± 1.8	18.0 ± 4.3
						S_Y (GPa)	153.0 ± 16.5	106.6 ± 34.6
						S_U (GPa)	161.8 ± 5.9	115.5 ± 34.1
				Tensile to failure	Cort.	E (GPa)	22.7 ± 1.7	17.7 ± 4.3
						S_Y (GPa)	83.9 ± 8.8	74.9 ± 15.7
				Tensile to failure	Cort.	S_U (GPa)	95.6 ± 10.9	86.2 ± 18.7
(Nazarian et al., 2008)	Human, 36-75yo, M/F	Mixed (breast, prostate, lung, colon)	Spine, femur cadaveric cores	Nano-indentation	Trab.	E (GPa)	0.47 ± 0.07	0.22 ± 0.03
						H (GPa)	0.52 ± 0.09	0.24 ± 0.03
				Compress to 20% strain	Trab.	E (GPa)	0.356 ± 0.09	0.202 ± 0.06
						S_Y (GPa)	100.5 ± 21.8	40.4 ± 10.1
(Mann et al., 2008)	Murine (NCr), F, 8wo	Breast cancer (F10), d.m.j.	Distal femur	Compress to failure	Cort, Trab.	E (GPa)	0.351 ± 0.78	0.193 ± 0.13
						S_U (N)	45.2 ± 8.9	28.6 ± 17.7
(Sekita et al., 2017)	Murine (C57Bl/6), F, 5wo	Melanoma (B16F10), i.c.	Femoral diaphysis	Nano-indentation	Cort.	E (GPa)	24.2 ± 2.3	18.3 ± 3.1
(Burke et al., 2018)	Rat (Foxn1), F, 5-6wo	Cervical (HeLa), i.c.	Spine (L1-L3)	Compress to failure	Trab.	E (GPa)	157.7 ± 22.1	82.1 ± 17.7

2.5.4 The Mechanosensitive Behaviour of Metastatic Breast Cancer Cells

Metastatic breast cancer cells have been shown to alter their behaviour in the event of changes within their mechanical environment. However, the precise impact of increased mechanical stimulation on breast cancer cells is currently unclear within the research field. In an vitro study, MDA-MB-231 breast cancer cells were seeded on 2D polyurethane films of different elastic moduli (70MPa – 3800MPa) and analysed for their expression of Iβ3, which upregulates TGF-β signalling and in turn increases PTHrP and Gli2 promotion of tumour proliferation (Page et al., 2015). This study found Iβ3 expression increased with matrix rigidity, specifically at stiffnesses equivalent to trabecular bone tissue or higher (Page et al., 2015). In a more recent in vitro study, MCF-7 breast cancer cells were cultured in conditioned media from osteocyte-like MYLO-4 cells, which had been mechanically stimulated with oscillatory fluid flow (OFF) for 24hrs (Dwivedi et al., 2021). This study found a significant upregulation of CXCL1 and CXCL2 cytokine expression, which are effective promoters of breast cancer cell migration (Dwivedi et al., 2021). The above studies demonstrated increased matrix rigidity and mechanical stimulation of breast cancer cells, in vitro, promote tumour cell migration and proliferation. However, an in vitro study where metastatic breast cancer cells (MDA-MB-231) were seeded within a microfluidic device, oscillatory fluid flow (OFF) was applied to mechanically stimulate osteocyte-like MYLO-4 cells seeded in an adjacent channel (Mei et al., 2019). This study found the cancer cells had undergone extravasation within 3 days, and that this migratory activity reduced significantly when osteocytes were stimulated with OFF compared to static conditions (Mei et al., 2019). In a more recent *in vivo* animal study, osteolytic metastatic cells (Py8119) were directly injected into the tibiae of mice, which were then subjected to various levels of mechanical stimulation via either a tibial loading rig (8N cycles) or a treadmill running regime (<4.5N) (Wang et al., 2021). From weekly micro-CT scans, this study found that rig-load stimuli accelerated osteolytic destruction as early as 2 weeks following inoculation, while moderate intensity exercise had inhibited osteolysis (Wang et al., 2021). Another study investigated the effects of mechanical stimulation on metastatic breast cancer cells (MDA-MB-231, MCF-7) in two ways; a) MLO-Y4 cells were mechanically stimulated via OFF and this conditioned media introduced to the cancer cells, b) a microfluidic organ-chip model contained parallel cancer cell and osteocyte cell microchannels, with MLO-Y4 cells mechanically stimulated via unidirectional fluid shear stress (Verbruggen et al., 2021). Interestingly, results from the first method found that while static osteocyte signalling inhibited proliferation, mechanical stimulation of MLO-Y4 cells reversed this effect; the organ-chip method involving fluid shear stress inhibited breast cancer cell proliferation (Verbruggen et al., 2021). Taking all the above studies into consideration, it is yet unclear what forms of mechanical stimuli applied to breast cancer cells would influence their migratory, proliferative or invasive behaviour.

By investigating the mechanobiological cues which may arise during early metastatic invasion, such findings could shed light on the preferred mechanical stimuli for perpetuating the cancer vicious cycle, and therefore provide clearer insight into the role of mechanobiology during the breast cancer metastatic process.

2.5.5 Modelling Bone Loss and Osteolytic Destruction

Published computational studies of bone tissue metastasis commonly analyse lumbar vertebrae (Salvatore et al., 2018, Atkins et al., 2019, Falcinelli et al., 2019, Shinoda et al., 2019) or the proximal and distal regions of the femur (Whyne et al., 2003, Keyak et al., 2007, Sas et al., 2020) because these regions are abundant in both cortical and trabecular bone tissue. Previous studies utilising micro-CT derived FE (µFE) models of healthy bone tissue have replicated metastatic osteolysis by introducing simulated lytic defects. These may be manually introduced by either drilling cavities into the bone tissue prior to CT scanning (Spruijt et al., 2006, Rennick et al., 2013, Anez-Bustillos et al., 2014, Alkalay et al., 2018) (see Figure 2.17) or by deleting elements within a µFE mesh (Benca et al., 2017, Salvatore et al., 2018), in an attempt to match the size and geometry of real osteolytic lesions seen in micro-CT scans. However, artificially produced defects replicating natural metastatic development are considered an inaccurate and unrepresentative model of metastatic osteolytic development (Keyak et al., 2005, Yosibash et al., 2014).

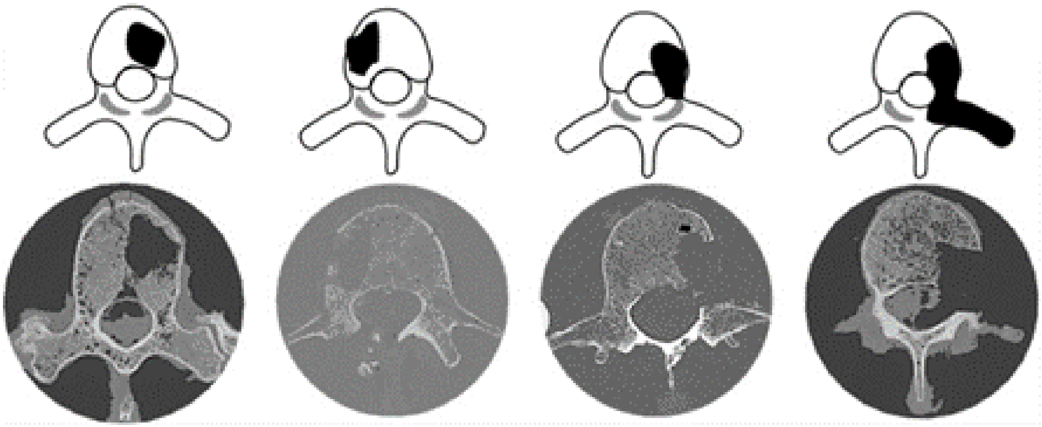

Figure 2.17: Simulated osteolytic lesions Axial views of osteolytic lesions in female patient vertebrae, where micro-CT scans (bottom row) are dimensioned and mapped to a corresponding sketch (top row) of black regions (Alkalay et al., 2018)

Changes in strain fields due to metastatic osteolysis have previously been visualised in human vertebrae using Digital Image Correlation (DIC) and concluded increased lesion size correlated with deviations in strain distribution (Palanca et al., 2021a). Regions of high strain energy density (SED), reported in *in vivo* micro-CT images of mouse vertebrae under cyclical loading over 3 weeks, reportedly correlate with high osteoblast and osteoclast activity (Webster et al., 2015). Following the intracardiac injection of osteolytic HeLa cells, strains within the vertebrae of metastatic rats were visualised using micro-CT imaging and high-contrast staining, and reported the reduction in bone density in metastatic bone leads to increased occurrence of micro-damage (Choudhari et al., 2016) (see Figure 2.18). While previous studies have successfully demonstrated how changes in mechanical stress, strain and SED fields can be analysed to accurately predict fracture failure risk, how these changes may come about as osteolytic lesions form is not fully understood. Furthermore, how such changes in mechanical strain within the bone microarchitecture could contribute to bone cellular behaviour and the mechanoregulation process has not yet been investigated.

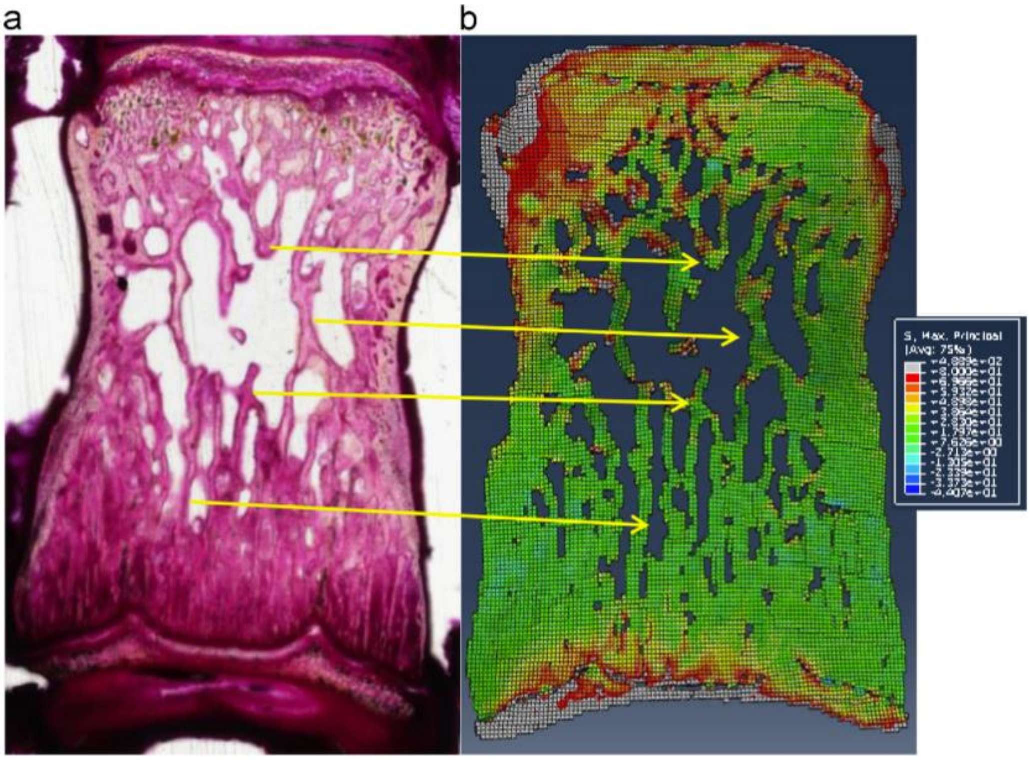

Figure 2.18: Visualising microdamage within a metastatic rat vertebra using finite element modelling. (A) Brightfield image of a histologically stained cross-section of a rat vertebral cross-section, with (B) corresponding µFE model of this region with a coloured contour plot of principal stress distribution (Choudhari et al., 2016).

2.6 Summary

This chapter has provided a detailed review of bone tissue composition and function, the bone remodelling process, the morphology and behaviours of key resident bone cells, and how regulation of the bone mechanical environment is disrupted by the cancer metastatic process. In summary, in healthy bone tissue, this remodelling process is dictated by osteoblast-driven bone formation, osteoclast-driven bone resorption and regulated by mechanosensitive osteocytes. During osteolytic metastasis, upon the invasion of metastatic cells, released osteolytic factors disrupt this regulation of the mechanical environment and stimulate the overactivity of osteoclasts, ultimately resulting in devastating osteolysis. However, while published research has established a fundamental understanding of metastatic invasion and the destructive behaviour of the cancer vicious cycle in bone tissue following osteolysis, it is unclear how the bone tissue material properties compare, prior to and following the development of breast cancer osteolytic lesions. In particular, the temporal changes in bone mineral content, physical properties and mechanical strains between cancer cell extravasation and subsequent overt osteolytic destruction have not yet been investigated. According to mechanoregulation theory, such changes within the mechanical microenvironment of bone may trigger osteocyte activity and subsequent activation of resident osteoblasts and osteoclasts. This thesis investigates how time-dependent changes in the bone mechanical environment, and the mechanobiological cues which could arise upon such changes, may contribute to the perpetuation of the cancer vicious cycle and tumour invasiveness during breast cancer metastasis to bone tissue.

Chapter 3 of this PhD thesis investigates how bone tissue mineral content and mechanical properties are altered, prior to and following overt osteolytic destruction, using an animal model of breast cancer metastasis. In Chapter 4, finite element analysis is implemented to establish how changes in tissue properties and composition (from Chapter 3) may alter mechanical strain stimulation within the bone microenvironment by simulating mouse femur models under physiological loads. Chapter 4 investigates the impact of early bone tissue mineralisation on mechanical strain distribution within the bone tissue microenvironment. Finally, Chapter 5 predicts the mechanoregulatory response of resident bone cells over 3 weeks of metastatic progression, using finite element simulations of mechanoregulation theory in pre-osteolytic bone tissue.

Chapter 3: Temporal and Spatial Changes in Bone Mineral Content and Mechanical Properties During Breast-Cancer Bone Metastases

The following chapter is based on a scientific paper which has been peer reviewed and published in the journal *Bone Reports* (Verbruggen et al., 2022) and is presented below in the format of this article. All tissue sample harvesting, micro-CT analysis, nanoindentation mechanical testing, statistical analyses, writing and editing were conducted by the author of this thesis. Model design, IVIS imaging, and scientific writing pertaining to IVIS imaging were conducted by our collaborators (Dr. Róisín M. Dwyer and Elan C. McCarthy, Lambe Institute for Translational Research, University of Galway, Ireland) with their co-authorships and contributions recognised upon publication.

3.1 Introduction

Metastasis occurs when cancer cells migrate from a primary tumour site and colonise a secondary organ, and is the primary cause of mortality in cancer patients (Weigelt et al., 2005, Langley and Fidler, 2007). Cancer cells favour metastasis to bone tissue for 70-80% of advanced breast cancer patients (Coleman and Rubens, 1987, Plunkett and Rubens, 1999) which leads to either bone destruction (osteolysis) or to tissue formation by a process known as osteoblastic metastasis (Mundy, 2002, Clines and Guise, 2005, Kozlow and Guise, 2005). Metastatic invasion of the skeletal environment leads to severe pain, increased fracture risk, nerve compression and hypercalcemia (Clines and Guise, 2005, Kozlow and Guise, 2005). In healthy bone the coordinated activities of osteocytes, osteoblasts, and osteoclasts govern bone tissue structure and composition, and ensure a constant remodelling process in response to mechanical cues due to skeletal loading (McNamara, 2010, Mellon and Tanner, 2012). Paget’s ‘Seed and Soil’ theory (1889) suggests that cancer cells migrate to bone tissue due to its easily manipulated remodelling process and attractive physical properties. Tumour cells first arrive within the bone marrow extracellular matrix (ECM), a mechanosensitive tissue that houses osteoblasts and osteoclasts and a source of mechanobiological cues for regular bone remodelling (Lynch et al., 2020), before tumour cells ultimately adhere to the bone tissue surface (Zheng et al., 2013, Allocca et al., 2019). During bone metastasis, invading tumour cells disrupt the normal bone remodelling process over time by releasing growth factors, most notably PTHrP. This growth factor activates osteoclasts to collaborate and resorb the bone matrix, in turn releasing chemotactic stimuli and additional growth factors (TGFβ, Ca^{2+}) (Yoneda et al., 1994, Guise, 2002, Kumar and Weaver, 2009). Growth factors and cytokines, stored within the ECM and released upon resorption, are key attractants for invading breast cancer cells, and facilitate further tumour cell proliferation (Yoneda et al., 1994). This process of tumour cell proliferation, osteoclast resorption and osteoblastic metastasis is thereby perpetuated in a ‘vicious cycle’ of cancer (Clines and Guise, 2005).

To understand fracture susceptibility following metastasis, bone mineral content analysis (including bone density, morphology and homogeneity) and mechanical assessment have been conducted to characterise bone tissue from patients with bone metastases (Kaneko et al., 2003, Nazarian et al., 2008). Micro-CT analyses of the femoral diaphysis of patients with mixed cancer metastases (lung, breast, prostate, 53-78 years old) revealed significantly decreased mean BMD in cadaveric cortical bone in patients with metastases (Kaneko et al., 2003). Mechanical tests were performed on patient cortical bone samples with metastatic lesions and compared to cancer-free bone regions (Kaneko et al., 2003), which revealed significantly lower Young’s modulus, yield strength and ultimate strength under compression, as well as lower Young’s modulus under tension. These findings were suggested to be a result of increased cortical bone ductility, measured as the strain from yield to ultimate failure, as osteolysis progresses (Kaneko et al., 2003). In a follow on study of distal femora of human metastatic patients (45-88 years old), no differences were reported in bone density or Young’s modulus between groups, which was attributed to low patient numbers and large metastatic variation (Kaneko et al., 2004). A later study analysed bone cores of metastatic male and female patient bone tissue (lung, breast, prostate, ovarian, colon, 36-83 years old), sourced from proximal femurs and vertebrae either at surgery for fracture treatment or autopsy, and compared to site-matched cadaveric bone tissue of cancer-free patients (Nazarian et al., 2008). This study found significantly lower bone mineral content (by micro-CT analysis), decreased weighted average gray levels (via backscatter emission, BSE), decreased compressive yield strength, and also decreased Young's modulus and hardness, via dry nanoindentation, in metastatic bone tissue compared to healthy samples (Nazarian et al., 2008). Although these studies established that osteolytic cancer metastasis is associated with a decrease in human bone mineral content and mechanical properties, it remains that patient variation arises due to differences in age, extent of metastasis, underlying conditions (e.g. osteoporosis) and treatment regimens (e.g. chemotherapy) (Yao et al., 2020). Such variability has limited a comprehensive understanding of changes in bone tissue during metastasis.

Pre-clinical animal models have enabled the study of changes in bone tissue composition and nanoscale mechanical (nano-mechanical) properties after metastasis by breast cancer cells. Three weeks following intracardiac inoculation of HeLa cervical cancer cells in female athymic rnu/rnu rats (5-6 weeks old) trabecular vertebral bone tissue presented osteolytic bone lesions of decreased crystallinity, crystal size and collagen quality as detected by Raman Spectroscopy (Burke et al., 2016). Notably, High performance Liquid Chromatography (HPLC) analysis revealed a significant increase in advanced glycation end product (AGE) collagen crosslink pentosidine compared to healthy controls, previously associated with increased risk of fracture failure. A similar study also found decreased crystal width (Burke et al., 2017), whereas another showed decreased bone mineral density, trabecular thickness, number and bone volume in rat vertebral bone tissue using micro-CT analysis (7.4µm), 3 weeks post-intracardiac inoculation of HeLa cells (Burke et al., 2018). Another animal study directly injected MDA-MD-231 derived F10 breast cancer cells into the intercondylar fossa of the right femurs of 8-week-old female NCr nude mice and compared to the left femurs of these animals receiving SHAM injections of culture medium as internal controls (Arrington et al., 2006). This study reported osteolytic lesions in 58% of animals by 3 weeks post tumour injection via radiography, but no significant differences in bone strength via whole bone torsion testing were reported, whereas dual-energy X-ray absorptiometry (DEXA) measurements of areal BMD had significantly increased in both contralateral femora (internal controls) and tumour-injected femora by 3 weeks (Arrington et al., 2006). By 6 weeks tumour-injected femora with osetolytic lesions had significantly lower areal BMD compared to those with no detectable lesions and to controls. Meanwhile, bone stiffness had significantly decreased in tumour injected femora, both with or without lesions, compared to contralateral femurs, and most animals did not reach the 9 week time point due to high risk of fracture (Arrington et al., 2006). In a later study, osteolytic destruction was visible within 3 weeks after direct innocculation of MDA-MD-231 cells into distal femora of nude NCr mice, yet no changes in BMD were detected (micro-CT at 12µm resolution) but by 6 weeks post-injection there was a significant reduction in BMD compared to contralateral limbs that did not receive injections (Arrington et al., 2008). A similar study involved reconstructing the tumour-bearing and contralateral mouse tibiae in silico, using finite element analysis, which was subjected to 3-point bend testing (Mann et al., 2008). This study separated cohorts according to osteolysis severity rather than time points. Interestingly, a strong correlation between bone density and corresponding mechanical properties was found, specifically in bone tissue stiffness and strength, and correlations were greatest in micro-CT derived densities as opposed to DEXA imaging (Mann et al., 2008). In another pre-clinical study, distal tibiae were analysed from athymic BALB/c mice (4 weeks old) after intravenous injection with MDA-MB-231 breast cancer cells. By 32 days after intravenous injection, both trabecular bone mineral content (via histomorphometry) and cortical bone elastic modulus, determined by atomic force microscopy (AFM), were significantly reduced (Richert et al., 2015). Another study reported significantly decreased dry nanoindentation modulus in femur diaphysis cortical bone samples by 14-days after intracardiac injection of osteolytic B16F10 melanoma cells into C57BL/6 female mice (Sekita et al., 2017). Interestingly, a comparative study of young (6 weeks) and mature (16 weeks) nude BALB/c mice that received intracardiac injections of MDA-MB-231 cells, demonstrated that the rate of osteolytic lesion development at 3 weeks was greatly increased in young mouse bone expressing higher rates of metabolic activity (Wang et al., 2015). A recent animal study performed daily intraperitoneal injections of MDA-MB-231 tumour-conditioned media into nude BALB/c mice for 3 weeks (Chiou et al., 2021), while also introducing mineral-binding dyes green calcein (at day 13) and xylenol orange (day 20) into the bone marrow cavity of the proximal tibiae. They reported an increased rate of bone mineral apposition in the endosteal cortical bone tissue, adjacent to the growth plate, within 7 days of early metastatic development, with no significant changes in rate of trabecular bone mineral apposition (Chiou et al., 2021). Interestingly, micro-CT analysis at 3 weeks of this study found significantly increased cortical and trabecular bone volume fraction and thickness compared to healthy controls (Chiou et al., 2021). The above studies characterise changes in bone mineral content and mechanical properties, and their timeline, upon overt osteolytic destruction of the bone tissue microenvironment. However, how these bone tissue material properties compare prior to and following the development of breast cancer osteolytic lesions is not fully understood. Furthermore, these animal studies involved inoculation of cancer cells directly into the femoral cavity or peripherally via intra-cardiac, intraperitoneal, or intravenous sites. Such approaches only partially recapitulate the breast cancer metastatic process *in vivo*, as they do not capture cancer cell extravasation from the primary tumour and homing to the bone environment (Kretschmann et al., 2012), which would dictate the timing of adhesion and colonisation of the bone. Furthermore, these studies involved immunocompromised (athymic or nude) animal models, albeit that the immune system may play an important role in tumour–bone cellular interactions during the metastatic process (Kretschmann and Welm, 2012).

One study investigated bone tissue after MDA-MB-231 breast cancer cells were injected into the mammary fat pads of female BALB/c mice, and confirmed via bioluminescent imaging that metastatic cells were present in the trabecular bone region of the proximal tibias 7 weeks post-inoculation (He et al., 2017). Moreover, in this study X-ray scattering analysis revealed significantly shorter HA crystals and large-area Raman imaging demonstrated decreased mineral crystallinity, in the tibiae of these mammary-inoculated mice when compared to healthy controls at this 7-week time point, which was proposed to indicate immature bone mineral (He et al., 2017). Inoculation of triple-negative 4T1 cells into the mammary pad of BALB/c immunocompetent mice results in primary tumour formation within one week post-inoculation and has a reported 100% incidence of metastasis to bone tissue 3-4 weeks post-inoculation, confirmed by H&E histological staining (Lelekakis et al., 1999, Yoneda et al., 2000). This 4T1-BALB/c mouse model recapitulates key steps of breast cancer metastasis from a primary tumour site to bone, whereby breast cancer cells which have intravasated into the capillary network subsequently extravasate to the bone marrow niche to initiate colonisation and the metastatic process (Kretschmann and Welm, 2012, Allocca et al., 2019). This animal model has enabled the study of biochemical treatments such as kinase inhibitors (A77636, PD407824, pitavastatin) for impeding the development of osteolytic lesions upon breast cancer metastasis (Minami et al., 2017, Jiang et al., 2018, Wang et al., 2019). However, the time-dependant and spatial evolution of bone tissue properties following primary tumour development has not been fully characterised. In particular, the temporal changes in bone physical properties between cancer cell extravasation and subsequent overt osteolytic destruction have not yet been investigated. These changes may alter the tumour-adjacent and non-tumour-bearing mechanical environments of bone and tumour cells over time, and might thereby play a role in perpetuating the cancer vicious cycle and tumour invasiveness during breast cancer metastasis to bone.

The objective of this study was to investigate changes in bone mass and microarchitecture, mineral content and nano-mechanical properties of bone tissue that arise upon breast cancer metastatic cell invasion, by micro-CT imaging and nanoindentation analysis of bone tissue from an immunocompetent BALB/c mouse model inoculated with 4T1 breast cancer cells in the mammary fat pad, and relate these findings to the temporal development and location of the primary tumour mass.

3.2 Methods

3.2.1 Animal Model

The current study utilises the 4T1-BALB/c animal model, both for its high metastatic rate and its ability to recapitulate the *in vivo* development of breast cancer metastasis from a primary tumour site to bone (Kretschmann and Welm, 2012). This research was conducted with approval from the Animal Care Research Ethics Committee (ACREC) at the University of Galway, and the Health Products Regulatory Authority (HPRA), the national authority for scientific animal protection in Ireland.

Female BALB/c immunocompetent mice (6 weeks old) were inoculated with 1 x 10^5 4T1 murine breast cancer cells via direct injection into the surgically exposed right 4th inguinal mammary fat pad, hereon referred to as the metastatic ipsilateral side (MET-IPS). These cells were previously transduced to express the luciferase gene, for downstream bioluminescent imaging. Femurs were also collected from the contralateral side (MET-CONTRA) to investigate and compare spatial changes in the bone tissue of non tumour-bearing femurs. Thus, contralateral samples were used to distinguish whether results are due to systemic metastatic development or potentially as a result of the primary tumour being in the direct vicinity of the bone tissue. The mice were maintained under normal laboratory conditions with food and water provided *ad libitum*. Healthy control models (CTRL) were sex-, strain- and age-matched, maintained under identical conditions but did not receive inoculations. The first animal cohorts were euthanised at 3 weeks post-inoculation (CTRL n = 5, MET-IPS n = 5, MET-CONTRA n = 5) and a second cohort had an endpoint of 6 weeks post-inoculation (CTRL n = 6, MET-IPS n = 7, MET-CONTRA n = 7). The 3 week timepoint was chosen because H&E staining confirmed metastatic tumour cell presence in femur trabecular bone tissue just 19 days following inoculation of 4T1 breast cancer cells into the mammary fat pad of BALB/c mice (Lelekakis et al., 1999), whereas 6 weeks was sufficient time for overt osteolytic lesions to develop (Arrington et al., 2006, Mann et al., 2008, Wang et al., 2015, Chiou et al., 2021). Although all left and right femurs of each control mouse were available for analysis (n = 12), a large sample size in the control group would exaggerate tendency to reject the null hypotheses (Faber and Fonseca, 2014). Therefore, control sample sizes similar to metastatic sample sizes were analysed. Bioluminescent imaging was performed at the conclusion of the 6 week cohort study to visualise disease progression. Animals received an intraperitoneal injection of D-luciferin (150 mg/kg), suspended in 150µl Dulbecco's Modified Phosphate Buffered Saline (DPBS), followed by imaging under inhalation anaesthesia (1-2% isoflurane) using an IVIS® Lumina LT (Perkin Elmer, USA). All femurs were harvested, muscle and tendon soft tissues removed, wrapped in PBS-soaked gauze and stored at -20˚C.

3.2.2 Micro-Computed Tomography

Micro-computed tomography (micro-CT) is a rapid, non-destructive analytical technique used for detailed quantification of bone mineral density throughout chosen volumes of interest (VOIs), and incorporates the use of hydroxyapatite phantoms to allow for analysis of bone tissue mineralisation (Bouxsein et al., 2010). Samples were thawed overnight at 4˚C, placed in 9 mm diameter chambers and immersed in phosphate buffered saline (PBS) at room temperature in a static, upright position during the imaging process. Two separate VOIs, at the proximal and distal metaphysis, were scanned to investigate cortical and trabecular bone mineral at locations near and far from the tumour site. The proximal VOI was defined as spanning from the most proximal point of the femoral head to 4mm in the distal direction. The distal VOI was chosen 0.25mm from the distal growth plate, to avoid mineral variation effects in that region, and spanned 2mm in length along the femoral shaft in the proximal direction. Quality calibrations were conducted weekly, which involved scanning a phantom of known mineral densities (0, 100, 200, 400, 800 mgHA/cm^3). Scans were taken at a voxel size of 5µm^3, suitable for detecting changes in mouse femur trabecular thickness (40-60µm). The following parameters were applied: 70kVp peak X-ray tube voltage, 57µA tube current, 900ms integration time, frame averaging of 5, 0.8 Gaussian filter and Support value of 1, Scanco Medial µCT100. A 0.5 ml aluminium filter was used to reduce the effects of beam hardening artefacts and a trinomial beam hardening correction was applied during reconstruction of the µCT scans. One MET femur from the 3 week cohort was scanned with varied parameters for optimal scan quality and reduced noise A global density threshold of 513.7 mg HA/cm^3 (3000 HU) captured both cortical and trabecular tissue, while eliminating soft tissues such as tendon or muscle fibers (Ravoori et al., 2010). A single global threshold value for all regions of interest was applied to eliminate compounding factors (Bouxsein et al., 2010). In sample scans where femoral bone features (femoral head, greater and lesser trochanters) were entirely absent, only scans where bone tissue was present were analysed. Cortical bone outlines were isolated using Scanco Medical (USA) integrated automated algorithms, while the trabecular region was manually delineated as standard (Bouxsein et al., 2010) (Figure 3.1B – 1D), maintaining approximately 50µm of space between the contour line and cortical bone internal edge. VOIs were reconstructed as 3D models and evaluation scripts, developed by Scanco Medical and generated using Image Processing Language (IPL), were applied to determine mineralisation parameters. Bone volume fraction (BV/TV), cortical and trabecular thickness (Ct.Th, Tb.Th), trabecular number (Tb.N) and trabecular separation (Tb.Sp) are indicators of bone loss and decreased vascularisation (Zeitoun et al., 2019). IPL was also used to determine mineral density ranges below, above and between the 25th and 75th percentiles (M_{low}, M_{high}, M_{med}), the most frequent mineral density value (M_{mode}), the Structure Model Index (SMI), which indicates trabecular shape (value range from 0 = flat plate, to 3 = cylindrical), and a heterogeneity indicator based on the full width at half maximum (FWHM) of the bone mineral density distribution (BMDD) curve, see Figure 3.1E. Weighted mean bone mineral density (M_{mean}), defined as the average density value weighed according to frequency, was calculated using the following equation (Roschger et al., 2008, O'Sullivan et al., 2020), which was initially developed for quantitative backscatter emission imaging (Ruffoni et al., 2007) and adapted for micro-CT anlaysis.

$$M_{mean} = \sum \frac{x_i \text{ x } freq_i}{100} \tag{3.1}$$

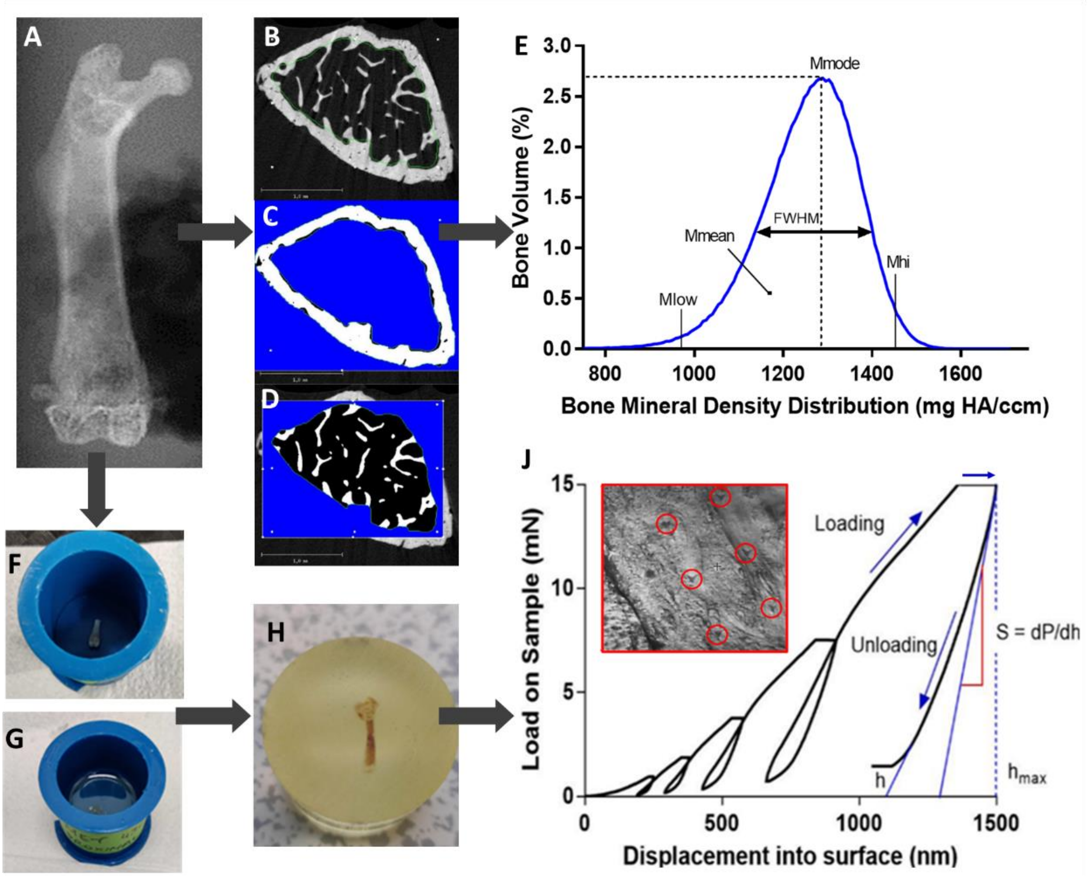

Figure 3.1 Sequence of sample analyses of a single BALB/c mouse femur. (A) Scout view prior to micro-CT scanning, (B) single distal femur greyvalue micro-CT scan, with (C) cortical and (D) trabecular bone region contours isolated and evaluated to generate each (E) bone mineral density distribution (BMDD) curve, including M_{low}, M_{med}, M_{hi}, FWHM, M_{mode} and M_{mean} parameters of bone mineralisation. (F) Femur sample, sectioned with a low speed saw and (G) covered in epoxy resin which is then (H) smooth polished to expose cortical and trabecular surface regions in preparation for (J) nanoindentation, using Oliver and Pharr equations (1992b) tests into the bone surface (inset) used to calculate nano-mechanical properties.

3.2.3 Nanoindentation

Nanoscale mechanical testing was performed to evaluate the effect of metastatic invasion and tumour presence on cortical and trabecular bone tissue elastic modulus and hardness, and this approach is widely used in human and murine studies (Lane et al., 2006, Tang et al., 2007, Nazarian et al., 2008, Burke et al., 2017, Sekita et al., 2017). Immediately following micro-CT scanning, femurs were sectioned in half, using a low speed saw (Buehler, Germany) and centrifuged to eject bone marrow (Amend et al., 2016), before dehydrating in ascending concentrations of dH_2O-diluted pure ethanol (50%, 70%, 80%, 90%, 100%, 100%) at 4˚C for 5 min intervals. Samples were embedded in a 2:1 ratio mixture of Epothin 2 epoxy resin and hardener (Buehler, Germany), vacuumed to eliminate trapped air and allowed to harden at room temperature over 72 hrs (Figure 3.1F, Figure 3.1G). Embedded samples (Buehler) were polished with diamond suspensions (9µm, 3µm, 1µm, 0.05µm) to expose proximal and distal femur halves for indentation testing in the transverse direction (Figure 3.1H). All mechanical testing of samples was performed within 2 months of the embedding process to avoid the long-term impact of epoxy resin on the nano-mechanical properties of bone tissue under nanoindentation (Mittra et al., 2006). A nanoindenter (G200, Keysight Technologies, USA), equipped with an Accutip Berkovich diamond indenter (ISO1518) was used for testing, with calibration performed on a standard fused silica sample (Corning 7980) to establish a relationship between the contact area and indenter depth. For each sample region of interest, at least 10 dry nanoindentation tests (and a maximum of 16 indents) were performed and averaged for cortical bone surfaces, and separately indented and averaged for trabecular bone surfaces. Cortical regions were indented with equidistant spacing of 40µm to avoid interference, while trabecular locations were manually selected more than 50µm from each indent and at least 10µm from the trabecular edge to avoid any influence of surrounding epoxy resin (Rho et al., 1997, Hay et al., 2000). Locations for proximal and distal region testing were selected for sufficient surface area to consistently perform at least 10 indents per bone region, while allowing for adequate spacing between indents and the epoxy resin barrier. To consider potential differences in areas near to osteolytic tumour involvement, tissue was indented in the proximal sub-region of interest on the medial (tumour) side of the femoral neck. To consider areas not adjacent to tumour tissue, a distal region on the medial side was studied, and both tumour-bearing and non-tumour-bearing femurs analysed. A 5-cycle loading regime, at 10nm/s loading rate and maximum load of 15mN, was applied (Figure 3.1J). A peak hold time of 30s was included in each cycle and environmental conditions were accounted for by performing these tests within a sealed chamber. Thermal drift effect was reduced in two ways: a) Test initiation was delayed until this measurement reached 0.1nm/s or lower and b) the indenter was unloaded to 10% load (1.5mN) and thermal drift recorded for 90s, then Young's modulus and hardness calculations adjusted accordingly (Nanosuite software, Keysight Technologies, USA). Nanoindentation equations demonstrated by Oliver and Pharr (1992b) were used to first determine contact stiffness, *S*, as the slope of the final unloading curve of each 5-cycle test, using:

$$S = \left.\frac{dP}{dh}\right|_{h_{max}} \tag{3.2}$$

where maximum load, *P*, reached indentation depth, *h*. Substituting in the above contact stiffness and applying projected contact area, *A*, reduced modulus E_r is given by:

$$E_r = \frac{\sqrt{\pi}}{2}\frac{S}{\sqrt{A}} \tag{3.3}$$

With known values of Berkovich indenter Young's modulus (1141 GPa) and Poisson's ratio (0.07), a Poisson's ratio of bone was assumed to be the value of 0.3 as standard, (Silva et al., 2004, Miller et al., 2007, Tang et al., 2007) and the Young's modulus *E* of the indented bone tissue was calculated under the assumption that the bone tissue is locally anisotropic (Equation 3). Finally, bone tissue contact hardness was quantified (Equation 4).

$$E = (1 - v^2)\left[\frac{1}{E_r} - \frac{(1 - {v_i}^2)}{E_i}\right]^{-1} \tag{3.4}$$

$$H = \frac{P}{A} \tag{3.5}$$

3.2.4 Statistical Analysis

Statistical analyses were performed using MiniTab (version 17) software with femur samples analysed from each group (CTRL, MET-IPS, MET-CONTRA) from each cohort (3 weeks, 6 weeks). Each parameter was confirmed for normal distribution in these groups (Kolmogorov-Smirnov test) and assessed for equal variance (F test). Student t-tests were implemented to determine whether averaged data was statistically significant between groups of equal variance, and Welsh's test applied where sample groups had unequal variance. Statistical outliers were identified via Grubb's test and were not rejected due to rarity and the natural variation expected in results between individual mouse bone geometries. The results are displayed as mean ± standard deviation, with significance defined as a p value of < 0.05, and greater significance ($p < 0.01$, $p < 0.001$) also indicated.

3.3 Results

3.3.1 *Primary Tumour Development and Disease Burden*

At 3 weeks post-inoculation of 4T1 breast cancer cells into the mammary fat pad animal models presented with mammary tumours, visible with the un-aided eye as subcutaneous protrusions formed within 1 cm of the femoral head, and continued to grow up to 6-weeks. The volume of these tumours was $0.328 \pm 0.046\text{cm}^3$ for the cohort euthanised at 3 weeks and increased significantly to $0.515 \pm 0.066\text{cm}^3$ for those euthanised at 6 weeks ($p = 0.004$) (Figure 3.2C) and all masses at 6 weeks expressed luciferase visualised using IVIS imaging. For both cohorts, heavy disease burden was evident whereby softer organs, including the lungs, reported to contain circulating tumour cells in all disease animal models, indicating the initiation of the metastatic phase (Figure 3.2A). However, no overt osteolytic lesions were detectable using micro-CT scanning in the 3-week cohort (Figure 3.3A – 3.3F). While all bone mineral density peaks resided within the 1000 – 1500 mg/cm^3 HA range, greater distributions of low mineral density range were seen prominent in the proximal femur cortical range compared to all other regions (see Figure 3.3G). During sample collection, it was noted tumour masses remained outside the femoral head and were not in direct contact with bone tissue.

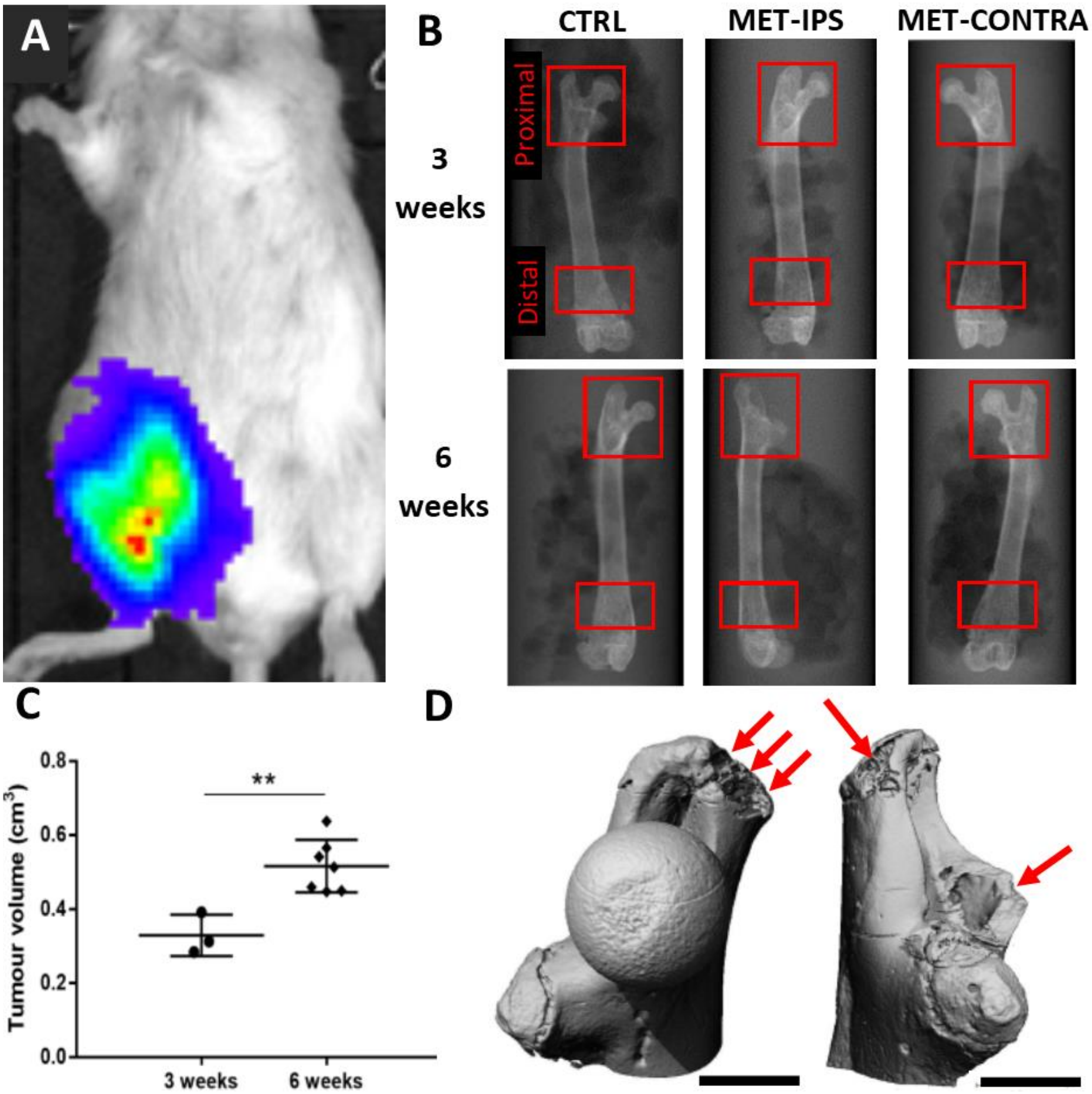

Figure 3.2: Tumour development and osteolytic destruction. (A) IVIS scan of BALB/c mouse, with 4T1 breast cancer cells populating greatest in regions highlighted in red according to the coloured contour. (B) Scout views of whole femurs from each disease group at 3- and 6-weeks post-inoculation of 4T1 breast cancer cells, including right-sided controls, with volumes of interest indicated (red boxes). (C) Measured tumour volumes at 3 weeks and 6 weeks post-inoculation (D) Two 3D reconstructions of MET-IPS proximal femurs at 6 weeks post-inoculation, with metastatic osteolytic destruction indicated (red arrows), scalebars 1mm.

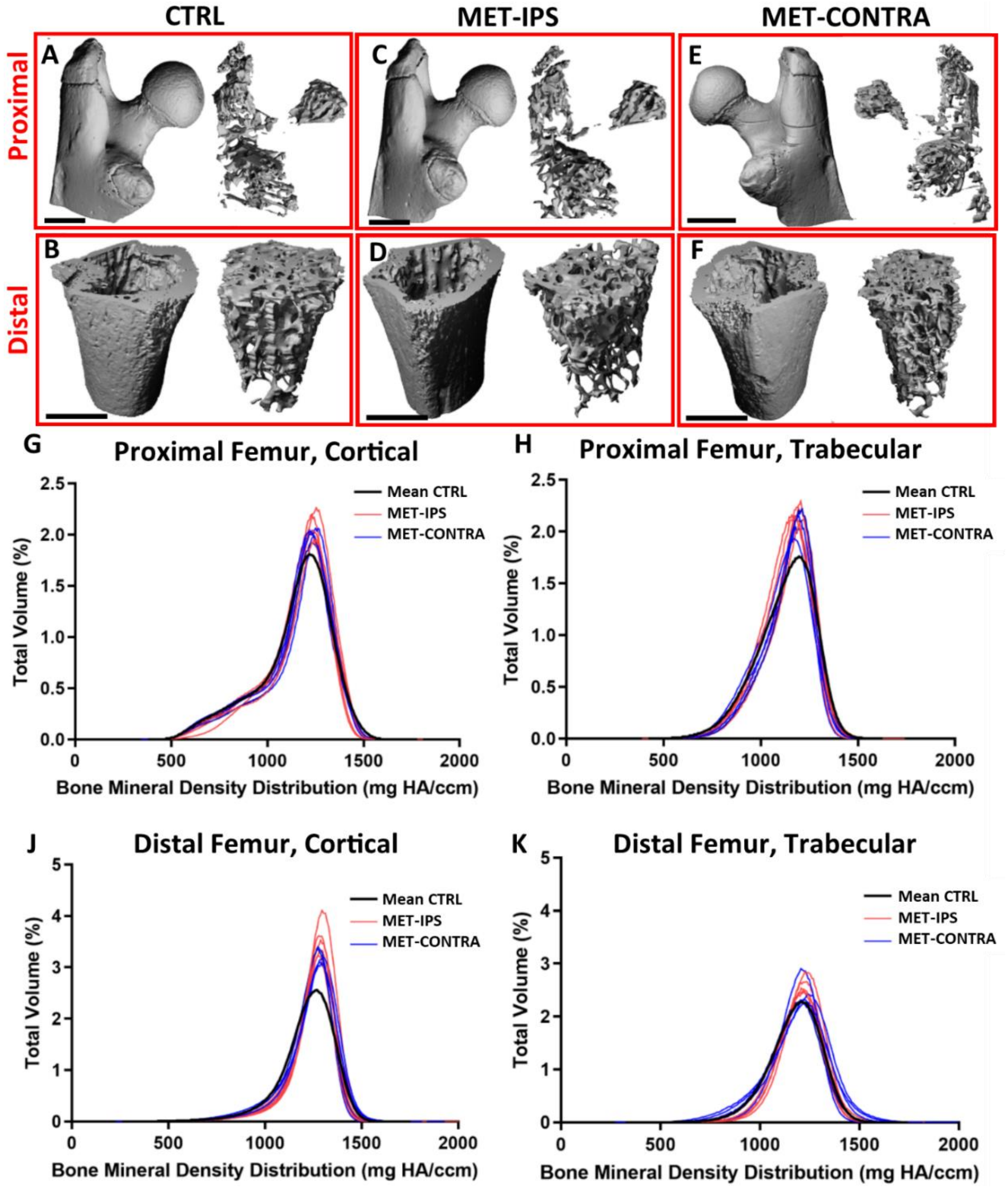

Figure 3.3: BALB/c disease and control mouse femurs at 3 weeks post-inoculation. 3D reconstructions of (A,C,E) proximal VOIs and (B,D,F) distal VOIs of a femur from each disease group, with contour isolation of (left) cortical and (right) trabecular bone regions. (G-K) Bone mineral density distribution (BMDD) curves in proximal and distal, cortical and trabecular regions of interest in BALB/c mouse femur VOIs at 3 weeks post-inoculation (CTRL n = 7, MET-IPS n = 5, MET-CONTRA n = 5).

3.3.2 *Osteolysis and bone loss (3 weeks post-inoculation):*

After 3 weeks of 4T1 primary breast cancer development, micro-CT analysis of the BALB/c mouse femurs revealed that overt osteolysis had not yet been established and there was no significant difference in bone tissue area fraction (Ct.Ar/Tt.Ar) or volume fraction (BV/TV) in proximal or distal regions of MET-IPS and MET-CONTRA femora, when compared to healthy mouse femurs (CTRL), see Figure 3.4A, Figure 3.4B. However, trabecular thickness (Tb.Th) was significantly lower in the proximal femur regions of MET-IPS samples (0.059 ± 0.002mm) compared to CTRL (0.062 ± 0.002mm, $p = 0.024$) (Figure 3.4C, 3.4D). In the distal femur regions, Tb.Th was also significantly lower both in MET-IPS (0.044 ± 0.001mm) and MET-CONTRA (0.044 ± 0.001mm) compared to CTRL samples (0.046 ± 0.002mm) ($p<0.05$). Despite changes in trabecular thickness, overall bone volume (BV) and spacing between trabeculae (Tb.Sp) did not differ significantly between groups at this early time point (see *Table 3.1*).

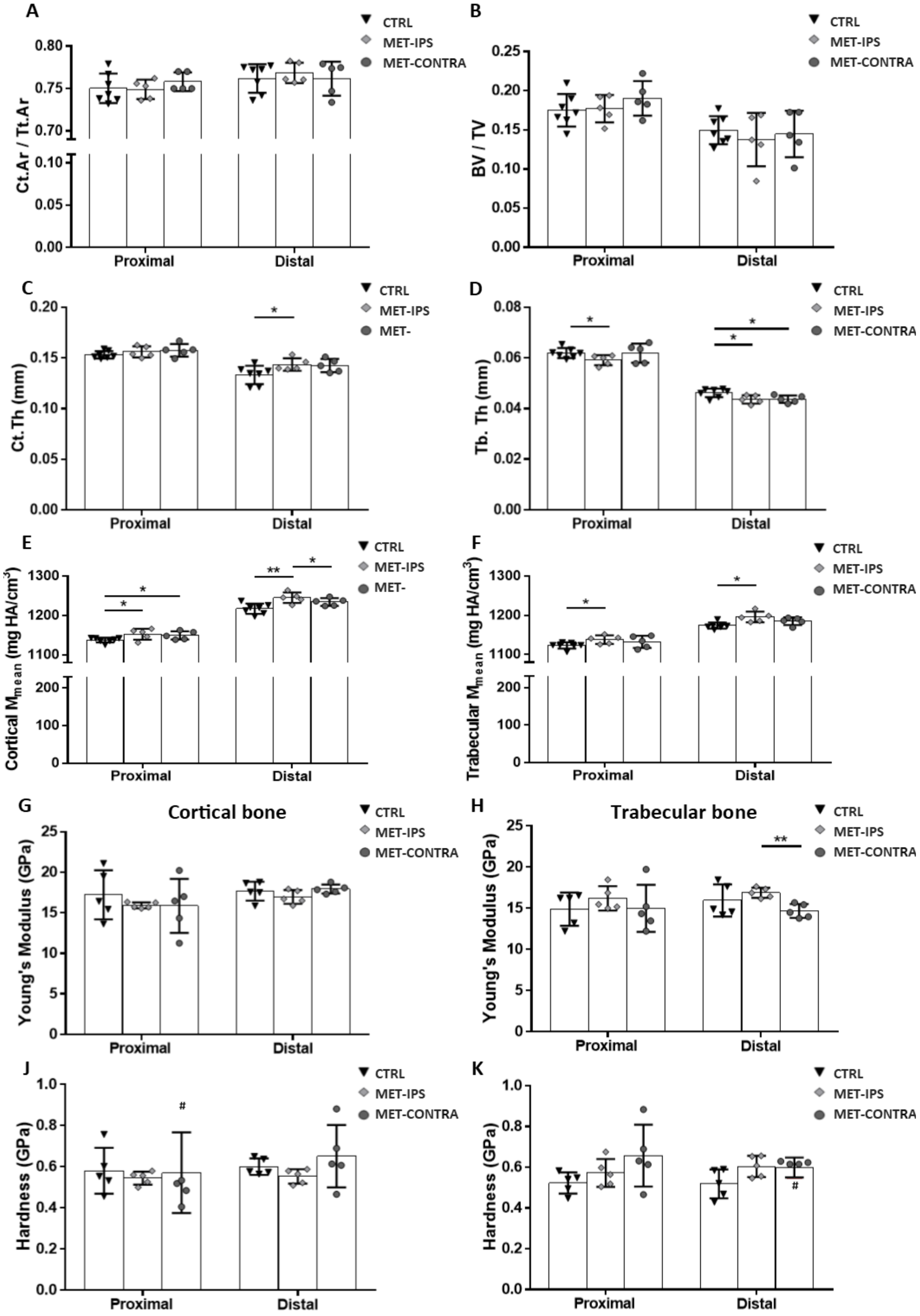

Figure 3.4: Mean parameters acquired from analyses of BALB/c mouse femurs 3 weeks post-inoculation. (A-F) Bone area fraction (Ct. Ar/Tt.Ar), bone volume fraction (BV/TV) cortical tissue thickness (Ct.Th), trabecular tissue thickness (Tb.Th), and mean mineral density (M_{mean}) values acquired from micro-CT and BMDD analysis of proximal and distal VOIs in delineated cortical and trabecular bone regions. (G, H) Young's modulus and (J, K) hardness of cortical and trabecular bone

tissue, obtained from nanoindentation tests in each bone region (CTRL n = 7, IPS n = 5, CONTRA n = 5). # Outlier, *p<0.05, **p<0.01.

3.3.3 *Early changes in bone mineralisation in the proximal femur (3 weeks post-inoculation):*

Bone mineral density distribution (BMDD) evaluations were conducted on micro-CT data from each animal after 3 weeks (Figure 3.3G-3.3K). No significant difference in mineral distribution (M_{low}, M_{high}, M_{med}), or homogeneity (FWHM) were detected between disease groups (MET-IPS and MET-CONTRA) in proximal femora when compared to healthy controls at 3 weeks, see *Table 3.1*, Figure 3.3. In the proximal femur, local to the primary tumour, cortical and trabecular weighted mean density (M_{mean}) were significantly higher in MET-IPS and MET-CONTRA samples compared to CTRL femurs (Figure 3.4E, 3.4F). While no differences in trabecular bone mode mineral density (M_{mode}) were detected between MET-IPS and CTRL proximal femurs ($p = 0.239$), the MET-CONTRA samples were significantly higher in M_{mode} (1197.19 ± 14.10 mg HA/cm^3) when compared to CTRL samples (1177.78 ± 4.33 mg HA/cm^3, $p<0.05$) (*Table 3.1*).

Table 3.1*:* Bone parameters, measured via micro-CT imaging, of healthy and disease mouse femurs 3 weeks post-inoculation (mean ± standard deviation) (CTRL n = 7, MET-IPS n = 5, MET-CONTRA n = 5) *p<0.05, **p<0.01, ***p<0.001 relative to CTRL.

		Proximal Femur			**Distal Femur**		
Cortical bone	Units	**CTRL**	**MET-IPS**	**MET-CONTRA**	**CTRL**	**MET-IPS**	**MET-CONTRA**
Tt. Ar	mm^2	1.39 ± 0.06	1.48 ± 0.07	1.41 ± 0.14	0.55 ± 0.03	0.55 ± 0.03	0.58 ± 0.04
Ct. Ar	mm^2	1.05 ± 0.05	1.11 ± 0.06	1.07 ± 0.11	0.42 ± 0.02	0.42 ± 0.02	0.44 ± 0.03
Ct.Ar/Tt.Ar	–	0.75 ± 0.02	0.75 ± 0.01	0.76 ± 0.01	0.76 ± 0.02	0.77 ± 0.01	0.76 ± 0.02
Ct.Th	mm	0.1530 ± 0.003	0.1559 ± 0.005	0.1575 ± 0.01	0.1332 ± 0.008	0.1434 ± 0.006*	0.1424 ± 0.006
M$_{mean}$	mg HA/cm^3	1137.21 ± 5.94	1152.44 ± 12.49*	1149.41 ± 9.50*	1216.93 ±12.10	1245.9 ± 12.09**	1234.07 ± 9.64*
M$_{mode}$	mg HA/cm^3	1223.41 ± 6.40	1234.12 ± 13.93	1228.67 ± 12.48	1268.17 ± 10.38	1284.68 ± 7.23*	1284.28 ± 10.40*
M low	%	4.17 ± 1.00	3.04 ± 0.85	2.74 ± 1.09	0.42 ± 0.11	0.37 ± 0.10	0.36 ± 0.07
M medium	%	89.01 ± 5.58	86.23 ± 6.79	84.57 ± 5.80	90.38 ± 7.81	92.29 ± 7.79	95.20 ± 3.68
M high	%	6.82 ± 6.19	10.73 ± 7.40	12.69 ± 6.15	9.20 ± 7.88	7.34 ± 7.86	4.43 ± 3.71
FWHM	mg HA/cm^3	253.64 ± 21.87	238.49 ± 9.86	242.69 ± 17.86	196.52 ± 8.93	191.01 ± 12.05	199.28 ± 14.33
Trabecular bone							
TV	mm^3	2.76 ± 0.18	2.92 ± 0.18	2.84 ± 0.19	2.60 ± 0.15	2.64 ± 0.14	2.71 ± 0.24
BV	mm^3	0.48 ± 0.04	0.52 ± 0.06	0.54 ± 0.06	0.39 ± 0.06	0.37 ± 0.09	0.40 ± 0.10
BV/TV	–	0.18 ± 0.02	0.18 ± 0.02	0.19 ± 0.02	0.15 ± 0.02	0.14 ± 0.03	0.14 ± 0.03
M$_{mean}$	mg HA/cm^3	1122.97 ± 7.30	1137.80 ± 9.65*	1132.10 ± 13.92	1173.73 ± 7.39	1195.8 ± 12.15*	1184.75 ± 8.82
M$_{mode}$	mg HA/cm^3	1177.78 ± 5.25	1189.43 ± 21.60	1197.19 ± 14.10*	1201.12 ±10.31	1224.24 ± 5.65**	1218.27 ± 16.92
Conn.D.	mg HA/cm^3	102.72 ± 15.35	118.35 ± 12.52	122.64 ± 11.88	230.52 ± 27.02	217.19 ± 40.76	228.24 ± 47.58
SMI	–	0.70 ± 0.12	0.68 ± 0.10	0.57 ± 0.12	1.44 ± 0.15	1.57 ± 0.32	1.44 ± 0.27
Tb.N	1/mm	2.42 ± 0.24	2.48 ± 0.16	2.59 ± 0.15	4.04 ± 0.24	4.11 ± 0.44	4.19 ± 0.42
Tb.Th	mm	0.0619 ± 0.002	0.0591 ± 0.002 *	0.0619 ± 0.003	0.0462 ± 0.002	0.0436 ± 0.001*	0.0437 ± 0.001*
Tb.Sp	mm	0.438 ± 0.05	0.419 ± 0.03	0.410 ± 0.02-	0.239 ± 0.02	0.234 ± 0.03	0.231 ± 0.03
M low	%	1.03 ± 1.25	0.43 ± 0.16	0.50 ± 0.31	0.22 ± 0.12	0.19 ± 0.08	0.38 ± 0.31
M medium	%	93.01 ± 3.18	90.99 ± 5.59	92.37 ± 3.02	96.40 ± 2.69	95.95 ± 1.72	94.66 ± 6.10
M high	%	5.96 ± 3.88	8.58 ± 5.71	7.09 ± 3.19	3.37 ± 2.75	3.87 ± 1.76	4.96 ± 6.26
FWHM	mg HA/cm^3	258.14 ± 50.24	241.51 ± 29.13	245.07 ± 20.30	249.65 ± 32.47	251.34 ± 17.63	261.82 ± 29.01

3.3.4 *Early changes in bone mineralisation and increased cortical thickness in the distal femurs (3 weeks post-inoculation):*

From micro-CT analyses of the distal femurs at 3 weeks, no significant difference in mineral distribution (M_{low}, M_{high}, M_{med}), or homogeneity (FWHM) were detected between disease groups (MET-IPS and MET-CONTRA) compared to healthy CTRL samples, see *Table 3.1*. Cortical bone M_{mean} and M_{mode} were significantly higher in both the MET-IPS and MET-CONTRA disease groups when compared to CTRL group (*Table 3.1*). Similarly, in the distal trabecular region, M_{mean} and M_{mode} were significantly higher in the MET-IPS group compared to CTRL samples ($p<0.05$, $p<0.001$) (*Table 3.1*). Interestingly, though not statistically significant, a trend of increasing M_{mean} in distal trabecular MET-CONTRA samples (1184.75 ± 8.82 mg HA/cm^3) is notable when compared to CTRL samples (1173.72 ± 7.39 mg HA/cm^3) ($p = 0.058$). Distal femur Ct.Th was also significantly higher in MET-IPS samples (0.143 ± 0.006mm) when compared to CTRL samples (0.133 ± 0.008mm).

3.3.5 *Cortical bone stiffness reduced in distal ipsilateral femurs compared to contralateral side (3 weeks post-inoculation):*

At 3 weeks, in the distal region, MET-IPS femora trabecular bone had significantly higher Young's modulus (16.88 ± 0.55 GPa) when compared to MET-CONTRA femurs (14.67 ± 0.76 GPa, $p = 0.002$) (Figure 3.4H) but did not differ compared to CTRL (15.94 ± 1.75 GPa, $p = 0.219$). Aside from this result, no differences were seen in Young's modulus or hardness values in any other regions analysed at 3 weeks (Table 3.2, Figure 3.4G, 3.4J, 3.4K).

Table 3.2: Young's modulus and hardness (mean ± standard deviation) at 3 weeks post-injection of breast cancer cells, obtained from nanoindentation mechanical tests in each region and bone tissue type of each femur. Includes mean ± standard deviation (CTRL n = 7, MET-IPS n = 5, MET-CONTRA n = 5). ††p<0.01, relative to MET-IPS.

	Proximal Femur			**Distal Femur**		
Cortical Bone	CTRL	MET-IPS	MET-CONTRA	CTRL	MET-IPS	MET-CONTRA
Young's modulus (GPa)	17.23 ± 2.71	15.92 ± 0.32	15.66 ± 3.29	17.95 ± 1.39	16.96 ± 0.76	18.18 ± 0.95
Hardness (GPa)	0.58 ± 0.10	0.54 ± 0.03	0.57 ± 0.18	0.60 ± 0.04	0.55 ± 0.03	0.65 ± 0.14
Trabecular Bone						
Young's modulus (GPa)	14.88 ± 1.80	16.20 ± 1.32	14.99 ± 2.56	15.94 ± 1.75	16.88 ± 0.55	14.67 ± 0.76††
Hardness (GPa)	0.52 ± 0.05	0.57 ± 0.06	0.66 ± 0.14	0.52 ± 0.06	0.60 ± 0.05	0.60 ± 0.04

3.3.6 *Cortical and trabecular bone loss occurred throughout disease mouse femora (6 weeks post-inoculation):*

At 6 weeks post-inoculation, all MET-IPS and MET-CONTRA femurs formed osteolytic lesions in the greater trochanter, visible from 3D reconstructions of micro-CT scans (Figure 3.5C, 3.5E). In 3 of 7 MET-IPS femur samples, the femoral head was entirely absent, with two of these samples also missing the femoral neck, while lesser and third trochanter bone tissue remained (Figure 3.2D). In the MET-CONTRA samples, 3 whole proximal regions were absent from femurs upon extraction. The working number of analysed MET-CONTRA femurs was therefore reduced to n = 4. Bone mineral density distributions ranges consistently peaked between 1000 to 1500 mg/cm^3 HA in all groups (Figure 3.5G – Figure 3.5K). The proximal femur cortical bone region showed all bone samples had a considerably quantity of tissue in the low mineral density range (500 – 1000 mg/cm^3) compared to other regions (see Figure 3.5G), as was seen above at 3 weeks post-inoculation. All diaphysis and distal femur regions remained intact. Cortical bone area fraction (Ct.Ar/Tt.Ar) in the proximal femur, local to the tumour mass, was significantly lower in MET-IPS group (0.75 ± 0.04, $p<0.01$) and MET-CONTRA group (0.79 ± 0.01mm^2, $p<0.05$) compared to the CTRL group (0.81 ± 0.004) (Figure 3.6A). Similarly, Ct.Th in this proximal region was significantly lower in the MET-IPS group (0.15 ± 0.01mm) and MET-CONTRA femurs (0.16 ± 0.11, $p<0.05$) compared to the CTRL group (0.17 ± 0.004mm, $p = 0.001$) (Figure 3.6C).

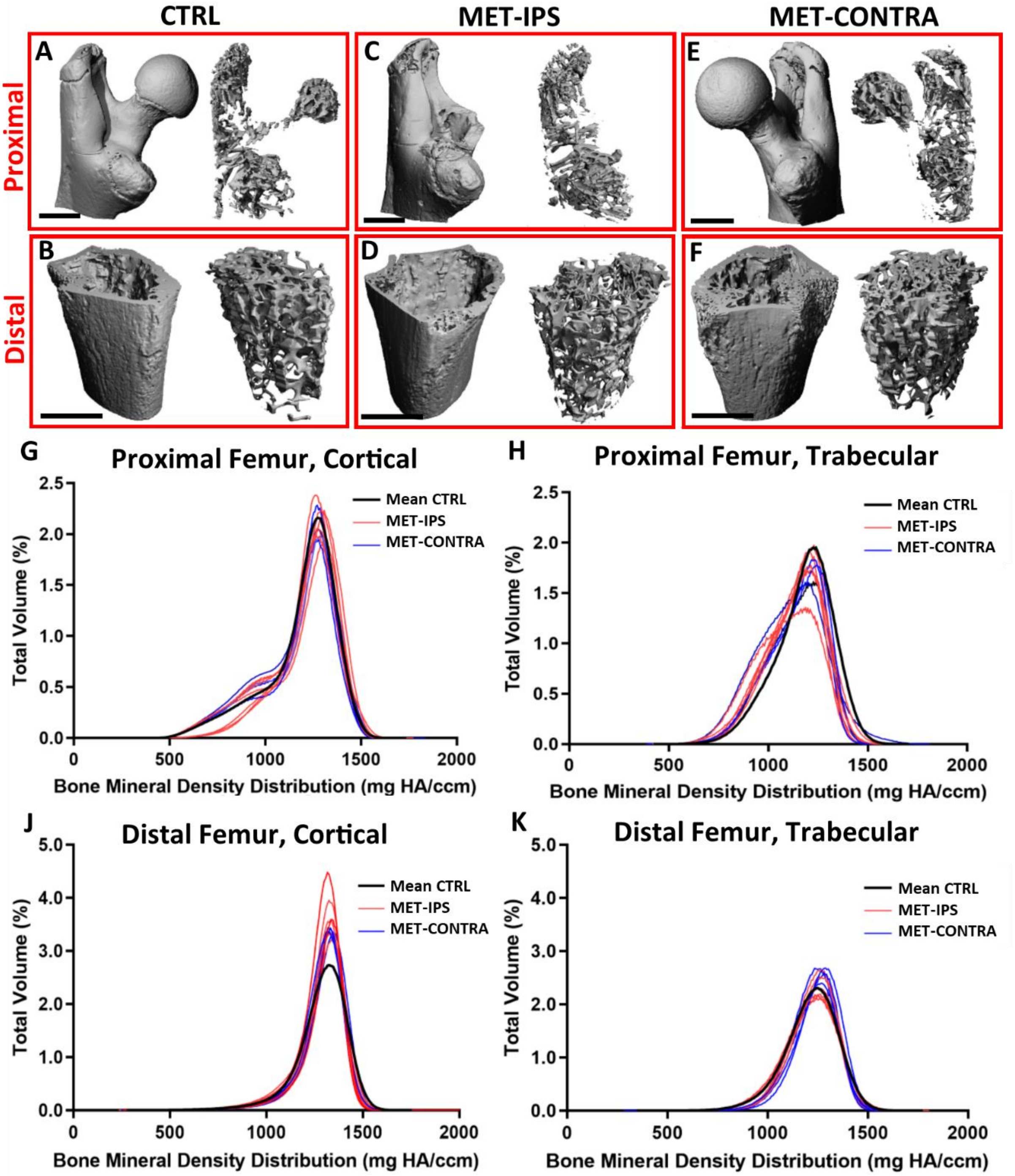

Figure 3.5: BALB/c disease and control mouse femurs at 6 weeks post-inoculation. 3D reconstructions of (A,C,E) proximal VOIs and (B,D,F) distal VOIs of a femur from each disease group, with contour isolation of (left) cortical and (right) trabecular bone regions. (G-K) Bone mineral density distribution (BMDD) curves in proximal and distal, cortical and trabecular regions of interest in BALB/c mouse femur VOIs at 3 weeks post-inoculation (CTRL n = 6, MET-IPS n = 7, MET-CONTRA n = 4).

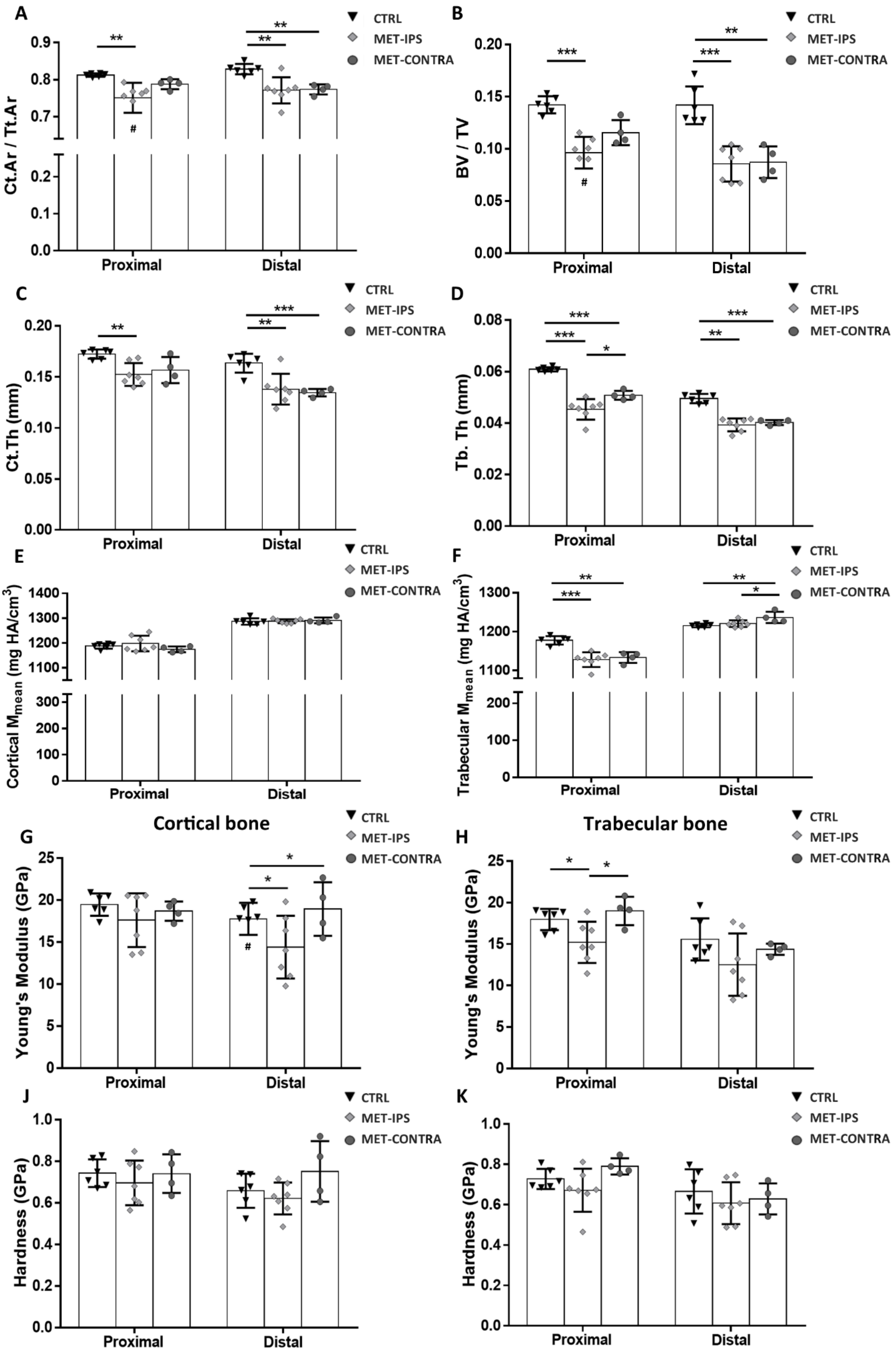
A
Ct.Ar / Tt.Ar
0.9
0.8
0.7
0.2
0.1
0.0
**
**
**
#
Proximal
Distal
▼ CTRL
◆ MET-IPS
● MET-CONTRA
B
BV / TV
0.20
0.15
0.10
0.05
0.00
***
***
**
#
Proximal
Distal
▼ CTRL
◆ MET-IPS
● MET-CONTRA
C
Ct.Th (mm)
0.20
0.15
0.10
0.05
0.00
**
**
***
Proximal
Distal
▼ CTRL
◆ MET-IPS
● MET-CONTRA
D
Tb. Th (mm)
0.08
0.06
0.04
0.02
0.00
***
***
*
***
**
Proximal
Distal
▼ CTRL
◆ MET-IPS
● MET-CONTRA
E
Cortical M_{mean} (mg HA/cm^3)
1400
1300
1200
1100
300
200
100
0
Proximal
Distal
▼ CTRL
◆ MET-IPS
● MET-CONTRA
F
Trabecular M_{mean} (mg HA/cm^3)
1300
1200
1100
200
100
0
**
***
**
*
Proximal
Distal
▼ CTRL
◆ MET-IPS
● MET-CONTRA
Cortical bone
G
Young's Modulus (GPa)
25
20
15
10
5
0
*
*
#
Proximal
Distal
▼ CTRL
◆ MET-IPS
● MET-CONTRA
Trabecular bone
H
Young's Modulus (GPa)
25
20
15
10
5
0
*
*
Proximal
Distal
▼ CTRL
◆ MET-IPS
● MET-CONTRA
J
Hardness (GPa)
1.0
0.8
0.6
0.4
0.2
0.0
Proximal
Distal
▼ CTRL
◆ MET-IPS
● MET-CONTRA
K
Hardness (GPa)
1.0
0.8
0.6
0.4
0.2
0.0
Proximal
Distal
▼ CTRL
◆ MET-IPS
● MET-CONTRA

Figure 3.6: Mean parameters acquired from analyses of BALB/c mouse femurs 6 weeks post-inoculation. (A-F) Bone area fraction (Ct.Ar/Tt.Ar), bone volume fraction (BV/TV) cortical tissue thickness (Ct.Th), trabecular tissue thickness (Tb.Th) and mean mineral density (M_{mean}) values acquired from micro-CT and BMDD analysis of proximal and distal VOIs in delineated cortical and trabecular bone regions. (G, H) Young's modulus and (J, K) hardness of cortical and trabecular bone tissue, obtained from nanoindentation tests in each region (CTRL n = 6, MET-IPS n = 7, MET-CONTRA n = 4). # Outlier, *p<0.05, **p<0.01, ***p<0.001.

In the proximal femur trabecular region, BV/TV (Figure 3.6B) was significantly lower in the MET-IPS group (9.35 ± 2.0%) and MET-CONTRA group (11.56 ± 1.03%) compared to CTRL regions (14.22 ± 0.74%) (p = 0.000, p<0.05) at 6 weeks post-inoculation. Furthermore, M_{mode} was significantly lower (p<0.05), and heterogeneity (FWHM) significantly higher (p<0.001), in MET-IPS proximal trabecular femurs compared to CTRL results (Table 3.3). Interestingly, proximal femur trabecular bone M_{mean} was found to be lower in both MET-IPS (1127.67 ± 17.65 mg HA/cm^3) and MET-CONTRA bone mineral (1133.22 ± 11.97 mg HA/cm^3) compared to CTRL (1177.53 ± 9.89 mg HA/cm^3, p = 0.000, p = 0.001), see Figure 3.6F. In the proximal femur region, Tb.Th was significantly lower in both the MET-IPS group (0.045 ± 0.004mm) and MET-CONTRA group (0.051 ± 0.002mm) compared to CTRL group (0.061 ± 0.001mm) (p = 0.000, p = 0.000). Notably, proximal femur Tb.Th was also significantly lower in the MET-IPS femurs (0.045 ± 0.004mm) compared to MET-CONTRA femurs from these same disease animals (0.051 ± 0.002mm) (p <0.05) (Figure 3.6D). As expected, trabecular spacing (Tb.Sp) was significantly higher in the MET-IPS (0.29 ± 0.07 mm) distal regions compared to healthy CTRL samples upon osteolysis (0.24 ± 0.01 mm, p<0.05) (see *Table 3.1*).

Table 3.3 Bone parameters, measured via micro-CT imaging, of healthy and disease mouse femurs 6 weeks post-inoculation (mean ± standard deviation) (CTRL n = 6, MET-IPS n = 7, MET-CONTRA n = 4) *$p<0.05$, **$p<0.01$, ***$p<0.001$ relative to CTRL. †$p<0.05$, ††$p<0.01$, relative to MET-IPS.

			Proximal Femur			**Distal Femur**	
Cortical bone	**Units**	**CTRL**	**MET-IPS**	**MET-CONTRA**	**CTRL**	**MET-IPS**	**MET-CONTRA**
Tt.Ar	mm^2	1.59 ± 0.06	1.24 ± 0.28*	1.44 ± 0.08*	0.58 ± 0.02	0.51 ± 0.04**	0.50 ± 0.02**
Ct.Ar	mm^2	1.29 ± 0.05	0.94 ± 0.23**	1.13 ± 0.07*	0.48 ± 0.02	0.39 ± 0.05**	0.39 ± 0.02**
Ct.Ar/Tt.Ar	–	0.81 ± 0.004	0.75 ± 0.04**	0.79 ± 0.01*	0.83 ± 0.01	0.77 ± 0.03**	0.77 ± 0.01**
Ct.Th	mm	0.1723 ± 0.004	0.1523 ± 0.010**	0.1565 ± 0.011*	0.1650 ± 0.011	0.1378 ± 0.014**	0.1344 ± 0.003**
M_{mean}	mg HA/cm^3	1187.52 ± 9.76	1197.98 ± 29.10	1174.16 ± 10.27	1286.61 ± 11.64	1287.77 ± 7.52	1290.73 ± 10.15
M_{mode}	mg HA/cm^3	1276.29 ± 6.99	1283.66 ± 19.78	1277.79 ± 3.92	1330.22 ± 8.55	1331.17 ± 8.47	1302.34 ± 35.39
M low	%	2.58 ± 0.45	2.20 ± 1.41	3.00 ± 0.72	0.22 ± 0.06	0.22 ± 0.07	0.18 ± 0.04
M medium	%	88.16 ± 2.19	83.25 ± 6.21	83.26 ± 6.47	76.04 ± 15.15	80.00 ± 17.46	65.12 ± 17.44
M high	%	9.41 ± 2.26	14.54 ± 6.74	13.74 ± 7.11	23.75 ± 15.17	19.78 ± 17.51	34.69 ± 17.48
FWHM	mg HA/cm^3	233.87 ± 16.84	229.32 ± 9.06	226.94 ± 16.65	192.55 ± 11.68	177.92 ± 12.35	185.66 ± 15.29
Trabecular bone							
TV	mm^3	3.57 ± 0.15	4.35 ± 0.46**	4.47 ± 0.20**	3.21 ± 0.06	3.74 ± 0.33**	3.68 ± 0.23**
BV	mm^3	0.51 ± 0.03	0.41 ± 0.11	0.52 ± 0.05	0.46 ± 0.05	0.32 ± 0.07**	0.32 ± 0.05*
BV/TV	–	0.14 ± 0.01	0.09 ± 0.02**	0.12 ± 0.01*	0.14 ± 0.02	0.09 ± 0.02***	0.09 ± 0.01**
M_{mean}	mg HA/cm^3	1177.53±9.89	1127.67 ± 17.65***	1133.22 ± 11.97**	1215.72 ± 4.2	1220.38 ± 8.04	1236.51 ± 12.47*†
M_{mode}	mg HA/cm^3	1228.39 ± 6.62	1209.63 ± 14.05*	1224.16 ± 16.46	1247.99 ± 8.38	1257.21 ± 8.83	1269.69 ± 20.73
Conn.D.	mg HA/cm^3	64.28 ± 8.31	83.02 ± 15.579	79.27 ± 9.17	140.75 ± 13.59	135.35 ± 40.75	141.63 ± 34.90
SMI	–	0.86 ± 0.03	1.38 ± 0.26***	1.13 ± 0.05**	1.48 ± 0.21	1.97 ± 0.31	2.11 ± 0.14**
Tb.N	1/mm	2.14 ± 0.15	2.14 ± 0.13	2.29 ± 0.29	3.86 ± 0.13	3.51 ± 0.57	3.71 ± 0.31
Tb.Th	mm	0.0611 ± 0.001	0.0454 ± 0.004***	0.0509 ± 0.002*** †	0.0496 ± 0.016	0.0393 ± 0.002**	0.0402 ± 0.001***
Tb.Sp	mm	0.49 ± 0.04	0.47 ± 0.03	0.45 ± 0.06	0.24 ± 0.01	0.29 ± 0.07*	0.26 ± 0.02
M low	%	0.54 ± 0.13	0.97 ± 0.46	1.18 ± 1.23	0.15 ± 0.06	0.12 ± 0.07	0.06 ± 0.02*
M medium	%	93.10 ± 5.62	93.49 ± 2.54	88.80 ± 5.30	94.73 ± 2.69	88.86 ± 9.69	78.81 ± 18.00
M high	%	6.36 ± 5.73	5.54 ± 2.41	10.02 ± 6.26	5.09 ± 2.75	11.01 ± 9.74	23.38 ± 16.14*
FWHM	mg HA/cm^3	253.36 ± 24.77	341.28 ± 41.26**	316.14 ± 69.34	267.50 ± 19.50	282.05 ± 18.52	244.09 ± 9.27††

In the distal femur cortical bone, Ct.Th and Ct.Ar/Tt.Ar were significantly lower in the MET-IPS and MET-CONTRA groups compared to CTRL femurs (Figure 3.6C). Similarly, in distal femur trabecular regions, BV/TV and Tb.Th were also significantly lower in the MET-IPS and MET-CONTRA femurs compared to CTRL (Table 3.3). It is notable that distal trabecular mineral heterogeneity (FWHM) was significantly higher in the MET-IPS group (282.05 ± 18.52 mg HA/cm^3) compared to the MET-CONTRA group (244.09 ± 9.27 mg HA/cm^3, $p<0.01$) but did not differ from CTRL samples (267.5 ± 19.5 mg HA/cm^3, $p = 0.231$). Interestingly, low range trabecular bone mineral density (M_{low}) had significantly decreased, and high range bone mineral density (M_{high}) had significantly increased, in MET-CONTRA samples compared to CTRL samples at the 6 week time point, while no differences were seen in these ranges between tumour-adjacent MET-IPS and CTRL femurs (Figure 3.5K, Table 3.3).

3.3.7 *Nano-mechanical properties lower in tumour-adjacent femurs (6 weeks post-inoculation):*

At 6 weeks in the proximal region trabecular bone, Young's modulus in the MET-IPS group (15.21 ± 2.30 GPa) was found to be significantly lower when compared to both CTRL femurs (17.96 ± 1.17 GPa, $p = 0.031$) and to MET-CONTRA femurs (18.99 ± 1.48 GPa, $p = 0.026$), see Figure 3.6H. In the distal region, mean Young's modulus was significantly lower in the cortical bone of the MET-IPS femurs (14.39 ± 3.47 GPa) when compared to MET-CONTRA (18.92 ± 2.76 GPa, $p<0.05$) (Figure 3.6G) but did not differ from CTRL (17.77 ± 1.75 GPa, $p = 0.698$). No significant differences in bone hardness were detected (Figure 3.6J, 6K) (*Table 3.4*).

Table 3.4: Young's modulus and hardness (mean ± standard deviation) 6 weeks post-inoculation of 4T1 breast cancer cells, obtained from 10 nanoindentation mechanical tests in each region and bone tissue type of each femur. Includes mean ± standard deviation (CTRL n = 6, MET-IPS n = 7, MET-CONTRA n = 4). *p<0.05, relative to CTRL. †p<0.05 relative to MET-IPS

	Proximal Femur			**Distal Femur**		
Cortical Bone	**CTRL**	**MET-IPS**	**MET-CONTRA**	**CTRL**	**MET-IPS**	**MET-CONTRA**
Young's modulus (GPa)	19.46 ± 1.20	17.61 ± 2.96	18.68 ± 0.99	17.77 ± 1.75	14.39 ± 3.47*	18.92 ± 2.76*
Hardness (GPa)	0.74 ± 0.07	0.70 ± 0.01	0.74 ± 0.08	0.74 ± 0.05	0.67 ± 0.099	0.75 ± 0.13
Trabecular Bone						
Young's modulus (GPa)	17.96 ± 1.17	15.21 ± 2.30*	18.99 ± 1.48†	15.56 ± 2.31	12.52 ± 3.47	14.37 ± 0.59
Hardness (GPa)	0.73 ± 0.05	0.67 ± 0.10	0.79 ± 0.04	0.67 ± 0.10	0.61 ± 0.10	0.63 ± 0.07

3.4 Discussion

This study reveals temporal changes in bone microarchitecture, mineral content and nano-mechanical properties local and distal to breast cancer metastatic tumours induced in an immunocompetent BALB/c mouse model inoculated with 4T1 breast cancer cells in the mammary fat pad. This is the first study to directly compare changes in bone tissue material properties upon breast cancer metastasis, both prior to and following the development of osteolytic lesions using the same immune competent animal model. In addition, analyses were conducted in two distinct proximal and distal regions in femurs of both tumour-bearing and non-tumour-bearing long bones within the same disease animals, allowing for a comprehensive understanding of the impact of tumour presence on resulting changes in the bone mechanical environment. Moreover, thanks to the non-destructive nature of micro-CT, 3D bone mineral content analysis and mechanical testing was conducted on the same femur samples, which is not possible when utilising backscattered electron imaging (BSE) or Raman spectroscopy methods. The results from this study reveal no overt osteolytic destruction by 3 weeks post-inoculation, but trabecular thinning and increased bone mineralisation suggest early compensatory response to breast cancer metastatic invasion of bone tissue. Upon overt osteolytic destruction at the later time point of 6 weeks, significant decreases in bone mineral content and tissue properties occurred throughout both the ipsilateral and contralateral bones of the metastatic animals. These results reveal the time-dependant and spatial nature of changes in bone tissue, and specifically reveal that bone tissue composition is altered prior to the development of overt metastatic osteolysis, local and distant from the primary tumour site. Such changes observed in this study may arise either as a result of tumour-derived growth factors released upon the arrival of disseminated tumour cells, or might be a mechanobiological mineralisation response by bone cells in regions of elevated strain, as discussed in detail below.

Some limitations to this study require consideration. Firstly, skeletal responses to metastatic invasion may differ in the mouse model from human patients due to biological, anatomical, and musculoskeletal differences. However, mice exhibit similar bone morphological changes during ageing to humans (Jilka and Sciences, 2013) and the 4T1-BALB/c mouse model consistently produces bone tissue metastasis and is not susceptible to the same degree of subject variation as arises in human studies. Secondly, only two time points were chosen for this study and later time points were not included, because by 6 weeks overt osteolysis was already established, and 9 weeks post-inoculation is reported to exceed the humane endpoint of mouse metastatic models due to high risk of fracture failure, determined from x-ray images, lameness or dramatic weight loss (Arrington et al., 2006). Thirdly, because methods required for histological analyses are destructive and impact bone properties (Currey et al., 1995, Nazarian et al., 2009), IVIS scans were used to confirm tumour cell presence in metastatic animals by 6 weeks in lieu of histology. However, micro-CT imaging from the current study detected extensive osteolysis, providing further evidence of successful metastatic invasion. Moreover, H&E staining has confirmed the presence of metastatic tumour cells in femoral trabecular bone tissue at just 19 days in the same animal model (Lelekakis et al., 1999). Fourthly, dry nanoindentation was used in this study, which is reported to result in higher Young’s modulus and hardness (compared to hydrated samples in C57BL/6 mice tibiae) (Rodriguez-Florez et al., 2013). However, nanoindentation of dry bone tissue is suitable for comparative studies (Rho and Pharr, 1999), as demonstrated in previous studies investigating patient and animal model breast cancer metastasis (Nazarian et al., 2008, Sekita et al., 2017). Testing of hydrated samples is limited to within 45 minutes of removal from storage in deionised water to avoid air drying effects (Rodriguez-Florez et al., 2013), which was not feasible given time taken for thermal drift to reach equilibrium (~1hr per batch test). It is important to note that all samples were tested dry, and so the differences reported between groups are valid. While most femurs were harvested from the right anatomical side of the mouse, two of five femurs in the 3-week control cohort were collected from the left side. However, studies have shown that bone geometry and tissue properties do not vary in female tibiae of the same species (Margolis et al., 2004, Vesper et al., 2017), and thus this is unlikely to have impacted FE results. Finally, tumour masses on one side of metastatic mouse anatomy may cause asymmetric gait, whereby mice would offload the tumour-bearing hindlimb and increase weight on the contralateral limb out of discomfort, possibly altering bone physical properties in both femurs. While precise changes in limb loading throughout the animal study had not been quantifiably measured, no visible changes in mouse physical gait were noted through daily observational checks on these animals. It should be noted that femoral heads were absent for three metastatic ipsilateral and three contralateral animals by 6 weeks, which likely arose due to fractures during extraction of the femoral head from pelvic bone after osteolysis. However, such fragility did not arise in healthy control bones and thus this brittle behaviour resulting in broken bone tissue, seen in both ipsilateral and contralateral femurs, is further evidence of the extent of bone loss in the metastatic animals. Had these femoral head regions remained intact, this may have revealed even greater changes in bone mineral content and nano-mechanical properties.

Breast cancer in late-stage patients undergoes metastatic spread to bone locations distant from the primary tumour, including the long bones, spine, pelvis, and ribs (Demers et al., 2000, Macedo et al., 2017). Key steps in the metastatic process are intravasation, circulation, evasion of host immune response, and subsequent extravasation of metastatic breast cancer cells from vasculature to arrive at the target tissue (Kretschmann and Welm, 2012). These processes are recapitulated in the immunocompetent mouse model utilised in the current study, in which a primary tumour was induced via mammary fat pad inoculation of breast cancer cells, and follows the metastatic cascade as would occur *in vivo,* rather than direct inoculation into the bone environment. This animal study has successfully replicated osteolysis due to breast cancer metastasis, as confirmed by micro-CT results in both tumour-adjacent ipsilateral femurs and contralateral femurs after 4T1 breast cancer cell inoculation. It is assumed that any evidence of metastatic invasion is a result of breast cancer cell extravasation from the vasculature within the bone microenvironment. Despite the development of tumour masses and evidence of heavy tumour burden at 3 weeks post-inoculation, micro-CT and bone mineral density distribution analysis revealed that overt osteolytic destruction was not detected until 6 weeks post-inoculation. However, trabecular thickness was reduced by 3 weeks and may indicate the initiation of osteolysis in the trabecular compartment. This finding is consistent with a study which reported breast cancer metastatic invasion was first detected in the trabecular bone marrow niche, 5 days after intracardiac or intravenous injection of cells into 12-week-old BALB/c mice (Allocca et al., 2019). Trabecular bone has a higher rate of bone turnover and metabolic activity compared to cortical bone tissue in patients (Clarke, 2008), and this higher bone metabolic activity is associated with higher rates of osteolytic destruction in BALB/c mouse models (Wang et al., 2015). BMD was similarly investigated in two studies involving MDA-MD-231 breast cancer cells directly injected into the distal femurs of female NCr nude mice (8-9 weeks old) (Arrington et al., 2006, Arrington et al., 2008). In both studies, osteolytic destruction was detected via radiography at 3 weeks post-injection but no significant changes in BMD were observed from micro-CT scans (10.46 μm^3 and 12 μm^3 voxel size, respectively), whereas by six weeks osteolytic tissue BMD was significantly lower compared to non-lesion and contralateral control femurs, and most animals did not reach the nine-week time point due to impending fracture. In a later study, 4-week-old BALB/c mice intravenously injected with MDA-MB-231 breast cancer cells were analysed for bone mineral content at 32 days, finding the bone volume fraction had decreased in metastatic trabecular bone of distal tibiae (9.5 ±

2.6%) compared to healthy controls (22.7 ± 1.8%) (Richert et al., 2015). Decreased cortical BMD (Kaneko et al., 2003) and trabecular bone volume fraction (Nazarian et al., 2008) have been reported in patient studies of mixed sex and cancer type (breast, prostate, lung, colon) metastatic bone lesions located in femurs, far from primary tumours, such as those originating in breast tissue, but the time sequence of these changes have not been determined due to patient variation.

Our results reveal reduced bone tissue thickness and bone volume throughout tumour-bearing femurs, as well as decreased bone stiffness in proximal femur regions, when compared to healthy controls 6 weeks following primary tumour induction. Bone mineral content has been shown to correlate with bone tissue stiffness and hardness in patients (Gourion-Arsiquaud et al., 2009) and in mice (Courtland et al., 2008) and has been proposed to be driven by collagen cross-linking, bone morphology and trabecular orientation (Paschalis et al., 2011). In studies of human mixed cancer metastatic lesions, decreased compressive and tensile elastic modulus has been reported for cortical bone from the femur diaphysis (Kaneko et al., 2003) and decreased elastic modulus from dry nanoindentation tests has been reported in trabecular bone cores of the spine and femur (Nazarian et al., 2008). Nanoindentation testing was performed on the medial side (i.e. tumour side) of the mouse femurs. Notably, it has previously been shown via dry nanoindentation that the medial section of BALB/c mouse tibiae are higher in stiffness and hardness when compared to posterior or anterior sections (Pepe et al., 2020). Though not as precise as analysis in larger bone specimens (human, rat long bones) due to limited scan resolution, micro-CT derived BMDD is utilised in the analysis of mouse femur bone tissue (Martín-Badosa et al., 2003, Bouxsein et al., 2010, Ravoori et al., 2010), and correlates closely with BSE imaging analysis in all instances except measurements for heterogeneity (full width at half maximum) (Mashiatulla et al., 2017). An animal study of female athymic rats (5-6 weeks old) receiving an intracardiac injection of HeLa osteolytic cancer cells reported significantly reduced bone mineral density (by BSE) in osteolytic lesions within lumbar vertebrae compared to healthy controls (Burke et al., 2017), which is in keeping with findings from the current study upon osteolysis at 6 weeks. Interestingly, this study found no differences in Young’s modulus or hardness by nanoindentation, citing mixed analysis of cortical and trabecular bone tissue locations to be a probable cause (Burke et al., 2017). Another animal study of C57BL/6 female mice inoculated with B16F10 cells via intracardiac injection (Sekita et al., 2017), reported reduced dry nanoindentation modulus in cortical bone from the femoral diaphysis after 14 days (metastatic: 18.3 ± 3.1GPa, control: 24.2 ± 2.3GPa). Interestingly, despite significant changes in bone tissue stiffness were found at both time points of the current study, no differences were found in bone tissue hardness upon nanoindentation testing. Though these mechanical properties correlate closely, tissue hardness is reported to produce a lower statistical contrast compared to Young's modulus outcomes (Zysset et al., 1999). Large bone loss observed in distal tumour-bearing femur regions at 6 weeks post-inoculation may be explained by tumour mass growth as it expands distally over time, as indicated by bioluminescence of IVIS scans which extended to distal femur regions (Figure 3.2-A). This is supported by an animal study of male SCID mice (8-10 weeks old) inoculated with prostate cancer cells (Ace1 or DU145) in the intramedullary cavity of the tibiae compared to saline-inoculated control mice (Sottnik et al., 2015), that reported increased intramedullary pressure exerted by a tumour mass, which induced osteocytes to secrete known promoters of prostate cancer metastasis in bone tissue (CCL5, MMPs). Alternatively, bone loss and reduced trabecular bone mineral density also occurred within the proximal and distal contralateral femurs at 6 weeks, which may be explained by systemic circulation of breast cancer cells during the migration step of the metastatic cascade (Langley and Fidler, 2007), resulting in the invasion of skeletal sites distant from the primary tumour, as seen in breast cancer metastatic patients (Demers et al., 2000, Macedo et al., 2017).

Interestingly, by 3 weeks post-inoculation, there was an increase in bone mineralisation in the metastatic femurs compared to healthy bone tissue, along with increased distal femur cortical thickness. There are a number of possible explanations for these changes, which are considered herewith. Firstly, resorption of low bone mineral density in the superficial layers of trabecular bone might occur upon initiation of osteolysis and, because the centre of trabeculae are more highly mineralised (Brennan et al., 2011), the remaining trabeculae may have a higher density. Secondly, mineralisation could by stimulated by either the release of bone matrix proteins (OSC, OPN, Collagen type I) upon bone resorption (Cox and Morgan, 2013) or by tumour-derived growth factors released by disseminated tumour cells (Clines and Guise, 2005), both of which can stimulate resident osteoblasts to increase bone deposition. Interestingly, blood serum analysis from breast cancer metastatic patients found increases in bone matrix proteins occur only once osteolytic destruction is detected (Suzuki et al., 1989, Singhal et al., 1997, Pollmann et al., 2007), and so these may not explain the early increases in bone mineralisation reported here. A recent study reported increased trabecular and cortical bone thickness and evidence of bone formation after 3 weeks in animals that received daily intraperitoneal injections of tumour-cell conditioned media (Chiou et al., 2021). They proposed that tumour-derived growth factors (VEGF, Lysyl Oxidase) released by disseminated tumour cells (DTCs) act for the purpose of 'priming' the bone ECM to facilitate a more favourable microenvironment for DTC attraction, survival and proliferation (Chiou et al., 2021). VEGF is a known regulator of bone resorption (Zheng et al., 2013), while lysyl oxidase (LOX) release is driven by signalling of hypoxia inducible factors (HIF) to promote invading tumour cell colonization and osteolysis at skeletal sites (Rankin et al., 2016). Thus, bone mineral priming, arising from hypoxic stress, might be responsible for the changes in tissue mineralisation reported here by 3 weeks. Alternatively, the early trabecular bone loss identified here may alter the normal distribution of mechanical strain within the bone and thus initiate a mechanobiological mineralisation response by the bone cells residing in regions of elevated strain. Indeed, decreased trabecular bone arising during osteoporosis has been shown to lead to elevated strain on the cortical bone of the proximal femoral neck (Van Rietbergen et al., 2003, Verhulp et al., 2008). Alteration of the mechanical environment may also dictate the production of growth factors by the tumour cells and tumour cell activity. An *in vitro* study introduced MDA-MB-231 to culture medium from osteoclasts, previously conditioned in the media of osteocytes (MLO-Y4) subjected to 2 hours of oscillatory fluid flow stimulation (Ma et al., 2018). This study reported reduced migration and increased apoptosis of these breast cancer cells, compared to non-mechanically stimulated osteocyte conditioned media (Ma et al., 2018). These findings are reflected in previous human and animal studies where exercise or direct mechanical loading regimes of long bones inhibit tumour progression, proposedly due to altered TGF-β signalling and sclerostin secretion in mechanosensitive osteocytes (Sarazin et al., 2021). Notably, a study of MDA-MB231 breast cancer cell-inoculated proximal tibiae, in SCID mice subjected to dynamic compressive loads for 6 weeks, reported inhibited osteolytic progression, via limited loss of bone volume and trabecular thickness, during metastasis suggested to be a result of mechanoregulation of osteoblast and osteoclast activity (Lynch et al., 2013). Interestingly, increased matrix rigidity has been shown, in vitro, to induce more active tumour invasion and osteolytic destruction of MDA-MB-231 breast cancer cells, via increased integrin β3 mediated expression of TGF-β and PTHrP (Page et al., 2015), and demonstrates the important role of mechanobiology in breast cancer metastatic invasion. Mechanical stimulation has also been reported to stimulate breast cancer cellular behaviour in the context of primary tumour development and cancer cell extravasation. In particular, increased bone marrow ECM interstitial fluid flow, hydrostatic pressure, tissue strain and ECM stiffness, known to actively drive resident bone cellular activity and remodelling, are suggested to provide mechanical cues which drive tumour malignancy and cancer cell extravasation (Lynch et al., 2020). In this way the mechanical environment might also play a key role in stimulating both tumour and bone cell activity and contribute to tumour cell behaviour during the cancer vicious cycle. Elevated bone stiffness by three weeks post-inoculation in this study, in only the distal ipsilateral femur regions, may be due to increased load-bearing upon the introduction of a tumour mass. However, the precise impact of mammary pad-inoculated tumour weight on murine bone mineral content and mechanical properties is not yet known. Figure 3.7 illustrates how early increases in bone mineral content and mechanical properties later decreased significantly over the progression of metastatic invasion. Both proposed mechanisms are detailed here, outlining how these may act simultaneously to drive the temporal changes in bone tissue observed here.

Changes in bone mineral content and mechanical properties during early metastatic invasion may alter the tumour-adjacent and non-tumour-bearing mechanical environments of bone and breast cancer metastatic cells over time. This highlights the potential role of mechanobiology in perpetuating tumour cell proliferation during the cancer vicious cycle and tumour invasiveness during breast cancer metastasis to bone. Further studies are required to delineate whether DTC ‘priming’ of the bone metastatic niche, or a mechanobiology-driven response to imbalanced strain distributions in the bone ECM, would elucidate these changes. Further analysis of the altered bone tissue mechanical environment during early bone metastatic invasion could provide a greater insight into the potential mechanobiological cues which arise prior to osteolytic destruction, potentially via tartrate-resistant acidic phosphatase (TRAP) histological staining to assess osteoclast activity during this early metastatic phase, or alternatively utilising micro-CT images to generate finite element models (FEM) of the bone tissue microenvironment, thereby simulating how mechanical stimuli within the bone microarchitecture may differ between groups prior to and following osteolytic development.

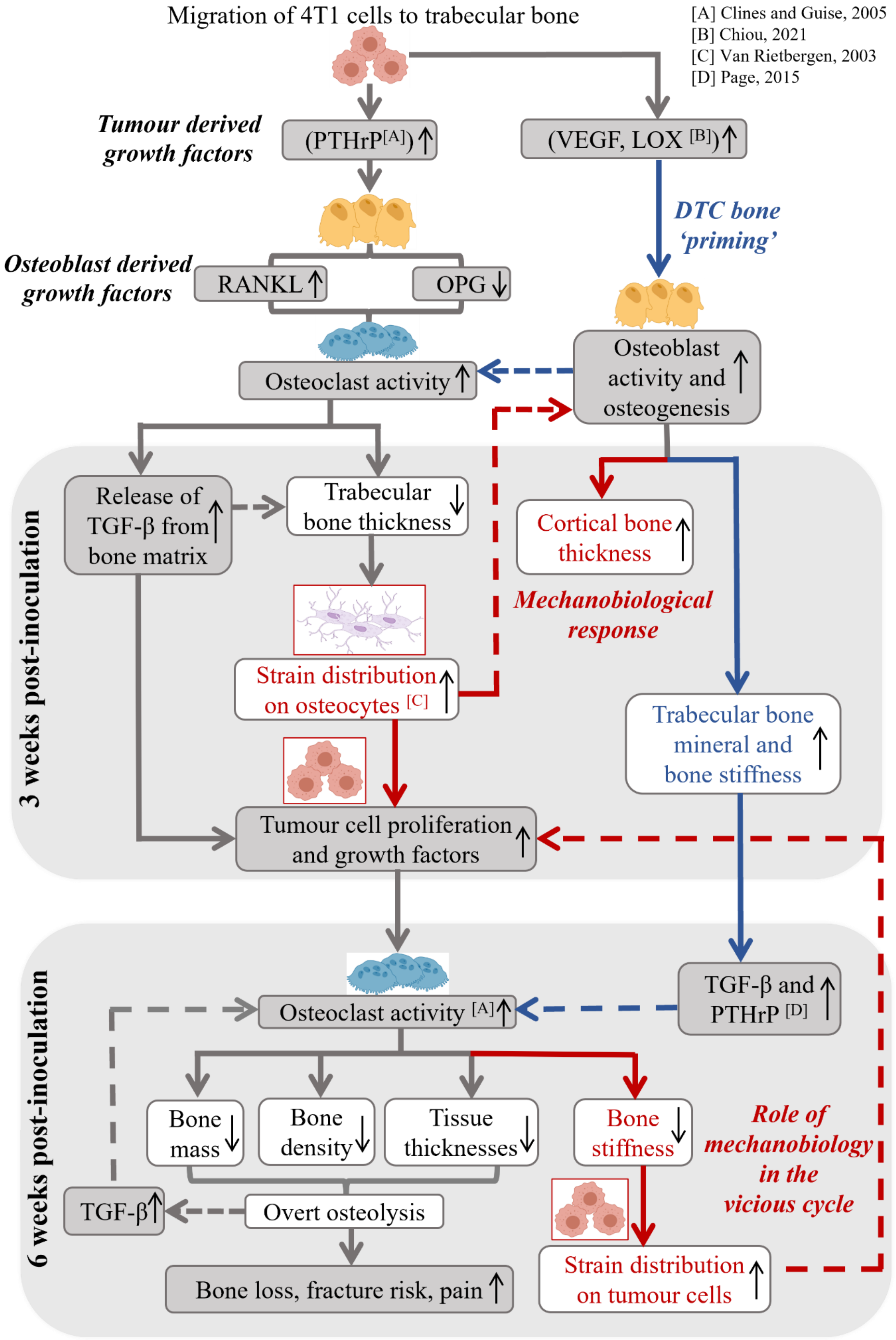

Figure 3.7: Proposed sequence of changes in bone microarchitecture and tissue composition during breast cancer metastatic invasion of bone tissue, 3 and 6 weeks after inoculation of breast cancer cells into the mammary fat pad. Growth factors released from

4T1 cells stimulate osteoclastogenesis and bone resorption. In addition to the known influence of growth factors released from the bone matrix in driving further tumour cell activity (Grey arrows), the current study reports increased bone mineralisation at the early stages of osteolysis. These are proposed to arise as a consequence of either, or both, of a) mechanobiologically driven responses by osteocytes to the altered mechanical environment following early osteolysis (Red arrows and textboxes) or b) bone niche ‘priming’ by factors produced by disseminated tumour cells (Blue arrows and textboxes) drive. These changes might lead to a secondary alteration in the mechanical environment of both the bone and tumour cells, driving further tumour cell proliferation and bone resorption, and thereby perpetuate the vicious cycle. Upward arrow, increase; downward arrow, decrease; dashed arrows, feedback mechanism; white boxes, results from this study. [A-D] References to relevant literature. Illustration made in ©BioRender - biorender.com.

3.5 Conclusion

Temporal and spatial analysis of bone physical properties upon breast cancer cell metastatic invasion provides an understanding of the changes in bone microarchitecture and tissue composition. Comprehensive analysis of bone mineralisation and nano-mechanical properties at 3 weeks post-inoculation indicates early bone tissue changes in response to breast cancer metastatic invasion. In the longer term, decreased mineral content and lower bone tissue stiffness in tumour-loaded femurs occurred upon osteolytic destruction. These changes may alter the mechanical environment of both the bone and tumour cells, and thereby play a role in perpetuating the cancer vicious cycle during breast cancer metastasis to bone tissue.

Chapter 4: Mechanoregulation may drive osteolysis during bone metastasis: A Finite Element Analysis of the mechanical environment within bone tissue during bone metastasis and osteolytic resorption

The following chapter is based on a scientific paper which has been peer reviewed and published in the *Journal of Mechanical Behaviour of Biomedical Materials* (Verbruggen and McNamara, 2023). The following is presented in the format of this article, and therefore the introduction and discussion (limitations) section contains some repetition. All micro-CT analysis, computational analysis (FEA), statistical analyses, writing and editing were conducted by the author of this thesis. Pre-clinical animal model design and weight measurements were conducted by our collaborators (Dr. Róisín M. Dwyer and Elan C. McCarthy, Discipline of Surgery, Lambe Institute for Translational Research, University of Galway, Ireland) with their co-authorships and contributions recognised upon publication.

4.1 Introduction

Metastasis is the final stage of cancer where cells migrate from a primary tumour to a secondary site and is the main cause of death in cancer patients (Weigelt et al., 2005, Langley and Fidler, 2007). For approximately 70-80% of advanced breast cancer patients, invasive cancer cells favour migration to bone where they stimulate bone resorption (osteolysis) or formation (osteoblastic metastasis) (Mundy, 2002, Clines and Guise, 2005) which propagates tumour growth and causes bone fragility, pain and hypercalcemia (Kozlow and Guise, 2005). According to Paget's 'Seed and Soil' theory (1889), bone tissue is favoured by cancer cells for migration, adhesion, and invasion due to its attractive physical properties and easily manipulated remodelling process. Bone remodelling is governed by osteoblasts and osteoclasts, which activate bone formation or resorption respectively, so that bone tissue structure and composition meets the mechanical demands on the tissue (McNamara, 2010, Mellon and Tanner, 2012). This process is regulated by mechanosensitive osteocyte cells, which communicate to osteoblasts and osteoclasts via biochemical signalling (Ashique et al., 2017). During metastasis, cancer cells release PTHrP, which upregulates the expression of factors (RANKL/OPG) that activate osteoclast differentiation and osteolysis. Bone tissue is an abundant source of growth factors (TGF-β, Ca^{2+}) and cytokines, and osteolytic bone resorption releases these factors, which subsequently attract and stimulate further tumour cell proliferation (Yoneda et al., 1994). This repeated system of invasion, active bone tissue resorption, growth factor release and further tumour proliferation has become known as the cancer ‘vicious cycle’ (Clines and Guise, 2005).

Mechanosensitive osteocytes monitor changes in mechanical stresses and strains within the physical bone tissue in which they reside. In healthy bone, osteocytes experiencing such changes would then signal to osteoclasts and osteoblasts to activate removal of old, damaged tissue on the bone surface and lay down new bone material to meet the mechanical demands. Mechanoregulation theory describes bone adaption on the basis of the assumption that the cells are driven to maintain a homeostatic mechanical environment within the tissue, whereby that mechanical stimuli beyond a specified threshold elicits new bone formation by osteoblasts whereas a reduction in mechanical stimulation results in bone resorption by osteoclasts (Frost, 1996, McNamara and Prendergast, 2007, Smotrova et al., 2022). Mechano-sensitive osteocytes produce factors, in particular sclerostin, in response to their mechanical environment and in this way can inhibit or activate Wnt signalling by osteoblasts, which in turn regulates osteoclastogenesis and bone loss (Yavropoulou and Yovos, 2007). Within a growing tumour, cancer and bone cells are subject to various mechanical signals, such as pressure, traction, and the tumour stiffness, which are known to activate tumour cell proliferation, differentiation and migration. But the invading tumour also changes the mechanical environment to the bone cells, by deforming the matrix and changing the stiffness of the bone itself. Previous studies have reported changes in bone tissue composition and mechanical properties from human cancer metastasis patients and animal breast cancer models, in particular decreased bone mineral density, bone volume, collagen quality and matrix stiffness (Kaneko et al., 2003, Nazarian et al., 2008, Richert et al., 2015, Sekita et al., 2017, Burke et al., 2018, Chiou et al., 2021). There is also evidence that bone loss during metastasis is temporal in nature (Arrington et al., 2006). Chapter 3 reported temporal and spatial changes in nano-mechanical properties and mineral distribution of bone tissue in an animal model of metastasis (Verbruggen et al., 2022). In early metastasis, osteolysis was only evident through the onset of trabecular resorption, whereas cortical thickening and increased bone mineralisation were also reported (Verbruggen et al., 2022). This chapter proposed that such changes may alter the mechanical environment of both the bone and tumour cells, and thereby activate mechanobiological responses in the bone cells to perpetuate the cancer vicious cycle (Verbruggen et al., 2022). However, the specific impact of temporal changes in bone structure and composition on the mechanical environment within the bone tissue during metastasis has not been established, and whether such changes are associated with osteolysis has not yet been investigated.

Computational modelling and experimental imaging approaches can enable characterisation of the mechanical environment within bone tissue and overcome challenges related to direct experimental quantification, which have been applied to study fracture susceptibility in metastatic bone disease. A study compared computational models of simulated osteolytic defects to CT-derived models of metastatic lesions in human femora, and predicted premature fracture failure in the simplified defect models (Keyak et al., 2005). Interestingly, this study found that simulated lesions accurately predicted failure loads compared to real metastatic defects (Keyak et al., 2005). In another study, finite element (FE) models were reconstructed from healthy human femur images, into which osteolytic lesions had been manually drilled into the cortical bone tissue to reflect metastatic patient scans, and fracture failure was accurately predicted along the femoral neck and greater trochanter (Anez-Bustillos et al., 2014). This study concluded both FE modelling or computed tomography rigidity analysis (CTRA) techniques equally effective in failure prediction (Anez-Bustillos et al., 2014). Osteolytic defects were introduced into FE models, derived from computed tomography (CT) scans of the lumbar vertebrae and proximal femur, to replicate bone loss from patient scans (Benca et al., 2017, Salvatore et al., 2018) and predict fracture risk. Subject-specific non-linear FE models of metastatic vertebrae were developed from Quantitative Computed Tomography (QCT) images of the thoracolumbar spine in patients with osteolytic lesions to predict fracture risk, which concluded that the impact of lytic lesions on this failure risk was specific to each patient (Costa et al., 2019). QCT-derived FE models of human cadaveric proximal femurs accurately predicted failure force of the femur when artificial cavities representing metastasis were introduced and compared to non-lesion contralateral controls (Sas et al., 2020). In addition, this study found good agreement between voxel-based hexahedral and tetrahedral FE models, and were similarly accurate and precise in predicting bone tissue strength and failure loads compared with experimental results (Sas et al., 2020). Patient specific models of metastatic proximal femurs were developed from QCT scans, and it was shown that these approaches were superior in predicting fracture risk, when compared to clinical approaches that predict risk based on lesion characteristics and axial cortical involvement measured from patient radiographs or clinical CT scans (Eggermont et al., 2020). This approach was also applied to investigate the efficacy of femoroplasty which, when this procedure was computationally simulated in reconstructed human femurs, reportedly reduced fracture risk for metastatic lesions located in within the femoral neck or head by 57% (Sas et al., 2022). The above studies have illustrated the impact of overt metastatic lesions on bone strength and risk of fracture failure in human cadaveric bone tissue. However, these findings are restricted to human factors which may influence metastatic development, such as age, sex, cancer type and patient-specific cancer therapies (radiology, chemotherapy, etc.) (Yao et al., 2020).

Pre-clinical animal models are widely used to study tumour progression. Two similar computational studies utilised µCT-derived FE models to generate and analyse lumbar vertebrae (T12 – L3) from osteolytic or mixed metastatic female Rowett nude rats, euthanised at 21 days (Atkins et al., 2019) and 25 days following intracardiac inoculation of HeLa cancer cells (Choudhari et al., 2016). Interestingly, both studies found regions of microdamage, arising secondary to metastasis, were spatially correlated with areas of elevated stress and strain (Choudhari et al., 2016, Atkins et al., 2019). A µCT-derived FE model of a human cadaveric vertebrae was developed and applied to investigate the impact of size and location of simulated lesions (Costa et al., 2020). This study revealed that increased lesion size was correlated to a reduction in structural properties of the vertebral body, whereas the location of the lesion did not have a strong influence (Costa et al., 2020). Interestingly, they reported a reduction in principal strain in bone tissue surrounding the lytic lesions, which was more pronounced for larger lesions (Costa et al., 2020). A later study of murine tibiae, subjected to cyclical axial compression over 2 weeks, found an SED-driven bone remodelling algorithm using µCT-FE models could accurately predict changes in the bone tissue mechanical environment experiencing microstrains as low as 12.8 ± 9.0 µε, verified using digital volume correlation (DVC) measurements to visualise changes in strain prior to and following compression testing (Cheong et al., 2021). In another pre-clinical animal study, artificial osteolytic lesions were introduced to healthy porcine vertebrae and these were experimentally subjected to compression loads to induce permanent damage (Palanca et al., 2021b). DVC measurements were again used to verify that principal strains increased approximately twofold in the presence of osteolytic lesions (Palanca et al., 2021b). µCT derived FE models were developed of these same porcine models and it was reported that the computationally predicted displacement fields, for loading of metastatic vertebrae in the elastic regime, were in excellent agreement with DVC measurements (Palanca et al., 2022). The above computational studies of bone metastases primarily focused on predicting fracture failure at specific time points after metastasis. However, the evolving bone tissue mechanical environment during metastasis has not been characterised.

The objective of this study is to characterise temporal changes in the bone mechanical environment during breast cancer metastasis via finite element analysis (FEA) derived from µCT images of metastatic mouse bone. A particular goal is to study time-dependent changes in mechanical stimuli within the bone microenvironment, local to and distant from an invading tumour mass, to investigate putative mechanobiological cues for osteolysis during bone metastasis.

4.1 Methods

4.1.1 Animal Model

The current study conducts a subject-specific computational analysis of femurs collected from the pre-clinical animal study of breast cancer metastasis analysed in Chapter 3 (Verbruggen et al., 2022). In brief, 6-week-old adult immunocompetent mice inoculated with murine breast cancer cells in the mammary fat pad were maintained under normal laboratory conditions with food and water provided *ad libitum*. Metastatic femurs (MET) were collected from the tumour-inoculated side and compared to control femurs (CTRL) in healthy mice which did not receive inoculations. The first animal cohorts were euthanised at 3 weeks post-inoculation (CTRL n = 5, MET n = 5) and a second cohort had an endpoint of 6 weeks post-inoculation (CTRL n = 5, MET n = 7). Femurs were collected from the anatomical right side of the mouse for healthy and control animals, with the exception of two femurs that were harvested from the left anatomical side for the healthy control group at 3 weeks. Each mouse was weighed weekly, and tumour weight were measured at the 3-week and 6-week endpoints. Each tumour mass was also dimensioned using callipers such that their volumes could be calculated according to the following formula: 0.52 x $(\text{width})^2$ x $(\text{height})^2$. All femurs were harvested, muscle and tendon soft tissues were removed, and bones were wrapped in PBS-soaked gauze and stored at -20˚C. This research was conducted with approval from the Animal Care Research Ethics Committee (ACREC) at the University of Galway and the Health Products Regulatory Authority (HPRA), the national authority for scientific animal protection in Ireland.

4.1.2 Micro-Computed Tomography and model reconstruction

Micro-computed tomography (µCT) is a non-destructive analytical technique used for detailed quantification of bone mineral density throughout chosen volumes of interest (VOIs). Samples were thawed overnight at 4˚C, placed in 9 mm diameter chambers and immersed in phosphate buffered saline (PBS) at room temperature in a static, upright position during the imaging process. Proximal and distal femur regions were imaged, with proximal femur VOIs defined as spanning from the most proximal point of the femoral head to 4mm in the distal direction, while distal femur VOIs spanned 2 mm toward the midshaft from the distal growth plate (Figure 3.1A). Scans (1000 projections per 180˚ rotation) were taken at a voxel size of 5µm^3. The following parameters were applied: 70kVp peak X-ray tube voltage, 57µA tube current, 900ms integration time, frame averaging of 5, 0.8 Gaussian filter and Support value of 1, Scanco Medical µCT100. A 0.5 ml aluminium filter was used to reduce beam hardening artefacts and a trinomial beam hardening correction was applied during reconstruction of the µCT scans. A density threshold (513.7 mg HA/cm^3) was chosen as the approximate midpoint between the background and peak density of the bone samples, and by visually comparing to scan grayscale images, which closely matched 3000HU previously reported as suitable for the ellimination of muscle and tendon tissue (Ravoori et al., 2010). Osteolytic lesions in the µCT reconstructed models were identified as regions of significant bone loss, whereby large bone cavities were overtly visible when cross-compared with identical anatomical bone sites of healthy samples where bone tissue was visible. DICOM files from healthy and metastatic proximal and distal femur VOI scans were exported for segmentation. µCT scans were segmented and reconstructed into 3D models via MIMICS software (18.0, Materialise, Belgium) (Figure 3.1B). Bone geometry was isolated from artefacts, while a smoothing factor of 0.4, including volume compensation, was applied to minimise edge effects.

4.1.3 Mesh Generation

Each model was meshed (3matic software 10.0, Materialise, Belgium) with 4-noded linear tetrahedral elements (Figure 3.1B) to generate cortical and trabecular bone tissue regions. This mesh design was chosen because tetrahedral elements are suited for the complex geometry of proximal femurs, while 4-noded elements produce stress and strain responses similar to 10-noded models of the proximal in a more computationally efficient manner (Ramos and Simoes, 2006). Bone marrow and tumour tissue were excluded during µCT thresholding and were therefore not present within the computational models. A maximum edge length of 0.075mm was applied to proximal femur models, and 0.04mm to distal femurs, following mesh convergence analysis on one model from each group (see Supplementary Figure 4.1). This resulted in an average element volume of 1.3x10^{-5} mm^3 in proximal models and 2.07x10^{-6} mm^3 in distal models. Each model was then imported into Abaqus (Dassault Systemes, version 2017) for finite element analysis.

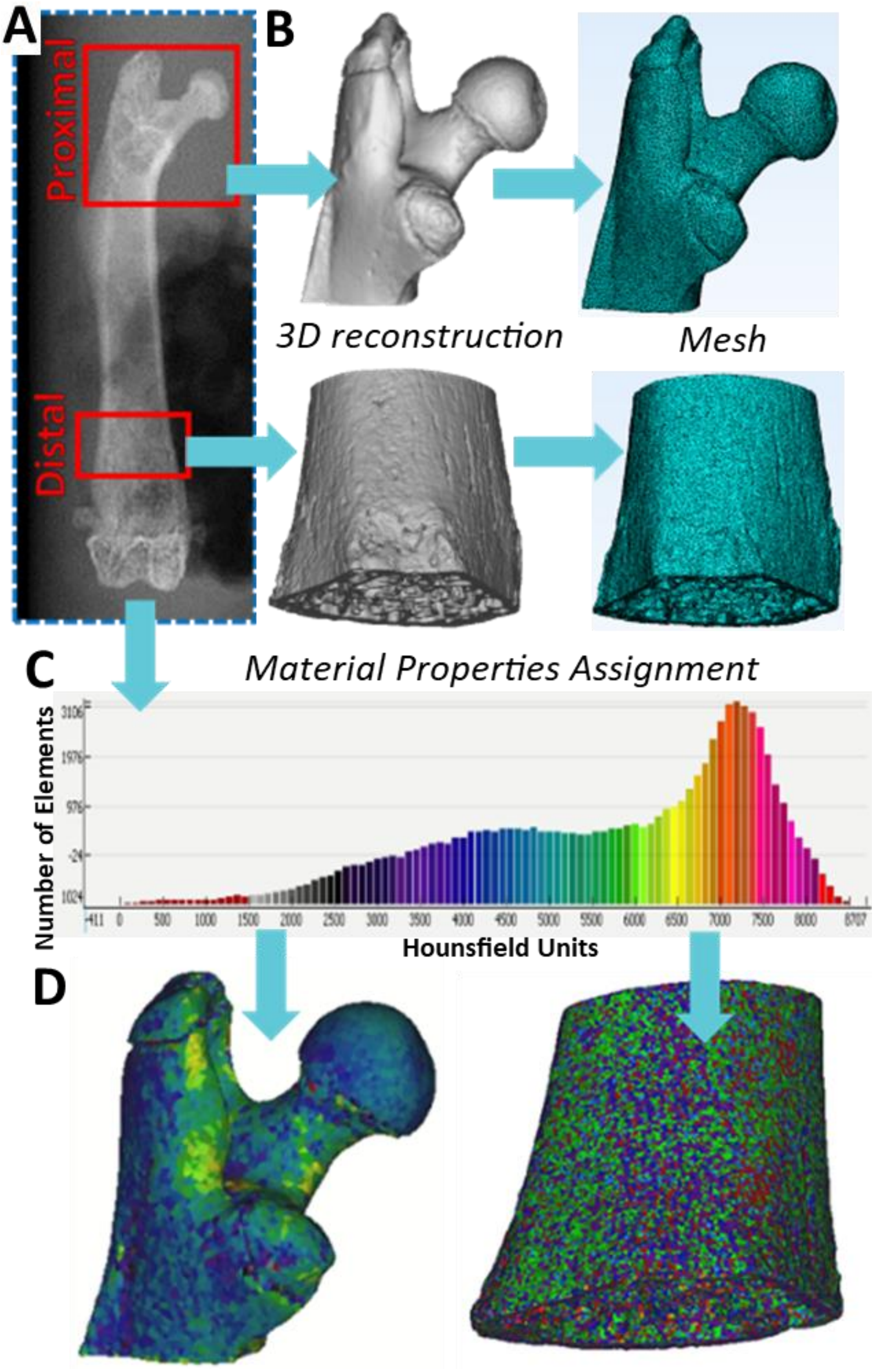

Figure 4.1 Finite Element model development. (A) Scout view of µCT scan from a murine femur. (B) Segmentation and reconstruction of µCT scans was conducted to extract solid models of the proximal and distal femur, and these were meshed with tetrahedral elements. using MIMICS software. (C, D) µCT data was processed (gray values in Hounsfield Units) to assign material properties to the mesh distribution assuming 100 distinct uniformly distributed material parameters.

4.1.4 Finite Element Analysis

4.1.4.1 Material Properties

Each model was mapped with 100 distinct uniformly distributed material parameters throughout the mesh which were mapped according to gray values from µCT scans (MIMICS sofware) (Figure 3.1C, 1D). In this way, heterogeneous material properties which vary with the distribution of the density provide structural anisotropy, while the material properties were assumed to be linear elastic. Mapping of material properties onto each mesh involved converting CT-derived bone mineral density (ρ_{CT}) to ash density (ρ_{ash}) (Schileo et al., 2008) and subsequently to Young's modulus, *E*, according to a power law relationship applied in female mouse tibiae (Keller, 1994, Lu et al., 2019) assuming a Poisson's ratio of 0.3 (Webster et al., 2008, Cheong et al., 2020b).

$$\boldsymbol{\rho_{CT} = -0.0056148 + 0.0007764\, HU} \tag{4.1}$$

$$\boldsymbol{\rho_{ASH} = 0.079 + 0.8772(\rho_{CT})} \tag{4.2}$$

$$E = 10.5{\rho_{ASH}}^{2.29} \tag{4.3}$$

The calculated Young's moduli were within the ranges of our experimental analysis by means of nanoindentation of bone tissue, from the same proximal and distal femur regions of cortical and trabecular bone within the animal cohorts as in Chapter 3 (Verbruggen et al., 2022) (see Supplementary Table 4.1).

4.1.4.2 Boundary and Loading Conditions

Each proximal femur model was loaded on a small circular surface on the femoral head of radius 0.25mm (area ~0.188 mm^2) to represent weight-bearing in the mouse anatomy (Blanchard et al., 2013). Assigned bodyweights, measured upon resection at time of sacrifice, were specific to each individual mouse. This surface was coupled to a reference node located at the centre of mass within each femoral head to distribute the load evenly over the joint surface (Figure 4.2A). For distal regions, the proximal cortical bone surface area was similarly coupled to a reference point normal to the surface area centroid (Figure 4.2B). In all cases, 120% of the specific mouse bodyweight was applied in the proximal-distal direction, and 10.9% in the posterior-anterior direction to reflect peak physiological loading in a mouse long bone (Charles et al., 2018). Distal surfaces were fixed in all directions. To investigate the impact of model alignment with the applied bodyweight load, a separate parameter variation study was conducted for a 3 week MET proximal femur model. The applied force was adjusted along the anterior-posterior and medial-lateral axes such that bodyweight load was tilted 1°, 2.5°, 5° and 10°, then compared to the neutral position and maximum principal strain distribution results were analysed (Supplementary Figure 4.2). On the basis of this analysis the bodyweight load was confirmed to be unaffected with a variation of alignment up to 10°.

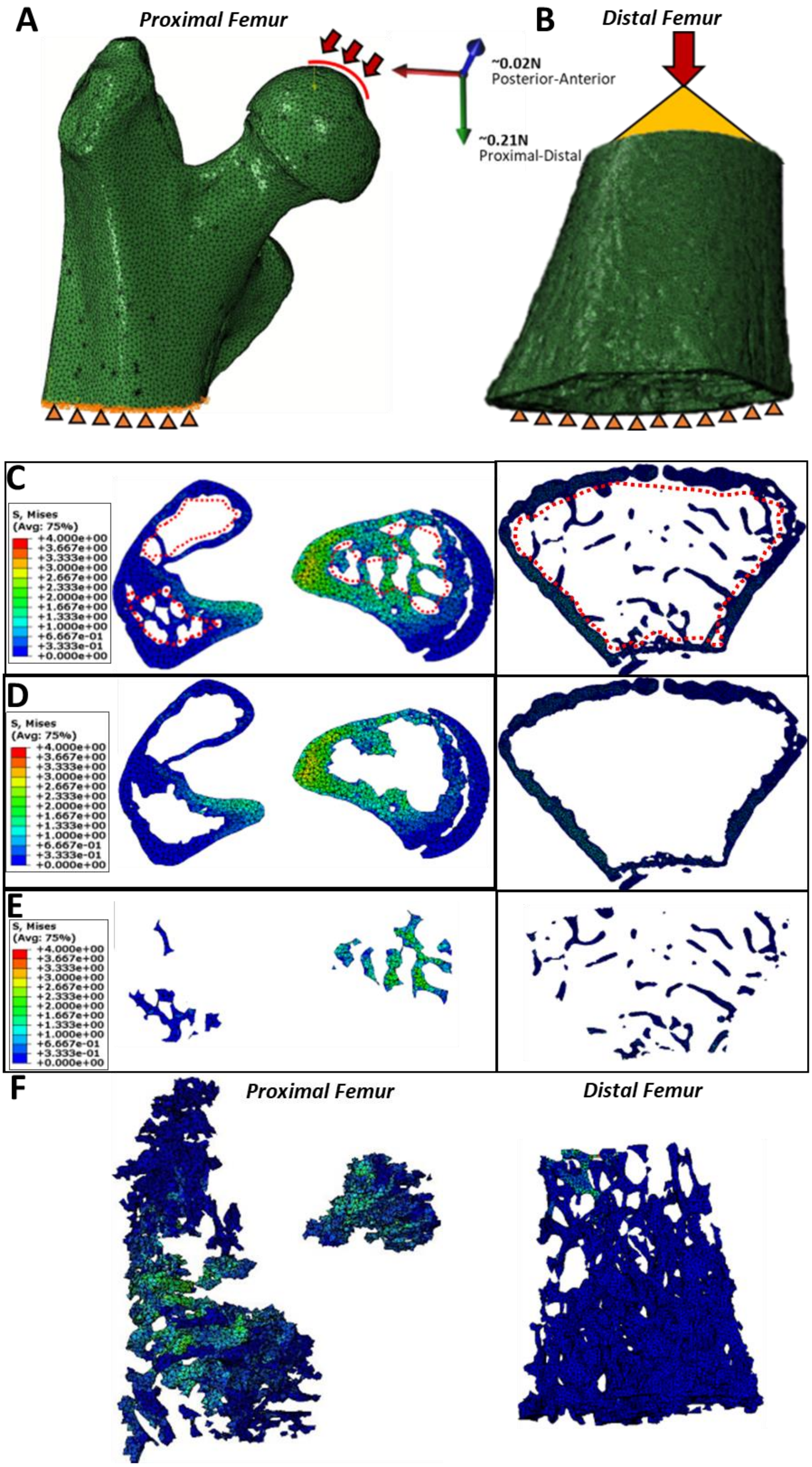

Figure 4.2: FE model development and sub-regional tissue isolation: (A) Proximal and (B) distal femur boundary conditions, including application of weight bearing loads (red

arrows), kinematic coupling (yellow triangle) and fixed distal surfaces (orange triangles). (C) Isolated cross-sections in the proximal-distal direction, indicating manual segregation (red dashed line) of (D) cortical and (E) trabecular bone tissue regions for separate analysis. (F) Resultant 3D display groups of elements isolated from the trabecular region in proximal and distal models.

4.1.4.3 FE model analysis

The objective of this study was to conduct temporal analysis of stress and strain distributions within the bone extracellular matrix (ECM), prior to and following overt osteolytic destruction. Whole proximal femur regions and distal regions were analysed for each control and metastatic femur, along with analysis of the femoral head sub-region, adjacent to where the primary tumour mass was inoculated. Cross-sections of each region were qualitatively assessed for distribution of Von Mises stress and maximum principal strain. Quantitative mean maximum principal stress and strain energy density (SED) analysis was conducted for each region. Histograms of maximum principal strain, as a percentage of bone tissue volume, were produced to quantify changes in strain distribution throughout the bone mechanical environment between metastatic and healthy control groups. Strain distribution ranges were calculated as an average of all models per cohort, per group, per region of interest. Maximum principal strain histogram ranges (0 – 300με) were chosen to reflect peak strains measured in female C57Bl/6 tibiae during walking (De Souza et al., 2005), with the lowest increment (0 - 50με) chosen to reflect a threshold below which faster bone resorption occurs due to ‘acute disuse’ (Frost, 1991).

To further investigate precisely where changes in mechanical strain may have originated within these models, these analyses were also conducted in separate cortical and trabecular bone sub-regions. Utilising a similar methodology to contouring in µCT analysis, cortical and trabecular sub-regions were manually delineated by highlighting and removing trabecular region elements in every cross-section view along the longitudinal (proximal-distal) direction (Figure 4.2C, 2D). Boolean operation was then used to invert this display group and analyse trabecular bone tissue elements separately (Figure 4.2F).

4.1.4.4 Statistical Analysis

Statistical analyses were performed using MiniTab (version 17) software comparing healthy controls (CTRL) and metastatic groups (MET) from each cohort (3 weeks, 6 weeks). Each parameter was confirmed for normal distribution in these groups (Kolmogorov-Smirnov normality test) and assessed for equal variance (F test). One maximum principal strain distribution per bone region and group analysed to confirm similar skew between groups. Student t-tests were implemented to determine whether averaged data was statistically significant between groups of equal variance, and Welsh's test applied where sample groups had unequal variance. The maximum principal strain distribution histogram of one sample per bone region per group was assessed to confirm close skewness (proximal CTRL: 18.9, MET: 20.6, distal CTRL: 4.94, MET: 5.3). Results are displayed as mean ± standard deviation, with significance defined as a p value of < 0.05, and greater significance ($p < 0.01$, $p < 0.001$, $p<0.0001$) also indicated.

4.2 Results

4.2.1 *Tumour Development and Osteolytic Destruction*

By 3 weeks after breast cancer cell inoculation, into the primary mammary fat pad, there was no evidence of overt osteolytic destruction from µCT scans of metastatic animals (Figure 4.3B). However, by 6 weeks of tumour development overt osteolysis was evident in metastatic femurs, particularly in the greater trochanter (Figure 4.3D). In three of the seven metastatic femurs the femoral head was absent. In total, 20 femur regions were suitable for analysis at 3 weeks ($n = 5$ per region) and 19 femur regions at 6 weeks post-inoculation (proximal CTRL $n = 4$, proximal MET $n = 4$, distal CTRL $n = 5$, distal MET $n = 7$).

When measured at times of sacrifice, metastatic mouse weights did not differ from healthy control mouse weights at either time point of the study (Figure 4.3E). The average weight of healthy control mice had increased significantly at 6 weeks post-inoculation (23.0 ± 1.6g) compared to this same control group at 3 weeks (18.6 ± 1.4g). Similarly, the metastatic mice had increased weight significantly between time points (6 weeks MET: 23.1 ± 2.2g vs. 3 weeks MET: 19.2 ± 1.2g). Tumour tissue weights were significantly greater by 6 weeks post-inoculation compared to 3 weeks post-inoculation (1.63 ± 0.4g vs. 0.286 ± 0.7g, $p<0.0001$), see Figure 4.3F.

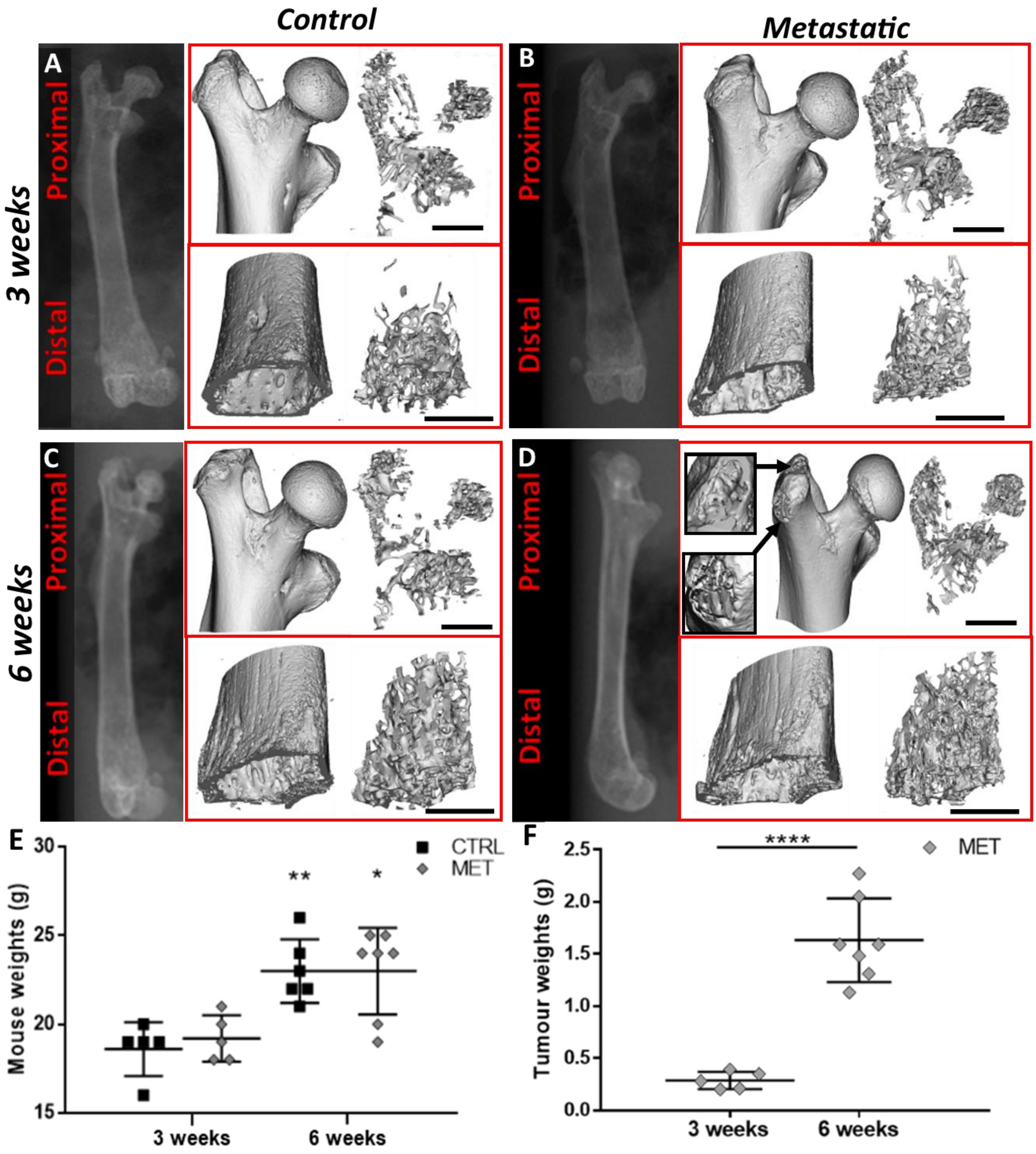

Figure 4.3: Osteolytic destruction and tumour development. (A-D) Scout views of disease and control mouse femurs at 3 weeks and 6 weeks post-inoculation, scalebar 1mm. Insets show 3D reconstructions of proximal and distal VOIs of a femur from each group, with contour isolation of (left) cortical and (right) trabecular bone regions. Osteolytic lesion development was confirmed in the cortical bone of the greater trochanter (D, black insets). (E) Recorded weights of mice and (F) tumour masses taken at 3-week and 6-week endpoints. * Significant difference, per group, between 3-week and 6-week time points. (*p<0.01, **p<0.001, ****p<0.0001).

4.2.2 *Early Changes in the Femur Bone Mechanical Environment (3 weeks post-inoculation)*

Finite element models were developed to simulate weight-bearing for healthy control and metastatic mice, prior to and following overt osteolytic destruction, specifically at 3- and 6-weeks post-inoculation. Temporal stress and strain analyses of the bone tissue microenvironment were conducted (Figure 4.4). At 3 weeks post-inoculation, elevated stress and strain were concentrated along the medial side of the femoral neck and the top of the femoral head where loading was applied (Figure 4.4A, 4B). In the distal femurs, Von Mises stress was more uniformly distributed throughout the cortical bone tissue region (Figure 4.4C). No overt differences in stress or strain distribution were discernible between metastatic and healthy groups at this early time point, either in the proximal (Figure 4.4A, 4.4B) or distal femur regions (Figure 4.4C, 4D).

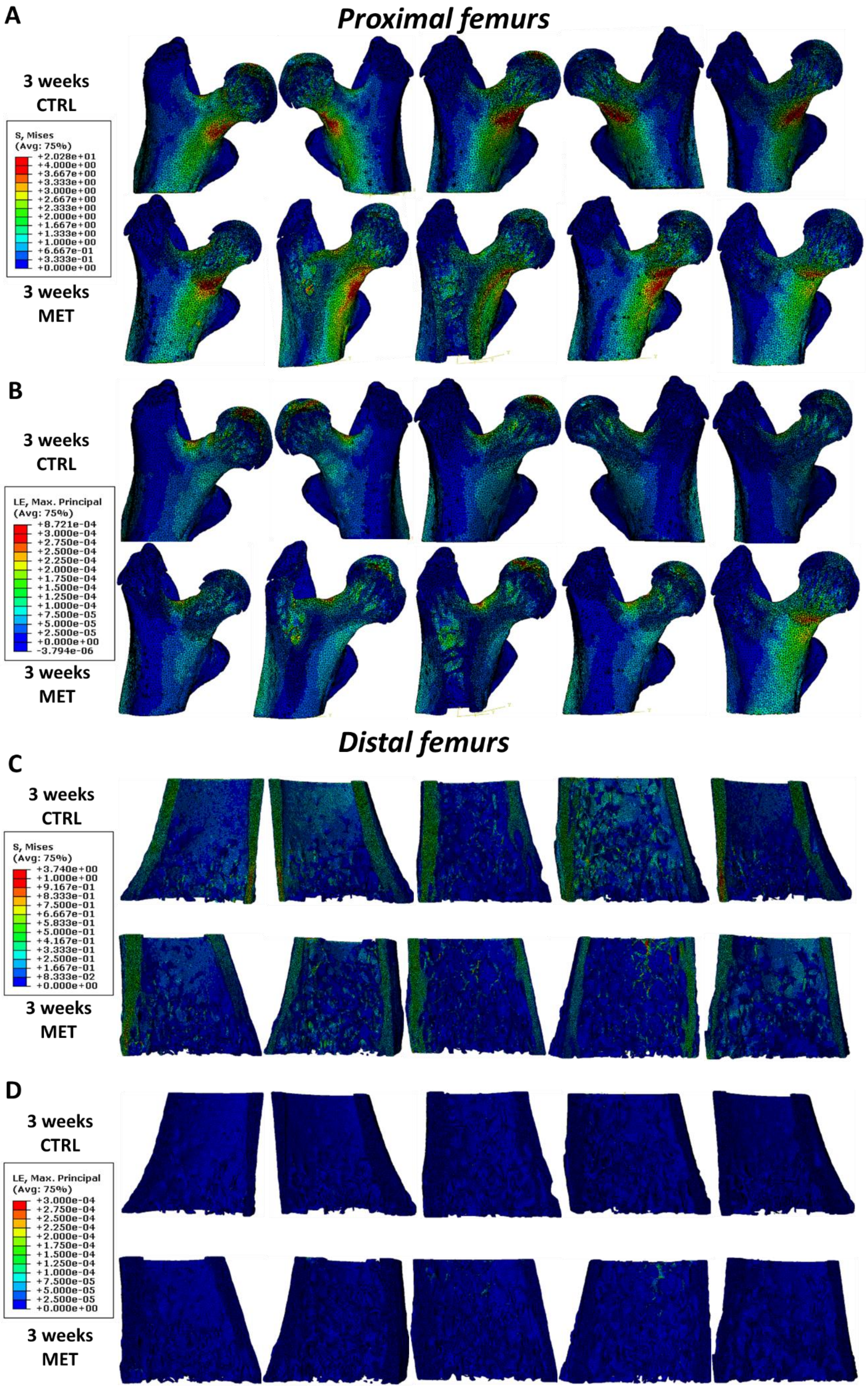
A
Proximal femurs
3 weeks
CTRL
S, Mises
(Avg: 75%)
+2.028e+01
+4.000e+00
+3.667e+00
+3.333e+00
+3.000e+00
+2.667e+00
+2.333e+00
+2.000e+00
+1.667e+00
+1.333e+00
+1.000e+00
+6.667e-01
+3.333e-01
+0.000e+00
3 weeks
MET
B
3 weeks
CTRL
LE, Max. Principal
(Avg: 75%)
+8.721e-04
+3.000e-04
+2.750e-04
+2.500e-04
+2.250e-04
+2.000e-04
+1.750e-04
+1.500e-04
+1.250e-04
+1.000e-04
+7.500e-05
+5.000e-05
+2.500e-05
+0.000e+00
-3.794e-06
3 weeks
MET
Distal femurs
C
3 weeks
CTRL
S, Mises
(Avg: 75%)
+3.740e+00
+1.000e+00
+9.167e-01
+8.333e-01
+7.500e-01
+6.667e-01
+5.833e-01
+5.000e-01
+4.167e-01
+3.333e-01
+2.500e-01
+1.667e-01
+8.333e-02
+0.000e+00
3 weeks
MET
D
3 weeks
CTRL
LE, Max. Principal
(Avg: 75%)
+3.000e-04
+2.750e-04
+2.500e-04
+2.250e-04
+2.000e-04
+1.750e-04
+1.500e-04
+1.250e-04
+1.000e-04
+7.500e-05
+5.000e-05
+2.500e-05
+0.000e+00
3 weeks
MET

Figure 4.4: Predicted stress and strain distributions at 3 weeks post-inoculation. Medial-lateral cross-sections of finite element models contour plots for (A, C) Von Mises stress and (B, C) maximum principal strain in CTRL and MET femur regions during early metastasis.

Quantitative analysis of proximal femurs and distal femurs at 3 weeks showed no significant changes in the strain distribution, when compared to healthy controls (Figure 4.5A, 5G). Furthermore, when analysing whole proximal femurs at this early time point of metastasis, no significant differences in mean SED or maximum principal strain were reported between groups, (Figure 4.5B, 5C). However, in the distal femur region, far from the primary tumour site, the metastatic group presented significantly lower maximum principal strain (5.02 ± 0.33 $\mu\varepsilon$ vs. 6.00 ± 0.405 $\mu\varepsilon$, $p<0.05$) and strain energy density (1.59 ± 0.23 Pa vs. 2.42 ± 0.57 Pa, $p<0.05$) when compared to controls at this early time point (Figure 4.5H, 5J).

Interestingly, strain distribution analysis of the femoral head sub-region at 3 weeks post-inoculation revealed that a significantly larger proportion of metastatic bone tissue experienced strains lower than 50 $\mu\varepsilon$ when compared to controls (81.7 ± 5.3% vs. 73.4 ± 2.97%, $p<0.05$) (Figure 4.5B). Correspondingly, a lower proportion of these femoral head sub-regions lay within the 50 - 100 $\mu\varepsilon$ (12.9 ± 3.8% vs. 17.5 ± 2.11%, $p<0.05$) and 150 - 200 $\mu\varepsilon$ ranges (1.32 ± 0.93% vs. 2.5 ± 0.36%, $p<0.05$) compared to controls at 3 weeks post-inoculation (Figure 4.5B). SED was significantly lower in metastatic femoral heads compared to healthy controls (30.5 ± 10.0 Pa vs. 57.8 ± 17.0, $p<0.05$ Pa) (Figure 4.5F). Taken together, the above results highlight a general trend toward decreased strain distribution, within the femoral head region, in the metastatic group at this early time point.

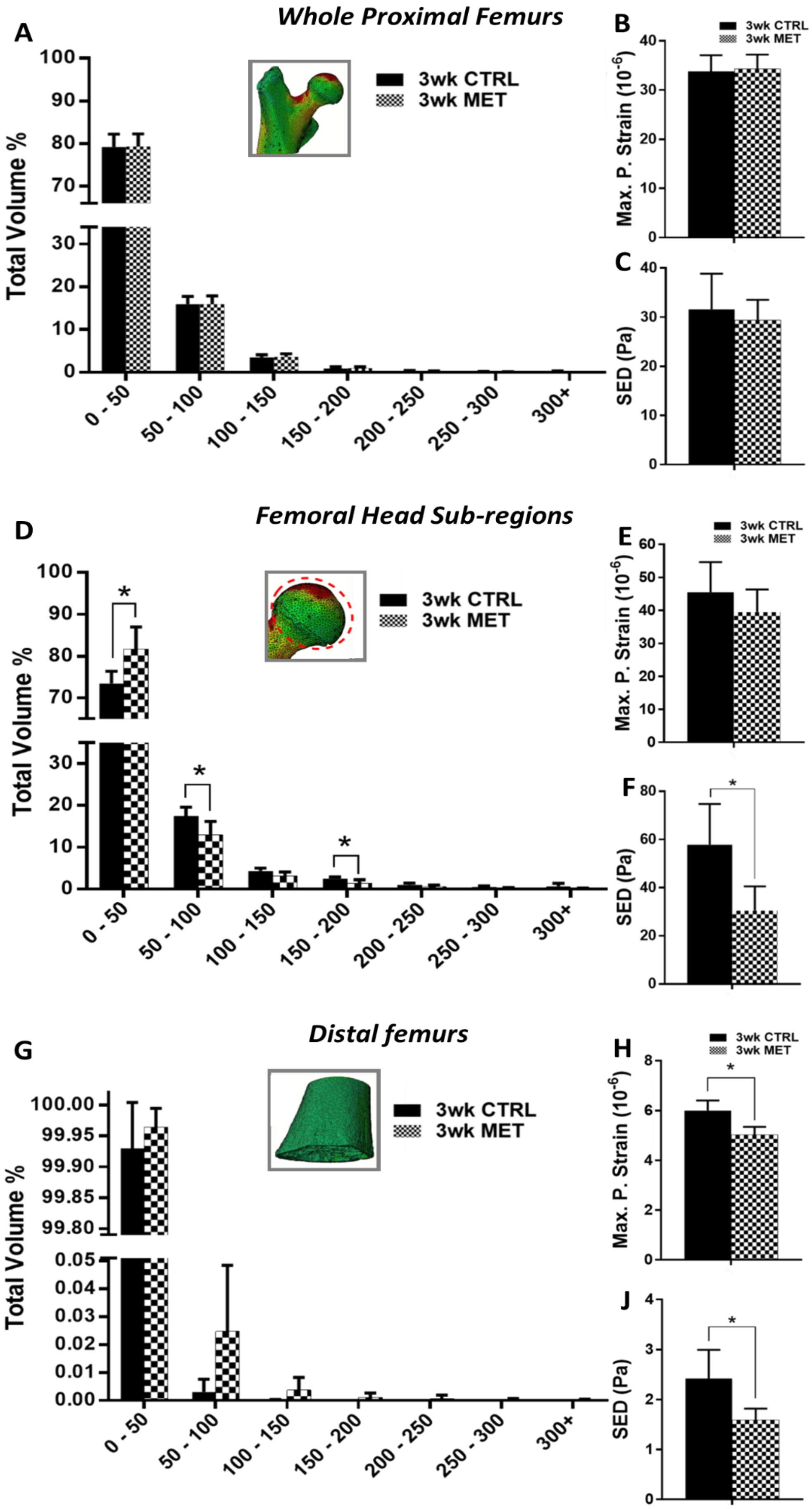
Whole Proximal Femurs
A
3wk CTRL
3wk MET
Total Volume %
100
90
80
70
30
20
10
0
0 - 50
50 - 100
100 - 150
150 - 200
200 - 250
250 - 300
300+
B
Max. P. Strain (10^{-6})
40
30
20
10
0
C
SED (Pa)
Femoral Head Sub-regions
D
*
E
60
50
F
80
60
40
20
Distal femurs
G
100.00
99.95
99.90
99.85
99.80
0.05
0.04
0.03
0.02
0.01
0.00
H
8
6
4
2
J
4
3
2
1

Figure 4.5: Predicted changes in bone tissue strain 3 weeks post-inoculation. Analysis was conducted in (A-C) whole proximal femur (D-F) femoral head sub-region and (G-J) distal femur regions. (A, D, G) Distribution of maximum principal strain as a percentage of bone volume. (B, E, H) Mean maximum principal strain (Max. P. Strain) and (C, F, J) strain energy density (SED) in healthy control (CTRL) and metastatic (MET) regions 3 weeks after tumour inoculation.

4.2.3 *Decreased strain distribution in proximal femur trabecular bone and distal cortical bone in early metastasis.*

To further investigate how metastasis influences the mechanical environment within bone tissue, reconstructed tissue from cortical and trabecular sub-regions were manually isolated and assessed separately for changes in strain distribution. At 3 weeks post-inoculation, a significant change in the mechanical environment occurred within the distal femur cortical bone (Figure 4.6C), with significantly lower maximum principal strain (5.23 ± 0.27 με vs. 6.22 ± 0.39 με, $p<0.01$), and also significantly lower SED (1.7 ± 0.21 Pa vs. 2.59 ± 0.56 Pa, $p<0.05$), compared to healthy controls. The proportion of bone tissue within a 50 – 100με range was significantly lower in the proximal trabecular region of metastatic femora when compared to healthy controls (20.07 ± 1.94% vs. 23.67 ± 0.55%, $p<0.05$), see Figure 4.6F. Furthermore, although not significant, the percentage volume of proximal trabecular bone tissue below 50 με is also predicted to increase in the metastatic group compared to healthy controls (74.5 ± 2.95 % vs. 70.91 ± 1.5 %, $p = 0.061$) (Figure 4.6F). Notably, all metastatic bone tissue regions were predicted to consistently skew toward the 0 – 50 με range, at 3 weeks post-inoculation, suggesting an overall decrease in strain distribution in metastatic bone tissue at this early time point (Figure 4.6E-H).

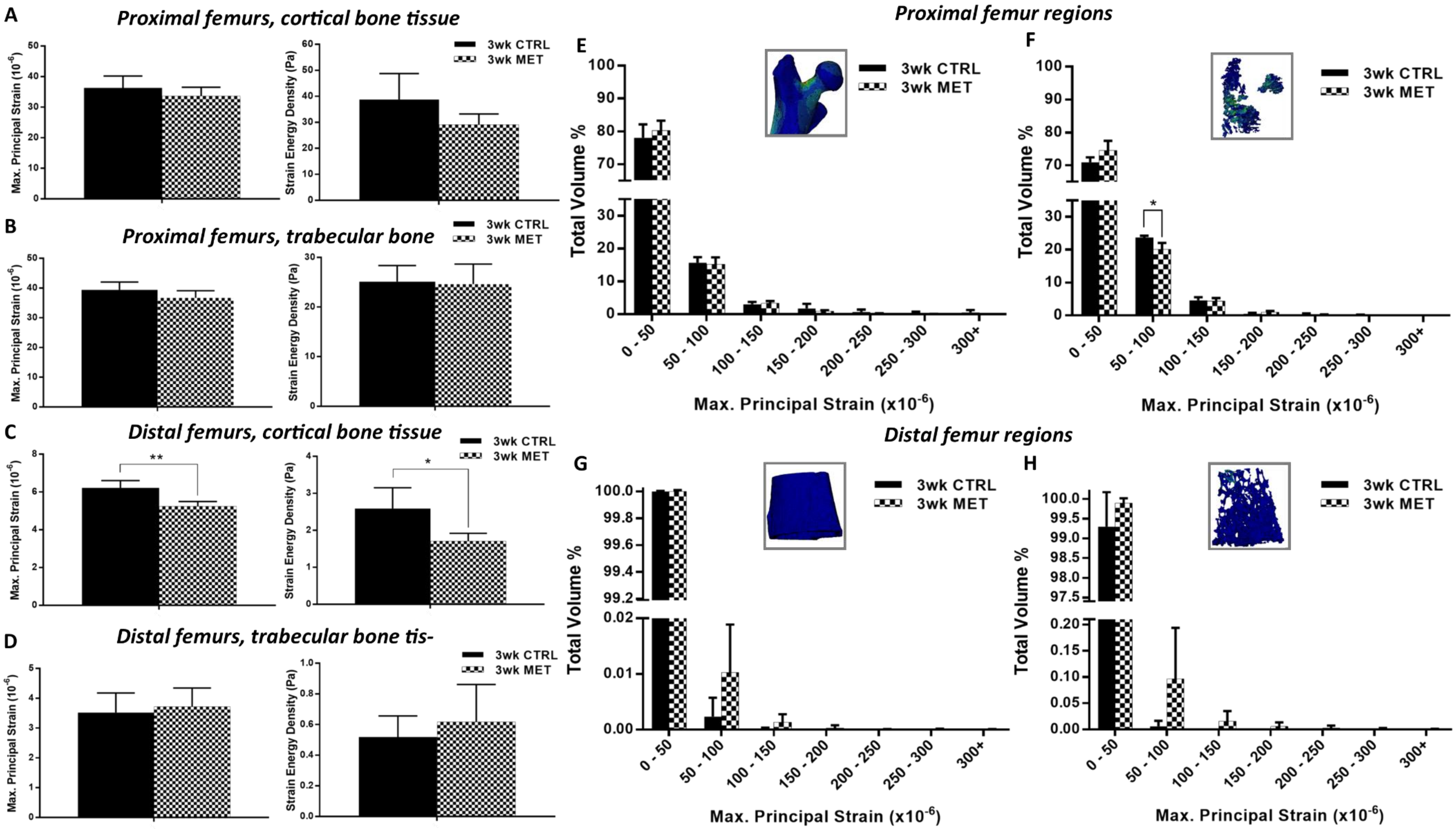

Figure 4.6: Strain stimuli predictions for cortical and trabecular bone sub-regions 3 weeks post-inoculation. Mean maximum principal strain and strain energy density of precise cortical and trabecular bone regions of (A, B) proximal and (C, D) distal femurs from the CTRL and MET groups. Distributions of maximum principal strain, analysed within (E, G) cortical and (F, H) trabecular bone tissue sub-regions of proximal and distal femurs, as a percentage of bone volume.

4.2.4 *Mechanical strain increased upon over osteolytic destruction (6 weeks post-inoculation)*

By 6 weeks post-inoculation, high concentrations of stress and strain were evident along the medial side of the femoral neck region and about the femoral head surface area (Figure 4.7A, B). At this later time point, following extensive osteolysis, a significantly lower volume of bone tissue from metastatic proximal femora experienced strains below 50 με when compared to healthy controls (71.6 ± 5.97% vs. 80.4 ± 2.18%, $p<0.05$), whereas a greater volume of bone tissue was observed in higher strain ranges compared to controls, in the whole proximal femurs (Figure 4.8A). Most notably, the volume of bone tissue under 50 - 100με strains was significantly higher in metastatic group simulations compared to controls (20.9 ± 3.7% vs. 15.0 ± 1.3%, $p<0.05$) (Figure 4.8A). In addition, the mean maximum principal strain (43.1 ± 5.1 με vs. 33.0 ± 2.0 με, $p<0.05$) and SED (46.2 ± Pa vs. 31.5 ± 4.4 Pa, $p<0.05$) were significantly higher in metastatic proximal femora compared to healthy controls (Figure 4.8B, 8C). The analysis of the femoral head sub-region showed similar changes in strain distribution (Supplementary Figure 4.3).

In the distal femur at 6 weeks post-inoculation, anterior-posterior FE model cross-sections depict osteolytic lesions within the MET bone tissue (Figure 4.7C,D). However, quantitative analysis of these distal regions, at 6 weeks post-inoculation, revealed that the volume of bone within each strain range was not altered significantly (Figure 4.8D). Changes in the mechanical environment of distal regions due to metastasis, at 6 weeks post-inoculation, were evident in terms of significantly higher mean maximum principal strain (8.69 ± 2.48 vs. 4.99 ± 0.25, $p<0.01$) and mean SED compared to healthy controls (4.08 ± 2.07 Pa vs. 1.31 ± 0.176 Pa, $p<0.05$) (Figure 4.8E, 8F). Detailed sub-regional analysis at this late time point revealed that all regions of interest had increased maximum principal strain and SED (Supplementary Figure 4.4A-D), with the exception of proximal femur trabecular bone tissue, which did not differ significantly. Strain distributions of all cortical and trabecular sub-regions trended toward an increase (i.e., skewed to the right) in the metastatic group, compared to healthy controls, following overt osteolysis at this late time point (Supplementary Figure 4.4E-H).

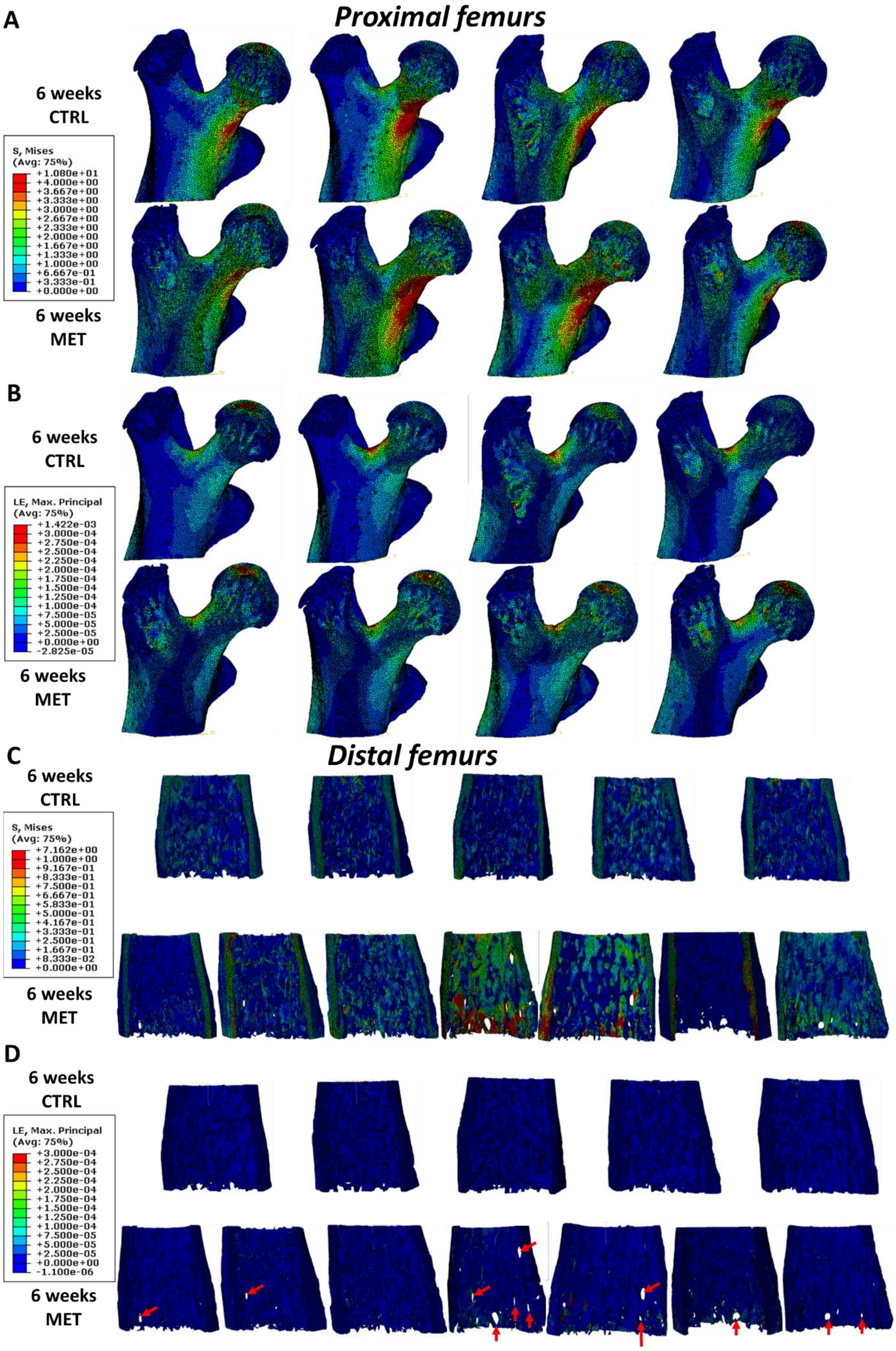
A
Proximal femurs
6 weeks
CTRL
S, Mises
(Avg: 75%)
+1.080e+01
+4.000e+00
+3.667e+00
+3.333e+00
+3.000e+00
+2.667e+00
+2.333e+00
+2.000e+00
+1.667e+00
+1.333e+00
+1.000e+00
+6.667e-01
+3.333e-01
+0.000e+00
6 weeks
MET
B
6 weeks
CTRL
LE, Max. Principal
(Avg: 75%)
+1.422e-03
+3.000e-04
+2.750e-04
+2.500e-04
+2.250e-04
+2.000e-04
+1.750e-04
+1.500e-04
+1.250e-04
+1.000e-04
+7.500e-05
+5.000e-05
+2.500e-05
+0.000e+00
-2.825e-05
6 weeks
MET
C
Distal femurs
6 weeks
CTRL
S, Mises
(Avg: 75%)
+7.162e+00
+1.000e+00
+9.167e-01
+8.333e-01
+7.500e-01
+6.667e-01
+5.833e-01
+5.000e-01
+4.167e-01
+3.333e-01
+2.500e-01
+1.667e-01
+8.333e-02
+0.000e+00
6 weeks
MET
D
6 weeks
CTRL
LE, Max. Principal
(Avg: 75%)
+3.000e-04
+2.750e-04
+2.500e-04
+2.250e-04
+2.000e-04
+1.750e-04
+1.500e-04
+1.250e-04
+1.000e-04
+7.500e-05
+5.000e-05
+2.500e-05
+0.000e+00
-1.100e-06
6 weeks
MET

Figure 4.7: Predicted stress and strain distributions at 6 weeks post-inoculation. Medial-lateral cross-sections of finite element models contour plots for (A, C) Von Mises stress and (B, C) maximum principal strain in CTRL and MET femur regions during later stage metastasis. Red arrows indicate osteolytic lesions.

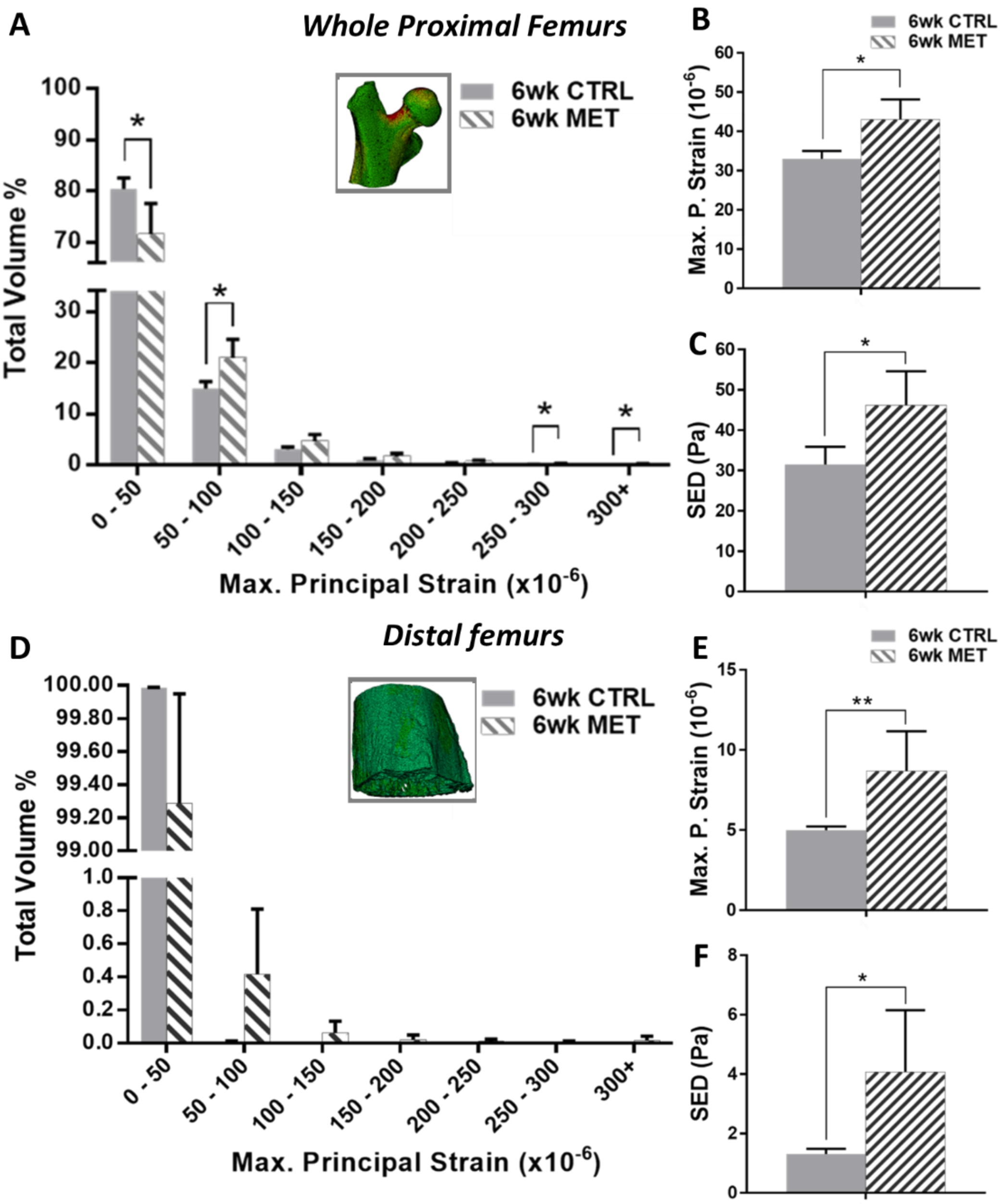

Figure 4.8: Predicted changes in bone tissue strain 6 weeks post-inoculation. Analysis was conducted in (A-C) whole proximal femur and (D-F) distal femur regions. (A, D) Distributions of maximum principal strain as a percentage of bone volume. (B, E) Mean maximum principal strain (Max. P. Strain) and (C, F) strain energy density (SED) in healthy control (CTRL) and metastatic (MET) regions 6 weeks after tumour inoculation.

4.3 Discussion

This study investigated temporal changes in the mechanical environment within bone by developing subject-specific finite element models derived from µCT scans of breast cancer inoculated mice. In particular, this study analysed time-dependent changes in mechanical stimuli within the bone microenvironment, local and distant from an invading primary tumour, to investigate putative mechanobiological cues for osteolysis during bone metastasis. From this study, strain within the cortical bone decreases prior to the onset of overt osteolysis (3 weeks post-inoculation), in distal femur regions far from the primary tumour mass. Notably, this coincides with the occurrence of cortical thickening within the distal femurs as previously reported in Chapter 3 (Verbruggen et al., 2022), which might explain the reduced mechanical strain observed here at this early time-point. Interestingly, the current study reveals that mechanical strain distribution within the trabecular bone of the proximal femur is also decreased at 3 weeks, despite the onset of early bone loss in terms of trabecular thinning as previously reported in Chapter 3 (Verbruggen et al., 2022), which might be expected to result in increased mechanical stimulation of the remaining trabeculae. However, also reported in Chapter 3 was increased mineralisation in trabecular bone by 3 weeks, which might explain this finding (Verbruggen et al., 2022). On the basis of these results, it is thus proposed that early changes in mechanical stimulation local to bone cells activates bone resorption via mechanoregulation, and thereby plays a role in driving later osteolytic destruction. These findings reveal that mechanobiology may play a role during the vicious cycle of metastasis upon breast cancer invasion of bone tissue.

Some limitations of this study require consideration. Firstly, the computational models were derived from µCT data of immunocompetent mice inoculated at two time points, representing the earliest time-point at which metastatic development is detected (Lelekakis et al., 1999) and a later timepoint sufficient to establish overt osteolysis (Arrington et al., 2006). Thus, the approach might not capture skeletal responses to metastatic invasion arising in human patients, and does not provide continual analysis as would be possible with *in vivo* micro-CT images of very limited image resolution. Secondly, the precise locations of the cancer cells that drive metastases and osteolysis in these animals are not known, because it was not possible to perform histology (e.g., H&E staining) because the samples were required for micro-CT and mechanical testing. However, IVIS imaging at 6 weeks post-inoculation, reported in our prior study (see Chapter 3) (Verbruggen et al., 2022), showed metastatic spread to the tumour-adjacent murine femur. Moreover, H&E staining at 19-days post-inoculation in animal models of the same cancer type, mouse species and inoculation method as in this study have reported consistent metastases within the proximal femur region (Lelekakis et al., 1999). Thirdly, tumour tissue and bone marrow were not included in the FE models. However, a separate analysis was conducted to investigate the impact of tumour pressure representative of that reported in tumour-inoculated SCID mouse tibiae (Sottnik et al., 2015), which revealed no changes in mechanical stimulation (Supplementary Figure 4.5). Moreover, µCT-derived FE models of human tibial cores revealed that the mechanical stimulation from the marrow phase were 0.005 times smaller than in adjacent trabecular bone (Sandino et al., 2017), and so inclusion of the marrow would be unlikely to influence results. Integration of a cartilage layer, which resides between the femoral head and pelvis and reportedly has a stiffness of 2 MPa (Cao et al., 2006), is unlikely to influence results but can be integrated into future iterations of the model. Thirdly, while most femurs were harvested from the right anatomical side of the mouse, two of five femurs in the 3-week control cohort were collected from the left side. However, studies have shown that bone geometry and tissue properties do not vary in female tibiae of the same species (Margolis et al., 2004, Vesper et al., 2017), and thus this is unlikely to have impacted FE results. Another potential limitation may be model alignment and the resulting load direction, which was previously reported to impact bone tissue stiffness and strength measurements (Voide et al., 2008), as well as boundary conditions causing an edge effect on results. However, sensitivity analysis of this parameter was performed, which shows that alignment does not significantly affect FE model strain distributions in the current study (Supplementary Figure 4.2), while visual analysis of stress and strain distributions in multiple models from this study show no evidence of edge effects on the results (see Supplementary Figure 4.6). The sample number for the metastatic proximal femurs at 6 weeks post-inoculation was lower because the femoral head was absent in 3 of 7 metastatic proximal femurs at this late time point. This likely occurred due to high stress along the lateral and medial sides, visible in the stress distributions of the metastatic FE models, which is a known location for failure from previous experimental and computational studies of bone fracture susceptibility during metastasis (Keyak et al., 2007, Yosibash et al., 2014, Falcinelli et al., 2019). Nonetheless, despite this low sample number, significant differences in strain distributions were still found in metastatic femoral head regions compared to healthy controls. Equations used for converting the grey-levels to elastic modulus (equations 1-3) closely corelated with our previous experimental results, which conducted nanoindentation to calculate the modulus of these same bone tissue samples (Supplementary Table 1). It must be noted that these equations were scanner-specific and therefore experimental validation would be required for alternative micro-CT scanners, acquisitions or reconstruction approaches.

Some limitations regarding FE model development also require discussion. Firstly, although 8-noded hexahedral elements are often used in micro-FE models (Choudhari et al., 2016, Benca et al., 2017, Atkins et al., 2019), tetrahedral elements were chosen as they are more suited to the geometrical complexity of bone regions in this study, and especially for the distinction of individual trabeculae. Furthermore, a study of a human proximal femur FE model reported that 4-noded tetrahedral elements more closely correlated with theoretical results compared to hexahedral (Ramos and Simoes, 2006). Secondly, low density connective tissues, such as bone marrow or immature bone tissue which has not yet become mineralised, were not included in the FE models. This may have resulted in the exclusion of some lower mineralised regions of the murine growth plate, and may have impacted strain energy density results (Webster et al., 2015). However, the density of these softer materials was not distinguishable, either via greyscale image visualisation or the assessment of micro-CT generated histograms. Therefore, lowering the density threshold in an attempt to capture these regions would result in the addition of CT scanning ‘background’ not representative of high-density bone mineral. Thirdly, the assumption of linear elasticity ignores the biphasic nature of bone tissue and does not account for potential plastic deformation. However, the yield strain (0.029 ± 0.005) of C57BL/6J female mouse bone tissue (Nazarian et al., 2009) far exceeds the strain range assessed in the current study (0 - 300με). Finally, poroelastic CT-derived FE models were predicted to have significantly higher reaction forces and SED when compared a purely elastic model (Falcinelli et al., 2020), thus current results might underestimate the mechanical environment to some degree. However, linear elastic models were implemented for both groups, and therefore control and metastatic results were directly comparable. Moreover, previous FE studies have implemented linear elasticity to study fracture risk in metastasis (Keyak et al., 2005, Mann et al., 2008, Choudhari et al., 2016, Atkins et al., 2019).

In the current study, the increased strain in the proximal femur regions at 6 weeks was expected and is in keeping with a μCT derived FE study of metastatic vertebrae, in which metastasis was induced by intracardiac injection of HeLa cells into female Rowett nude rats, which reported increases in von Mises stress and maximum principal strain in osteolytic vertebrae compared to healthy controls (Choudhari et al., 2016). While these changes in strain are within relatively small ranges (50με equivalent to 0.005% strain) this does not lie beyond the limitations of Abaqus FE models, previously demonstrated in µCT-derived FE models of murine tibiae which accurately predicted bone adaption under 10-50με ranges (Cheong et al., 2021). Findings from the current article also compare to a recent study of human osteolytic spines in which digital image correlation techniques were applied to quantify strain in vertebrae under different loading configurations (Palanca et al., 2021a). The results of that study revealed an increase in strain in the presence of lytic lesions compared to healthy controls (Palanca et al., 2021a). Here, sub-regional analysis of the trabecular tissue the in distal femur, far from the invading tumour mass, high mechanical stress and strain were in regions adjacent to osteolytic lesions at 6 weeks post-inoculation. This is in contrast to a study that implemented µCT derived FE models of simulated osteolytic lesions in vertebral models, which demonstrated low principal strains surrounding simulated lytic lesions (Costa et al., 2020). The differences between study findings might be explained by differences in bone skeletal location (i.e., femur versus vertebra) and lesion type and size (i.e., simulated versus naturally occurring).

Sub-regional computational analysis of the distal cortical region at 3 weeks post-inoculation predicted a decrease in mechanical strain. Interestingly, previous µCT analysis of these same mouse femurs from Chapter 3 (Verbruggen et al., 2022) reported that bone tissue thickness and mineralisation had also increased in the distal femur cortical bone at this early time point and likely explain these predictions. At 3 weeks post-inoculation, this study reports that mechanical strain stimulation within the femoral head trabecular sub-regions had decreased significantly during breast cancer metastasis, prior to osteolytic development. These changes coincide with trabecular thinning throughout proximal and distal regions of interest, as in Chapter 3 at 3 weeks (Verbruggen et al., 2022), and so might seem counterintuitive. However, this chapter also reported an increase in bone mineralisation in the trabecular bone tissue, and so this might explain the reduction in trabecular mechanical stimulation reported here. Specifically, significantly increased bone mineral density reported at 3 weeks (Verbruggen et al., 2022) would reduce loading experienced by resident bone cells within the trabecular tissues, thereby reducing mechanical stimuli in these regions. An alternative explanation for decreased strain is possible discontinuities within the bone tissue, where resorbed bone tissue areas are offloaded, thereby resulting in lower stiffness and strains at these regions. However, at the micro-CT resolution utilised in this study, osteolytic lesions which would elicit such discontinuities were not detectable in the proximal femur models, where decreased strain is reported. According to mechanoregulation theory, active osteoclast activity and bone resorption is an adaptive response to low or minimal mechanical stimuli within their microenvironment (Frost, 1996, McNamara and Prendergast, 2007). Thus, osteoclast resorption may be activated in response to the significantly lower strain stimulation in both the cortical and trabecular regions, which might drive the extensive osteolysis that occurs between 3 and 6 weeks. Indeed, analysis of the distal femur at 6 weeks post-inoculation predicted higher mechanical stimulation, which coincided with evidence of overt osteolytic destruction, decreased bone mechanical properties and mineral content in Chapter 3 (Verbruggen et al., 2022).

It is well established that biochemical signalling and bone tissue resorption release factors that influence both bone and cancer cells during metastasis. On the basis of predictions during early breast cancer metastasis, this study proposes how mechanobiological cues play a role in activating osteoclast resorption and thus contribute toward driving subsequent osteolysis (Figure 4.9). Specifically, decreased mechanical stimulation of bone tissue stimulates mechano-sensitive osteocytes embedded within the bone tissue to upregulate sclerostin and inhibit the Wnt signalling pathway (Yavropoulou and Yovos, 2007). This increases osteoclast activity and osteolytic degradation of trabecular bone as shown in Chapter 3 (Verbruggen et al., 2022). As a result of the altered bone mechanical environment and stimuli to resident bone cells, osteolysis causes the release of growth factors abundant within bone ECM (TGF-β, Ca^{2+}) to promote further tumour proliferation and osteolytic destruction. In addition to activation of resident osteoclasts, early changes in the bone tissue mechanical environment may also influence tumour cellular behaviour, through altered TGF-β signalling and sclerostin secretion by mechanosensitive osteocytes (Sarazin et al., 2021) and leaving resorption unchecked (Lynch et al., 2013), thus allowing tumour cells to proliferate and upregulate osteolytic factors (IL-11, PTHrP), altering RANKL/OPG signalling and ultimately perpetuating osteoclastogenesis and osteolysis (Yoneda et al., 1994). Taken together, it is now proposed that decreased strain stimuli within the bone microenvironment may provide mechanobiological cues for resident osteoclasts to activate excess bone resorption, and may also influence metastatic breast cancer cells to continue signalling for osteolytic degradation. In both cases, mechanoregulation may play a role in driving osteolysis during breast cancer metastatic invasion, driving the subsequent release of yet more osteolytic factors and thus possibly contributing to the perpetuation of the cancer ‘vicious cycle.’

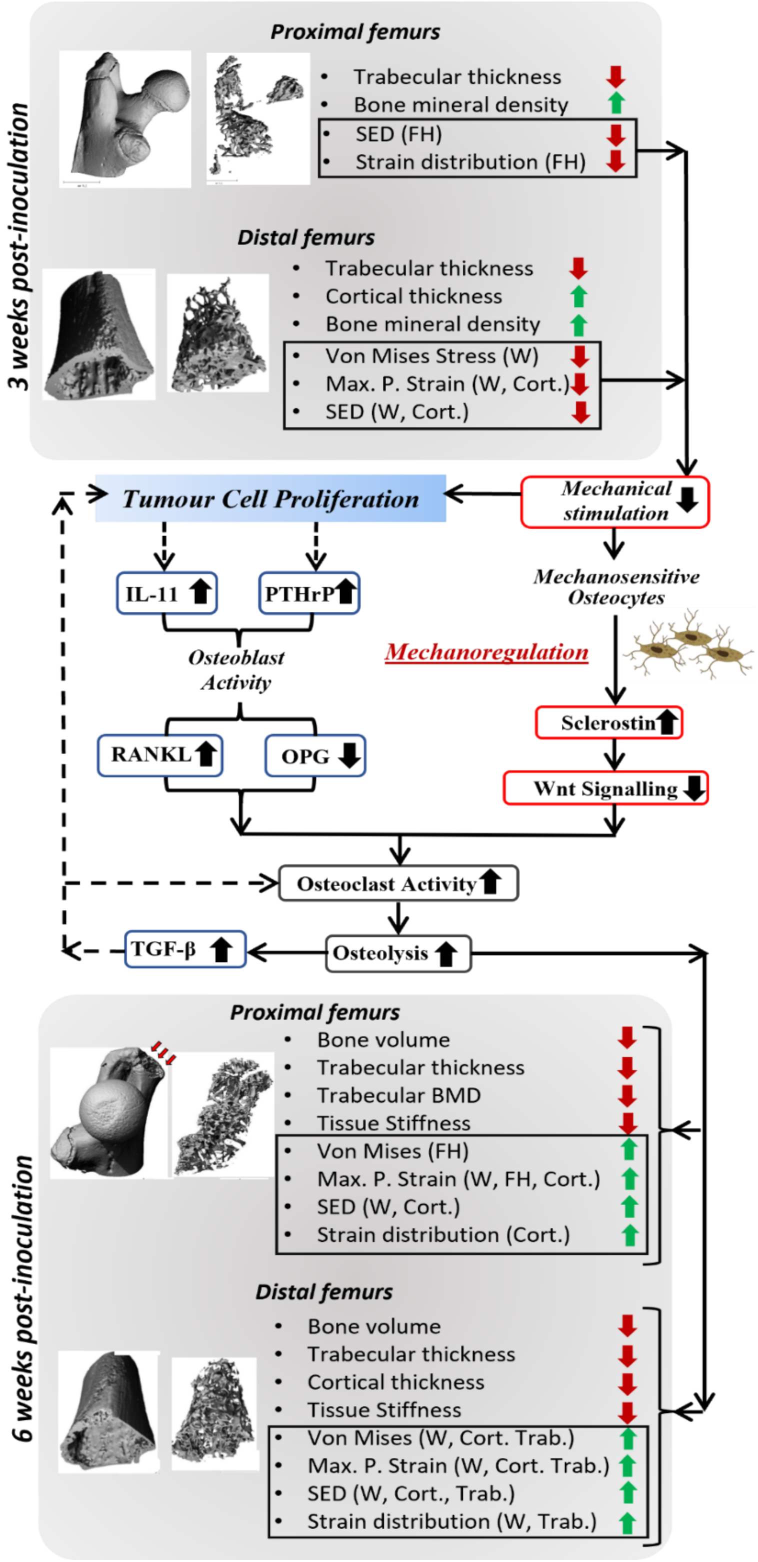

Figure 4.9: Mechanoregulatory responses in bone remodelling cells may contribute to subsequent osteolysis and tumour proliferation during breast cancer metastatic invasion. Early changes in the mechanical environment coincide with altered bone microarchitecture and mineralisation at 3 weeks post-inoculation. The reduced stimulation might upregulate sclerostin expression by osteocytes and inhibit the Wnt pathway, which would stimulate osteoclast activity and thereby contribute to overt osteolysis seen at 6 weeks post-inoculation. Additionally, decreased mechanical stimulation and resorption would allow for release of

osteolytic factors (IL-11, PTHrP), inducing osteoblasts to alter RANKL/OPG signalling and contribute to further osteoclast activity and subsequent osteolytic destruction. This resorption would release TGF-β to stimulate further tumour proliferation, thereby perpetuating the cancer vicious cycle. Green arrows: increase in bone tissue property, red arrows: decrease in bone tissue property compared to controls. W, whole FE model regions of interest; FH, Femoral head sub-regions; Cort, cortical tissue sub-regions; Trab, trabecular tissue sub-regions; Max. P. Strain, maximum principal strain; SED, strain energy density.

4.4 Conclusion

This study provides an insight into the putative mechanobiological cues which may perpetuate the cancer vicious cycle, by developing micro-CT derived FE models of metastatic mouse femurs and providing temporal and spatial analysis of changes within the bone mechanical environment during breast cancer metastatic invasion. This study reports that in early metastasis, prior to extensive osteolytic destruction (3 weeks after tumour inoculation), there was a decrease in strain distribution within the distal cortical bone tissue, where tissue thickening had been previously reported, and in proximal femur trabecular bone tissue. In light of these findings, it is proposed that reduced mechanical environment at this early time-point activates further resorption and drives the extensive osteolysis at later stage metastasis.

4.5 Supplementary Figures and Tables:

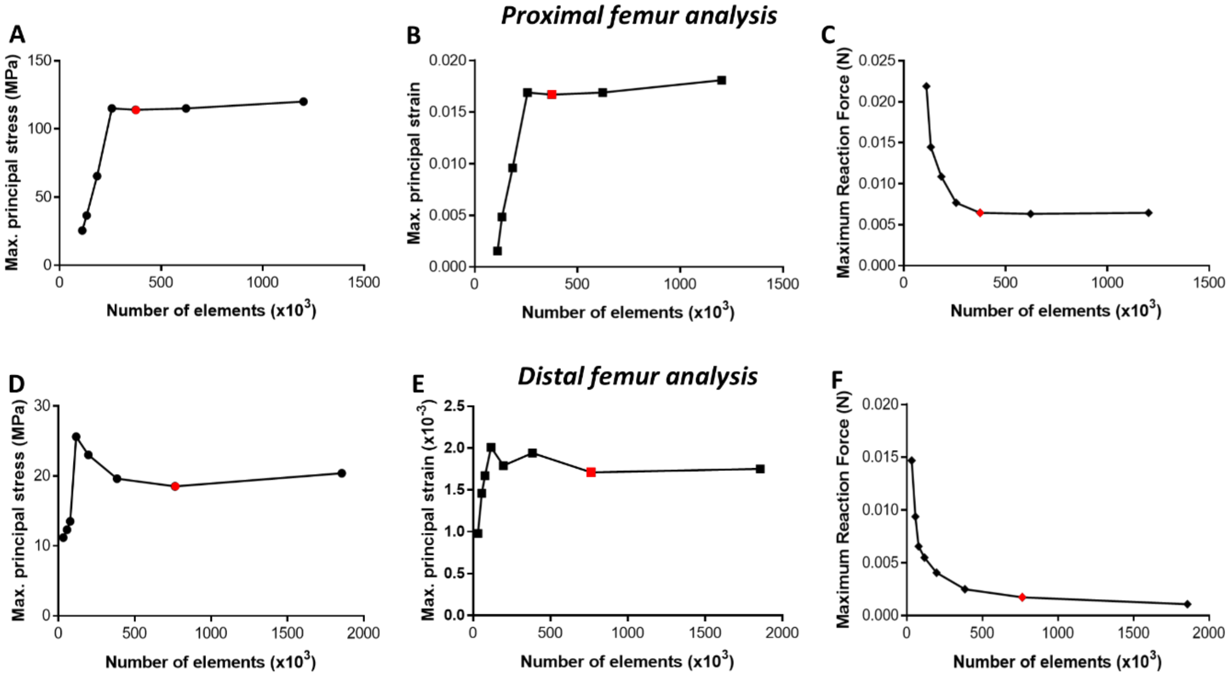

Supplementary Figure 4.1: Mesh Convergence Analysis (A-C) Analysis was conducted on and results obtained from a control whole proximal femur model and (D-F) distal femur model at 3 weeks and under typical weight-bearing loads. Outputs analysed for convergence were (A, D) maximum principal stress, (B, E) maximum principal strain and (C, F) maximum measured reaction force. Red datapoints indicate output from the chosen maximum triangle edge length (0.075 mm in proximal femur models, 0.04 mm in distal femur models).

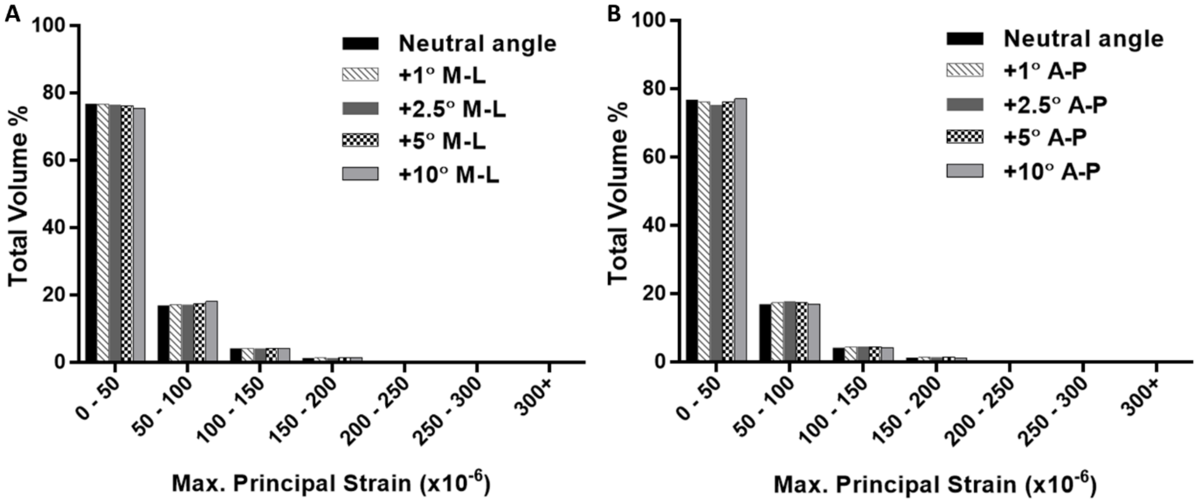

Supplementary Figure 4.2: Model Alignment Analysis. Distributions of maximum principal strain as a percentage of bone volume, in a single 3 week MET proximal femur model. The bodyweight was applied at an additional 1˚, 2.5˚, 5˚ and 10˚ from the neutral position along the (A) medial-lateral and (B) anterior-posterior axes. The maximum difference in percentage volume between these results was 1.4% (+10˚ M-L vs. neutral, 0-50με) and therefore not likely to effect quantitative results.

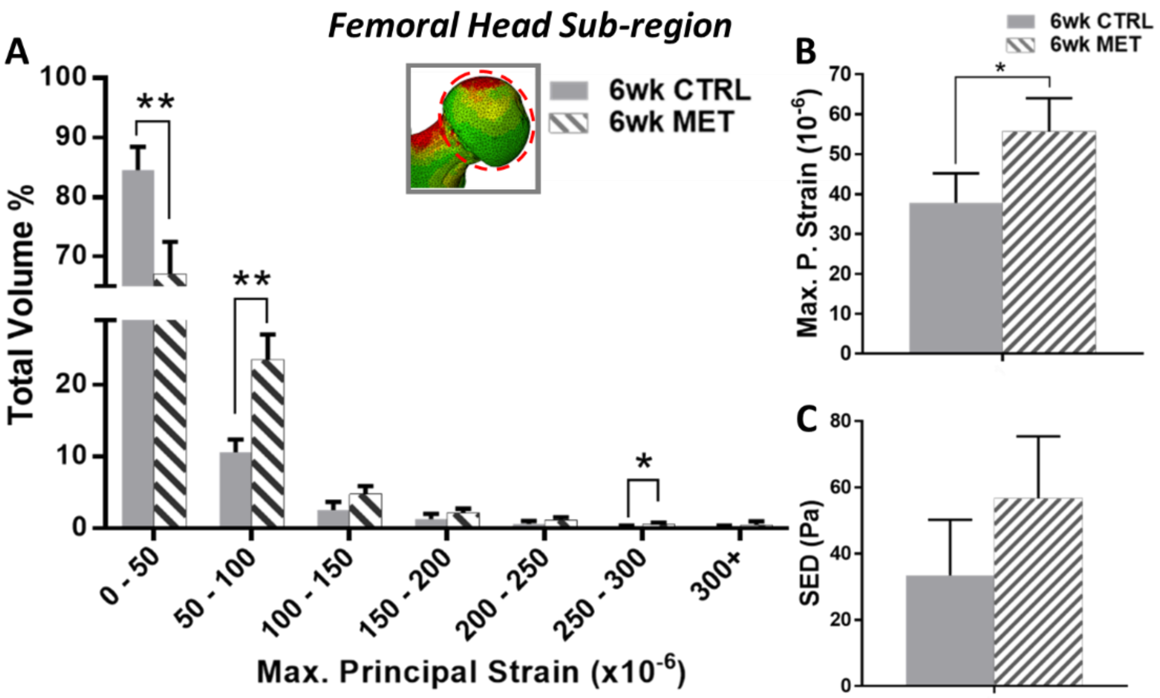

Supplementary Figure 4.3: Predicted changes in bone tissue strain of femoral heads 6 weeks post-inoculation. (A) Distributions of maximum principal strain as a percentage of bone volume. (B) Mean maximum principal strain (Max. P. Strain) and (C) strain energy density (SED) in healthy control (CTRL) and metastatic (MET) regions 6 weeks after tumour inoculation.

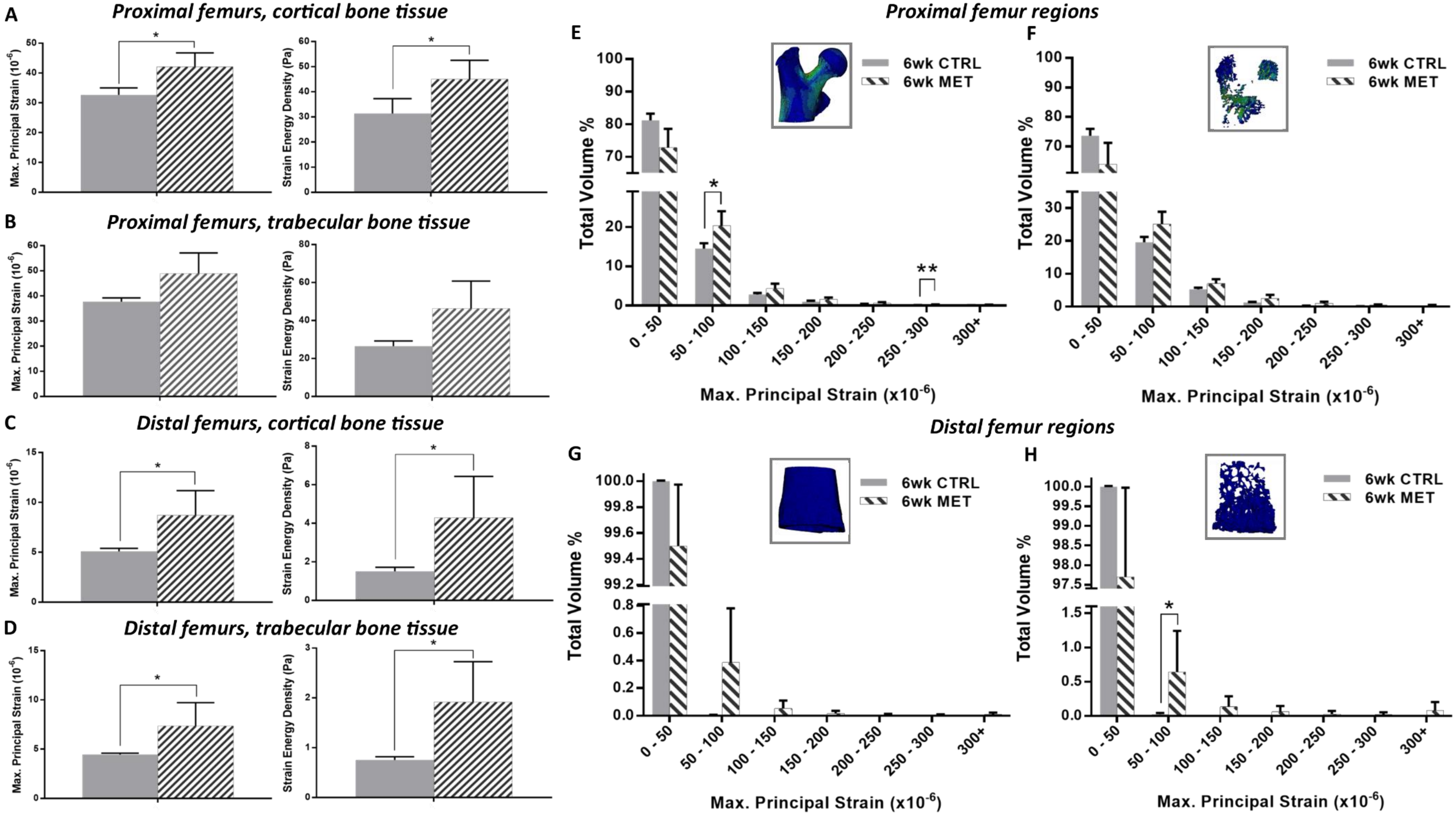

Supplementary Figure 4.4: Strain predictions for cortical and trabecular bone sub-regions 6 weeks post-inoculation. Mean maximum principal strain and strain energy density of precise cortical and trabecular bone regions of (A, B) proximal and (C, D) distal femurs from the CTRL and MET groups. Distributions of maximum principal strain, analysed within (E, G) cortical and (F, H) trabecular bone tissue sub-regions of proximal and distal femurs, as a percentage of bone volume.

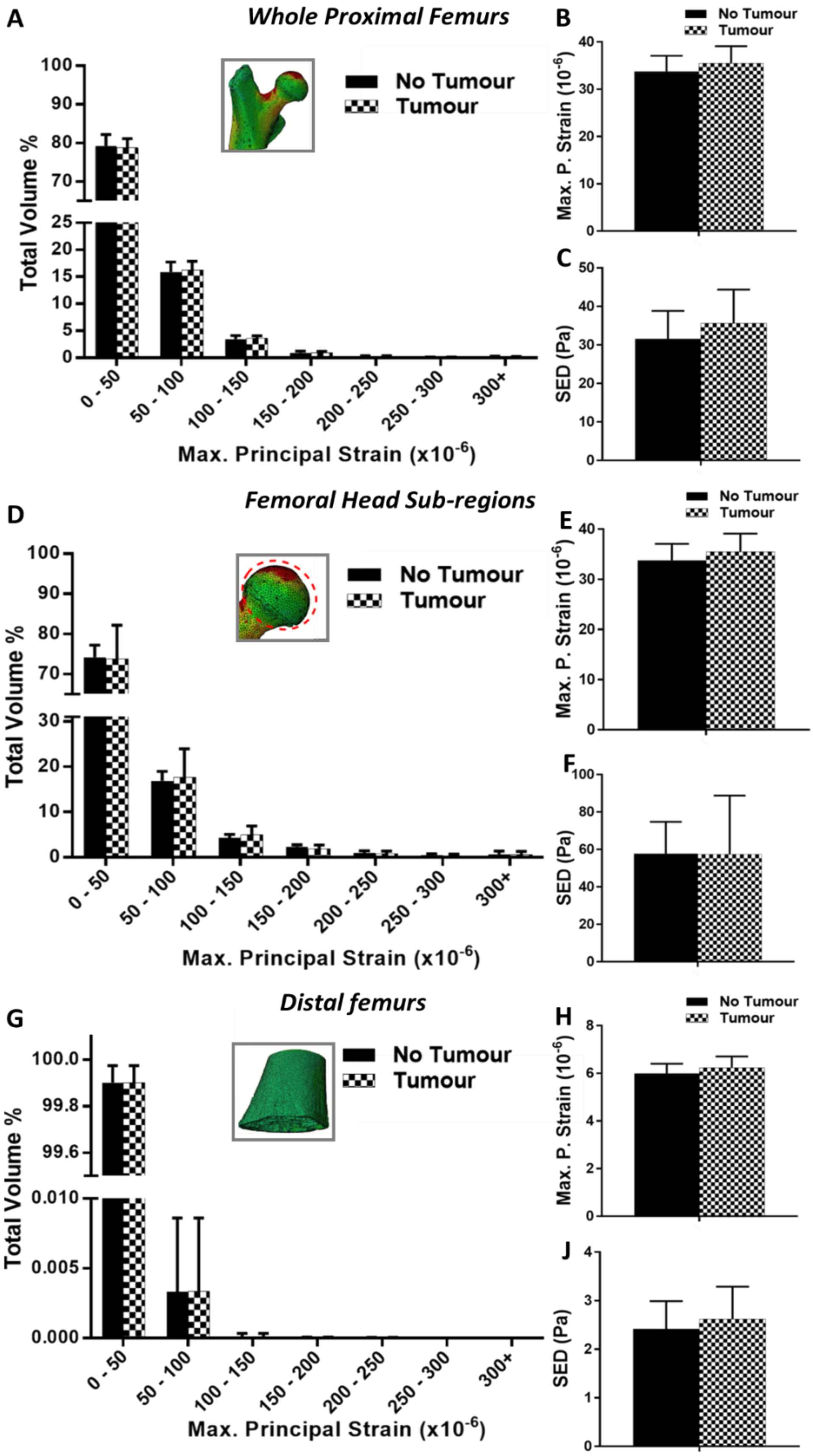

Supplementary Figure 4.5: Predicted changes in bone tissue strain with or without tumour pressure. To investigate the influence of primary tumour pressure presence, a pressure (5kPa) was applied to the femoral head surface of the 3-week metastatic proximal femur models (‘Tumour’). These were compared to identical FE models without applied pressure (‘No Tumour’). The tumour pressure was based on reported peak interstitial fluid pressure (IFP, 37.84 mmHg) within the tibiae of male SCID mice (8-10 wo) 16 days following the direct inoculation of DU145 prostate cancer cells (Sottnik et al., 2015). Percentage volume distribution in Maximum principal strain within (A-C) proximal femur (D-F) femoral head and (G-J) distal femur regions. (B, E, H) Mean maximum principal strain (Max. P. Strain) and (C, F, J) strain energy density (SED) in healthy control (CTRL) and metastatic (MET) regions 6 weeks after tumour inoculation.

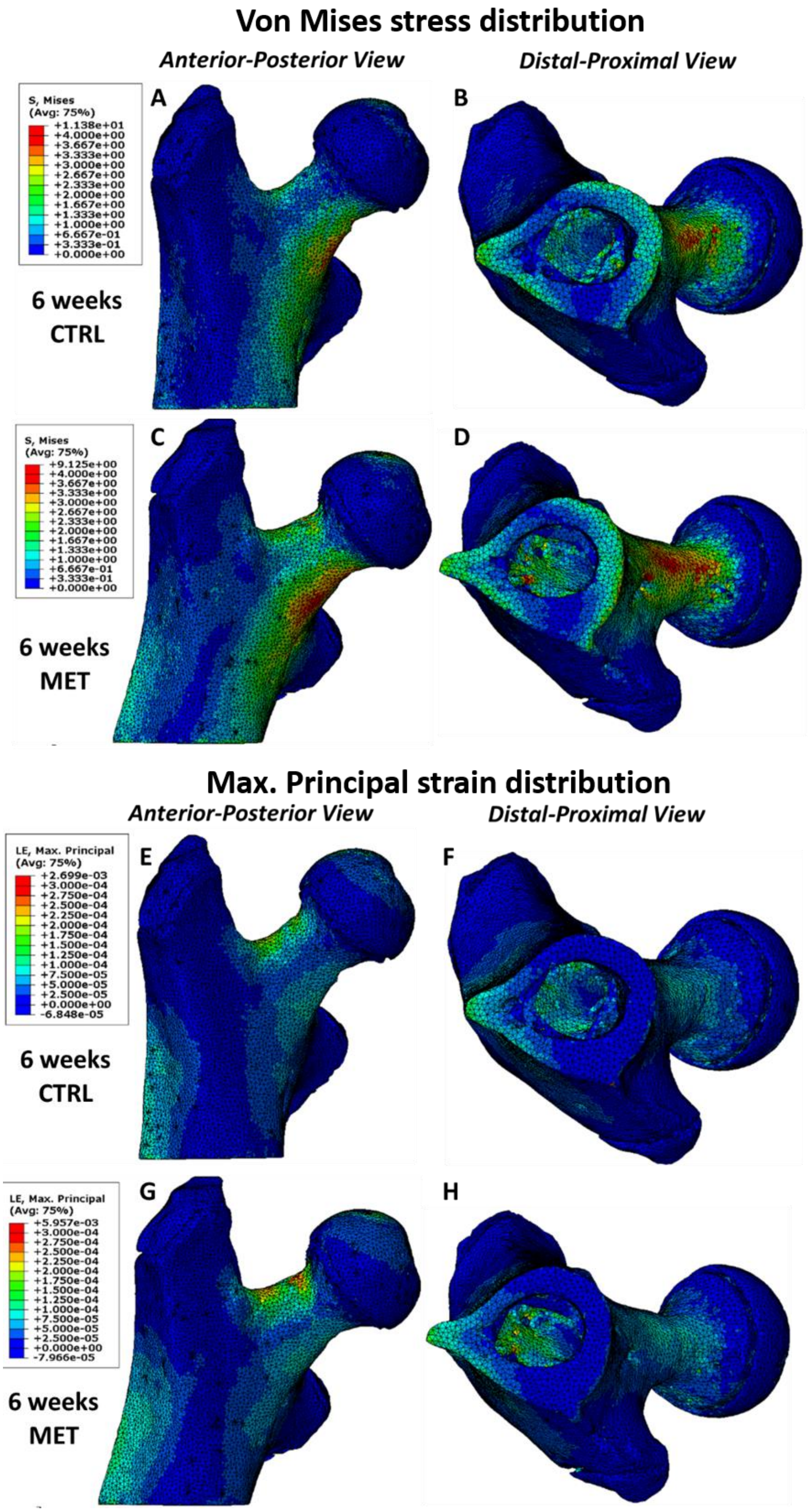
Von Mises stress distribution
Anterior-Posterior View
Distal-Proximal View
S, Mises
(Avg: 75%)
+1.138e+01
+4.000e+00
+3.667e+00
+3.333e+00
+3.000e+00
+2.667e+00
+2.333e+00
+2.000e+00
+1.667e+00
+1.333e+00
+1.000e+00
+6.667e-01
+3.333e-01
+0.000e+00
6 weeks
CTRL
A
B
S, Mises
(Avg: 75%)
+9.125e+00
+4.000e+00
+3.667e+00
+3.333e+00
+3.000e+00
+2.667e+00
+2.333e+00
+2.000e+00
+1.667e+00
+1.333e+00
+1.000e+00
+6.667e-01
+3.333e-01
+0.000e+00
6 weeks
MET
C
D
Max. Principal strain distribution
Anterior-Posterior View
Distal-Proximal View
LE, Max. Principal
(Avg: 75%)
+2.699e-03
+3.000e-04
+2.750e-04
+2.500e-04
+2.250e-04
+2.000e-04
+1.750e-04
+1.500e-04
+1.250e-04
+1.000e-04
+7.500e-05
+5.000e-05
+2.500e-05
+0.000e+00
-6.848e-05
6 weeks
CTRL
E
F
LE, Max. Principal
(Avg: 75%)
+5.957e-03
+3.000e-04
+2.750e-04
+2.500e-04
+2.250e-04
+2.000e-04
+1.750e-04
+1.500e-04
+1.250e-04
+1.000e-04
+7.500e-05
+5.000e-05
+2.500e-05
+0.000e+00
-7.966e-05
6 weeks
MET
G
H

Supplementary Figure 4.6: Visualising the impact of boundary conditions. Distributions of (A-D) Von Mises stress and (E-H) maximum principal strain in one CTRL and one MET proximal femur model from each group at 6 weeks post-inoculation, presented in anterior-posterior and distal-proximal views. These views show no evidence of appreciable edge effects on stress and strain response as a result of the applied boundary conditions.

Supplementary Table 4.1: Peak Young's modulus (GPa) calculated based on equations (1-3) ('calculated') compared to Young's modulus obtained from nanoindentation results for cortical and trabecular bone tissue regions as reported in Chapter 3 (Verbruggen et al., 2022) (mean ± standard deviation).

	Proximal femur region			***Distal femur region***		
3 weeks	**Calculated**	**Cortical**	**Trabecular**	**Calculated**	**Cortical**	**Trabecular**
CTRL	17.12 ± 1.55	17.23 ± 2.71	14.88 ± 1.80	16.66 ± 0.65	17.95 ± 1.39	15.94 ± 1.75
MET	16.82 ± 0.74	15.92 ± 0.32	16.20 ± 1.32	16.28 ± 0.73	16.96 ± 0.76	16.88 ± 0.55
6 weeks						
CTRL	16.47 ± 0.24	19.46 ± 1.20	17.96 ± 1.17	18.01 ± 1.02	17.77 ± 1.75	15.56 ± 2.31
MET	16.97 ± 0.58	17.61 ± 2.96	15.21 ± 2.30	15.97 ± 0.26	14.39 ± 3.47	12.52 ± 3.47

Chapter 5: Predicting mechanoregulatory responses in bone during breast cancer metastasis: A Finite Element Analysis

In keeping with the format of previous chapters, the following chapter was written in the style of a scientific article. As a consequence, Chapter 5 Introduction, Methods and Discussion (limitations) sections may contain some repetition to previous chapters. This was necessary, however, so that it is readily available for future publication in a relevant journal.

5.1 Introduction

Breast cancer commonly migrates from the primary tumour and metastasises to bone, and it has been proposed that breast cancer cells have a particular affinity to the physical properties of bone tissue, which provides an attractive environment for metastatic development (Paget, 1889). Bone cells are instrumental in the tumour metastasis, whereby osteoclasts activate bone tissue resorption, resulting in osteolysis. Osteolysis not only provides a space for tumour invasion but also releases biochemical factors from the bone matrix that stimulates tumour cell proliferation. In healthy bone, mechanosensitive osteocyte cells, which reside within the bone lacunae, release biochemical signals that signal to osteoblasts and osteoclasts to activate bone formation or bone resorption, depending on the mechanical demands on the tissue. Frost’s ‘Mechanostat’ theory proposed that bone cells remodel the tissue in response to changes in the tissue strain. Specifically, it was proposed that there is a homeostatic strain range (‘lazy zone’), within which no tissue net formation or resorption occurs, but increased strain beyond this threshold induces bone formation, whereas bone resorption is activated below the lower strain threshold (Frost, 1987).

As bone tumours evolve, the local mechanical environment of bone tissue is altered over time (Arrington et al., 2006, Nazarian et al., 2008, Richert et al., 2015, Verbruggen et al., 2022). In particular, a recent pre-clinical animal study of metastatic mouse femurs has revealed bone mineral content and mechanical properties were significantly altered, prior to the development of overt osteolytic lesions as shown in Chapter 3. Specifically, an increase in bone mineral content and distal femur cortical bone tissue thickness was reported by 3 weeks of tumour development, while osteolysis and significantly decreased bone mineral content were not reported until the later time point of 6 weeks post-inoculation as in Chapter 3. Next, micro-CT-derived finite element (FE) models of the proximal femurs of these animal cohorts were developed and applied to study the mechanical environment within bone tissue during bone metastasis and osteolytic resorption (see Chapter 4). Interestingly, in early metastasis there was a decrease in strain distribution within the bone tissue of the proximal femur, which coincided with the onset of early osteolysis, cortical thickening and mineralisation of proximal and distal femur bone, reported in Chapter 3. It was proposed that this altered mechanical environment might stimulate resident osteocytes to activate osteoclast resorption, and thereby play a role in the cancer vicious cycle. However, how such an altered mechanical environment could drive the remodelling behaviour of resident bone cells remains unclear.

Mathematical and computational models have been applied to simulate and predict the role of biochemical processes and cell-cell signalling in tumour growth, and to a lesser extent have considered biophysical processes (Tracqui, 2009, Rejniak and Anderson, 2011, Araujo et al., 2014, Zhou and Liu, 2014, Kim and Othmer, 2015, Cook et al., 2016). The mechanoregulatory behaviour of bone tissue has been investigated through a combination of FE models and mechanoregulation theory. The basis of mechanoregulation theory is that the tissue is adapted to reach a homeostatic mechanical environment, and so mathematical relationships between the tissue stress/strain and adaptation have been developed. A bone remodelling algorithm incorporating two mechanical stimuli, strain and microdamage, was developed (McNamara and Prendergast, 2007), which was applied to study trabecular remodelling in healthy bone and during osteoporosis (McNamara and Prendergast, 2007, Mulvihill et al., 2008). A study reported the development of a microstructural, load-dependent remodelling algorithm for trabecular bone adaptation, which was successfully validated by *in-vivo* micro-CT data and was capable of predicting formation and resorption of trabeculae in both healthy and ovariectomised (OVX) vertebrae (Schulte et al., 2013). Later, a mechanoregulation algorithm, driven by fluid velocity stimulation, accurately predicted the distributions of cortical thickening in healthy cortical bone tissue in response to axial compression observed in experimental data, where the contralateral non-stimulated tibiae served as controls (Pereira et al., 2015). A more recent study sought to predict cortical and trabecular bone adaptation in response to either strain energy density (SED) or maximum principal strain, informed by micro-CT scans performed every 2 weeks in 14-22 week old mice (Cheong et al., 2020a). Interestingly, this study found predictions of bone apposition to be more accurate using maximum principal strain as a stimulus, while bone resorption was more accurate when driven by strain energy density (SED) stimuli (Cheong et al., 2020a). Another study applied a SED-driven remodelling algorithm to µCT-derived FE models of mouse tibiae, to investigate bone adaptation following ovariectomy and subsequent mechanical loading treatments (Cheong et al., 2020b). This approach was able to predict regions of bone apposition that were well correlated to experimental findings, whereas bone tissue resorption was not as precisely or spatially matched to experimental data (Cheong et al., 2020b). Bone tissue resorption has been predicted in µCT-derived FE models of healthy human vertebral bone cores (Mc Donnell et al., 2009), whereby bone resorption was implemented on the basis of strain and microdamage stimuli. Machine learning has also been applied to analyse micro-CT imaging and changes in bone tissue stiffness within the trabeculae of osteoporotic patients to determine the key variables that influenced bone tissue resorption (yield stress, yield strain). These parameters were then implemented in an algorithm, derived from the machine-learning approach, to accurately predict changes in tissue morphology in a single 2D trabecular strut model (Sohail et al., 2019). Each element underwent bone tissue adaption or resorption, governed by a stress-strain stimulus, and elements were considered resorbed when stiffness has decreased to match that of surrounding bone marrow (Sohail et al., 2019).

While the above studies have successfully demonstrated the prediction of mechanoregulatory responses within the bone microenvironment of healthy and osteoporotic bone models, adaption of mechanoregulation theory to investigate the contribution of bone remodelling in the development of bone metastasis has not been conducted. Simulating such responses at an early time point in metastasis may shed light on the potential role of mechanobiology in the development of osteolysis as it evolves. Thus, the objective of this study is to apply mechanoregulation theory to investigate whether mechanoregulatory responses may contribute to bone resorption during metastasis.

5.2 Methods

In this study an iterative approach is taken, whereby subject-specific FE models are applied to predict the mechanical environment within the bone tissue at the early stage of metastasis. A mechanoregulation approach is applied to predict how material properties are altered as a function of the evolving mechanical environment within the bone tissue.

5.2.1 Obtaining bone tissue geometry and material properties

The current study utilises and builds upon µCT-derived FE models, developed in a previous computational study of strain distribution during breast cancer metastasis (see Chapter 4). In brief, immune competent BALB/c mice, inoculated into a femur-adjacent mammary fat pad with 4T1 breast cancer cells, were euthanised, at either 3 or 6 weeks post-inoculation, and µCT scanning and reconstruction was conducted to develop solid models of the proximal femora. In the current study, computational models from the 3-week murine cohort were developed by meshing with 4-noded linear elastic, homogeneous, tetrahedral elements, following mesh convergence analysis, using 3Matic and Abaqus software (Figure 5.1A, 1B). Loading was applied to the femoral head surface equating to 120% of bodyweight (recorded for each animal during the experimental study of Chapter 3) applied in the proximal-distal direction and 10.9% in the posterior-anterior direction (Charles et al., 2018) (see Figure 5.1C). The distal surface was fixed in all directions (Figure 5.1C). For the current study, each computational model was assumed an initially homogeneous, isotropic structure, with the mean bone mineral density assigned according to µCT imaging of the metastatic femoral bone (1.262 ± 0.02 g/cm^3), converted to ash density as reported in Chapter 4 (Schileo et al., 2008), and the corresponding Young’s modulus applied according to a power law relationship used in female mouse tibiae, according to the following equation (Lu et al., 2019).

$$E = 10.5\rho^{2.29} \tag{5.1}$$

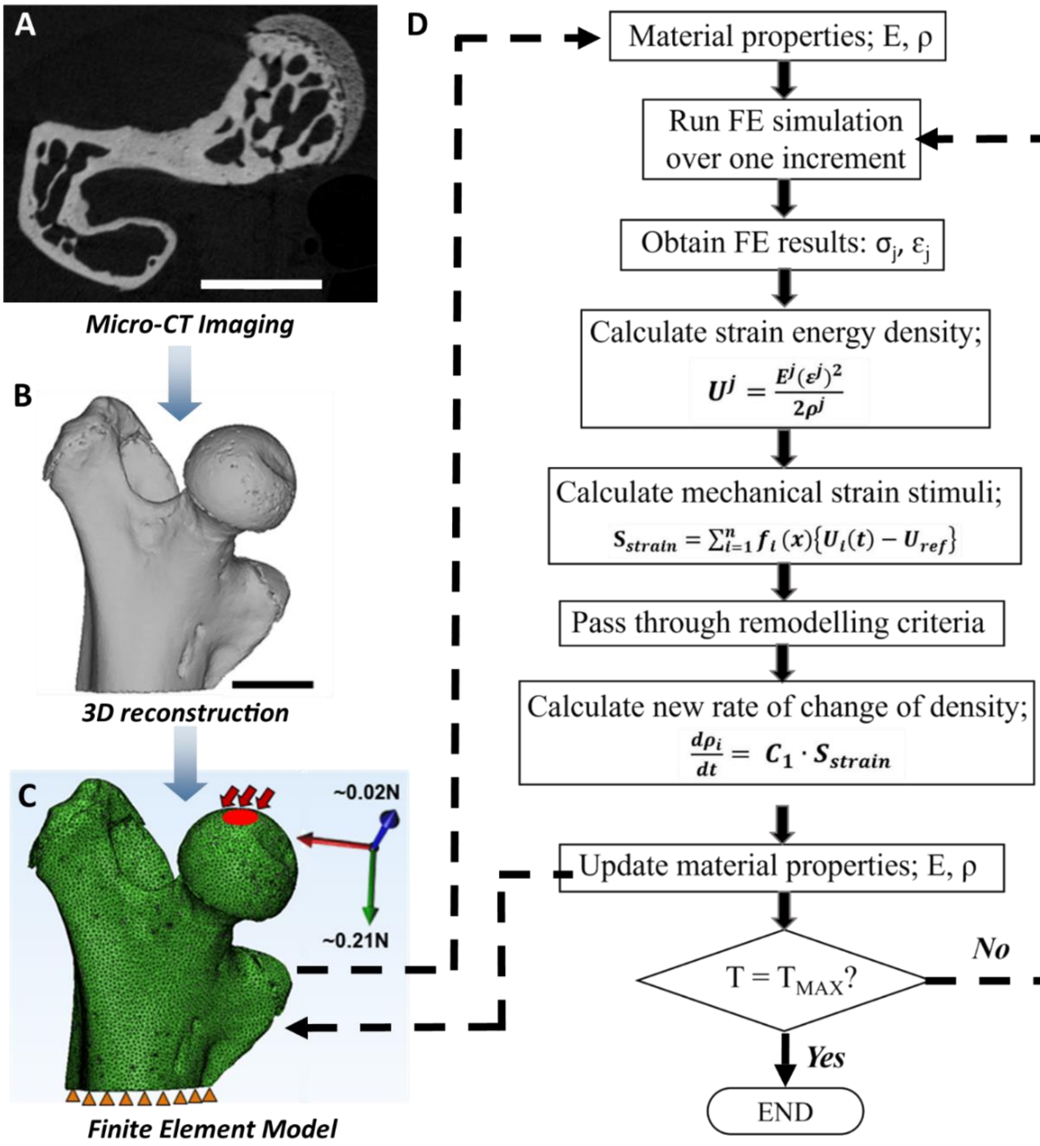

Figure 5.1: Flowchart of methods and iterative results upon application of a bone remodelling algorithm to metastatic bone tissue. (A) µCT imaging slice cross-section within the proximal femur of a metasetatic mouse at 3 weeks post-inoculation of breast cancer cells. (B) 3D reconstructed model from µCT scans, scalebars 1mm. (C) Load applied to the femoral head surface (in red) and fixed distal surface (in orange) to reflect physiological loading in a mouse hindlimb. (D) Sequence of calculations performed within the applied bone remodelling algorithm, up to a maximum time T_{MAX}.

5.2.2 Bone Remodelling Algorithm

To introduce mechanoregulation theory to the above models, a USDFLD (user-defined field) subroutine was applied, whereby the density and Young's modulus of each element within the model mesh was incrementally updated according to the rate of change of density predicted by a remodelling algorithm. Specifically, density adaption was predicted on the assumption that a mechanoregulatory response occurs, driven by a mechanical stimulus, strain energy density, U ^{j} (Huiskes et al., 1987, McNamara and Prendergast, 2007), calculated according to:

$$\boldsymbol{U^{j}} = \frac{\boldsymbol{E^{j}(\varepsilon^{j})^{2}}}{\boldsymbol{2\rho^{j}}} \tag{5.2}$$

where, for each location within a mesh, *j*, the tissue Young's modulus, E^{j} (MPa) and density, ρ^{j} (g/cm^3) are defined and the strain (ε^{j}) is predicted by solving the finite element model. The stimulus, S_{strain}, is calculated by comparing to the reference strain energy density, U_{ref}, which is calculated at homeostatic equilibrium, according to the following equation:

$$\mathrm{S}_{strain} = \sum_{i=1}^{n} f_i\,(x)\left\{U_i(t) + U^{ref}\right\} \tag{5.3}$$

The homeostatic region was defined according to Frost's 'Mechanostat' theory (1987), adapted for bone tissue mechanoregulation. Reference strain energy density, U^{ref}, is calculated as a function of reference modulus E^{ref}, density ρ^{ref} and strain ε^{ref}, when bone remodelling is at equilibrium (see equation 5.4). This 'lazy zone' of equilibrium is defined by strain thresholds for net bone resorption and formation are ε^{R} and ε^{F}, respectively. The value of ε^{ref} is thus determined by the current value of ε^{j}, according to conditions outlined below:

$$U^{ref} = \frac{E^{ref}(\varepsilon^{ref})^{2}}{2\rho^{ref}} \tag{5.4}$$

$$\left\{\begin{array}{lll} \psi = -1, & \varepsilon^{ref} = \varepsilon^{R} & if\ 0 < \varepsilon^{j} < \varepsilon^{R} \\ \psi = 0, & \varepsilon^{ref} = \varepsilon^{j} & if\ \varepsilon^{R} < \varepsilon^{j} < \varepsilon^{F} \\ \psi = 1, & \varepsilon^{ref} = \varepsilon^{F} & if\ \ \varepsilon^{j} > \varepsilon^{F} \end{array}\right\} \tag{5.5}$$

where ψ is the mechanical signal ensuring density decreases under resorption conditions and increases upon bone formation. Finally, the rate of change of density in response to mechanical stimuli, $d\rho i/dt$, and a new resulting density, (ρ_{i+1}), are calculated using the following equations:

$$\boldsymbol{\frac{d\rho_i}{dt} = C_1 \cdot \psi S_{strain}} \tag{5.6}$$

$$\rho_{i+1} = \rho_i + \frac{d\rho_i}{dt} \tag{5.7}$$

where a time constant, C_1, governs the rate of remodelling. This constant was determined separately for bone tissue resorption (C_1^R = 1600) and formation (C_1^F = 1.79), via simulations in a simplified trabecular strut model and through parameter variation analysis, described below (section 5.2.3) using experimental data from Chapter 3. Maximal and minimal apparent density limits of 1.73 g/cm^3 and 0.01 g/cm^3 were assigned as standard, where density below 0.01 g/cm^3 represents complete resorption (Van Rietbergen et al., 1993, Scannell and Prendergast, 2009). These equations (5.1 – 5.5) are thus implemented sequentially as part of the remodelling algorithm to iteratively predict a new density and Young's modulus for each element within a given model mesh, as illustrated in a flowchart (Figure 5.1D).

5.2.3 Deriving the bone remodelling constant, C1, and sensitivity analysis

To derive the rate of change of density value for bone tissue resorption, C_1^R, and formation, C_1^F, a simplified model of a murine bone trabecular strut was developed based on previous studies (McNamara and Prendergast, 2007, Mulvihill et al., 2008). The trabecular strut model was composed of isotropic 8-noded hexahedral elements, assumed linear elastic, assigned properties for trabecular metastatic bone at 3 weeks post-inoculation (Young's modulus = 14.117 GPa, Poisson's ratio = 0.3, density = 1.138 g/cm^3) and a surrounding 'non-bone' region of minimal material properties (Young's modulus = 0.001Gpa, Poisson's ratio = 0.3, density = 0.001) to minimise edge effects (*Figure 5.2*A). The axial surface of the trabecular strut was fixed in all directions, while the opposing face was applied a controlled displacement in the longitudinal direction (*Figure 5.2*B). The model was first applied a low strain (25με) and the C_1^R constant adjusted until bone tissue resorption lead to a density decrease from 1.138 g/cm^3 to 1.128 g/cm^3 over 21 increments, which was defined on the basis of the average change in bone mineral density (M_{mean}) measured in the proximal femur trabecular region of metastatic animals between 3 and 6 weeks post-inoculation (see Chapter 3) (*Figure 5.2*D). The model was then assigned a high strain (1250με) and C_1^F adjusted until density increased from 1.123 g/cm^3 to 1.178 g/cm^3 to reflect healthy trabecular bone which had increased in mineralisation from 3 weeks and 6 weeks in the same study (Chapter 3). The resulting values were determined to be C_1^R = 160 and C_1^F = 1.79.

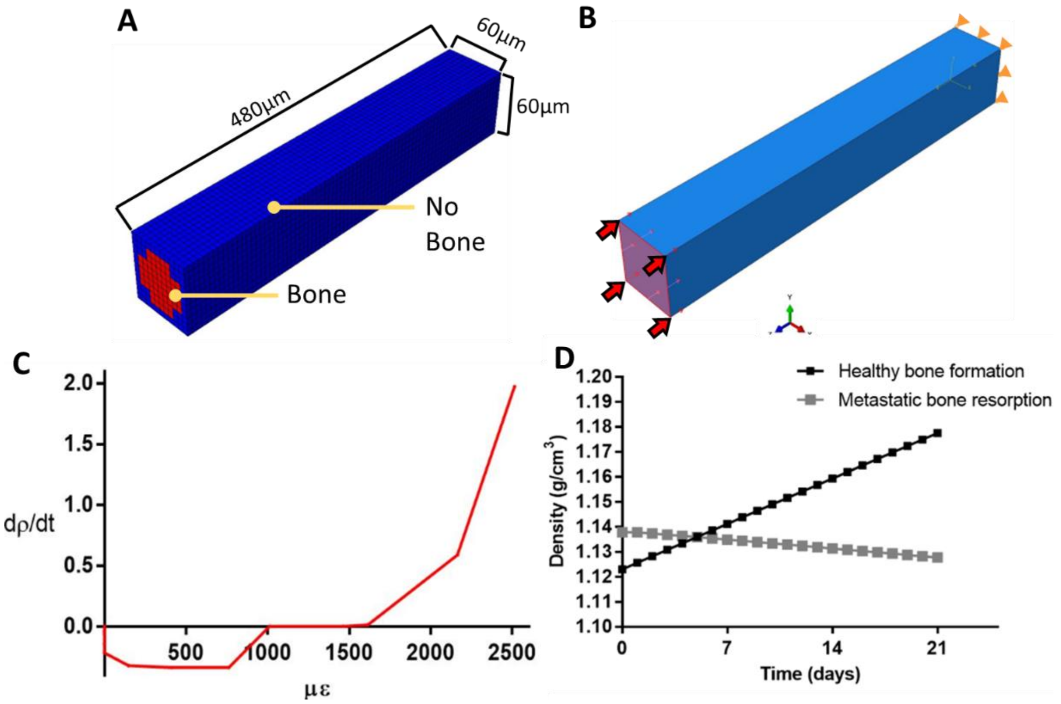

Figure 5.2: Trabecular model. A) Dimensions and B) boundary conditions applied to the simplified model of a trabecular strut used to C) demonstrate changes in density at different mechanical strain thresholds in accordance with mechanoregulation theory and predict the D) Density in simulated in healthy and metasetatic bone materials, such that C_1^R constant and C_1^F constants, respectively, change these densities at rates previously reported in proximal femur trabecular bone (Verbruggen et al., 2022).

The above method and resulting value of $C_1^R = 160$ did not capture bone tissue resorption reported in a prior study (see Chapter 3) (Verbruggen et al., 2022). Thus, a parameter variation analysis of C_1^R was performed and qualitative analysis of the models at different C_1^R values was conducted (Figure 5.3), which revealed that a C_1^R value of 1.6×10^3 predicts bone resorption within the greater trochanter regions. Constant values higher than 1.6×10^3 inaccurately predict the majority of the proximal femur model to be resorbed (Figure 5.3). Importantly, overt osteolytic degradation in the greater trochanter region was reported in Chapter 3, in proximal femurs at 6 weeks post-inoculation. Therefore, $C_1^R = 1.6 \times 10^3$ was applied in the remodelling algorithm for all models in this study as this is more representative of *in vivo* outcomes.

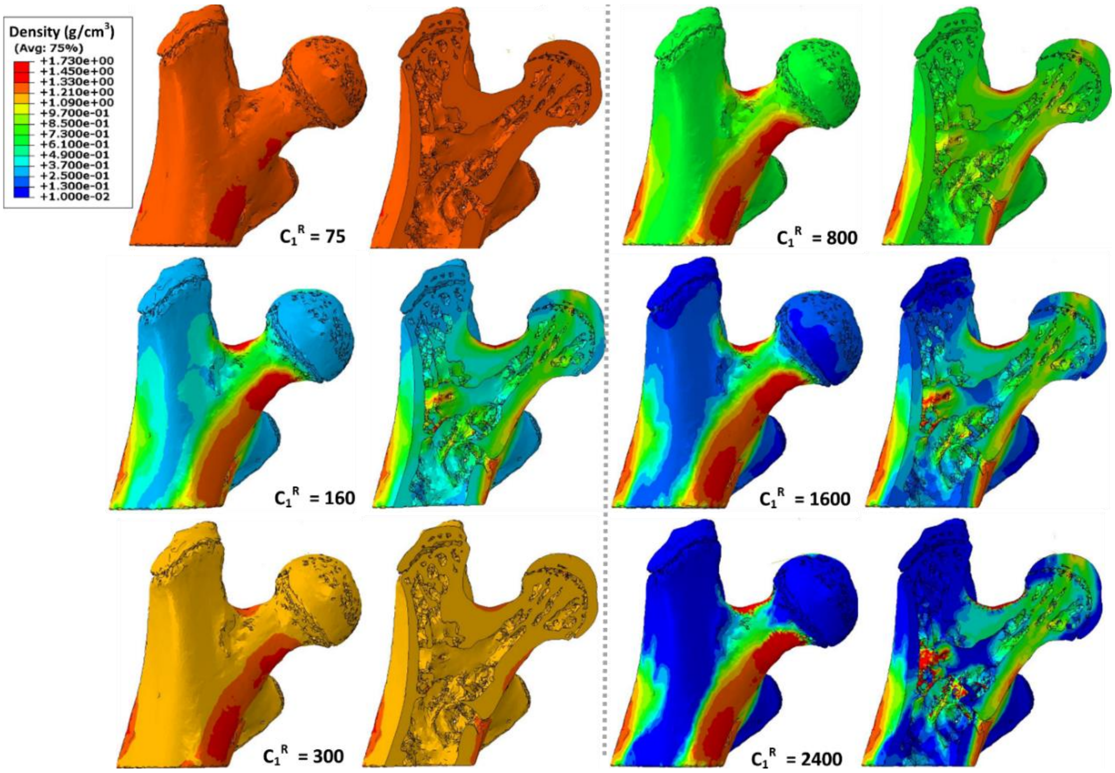

Figure 5.3: C1 parameter variation assessment. Bone mineral density distribution in one metastatic model where multiple values for the resorption constant (C_1^R) have been applied.

An upper strain threshold, beyond which murine bone tissue undergoes formation, is commonly reported to be approximately 1000με (Turner et al., 1994, De Souza et al., 2005, Razi et al., 2015) and applied to the remodelling algorithm for this study. In contrast, a wide variety of resorption threshold values have been theorised, ranging from 27.9 - 250με (Frost, 1987, Geraldes and Phillips, 2014, Cheong et al., 2020a). Considering this range of thresholds, a parameter variation study (Supplementary Figure 5.1B) was conducted and, on this basis an interim value of 100με was chosen for this model, below which bone resorption would occur.

5.2.4 FE model analysis:

This study sought to predict osteolysis in response to changes in the mechanical environment of metastatic bone, using finite element analysis (FEA) and mechanoregulation theory, and compare these to findings from previous experimental and computational studies. Qualitative analysis of the distribution of bone tissue density and SED throughout the proximal femur was performed. In terms of quantitative analysis, maximum principal strain distribution was assessed, along with mean Von Mises stress, maximum principal strain and SED in these models. Density resorption was also analysed quantitatively, by calculating the percentage volume of each model which underwent a notable decrease throughout the remodelling process. This threshold of considerable density decrease was chosen as 0.1 g/cm^3, an interim value between mean model density (1.262 ± 0.02 g/cm^3) and complete resorption (0.01 g/cm^3), whereby elements with a value below this threshold have reduced in density by over 90%. All metastatic proximal femur models predicted by the bone remodelling algorithm were compared to results analysed in chapter 3 and chapter 4; the subscript ***m*** describes results from homogeneous FE models with applied mechanoregulation theory (i.e. findings from the current chapter 5), while subscript ***s*** denotes the metastatic (MET) heterogeneous FE models imaged separately at 3 weeks and at 6 weeks post-inoculation (Chapter 4). In this way, MET$_s$ models present the mechanical environment of bone tissue at two time points of the study and can serve as a direct comparison for the 3-week and 6-week time points predicted by the bone remodelling algorithm as predicted my mechanoregulation theory (MET$_m$).

5.2.5 Statistical Analysis

Statistical analyses were performed using MiniTab (version 17) software. Each parameter was assessed for equal variance (F test) and student t-tests were implemented to determine whether averaged data was statistically significant between groups of equal variances. Welsh's test was applied where sample groups had unequal variance. Results are displayed as mean ± standard deviation, with significance defined as a p value of < 0.05, and further significance also identified ($p<0.01$, $p<0.001$). Error bars in all bar charts represent standard deviation.

5.3 Results

5.3.1 *Predicted density changes in metastatic proximal femurs from 3 to 6 weeks*

The bone remodelling algorithm was applied to each model and qualitatively assessed for changes in SED and bone mineral density distributions, beginning prior to the first increment ('3 weeks'), and at every 7 increments of the algorithm to the final time point ('6 weeks') (see Figure 5.4, Figure 5.5). At this 6 week timepoint, the models had not reached homeostasis. The models consistently predicted that SED was highest within the cortical bone tissue of the femoral neck and at the loaded surface of the femoral head in all models upon phsyiological loading (Figure 5.4). Interestingly, by

6 weeks application of the bone remodelling algorithm predicted that bone mineral density distributions became elevated in these same regions.(Figure 5.5). This demonstrates that the bone remodelling algorithm has succeeded in incrementally driving changes in bone density throughout the model meshes.

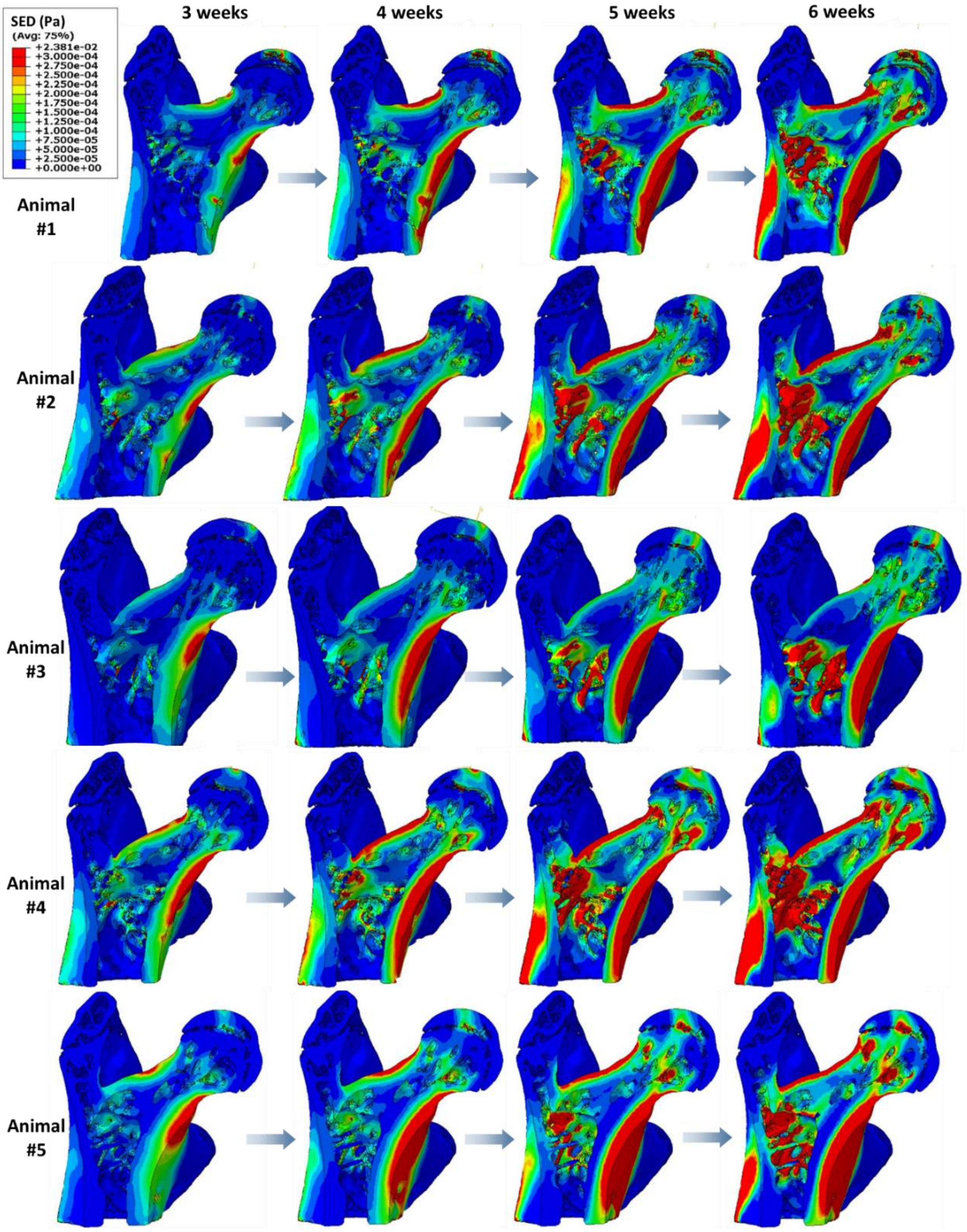

Figure 5.4: Predicted change in strain energy density distributions from 3 to 6 weeks. Anterior-posterior cross-section views of distributions of SED (Pa) at 3, 4, 5, and 6 weeks of metastasis according to mechanoregulation theory in computational models of proximal femurs.

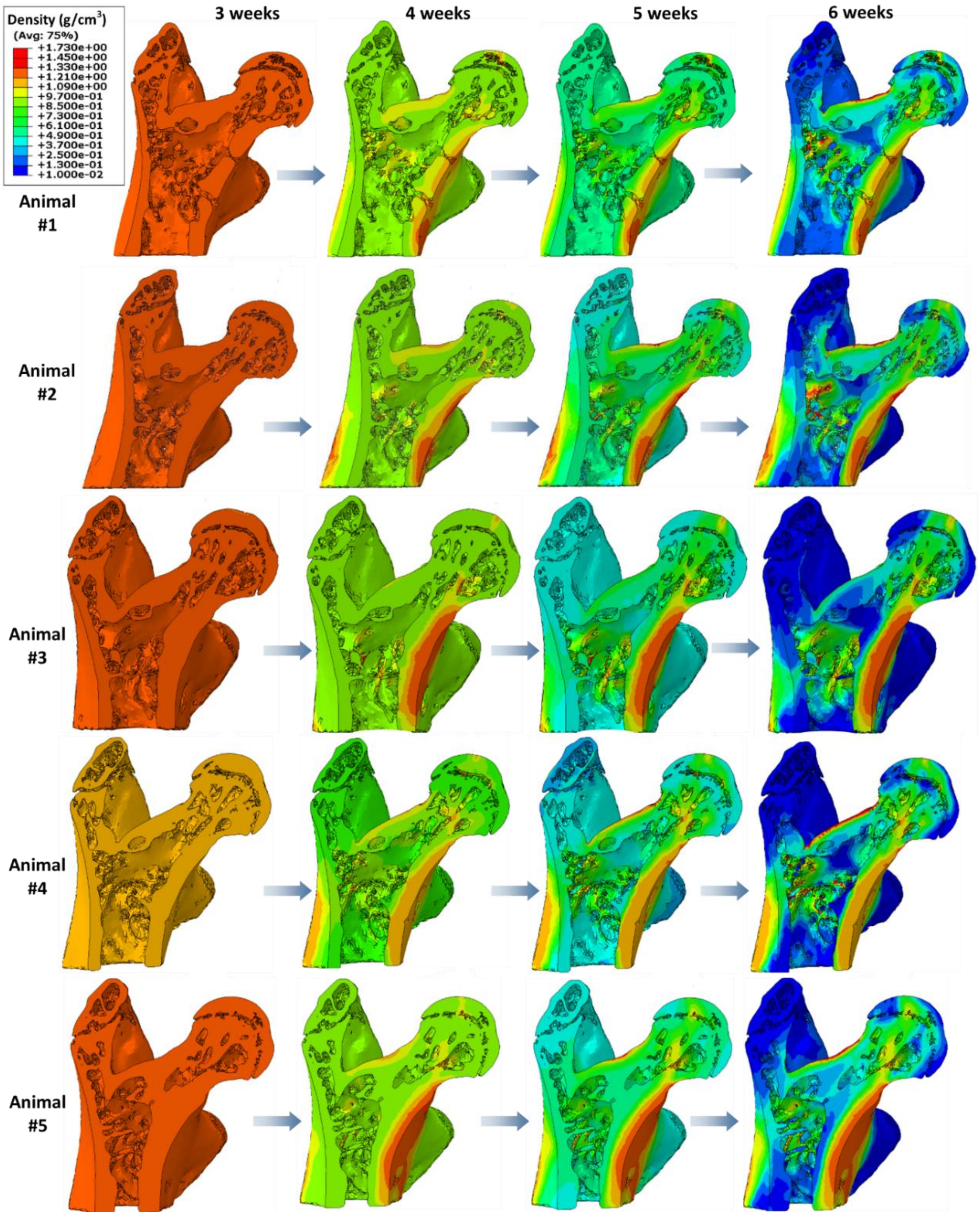

Figure 5.5: Predicted change in bone mineral density from 3 to 6 weeks. Anterior-posterior cross-section views of bone resorption at 3, 4, 5, and 6 weeks of metastasis of metastasis according to mechanoregulation theory in computational models of proximal femurs.

5.3.2 *Predicted strain distributions upon mechanoregulation between 3 and 6 weeks of metastasis*

The homogeneous µCT-FE models of this study were compared to previously reported heterogeneous models, which had been µCT scanned at both 3- and 6-weeks post-inoculation and analysed under identical boundary conditions at these single time points (3wk METs, 6wk METs). Quantitative analysis of strain distributions within the models (Figure 5.6A) show this method has succeeded in demonstrating increased strain distribution (i.e., positive skew) as bone tissue is resorbed. This increase was significant in all ranges up to 250με, with the greatest difference in the 0 – 50με range (3wk MET$_m$: 88.33 ± 3.96%, 6wk MET$_m$: 23.86 ± 3.96%, $p<0.001$). Mean values of maximum principal strain and SED had increased significantly in both the MET$_s$ and MET$_m$ models between the two time points in question (Figure 5.6D). Interestingly, Von Mises stress were predicted to decrease in the MET$_s$ models (6wk MET$_s$: 0.66 ± 0.06 vs. 6wk MET$_s$: 0.84 ± 0.1, $p<0.05$), while the algorithm predicted stress to increase over this time period (3wk MET$_m$: 0.718 ± 0.05 vs. 6wk MET$_m$: 0.60 ± 0.38, $p<0.05$).

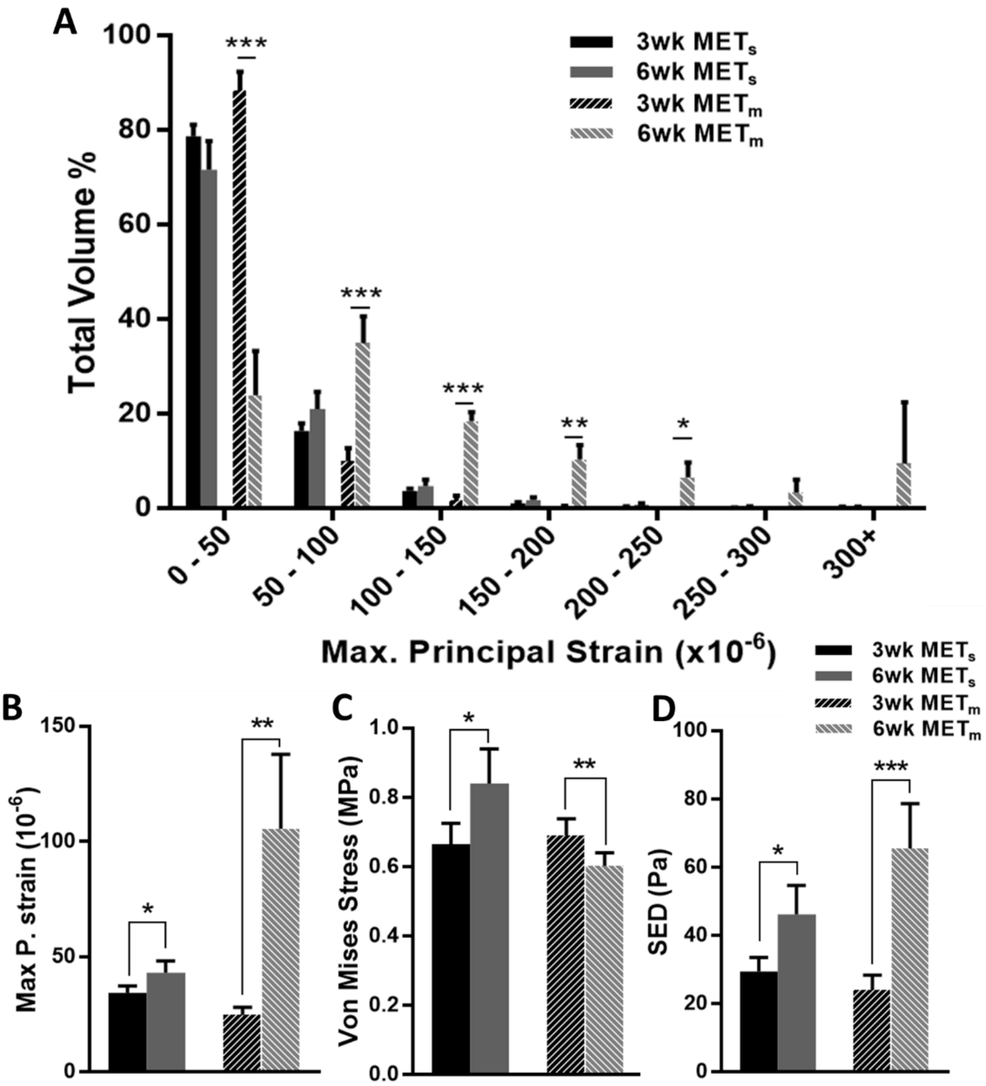

Figure 5.6: Changes in stress and strain distributions compared to a previous study. Heterogeneous FE proximal femur models from a previous study at 3 and 6

weeks post-inoculation, loaded and analysed at a single time point, (3wk MET$_s$, 6wk MET$_s$) were compared to bone remodelling algorithm simulations of these same models with homogeneous material properties, at the 1st and 21st increments (3wk MET$_m$, 6wk MET$_m$). (A) Distribution of maximum principal strain as a percentage of bone volume, including inset of higher microstrain ranges (150-200με to 300με+), *p<0.05, **p<0.01, p***<0.001.

By the 6-week timepoint of application of the remodelling algorithm predicted that 26.51 ± 9.96% of the model volume decreased below a bone mineral density of 0.1 g/cm^3. Interestingly, bone volume in the trabecular regions of proximal femurs reported from prior micro-CT analysis had decreased by 21.15% between 3 weeks and 6 weeks post-inoculation of metastatic breast cancer cells (see Chapter 3). In addition, the area of lowest density in each model consistently presented in the greater and lesser trochanter regions, as is illustrated in the anterior-posterior cross-sectional views of cortical and trabecular bone (Figure 5.7A). This correlates with Chapter 3, in which osteolysis was reported in the greater trochanter regions by 6 weeks post-inoculation (Figure 5.7B, 5C). Density was highest in the cortical bone tissues of the femoral neck and the inter-trochanter space (Figure 5.7A).

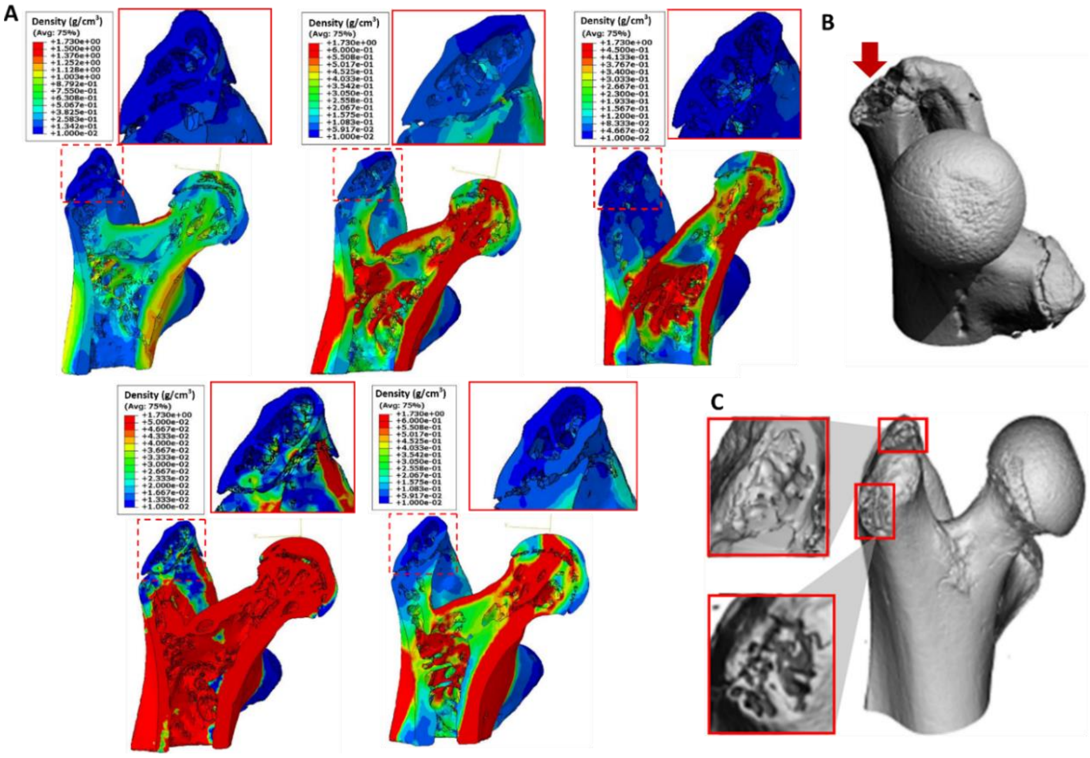

Figure 5.7: Density decreasing in the trochanter regions. A) Anterior-posterior cross-section views of bone mineral density in each metastatic model (n=5), where distribution limits were adjusted in each model for visualisation of low density regions. Inset: Greater trochanter regions, which consistently present resorption at 6 weeks (B, C) 3D reconstructions of µCT images where overt osteolysis was detected

in the greater trochanter (in red), previously reported at 6 weeks post-inoculation (Verbruggen et al., 2022).

5.4 Discussion

This study is the first to implement mechanoregulation theory in combination with FE models of bone tissue from an animal model of bone metastasis. This study aimed to test the hypothesis that changes in the physical environment of bone tissue may elicit mechanobiological cues for resident bone cells during metastasis, and investigate how these responses may contribute to later osteolytic destruction. By implementing mechanoregulation theory, the bone remodelling algorithm predicted that bone mineral density would decrease in the same regions as were reported to develop osteolytic lesions from previously published experimental results. These models also demonstrated a significant increase in mechanical strain distribution within the bone tissue microenvironment, which arises upon the continuous adaption of bone tissue density and Young's modulus throughout the proximal femur region.

Some limitations and assumptions in this study must be considered. Firstly, models in the current study were meshed with 4-noded tetrahedral elements, which could generate unnecessary stiffness compared to 10-noded tetrahedral elements. However, a study which compared 4- and 10-noded tetrahedral meshes in a human proximal femur FE model under compression reported no significant differences in their output stress, strain or overall accuracy compared to experimental results (Ramos and Simoes, 2006). Secondly, the bone tissue was assumed to be a linear elastic material, which ignores bone poroelasticity and the potential for plastic deformation. However, linear elasticity is a standard assumption in µCT-FE models implementing mechanoregulation theory (Schulte et al., 2013, Cheong et al., 2020a, Cheong et al., 2020b). Thirdly, at the initial stage the material properties were assumed homogeneous, whereas bone tissue is heterogeneous and the previous study (Chapter 4) utilised a heterogeneous mesh of 100 uniformly distributed material properties. During model development a combined UMAT and USDFLD subroutine was investigated to predict bone remodelling within a heterogeneous model. However, large boundary discrepancies between neighbouring elements of differing properties and stress concentrations lead to challenges solving the models. Fourthly, the same remodelling rate constant (C_1) was implemented in the bone remodelling algorithm for the whole (cortical and trabecular), whereas the previous study revealed differences between these regions in terms of bone adaptation. Manual delineation of cortical and trabecular bone tissue regions could be conducted to implement separate C_1 constants for cortical and trabecular bone, but separating these regions as individual parts prior to importing into Abaqus would introduce complex surface interactions not reflective of *in vivo* conditions. In addition, while the current FE models have captured peak loading during murine locomotion, and therefore the greatest instance of mechanical stress and strain in the most common physiological loading condition, variations in loading angle and magnitude during each step cycle (Charles et al., 2018) were not captured and therefore the complete stress state of the model may not be simulated.. Future models incorporating these variations could reveal whether boundary conditions within the current study influence predicted regions of bone tissue resorption. Despite the prominent involvement of growth factors in the progression of metastasis, the current study did into incorporate biochemical signalling, focusing on the mechanobiological aspect of metastatic invasion. An explicit cell model could be integrated, such that biochemical signaling would influence cell behavior at the local level. This was previously demonstrated in an FE model predicting osteoblast and osteoclast populations according to autocrine and paracrine signaling, respectively, driven by SED and fatigue damage stimuli (Hambli, 2014) and in a later model which adjusted bone tissue resorption and formation rates according to experimental *in vivo* measurements (Cheong et al., 2020a). The threshold for tissue formation was assigned at 1000με and no sensitivity analysis was performed on the formation rate, C_1^R. However, the average percentage volume which exceeded the upper threshold of 1000με for bone formation in these models was negligibly low (<0.001%), therefore the study was not considered sensitive to these parameters. A parameter variation analysis showed differences in strain distribution between models of varied resorption thresholds (see Supplementary Figure 5.1B). However, given the large differences in all outputs between week 3 and week 6 of the study, changes in this parameter were deemed unlikely to affect results. Finally, changes in stress and strain distribution in the current models were validated by comparing results to FE models from Chapter 4, however inter-comparability between *in silico* models is a limited form of validation. While osteolytic regions predicted by mechanoregulation theory coincides with regions of osteolysis from experimental study (Chapter 3) further validation of stress and strain distributions should be conducted, perhaps in the form of direct strain gauge measurements at the regions of interest or more precisely via longitudinal Digital Volume Correlation (DVC) analysis (Palanca et al., 2022).

In this study, mechanoregulation theory was first applied to a simplified trabecular strut model. This model successfully demonstrated bone resorption and formation upon changes in the strain energy density to reflect the criteria described in Frost's Mechanostat theory (1987) (Figure 5.2C). The resorption constant value which governed the rate of change of density upon remodelling was analysed both qualitatively and quantitatively (see Supplementary Figure 5.1). A parameter variation study was conducted to establish a resorption constant that reflects the degree of bone loss observed in experimental findings, and which had predicted approximately 27% of the model volumes would reduce to low bone tissue stiffness, reflective of bone volume fraction reductions in the trabecular space as seen in Chapter 3. At approximately 2N of load on the femoral head surface, the predicted bone tissue resorption is more prominent within these models than bone tissue formation. This finding correlates well with similar studies of female C57BL/6 murine tibiae, which found cyclical compressive loads between 10N and 13N over a 2 week period (producing 1150με to 2000 με) (De Souza et al., 2005), *in vivo* µCT analysis of female C57BL6/J murine tibiae under 12N of cyclical axial compression (Cheong et al., 2021), or 9N loads at 360 loads/day and 3 days per week over 4 weeks (Weatherholt et al., 2013) were sufficient for bone tissue formation. Both studies investigated load values as low as 5N and deemed this insufficient for significantly increased cortical or trabecular bone morphology (De Souza et al., 2005, Weatherholt et al., 2013).

Physiological loads were applied to geometrically accurate proximal femur models and a bone remodelling algorithm introduced to the model mesh to predict element-specific mechanoregulatory changes over 21 days according to mechanical stimuli. Qualitative analysis revealed that the lowest bone mineral density values were predicted to occur in the greater and lesser trochanter of the femurs. Interestingly, a separate cohort of proximal femurs scanned at 6 weeks after tumour-inoculation consistently produced overt osteolytic lesions in the greater trochanter region (see Chapter 3). Thus, the application of the mechanoregulation theory has accurately predicted the spatial nature of bone resorption within the proximal femur that correspond to previously reported bone resorption in these same femurs. Interestingly, a study that applied a bone remodelling algorithm to investigate adaptation in a healthy human proximal femur over 5 years of physiological loads predicted that density was lowest in the femoral trochanter (Hambli, 2014). Notably, a study which inoculated female BALB/c with breast cancer cells found metastatic cells had migrated to the proximal tibia growth plates within 5 days of injection, and that the majority of tumours developed in these highly vascularised regions where haematopoietic stems cells also reside (Allocca et al., 2019). Such an active remodelling site would therefore provide an suitable environment for active biochemical signalling and therefore contribute to metastatic invasion (Kakinuma and Hwang, 2006). In this way, the presence of a highly vascularised growth plate region which is in close proximity to the primary tumour, and is minimally loaded (Charles et al., 2018), may provide an explanation for such extensive bone tissue resorption in the specific area of the greater trochanter within the proximal femur.

In the current study, bone mineral density was predicted to be highest along the femoral neck region and femoral head surface, which corresponds to previously reported CT-imaged and DXA-imaged density maps of a healthy human proximal femur under stance and side-loading configurations (Dall'Ara et al., 2016). Notably, strain distributions had similarly been found to increase along this cortical bone region of the femoral neck in a human osteoporotic femur which had undergone trabecular thinning (Verhulp et al., 2008). Interestingly, femoral head regions were reported absent in 3 of 7 metastatic proximal femur scans from micro-CT analysis during experimental analysis (see Chapter 3). FE analysis from the current study suggests such absences may be due to fracture failure along the femoral neck, where Von Mises stresses and maximum principal strains are highest and continue to increase as metastasis progresses. Overall, application of mechanoregulation theory in the FE models of metastatic bone tissue at 3 weeks, demonstrated the spatial nature of resorption by 6 weeks that correlated to the experimental findings. Therefore, this study supports the theory that mechanoregulation may play a role in contributing to the osteolytic destruction which occurs at the later time point of bone metastasis.

Upon application of mechanoregulation theory, homogeneous FE models predicted mechanical strain distribution, principal strain and SED to increase significantly from 3 to 6 weeks, corresponding to outcomes from single time-point predictions of heterogeneous models at 3 weeks and 6 weeks post-inoculation from a prior computational study (Chapter 4). This further validates the application of mechanoregulation theory to predict changes in the mechanical environment of bone tissue during breast cancer metastasis. However, Von Mises stress was predicted to decrease in the algorithm-governed models, contradicting the prior FE study which had predicted this parameter would significantly increase (Chapter 4). One explanation for these differences is the potential disparity between homogeneous and heterogeneous FE models in analysing altered mechanical stress. Indeed, a published study which compared µCT-FE models of BALB/c murine tibiae found heterogeneity to be less accurate in predicting model failure loads and stiffness under physiological loads compared to homogeneous models (Oliviero et al., 2021), and therefore decreased Von Mises stress may be a more accurate prediction of changes within the bone extracellular matrix. Alternatively, the differences observed in stress predictions may be due to morphology, as the 3-week and 6-week proximal femur models were imaged using *in vitro* micro-CT analysis and were taken from two separate cohorts, while models in the current study involve incremental changes within the same proximal femur geometries. However, morphology does not affect any other output parameters, which are consistent between analysed groups. A third explanation is the accelerated behaviour of the bone remodelling algorithm, which may have reached mechanoregulatory equilibrium at a faster rate than occurred *in vivo* and therefore stress within the bone tissue microenvironment is reduced as the model converges to a more mechano-regulated state. This is supported by additional analysis of these same FE models utilising a lower remodelling constant, i.e., they had undergone a slower mechanoregulation process (Supplementary Figure 5.2). Although not significant, these results show a subtle trend toward increased, rather than decreased Von Mises stress at the applied slower resorption rate.

In conclusion, this study is the first of its kind to predict, using mechanoregulation theory, bone remodelling in µCT-derived finite element models of metastatic bone tissue, prior to the development of overt osteolytic lesions. The bone remodelling algorithm predicted bone mineral density to decrease in regions which coincide with previously reported osteolysis. This study also found changes in strain distribution from 3 weeks to 6 weeks, which trended similarly to those previously reported from FE models of femurs at 3 weeks and 6 weeks post-inoculation of metastatic cells.

Findings indicate that mechanobiology may play a role in the adaption of the bone tissue extracellular matrix to metastasis and contribute to the later development of osteolysis.

5.5 Supplementary Figures:

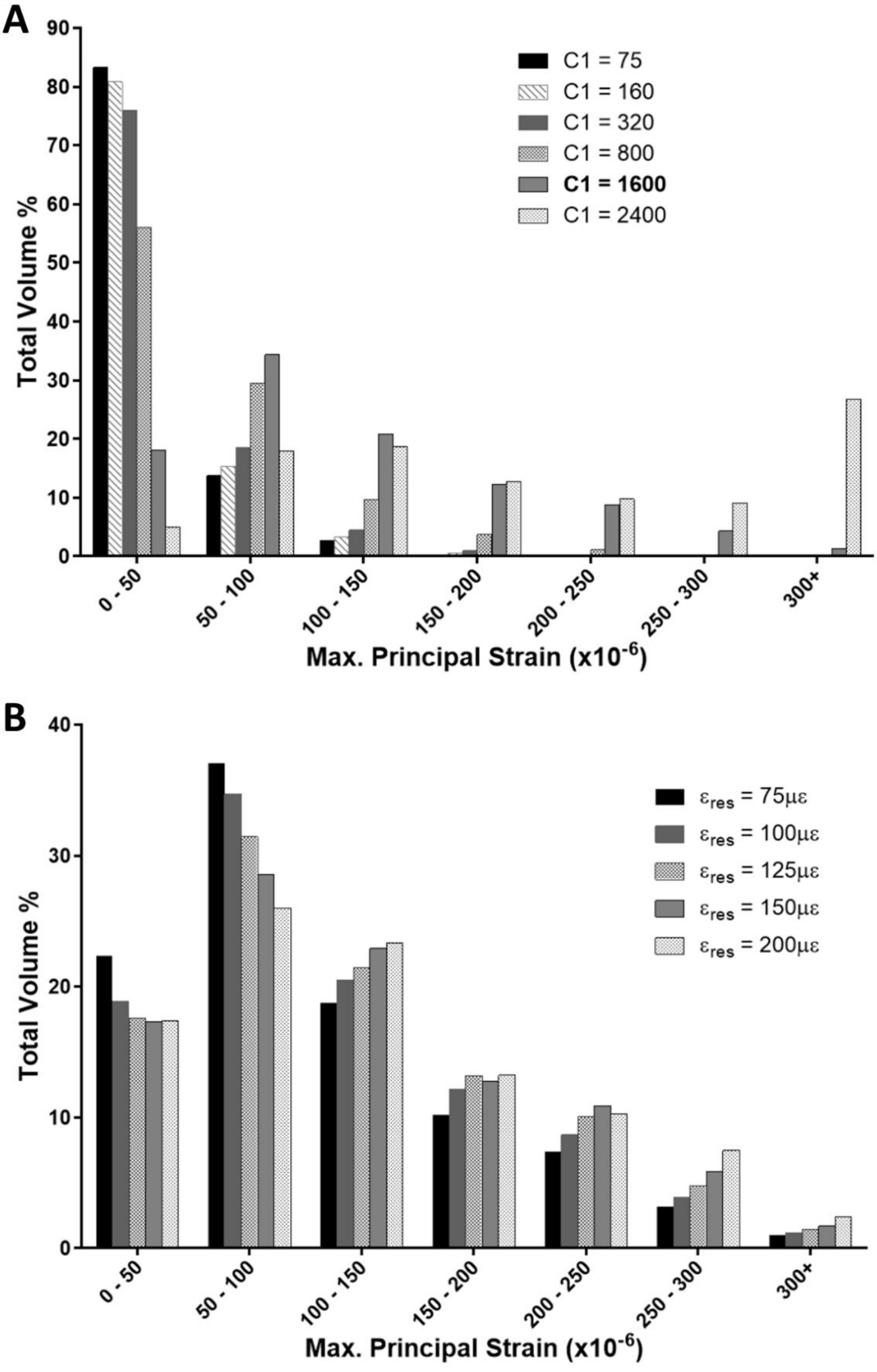

Supplementary Figure 5.1: Parameter sensitivity analyses. Distribution of maximum principal strain as a percentage of bone volume in one metastatic proximal femur model, predicted at 6 weeks, comparing between values of (A) bone tissue resorption constant, C_1, and (B) resorption threshold strain value (ε_{res}) applied to one proximal femur model. The greatest difference in percentage volume for altered ε_{res} was between 75 and 200με in the 50-100 range, at 11.09%.

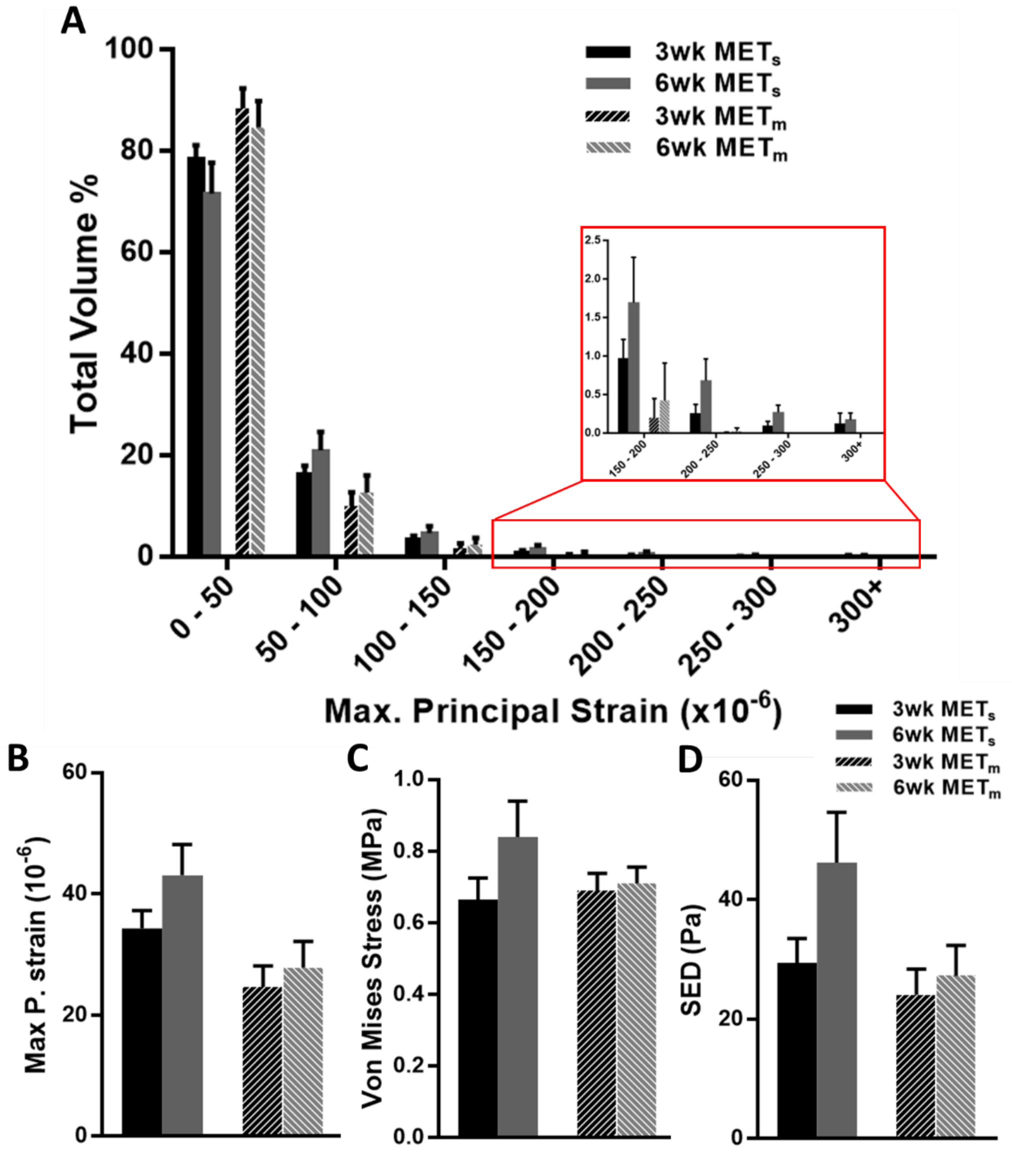

Supplementary Figure 5.2: Predicted changes in bone tissue strain at 3 and 6-week time points compared to bone remodelling algorithm predictions, where C1 is 160. Heterogeneous FE proximal femur models from a previous study at 3 and 6 weeks post-inoculation, loaded and analysed at a single time point, (3wk MET_s, 6wk MET_s) were compared to bone remodelling algorithm simulations of these same models with homogeneous material properties, at the 1st and 21st increments (3wk MET_m, 6wk MET_m). (A) Distribution of maximum principal strain as a percentage of bone volume, including inset of higher microstrain ranges (150-200με to 300με+).

Chapter 6: Discussion

6.1 Introduction

This chapter summarises the main findings of this thesis, drawing together insights gained from micro-CT analysis, nanoindentation, mechanical testing, finite element analysis of bone tissue under physiological loads and predictions of mechanoregulatory response in bone tissue to changes within the mechanical environment upon metastatic invasion by breast cancer. Collectively, these analyses have shed light on temporal and spatial changes in bone mechanical properties during breast cancer metastatic invasion, and how such changes may alter the mechanical environment within the bone tissue and elicit mechano-sensitive bone cellular responses in contribution to the cancer vicious cycle. The results of the individual chapters of this thesis are summarised in section 6.2 and graphically represented in section 6.3. The relationship between the individual chapters of this thesis and previous relevant publications are graphically represented and discussed in more detail in section 6.3. Finally in section 6.4, recommendations for further work and future perspectives in the field are discussed.

6.2 Main Findings of the Thesis

The research described in this thesis has focused on deriving an advanced understanding of changes in bone mineral content and mechanical properties, and the mechanical environment of bone cells, prior to and following osteolytic destruction. In particular, the results from this study determined how the bone extracellular matrix is physically altered during metastatic invasion, at two distinct time points and predicted how these changes may drive mechanoregulatory responses. Bone tissue from a pre-clinical animal model, designed to recapitulate the *in vivo* metastatic process, was analysed via micro-CT imaging and nanoindentation to determine changes in the bone mineral content and mechanical properties. Finite element analysis was conducted on 3D reconstructions of tumour-bearing femur micro-CT scans, which sought to determine how changes in the bone tissue microarchitecture could influence the mechanoregulatory responses of resident bone cells and thereby effect the bone metastatic process. Finally, a bone remodelling algorithm was applied to investigate whether mechanobiological cues might drive osteolytic bone loss during metastatic progression. Collectively, these studies provide a key insight into early changes in the bone tissue mechanical environment during metastasis and osteolysis, and highlights the importance of mechanobiology and mechanoregulation processes in bone tissue during the cancer vicious cycle. The key contributions with respect to each hypothesis are summarised below.

Hypothesis 1: Bone mineral content and mechanical properties are altered during breast cancer bone metastasis

The first study, presented in Chapter 3 of this thesis, revealed that bone mineral density, bone tissue thickness and stiffness were significantly altered at both 3 weeks and 6 weeks following the inoculation of breast cancer cells into the mammary fat pad of a murine pre-clinical model. Furthermore, this study revealed the spatial nature of such changes, whereby bone mineralisation increased throughout the proximal and distal cortical and trabecular bone regions at 3 weeks, while osteolytic lesions were present in the greater trochanter regions of all femurs in the 6-week cohort. Together, the above findings provide evidence in support of **hypothesis 1**. In addition, bone tissue stiffness in the proximal femur trabeculae had decreased in the ipsilateral femurs compared to contralateral and control sites. Overall, these findings revealed changes in bone tissue composition prior to and following overt metastatic osteolysis, local and distant from the primary tumour site. These changes were proposed to alter the mechanical environment of both the bone and tumour cells, and thereby play a role in perpetuating the cancer vicious cycle during breast cancer metastasis to bone tissue.

Hypothesis 2: Mechanical stimuli within the bone tissue microenvironment are altered during breast cancer bone metastasis and osteolysis

The second study, presented in Chapter 4, provides an insight into changes in the bone tissue microenvironment during metastasis, by developing µCT derived FE models of metastatic mouse femurs and performing detailed temporal and spatial qualitative and quantitative analysis of these changes at two distinct time points of metastasis. It was reported here that in early metastasis, prior to extensive osteolytic destruction (3 weeks after tumour inoculation), there was a decrease in strain distribution within the distal cortical bone tissue, where tissue thickening had been previously reported, and in proximal femur trabecular bone tissue. On this basis, it was proposed that the reduced mechanical properties within this environment at an early time-point activates further resorption and drives the extensive osteolysis evident at later stage metastasis. Therefore, this second study provides evidence in support of **hypothesis 2**.

Hypothesis 3: Changes in mechanical strain of bone tissue during metastasis may drive bone cell activity and subsequent bone tissue resorption, thereby contributing to osteolysis and the cancer vicious cycle

The third study of this thesis, presented in Chapter 5, sought to apply mechanoregulation theory to investigate whether mechanobiological cues might drive osteolytic bone loss during metastatic progression, building upon the predictions of changes in mechanical stimuli reported in Chapter 4. Implementation of mechanoregulation theory in metastatic models at week 3 successfully predicted bone loss by week 6. Interestingly, bone loss was predicted to be substantial in the greater trochanter region, which directly coincides with findings from Chapter 3, where overt osteolytic lesions were observed in the greater trochanter by 6 weeks post-inoculation. Thus, the bone remodelling algorithm predicted bone tissue resorption, which may contribute to the perpetuation of the cancer vicious cycle and therefore supports **hypothesis 3.** Increased strain distribution, strain energy density and maximum principal strain over the simulated 21-day period reported in this study also reflect changes observed in FE models of Chapter 4. Chapter 5 has thus provided an enhanced understanding of the contributions of mechanobiology to resident bone remodelling behaviour within the extracellular matrix during early metastasis.

6.3 Insight into the Role of Mechanobiology Prior to Osteolysis

The findings of this thesis provide an advanced understanding of the temporal and spatial nature of bone mineralisation, mechanical properties, and the mechanical environment within murine femoral bone tissue during bone metastasis. A seminal theory on breast cancer bone metastasis, Paget’s Theory (1889), stated that breast cancer cells (‘seed’) had a precise affinity to bone tissue (‘soil’) for invasion, and it was theorised the physical properties of bone facilitated this attraction. The ‘Vicious Cycle’, describes how osteolytic growth factors released by invading cancer cells induce excess bone tissue resorption by resident osteoclasts, in turn releasing stored growth factors from the resorbed bone tissue to trigger further tumour cell proliferation, thereby continuing the cycle in perpetuity (Guise and Mundy, 1998). A pre-clinical animal model was developed to consistently demonstrate breast cancer metastasis in bone tissue for analysis of the effects of the vicious cycle, and found breast cancer cells had metastasised to the trabecular niche of proximal femurs by 19 days post-inoculation (Lelekakis et al., 1999). Much research had also been conducted into the biochemical factors, such as growth factors (VEGF, IGF, BMPs, TGF-β) and chemokines (CXCL1-3 and CXCL8), released from invading breast cancer cells, concluding these factors play a major role in encouraging bone tissue resorption during osteolytic metastasis (Kakinuma and Hwang, 2006, Langley and Fidler, 2007, Chen et al., 2010). Studies of human osteolytic bone tissue revealed that these regions demonstrated a decrease in bone mineral content and mechanical properties (Kaneko et al., 2003, Nazarian et al., 2008), which was later corroborated with animal studies of metastatic bone tissue (Arrington et al., 2006, Arrington et al., 2008, Mann et al., 2008, Burke et al., 2018). Finite element (FE) models of simulated (Keyak et al., 2005, Anez-Bustillos et al., 2014, Benca et al., 2017, Salvatore et al., 2018, Palanca et al., 2021b) and CT-imaged osteolytic lesions (Costa et al., 2019, Eggermont et al., 2020, Sas et al., 2020, Sas et al., 2022) have been developed and analysed, with the primary objective of accurately predicting fracture failure. Most notably, a study of a µCT-FE model of human vertebrae reported increased osteolytic lesion size significantly reduced tissue stiffness and principal strain in local bone tissues (Costa et al., 2020). While the above studies have provided vital insight into the impact of osteolytic lesion formation on the bone tissue mechanical environment, how this environment evolves prior to established lesion formation is not yet fully understood.

Recently it has been proposed that, prior to the cancer vicious cycle, targeted bone tissue is ‘primed’ by disseminated tumour cells (DTCs) by releasing growth factors (VEGF, Lysyl Oxidase) to increase mineralisation and thereby optimise the bone tissue microenvironment for metastatic invasion (Chiou et al., 2021). This theory was presented in light of increased bone tissue thickness and bone formation rates after 3 weeks in murine animal models that received daily intraperitoneal injections of tumour-cell conditioned media (Chiou et al., 2021). Considering the above studies, it was previously understood that osteolytic bone tissue has decreased in bone mineral content and mechanical properties as a consequence of the cancer vicious cycle. Metastatic cells have also previously been reported to migrate to highly vascularised growth plate regions (Allocca et al., 2019) as a niche site for biochemical signalling which could in turn contribute to later osteolysis (Kakinuma and Hwang, 2006). This finding, combined with the lack of physiological loading reported in the greater trochanter region of the proximal femur in mice (Charles et al., 2018) may mean this specific region is susceptible to osteolytic development, as low mechanical loading would reduce the potential for mechanical stimulation to inhibit metastatic progress as reported previously (Lynch et al., 2020). However, the specific changes that arise, and the temporal nature of such changes that occur within the bone tissue microenvironment, from initial metastatic cellular invasion to subsequent osteolytic destruction, remained unclear.

Research regarding the behaviour of bone tissue has provided some possible insight into the 'soil' response to changes within the bone microenvironment. Wolff's Law (1893) established that bone tissue morphology and function adapts to changes in external loads, while Frost's 'Mechanostat' Theory (1987) further elaborated that bone tissue undergoes resorption, acquiescence or formation, dependent on precise thresholds of strain stimuli. Prendergast et al. (1997) further theorised that mesenchymal stems cells alter their differentiation and expression within bone tissue in response to biophysical stimuli in an effort to maintain a regulated mechanical environment (mechanoregulation). Mechanical stimuli arising in the surrounding bone microenvironment, such as fluid shear stress, hydrostatic pressure or tissue strain, regulate proliferation, gene expression, protein synthesis, matrix production and apoptosis of the resident bone cells (Sikavitsas et al., 2001) and are crucial for organ homeostasis. Thus, the evolving mechanical environment during bone tissue metastasis and subsequent changes in the extracellular matrix may alter the behaviour of both bone remodelling cells and invading tumour cells. FE models, coupled with a bone remodelling algorithm, has been utilised to simulate bone mechanoregulatory responses to changes in strain stimuli, and were shown to predict bone tissue resorption, acquiescence and formation within these models (McNamara and Prendergast, 2007, Mulvihill et al., 2008, Schulte et al., 2013). The precise physiological loads and strain thresholds in the long bones of C57Bl/j6 mice has also been published, allowing for accurate *in vivo* simulations of murine model locomotion (De Souza et al., 2005). More recently, CT-derived FE models have been utilised to predict bone tissue adaption over time, according to strain stimuli in linear elastic models (Phillips et al., 2015, Badilatti et al., 2016, Cheong et al., 2020a, Cheong et al., 2020b), and in response to fluid velocity in a poroelastic model (Pereira et al., 2015). However, such an approach has not been applied to predict changes in the bone tissue microenvironment as metastatic invasion evolves. An *in vitro* study of breast cancer cells adherent to various substrate stiffnesses reported the expression of tumour-derived factors (TGF-β and PTHrP) had increased in correlation with increased matrix rigidity (Page et al., 2015). However, it has also been reported from *in vitro* and *in vivo* studies that mechanical stimulation of osteolytic breast cancer cells cause increased apoptosis, reduced migration and inhibited osteolytic progression (Lynch et al., 2013, Ma et al., 2018). In light of the above findings, there is some evidence that bone mechanobiological processes play a role in breast cancer cellular behaviour. However, the precise impact of mechanobiological cues on the bone cells for stimulating osteolytic bone resorption and facilitating metastatic invasion into bone tissue is not yet fully understood.

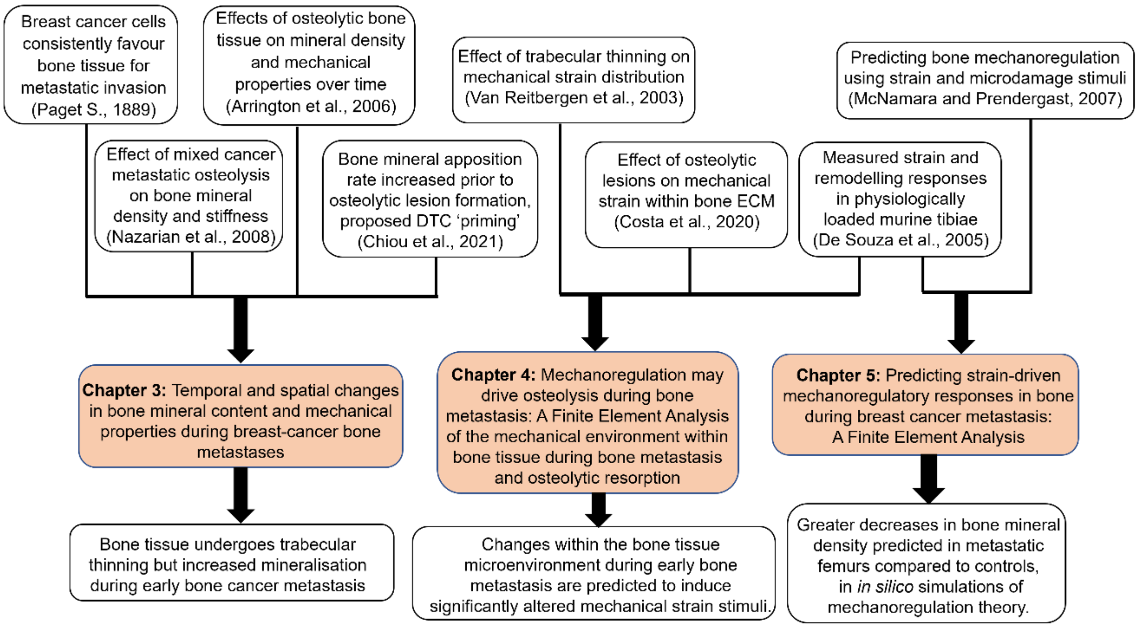

Figure 6.1: Flowchart of the work of this thesis in the context of previous studies.

Based on findings from this thesis, the author proposes an evolved sequence of events (Figure 6.2). The results from Chapter 3 revealed increased bone mineralisation and distal femur cortical thickening at the early stage of osteolysis (3 weeks post-inoculation). It has also been theorised that, prior to osteolysis, disseminated tumour cells 'prime' the bone tissue ECM via growth factors (VEGF, Lysyl Oxidase) to increase mineralisation and develop a more favourable microenvironment for metastatic invasion (Chiou et al., 2021). In light of the above, it is proposed that these arise due to either, or both, of two pathways a) mechanobiologically driven responses by osteocytes to the altered mechanical environment, following early osteolysis or b) bone niche ‘priming’ by factors produced by DTCs. Findings from Chapter 4 revealed that these early changes in bone tissue mineralisation were associated with decreased region-specific strain mechanical stimulation within the extracellular matrix. This reduced mechanical stimulation may drive osteocytes to upregulate osteoclastogenesis and thereby contribute to later osteolytic destruction. Indeed, findings from Chapter 5 further support this theory by demonstrating that application of a mechanoregulation theory successfully predicted decreased bone density in metastatic femurs over 21 days under physiological loading conditions.

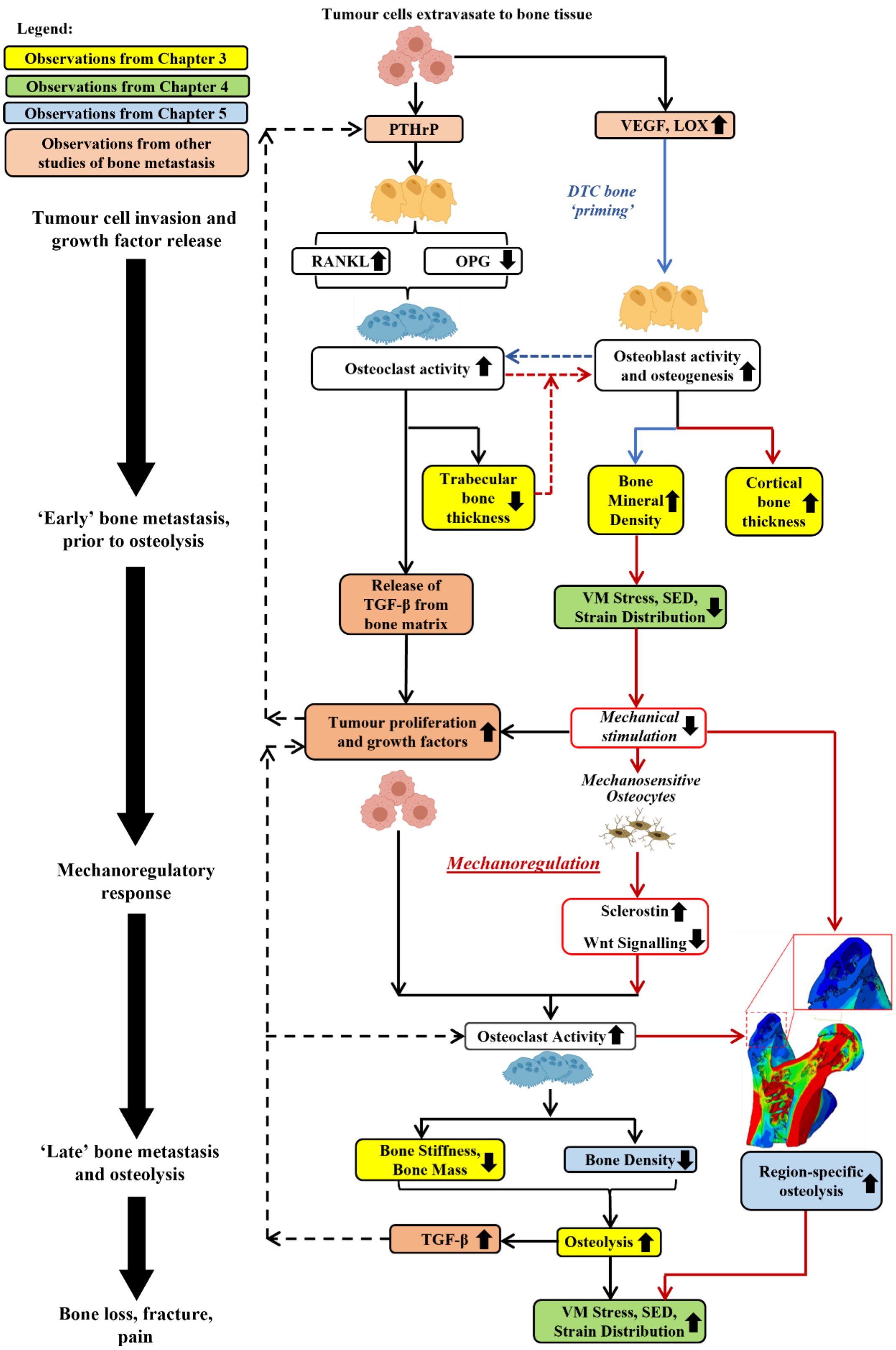

Figure 6.2: Flowchart depicting research from Chapters 3-5 in the context of a proposed theory of the timeline of events during breast cancer metastatic invasion of bone tissue, which leads to osteolysis. Blue arrows, influence of DTC 'priming' on bone ECM; red arrows, influence of mechanoregulation on bone remodelling; dashed lines, feedback mechanism.

6.4 Recommendation for Future Work

The studies provided in this thesis have provided insight into changes in the bone tissue mechanical environment of bone tissue prior to osteolytic metastasis, and how these changes may incite changes in bone cell mechanoregulatory responses during metastatic invasion. Based on the findings of this thesis, the following recommendations are made for future research.

6.4.1 Experimental analyses of the pre-clinical metastatic model

The first chapter of this thesis revealed changes in bone mineral content and mechanical properties in metastatic bone tissue prior to osteolytic destruction in a pre-clinical animal model. This analysis was conducted at two distinct time points, 3 weeks and 6 weeks following the inoculation of 4T1 breast cancer cells into the mammary fat pad, and produced distinct time points prior to and following osteolytic destruction. This metastatic model, first developed by (Lelekakis et al., 1999), is excellent in producing bone tissue metastasis representative of *in vivo* conditions. However, findings from Chapter 3 reveal time-sensitive changes in bone tissue and mechanical properties, and this timeline should be investigated further. This pre-clinical study could be repeated to include additional time points and more frequent intervals, such as every 2 weeks, and analysed via micro-CT and nanoindentation as previously demonstrated. In this way, such analysis would shed further light on the timeline of bone tissue adaptation and osteolysis. While *in vivo* micro-CT of the same animals over this time period would reduce animal numbers, this would also result in lower resolutions (10µm voxel size or higher), which could significantly reduce the accuracy of bone mineralisation results, thus *in vitro* micro-CT is still recommended.

Histological analysis, such as haematoxylin and eosin (H&E) staining, should be performed to analyse the exact locations of invading metastatic cells. This methodology would mean the progression of metastatic cellular invasion, and their precise regions of extravasation within the femur, can be monitored throughout the study. It would be interesting to also perform tartrate-resistant acid phosphatase (TRAP) staining in these same bone regions, to investigate whether osteoclasts have been recruited within the same areas during early metastatic invasion, to later perpetuate osteolytic destruction. In light of osteolytic lesions developed in the greater trochanter at 6 weeks post-inoculation (reported in Chapter 3), histological staining for biochemical factors specifically in these regions – along with staining of other regions in the proximal femur for comparison – would demonstrate whether these growth factors become upregulated and in turn possibly explain the consistent development of osteolytic lesions in the greater trochanter regions of all tumour-bearing metastatic femur samples.

Two regions of interest were selected for analysis for the purpose of this thesis: a) the proximal femur region, which is anatomically located adjacent to the primary tumour inoculation site and b) the distal region, which is abundant with trabecular bone tissue and is not in the presence of the further distal growth plate region, where continuously altered mineralisation could have otherwise affected analytic results. In order to utilise the highest possible resolution micro-CT at the time of this thesis, only these two regions were selected and analysed for the remainder of the project. However, the first study of this thesis (see Chapter 3) reported region-specific differences in bone tissue morphology (proximal femur trabecular thinning, distal femur cortical thickening). Therefore, whole-femur micro-CT scans of metastatic femurs would be beneficial in understanding how changes in the tumour-adjacent region could alter mechanical cues in more distant regions. Additionally, nanoscale computed tomography (nano-CT) is becoming more readily available for imaging of bone tissues, and would allow for the precise analysis of bone tissue at ultra-high resolutions, including measurement of osteocytes within the cortical regions of murine bone tissue, currently unavailable using optimal micro-CT resolutions (Kampschulte et al., 2016). Therefore, implementation of nano-CT analysis would be beneficial in understanding how the mechanical environment of bone tissue changes at the sub-cellular level in response to metastatic invasion.

6.4.2 Computational modelling future studies

As previously discussed, femoral diaphysis and distal femur epiphyses were not analysed by micro-CT, and as a result FE models of each whole femur sample could not be generated analysis in Chapter 4 and Chapter 5. Future studies could conduct micro-CT analysis of whole metastatic mouse femurs, followed by 3D reconstruction, FE analysis and subroutine simulations as detailed in this thesis. Furthermore, the mechanoregulation algorithm described in Chapter 5 could be implemented on these whole femur models to demonstrate how changes in the proximal femur region could alter stresses and strain fields in the distal femur regions, thereby shedding light on how mechanoregulatory response evolves, systemically, as metastatic invasion progresses.

Finite element analysis of proximal and distal femurs of metastatic bone tissue, as reported in Chapter 4, revealed strain distribution had significantly decreased within the 3-week post-inoculation cohort compared to healthy controls. However, these models had some assumptions and limitations in their development. Each mesh was linear elastic, 4-noded tetrahedral and was fixed with boundary conditions in the distal region of the model. In addition, these models applied a single static load. Future research could optimise these FE models to more closely replicate *in vivo* conditions. For instance, introducing poroelasticity to these models, by incorporating both fluid and solid constituents as occur in vascularised bone tissue *in vivo*, has been shown to produce significantly higher reaction forces and strain energy densities compared to linear elastic models (Falcinelli et al., 2020). The introduction of 10-noded rather than 4-noded elements has previously been investigated in human proximal femurs under compression, which reported no change in the resulting reaction force, stress and strain fields, and thereby deemed an ‘unnecessary computational effort’ (Ramos and Simoes, 2006). However, given that human femurs were approximately 40x larger (~500cm in length) than BALB/c mice (~14cm in length), a smaller scale FE model of murine bone could be impacted by the incorporation of second order elements. It would be interesting to perform a comparative test, simulating all FE models in both first and second order conditions and analyse their resulting stress, strain and SED responses to determine whether this would truly make an impact, and this result could determine all FE model developments moving forward for murine FEA research.

These proximal femur FE models, which were first introduced in Chapter 4, were then assigned a mechanoregulatory algorithm to predict bone remodelling over a period of 21 days in Chapter 5. This final study depicted reduction in bone tissue density in the greater trochanter region, adequately reflecting the experimental findings of Chapter 3 and revealing that mechanobiology may indeed play a role in the progression of osteolysis during metastasis. The FE models utilised for this final study were homogeneous in nature for the first increment, and therefore did not incorporate the anisotropic variation in material properties that occur *in vivo* and were captured in Chapter 4. While the introduction of heterogeneity to µCT-derived FE models of BALB/c mouse tibiae might decreased accuracy in predicting failure load and stiffness compared to homogeneous models (Oliviero et al., 2021), it would still be worth exploring this methodology specifically in the models of this study. This would entail solving both user-defined field (USDFLD) and user material (UMAT) subroutines separately and storing these results in a user external database (UEXTERNALDB) as a data history storage until the next increment begins, all of which are featured within Abaqus software, as previously demonstrated in a study of damage in hyper-elastic soft materials (Li, 2016). This incorporation of a heterogeneous metastatic bone model could more accurately predict changes in the stress and strain fields within these models, and in turn demonstrate more precise mechanoregulatory response over time, thereby further shedding light on the influence of mechanobiology on metastatic progression in bone tissue. To avoid compounding factors and maintain focus on bone tissue mechanobiology, Chapter 5 models did not include biochemical signalling as a driving factor for osteoblast and osteoclast activity. Future adaptions of the FE models and associated mechanoregulation-driven algorithm in Chapter 5 could include the gradual growth of remodelling cell populations according to autocrine and paracrine signalling (Hambli, 2014). As a more robust form of experimental validation of the current studies, either *in vivo* micro-CT analysis of bone tissue resorption and formation, or alternatively DVC analysis of bone tissue morphology in a longitudinal study, of the pre-clinical metastatic animal model could inform the precise rates of bone tissue growth and osteolysis according to experimental *in vivo* measurements (Cheong et al., 2020a).

6.5 Conclusion

In conclusion, this thesis has presented experimental and computational studies performed throughout the course of the author’s PhD studies in the field of bone tissue mechanobiology to investigate temporal and spatial changes in the bone mechanical environment upon breast cancer metastatic invasion and osteolysis. Micro-CT imaging, mineralisation analysis and nanoindentation were implemented and revealed increased bone mineral content and mechanical properties prior to the development of overt osteolytic destruction in an *in vivo* representative animal model of breast cancer metastasis. In addition, this first study demonstrated that changes in bone mineral content upon osteolytic destruction were systemic, while changes in the mechanical properties of bone tissue were specific to only the bone tissue located adjacent to the developing breast cancer primary tumour site. In the second study of this thesis, FEA of 3D models reconstructed from these micro-CT scans predicted a reduction in mechanical stimulation within the microenvironment of bone tissue during early breast cancer metastatic invasion. It was thus proposed that this may drive osteoclastogenesis and thereby contribute to subsequent osteolysis. Finally, the third study of this thesis applied a previously established bone remodelling algorithm to predict the evolution of the bone mechanical environment during metastasis and investigate the putative mechanobiological cues for osteolysis. This final study demonstrated that mechanobiological cues within the bone extracellular matrix could drive subsequent reduction in bone mineral density in the regions where osteolysis is reported experimentally, and supports the theory that mechanobiology plays a role in the development of osteolysis. The findings in this thesis provide an enhanced understanding of the temporal and spatial nature of bone tissue physical properties during bone tissue metastasis and the role of mechanobiology during the cancer vicious cycle, and the knowledge gained from this body of work may inform future treatments of bone metastasis.

References

Adachi, T., Tsubota, K.-I., Tomita, Y. & Hollister, S. J. 2001. Trabecular surface remodeling simulation for cancellous bone using microstructural voxel finite element models. *Journal of Biomechanical Engineering*, 123**,** 403-409.https://doi.org/10.1115/1.1392315

Alkalay, R., Adamson, R., Miropolsky, A. & Hackney, D. 2018. Female human spines with simulated osteolytic defects: CT-based structural analysis of vertebral body strength. *Radiology*, 288**,** 436.https://doi.org/10.1148/radiol.2018171139

Allocca, G., Hughes, R., Wang, N., Brown, H. K., Ottewell, P. D., Brown, N. J. & Holen, I. 2019. The bone metastasis niche in breast cancer-potential overlap with the haematopoietic stem cell niche in vivo. *J Bone Oncol*, 17**,** 100244.https://doi.org/10.1016/j.jbo.2019.100244

Ambrosi, D. & Mollica, F. 2002. On the mechanics of a growing tumor. *International journal of engineering science*, 40**,** 1297-1316.https://doi.org/10.1016/s0020-7225(02)00014-9

Amend, S. R., Valkenburg, K. C. & Pienta, K. J. 2016. Murine Hind Limb Long Bone Dissection and Bone Marrow Isolation. *J Vis Exp***,** e53936.https://doi.org/10.3791/53936

Anez-Bustillos, L., Derikx, L. C., Verdonschot, N., Calderon, N., Zurakowski, D., Snyder, B. D., Nazarian, A. & Tanck, E. 2014. Finite element analysis and CT-based structural rigidity analysis to assess failure load in bones with simulated lytic defects. *Bone*, 58**,** 160-167.https://doi.org/10.1016/j.bone.2013.10.009

Araujo, A., Cook, L. M., Lynch, C. C. & Basanta, D. 2014. An integrated computational model of the bone microenvironment in bone-metastatic prostate cancer. *Cancer Res*, 74**,** 2391-401.10.1158/0008-5472.CAN-13-2652

Arrington, S. A., Damron, T. A., Mann, K. A. & Allen, M. J. 2008. Concurrent administration of zoledronic acid and irradiation leads to improved bone density, biomechanical strength, and microarchitecture in a mouse model of tumor-induced osteolysis. *Journal of Surgical Oncology*, 97**,** 284-90.https://doi.org/10.1002/jso.20949

Arrington, S. A., Schoonmaker, J. E., Damron, T. A., Mann, K. A. & Allen, M. J. 2006. Temporal changes in bone mass and mechanical properties in a murine model of tumor osteolysis. *Bone*, 38**,** 359-67.https://doi.org/10.1016/j.bone.2005.09.013

Ashique, A., Hart, L., Thomas, C., Clement, J., Pivonka, P., Carter, Y., Mousseau, D. & Cooper, D. 2017. Lacunar-canalicular network in femoral cortical bone is reduced in aged women and is predominantly due to a loss of canalicular porosity. *Bone Reports*, 7**,** 9-16.https://doi.org/10.1016/j.bonr.2017.06.002

Atkins, A., Burke, M., Samiezadeh, S., Akens, M. K., Hardisty, M. & Whyne, C. M. 2019. Elevated microdamage spatially correlates with stress in metastatic vertebrae. *Annals of Biomedical Engineering*, 47**,** 980-989.https://doi.org/10.1007/s10439-018-02188-8

Augat, P. & Schorlemmer, S. 2006. The role of cortical bone and its microstructure in bone strength. *Age and ageing*, 35**,** ii27-ii31

Badilatti, S. D., Christen, P., Parkinson, I. & Müller, R. 2016. Load-adaptive bone remodeling simulations reveal osteoporotic microstructural and mechanical changes in whole human vertebrae. *Journal of Biomechanics*, 49**,** 3770-3779.https://doi.org/10.1016/j.jbiomech.2016.10.002

Baron, R., Ferrari, S. & Russell, R. G. G. 2011. Denosumab and bisphosphonates: different mechanisms of action and effects. *Bone,* 48**,** 677-692.https://doi.org/10.1016/j.bone.2010.11.020

Bembey, A., Bushby, A., Boyde, A., Ferguson, V. & Oyen, M. 2006. Hydration effects on the micro-mechanical properties of bone. *Journal of materials research,* 21**,** 1962-1968.https://doi.org/10.1557/jmr.2006.0237

Benca, E., Reisinger, A., Patsch, J. M., Hirtler, L., Synek, A., Stenicka, S., Windhager, R., Mayr, W. & Pahr, D. H. 2017. Effect of simulated metastatic lesions on the biomechanical behavior of the proximal femur. *Journal of Orthopaedic Research,* 35**,** 2407-2414.https://doi.org/doi.org/10.1002/jor.23550

Birney, E., Goldman, N., Kasprzyk, A., Mongin, E., Rust, A. G., Slater, G., Stabenau, A., Ureta-Vidal, A., Whelan, S., Abril, J. F., Guigó, R., Parra, G., Agarwal, P., Agarwala, R., Church, D. M., Hlavina, W., Maglott, D. R., Sapojnikov, V., Alexandersson, M., Pachter, L., Antonarakis, S. E., Dermitzakis, E. T., Reymond, A., Ucla, C., Baertsch, R., Diekhans, M., Furey, T. S., Hinrichs, A., Hsu, F., Karolchik, D., Kent, W. J., Roskin, K. M., Schwartz, M. S., Sugnet, C. & Weber, R. J. 2002. Initial sequencing and comparative analysis of the mouse genome. *Nature,* 420**,** 520-562.https://doi.org/10.1038/nature01262

Blanchard, R., Dejaco, A., Bongaers, E. & Hellmich, C. 2013. Intravoxel bone micromechanics for microCT-based finite element simulations. *Journal of Biomechanics,* 46**,** 2710-2721.https://doi.org/10.1016/j.jbiomech.2013.06.036

Boivin, G. & Meunier, P. 2002. The degree of mineralization of bone tissue measured by computerized quantitative contact microradiography. *Calcified Tissue International,* 70**,** 503

Bolshakov, A. & Pharr, G. 1998. Influences of pileup on the measurement of mechanical properties by load and depth sensing indentation techniques. *Journal of materials research,* 13**,** 1049-1058.https://doi.org/10.1557/jmr.1998.0146

Bonewald, L. F. 2011. The amazing osteocyte. *Journal of Bone and Mineral Research,* 26**,** 229-238.https://doi.org/10.1002/jbmr.320

Bonucci, E. 2012. Bone mineralization. *Frontiers in Bioscience-Landmark,* 17**,** 100-128

Börjesson, A. E., Windahl, S. H., Karimian, E., Eriksson, E. E., Lagerquist, M. K., Engdahl, C., Antal, M. C., Krust, A., Chambon, P. & Sävendahl, L. 2012. The role of estrogen receptor-α and its activation function-1 for growth plate closure in female mice. *American Journal of Physiology-Endocrinology and Metabolism,* 302**,** E1381-E1389.https://doi.org/10.1152/ajpendo.00646.2011

Boskey, A., Spevak, L. & Weinstein, R. 2009. Spectroscopic markers of bone quality in alendronate-treated postmenopausal women. *Osteoporosis International,* 20**,** 793-800

Bouxsein, M. L., Boyd, S. K., Christiansen, B. A., Guldberg, R. E., Jepsen, K. J. & Müller, R. 2010. Guidelines for assessment of bone microstructure in rodents using micro–computed tomography. *Journal of bone mineral research,* 25**,** 1468-1486.https://doi.org/10.1002/jbmr.141

Bray, F., Ferlay, J., Soerjomataram, I., Siegel, R. L., Torre, L. A. & Jemal, A. 2018. Global cancer statistics 2018: GLOBOCAN estimates of incidence and mortality worldwide for 36 cancers in 185 countries. *CA: A Cancer Journal for Clinicians,* 68**,** 394-424.https://doi.org/10.3322/caac.21492

Brennan, M. A., Gleeson, J. P., Browne, M., O'brien, F. J., Thurner, P. J. & Mcnamara, L. M. 2011. Site specific increase in heterogeneity of trabecular bone tissue mineral during oestrogen deficiency. *European Cells and Materials,* 21**,** 396-406.https://doi.org/10.22203/ecm.v021a30

Buenzli, P. R. & Sims, N. A. 2015. Quantifying the osteocyte network in the human skeleton. *Bone,* 75**,** 144-150.https://doi.org/10.1016/j.bone.2015.02.016

Burke, M., Akens, M., Kiss, A., Willett, T. & Whyne, C. 2018. Mechanical behavior of metastatic vertebrae are influenced by tissue architecture, mineral content, and organic feature alterations. *Journal of Orthopaedic Research,* 36**,** 3013-3022.https://doi.org/10.1002/jor.24105

Burke, M., Atkins, A., Kiss, A., Akens, M., Yee, A. & Whyne, C. 2017. The impact of metastasis on the mineral phase of vertebral bone tissue. *Journal of the Mechanical Behavior of Biomedical Materials,* 69**,** 75-84.https://doi.org/10.1016/j.jmbbm.2016.12.017

Burke, M. V., Atkins, A., Akens, M., Willett, T. L. & Whyne, C. M. 2016. Osteolytic and mixed cancer metastasis modulates collagen and mineral parameters within rat vertebral bone matrix. *Journal of Orthopaedic Research,* 34**,** 2126-2136.https://doi.org/10.1002/jor.23248

Cao, L., Youn, I., Guilak, F. & Setton, L. A. 2006. Compressive properties of mouse articular cartilage determined in a novel micro-indentation test method and biphasic finite element model.

Cappariello, A., Maurizi, A., Veeriah, V. & Teti, A. 2014. The Great Beauty of the osteoclast. *Archives of Biochemistry and Biophysics,* 558**,** 70-78.https://doi.org/10.1016/j.abb.2014.06.017

Cardoso, F., Spence, D., Mertz, S., Corneliussen-James, D., Sabelko, K., Gralow, J., Cardoso, M.-J., Peccatori, F., Paonessa, D. & Benares, A. 2018. Global analysis of advanced/metastatic breast cancer: decade report (2005–2015). *The breast*, 39**,** 131-138.https://doi.org/10.1016/j.breast.2018.03.002

Casanova, M., Balmelli, A., Carnelli, D., Courty, D., Schneider, P. & Müller, R. 2017. Nanoindentation analysis of the micromechanical anisotropy in mouse cortical bone. *Royal Society open science,* 4**,** 160971.https://doi.org/10.1098/rsos.160971

Charles, J. P., Cappellari, O. & Hutchinson, J. R. 2018. A dynamic simulation of musculoskeletal function in the mouse hindlimb during trotting locomotion. *Frontiers in Bioengineering Biotechnology,* 6**,** 61.https://doi.org/doi.org/10.3389/fbioe.2018.00061

Chen, H.-L., Tung, Y.-T., Chuang, C.-H., Tu, M.-Y., Tsai, T.-C., Chang, S.-Y. & Chen, C.-M. 2015. Kefir improves bone mass and microarchitecture in an ovariectomized rat model of postmenopausal osteoporosis. *Osteoporosis International*, 26**,** 589-599

Chen, Q., Rho, J. Y., Fan, Z., Laulederkind, S. J. & Raghow, R. 2003. Congenital lack of COX-2 affects mechanical and geometric properties of bone in mice. *Calcif Tissue Int,* 73**,** 387-92.10.1007/s00223-002-0009-x

Chen, Y.-C., Sosnoski, D. M. & Mastro, A. M. J. B. C. R. 2010. Breast cancer metastasis to the bone: mechanisms of bone loss. 12**,** 215

Cheong, V. S., Campos Marin, A., Lacroix, D. & Dall'ara, E. 2020a. A novel algorithm to predict bone changes in the mouse tibia properties under physiological conditions. *Biomechanics and Modeling in Mechanobiology,* 19**,** 985-1001.https://doi.org/10.1007/s10237-019-01266-7

Cheong, V. S., Kadirkamanathan, V. & Dall'ara, E. 2021. The Role of the Loading Condition in Predictions of Bone Adaptation in a Mouse Tibial Loading Model.

Frontiers in Bioengineering and Biotechnology, 9**,** 676867.https://doi.org/10.3389/fbioe.2021.676867

Cheong, V. S., Roberts, B. C., Kadirkamanathan, V. & Dall'ara, E. 2020b. Bone remodelling in the mouse tibia is spatio-temporally modulated by oestrogen deficiency and external mechanical loading: A combined in vivo/in silico study. *Acta Biomaterialia,* 116**,** 302-317.https://doi.org/10.1016/j.actbio.2020.09.011

Chiou, A. E., Liu, C., Moreno-Jiménez, I., Tang, T., Wagermaier, W., Dean, M. N., Fischbach, C. & Fratzl, P. 2021. Breast cancer–secreted factors perturb murine bone growth in regions prone to metastasis. *Science Advances,* 7**,** eabf2283.https://doi.org/10.1126/sciadv.abf2283

Choudhari, C., Chan, K., Akens, M. K. & Whyne, C. M. 2016. µFE models can represent microdamaged regions of healthy and metastatically involved whole vertebrae identified through histology and contrast enhanced µCT imaging. *Journal of Biomechanics,* 49**,** 1103-1110.https://doi.org/10.1016/j.jbiomech.2016.02.034

Clarke, B. J. C. J. O. T. a. S. O. N. 2008. Normal bone anatomy and physiology. 3**,** S131-S139

Clezardin, P. & Teti, A. 2007. Bone metastasis: pathogenesis and therapeutic implications. *Journal of Clinical and Experimental Metastasis,* 24**,** 599-608.https://doi.org/10.1007/s10585-007-9112-8

Clines, G. A. & Guise, T. A. 2005. Hypercalcaemia of malignancy and basic research on mechanisms responsible for osteolytic and osteoblastic metastasis to bone. *Endocrine-Related Cancer,* 12**,** 549-83.https://doi.org/10.1677/erc.1.00543

Cole, H. A., Yuasa, M., Hawley, G., Cates, J. M., Nyman, J. S. & Schoenecker, J. G. 2013. Differential development of the distal and proximal femoral epiphysis and physis in mice. *Bone,* 52**,** 337-346.https://doi.org/10.1016/j.bone.2012.10.011

Coleman, R. E. & Rubens, R. D. 1987. The clinical course of bone metastases from breast cancer. *British Journal of Cancer,* 55**,** 61-6.https://doi.org/10.1038/bjc.1987.13

Cook, L. M., Araujo, A., Pow-Sang, J. M., Budzevich, M. M., Basanta, D. & Lynch, C. C. 2016. Predictive computational modeling to define effective treatment strategies for bone metastatic prostate cancer. *Sci Rep,* 6**,** 29384.10.1038/srep29384

Cooper, G. & Hausman, R. 2000. The development and causes of cancer. *The Cell: A Molecular Approach. 2nd edition.*: Sinauer Associates.

Costa, M., Campello, L. B., Ryan, M., Rochester, J., Viceconti, M. & Dall'ara, E. 2020. Effect of size and location of simulated lytic lesions on the structural properties of human vertebral bodies, a micro-finite element study. *Bone Reports,* 12**,** 100257.https://doi.org/10.1016/j.bonr.2020.100257

Costa, M., Eltes, P., Lazary, A., Varga, P., Viceconti, M. & Dall'ara, E. 2019. Biomechanical assessment of vertebrae with lytic metastases with subject-specific finite element models. *Journal of the Mechanical Behavior of Biomedical Materials,* 98**,** 268-290.https://doi.org/10.1016/j.jmbbm.2019.06.027

Costa, M. C., Tozzi, G., Cristofolini, L., Danesi, V., Viceconti, M. & Dall'ara, E. 2017. Micro finite element models of the vertebral body: validation of local displacement predictions. *PloS One,* 12**,** e0180151.https://doi.org/10.1371/journal.pone.0180151

Courtland, H.-W., Nasser, P., Goldstone, A. B., Spevak, L., Boskey, A. L. & Jepsen, K. J. 2008. Fourier transform infrared imaging microspectroscopy and tissue-level mechanical testing reveal intraspecies variation in mouse bone mineral and matrix composition. *Calcified Tissue International,* 83**,** 342-353.https://doi.org/10.1007/s00223-008-9176-8

Cowin, S. & Hegedus, D. 1976. Bone remodeling I: theory of adaptive elasticity. *Journal of Elasticity,* 6**,** 313-326.https://doi.org/10.1016/0092-8674(80)90501-2

Cox, R. F. & Morgan, M. P. J. B. 2013. Microcalcifications in breast cancer: Lessons from physiological mineralization. 53**,** 437-450

Currey, J. D., Brear, K., Zioupos, P. & Reilly, G. C. 1995. Effect of formaldehyde fixation on some mechanical properties of bovine bone. *Biomaterials,* 16**,** 1267-1271.https://doi.org/10.1016/0142-9612(95)98135-2

Dai, J., Hensel, J., Wang, N., Kruithof-De Julio, M. & Shiozawa, Y. 2016. Mouse models for studying prostate cancer bone metastasis. *BoneKEy reports,* 5.https://doi.org/10.1038/bonekey.2016.4

Dall'ara, E., Eastell, R., Viceconti, M., Pahr, D. & Yang, L. 2016. Experimental validation of DXA-based finite element models for prediction of femoral strength. *Journal of the Mechanical Behavior of Biomedical Materials,* 63**,** 17-25.https://doi.org/10.1016/j.jmbbm.2016.06.004

De Souza, R., Matsuura, M., Eckstein, F., Rawlinson, S., Lanyon, L. & Pitsillides, A. 2005. Non-invasive axial loading of mouse tibiae increases cortical bone formation and modifies trabecular organization: a new model to study cortical and cancellous compartments in a single loaded element. *Bone,* 37**,** 810-818.https://doi.org/10.1016/j.bone.2005.07.022

Del Fattore, A., Teti, A. & Rucci, N. 2012. Bone cells and the mechanisms of bone remodelling. *Front Biosci (Elite Ed),* 4**,** 2302-21.https://doi.org/10.2741/543

Demers, L. M., Costa, L. & Lipton, A. J. C. I. I. J. O. T. a. C. S. 2000. Biochemical markers and skeletal metastases. 88**,** 2919-2926

Dwivedi, A., Kiely, P. A. & Hoey, D. A. 2021. Mechanically stimulated osteocytes promote the proliferation and migration of breast cancer cells via a potential CXCL1/2 mechanism. *Biochemical and Biophysical Research Communications,* 534**,** 14-20.https://doi.org/10.1016/j.bbrc.2020.12.016

Eggermont, F., Van Der Wal, G., Westhoff, P., Laar, A., De Jong, M., Rozema, T., Kroon, H. M., Ayu, O., Derikx, L. & Dijkstra, S. 2020. Patient-specific finite element computer models improve fracture risk assessments in cancer patients with femoral bone metastases compared to clinical guidelines. *Bone,* 130**,** 115101.https://doi.org/10.1016/j.bone.2019.115101

Faber, J. & Fonseca, L. M. J. D. P. J. O. O. 2014. How sample size influences research outcomes. 19**,** 27-29

Falcinelli, C., Di Martino, A., Gizzi, A., Vairo, G. & Denaro, V. 2019. Mechanical behavior of metastatic femurs through patient-specific computational models accounting for bone-metastasis interaction. *Journal of the Mechanical Behavior of Biomedical Materials,* 93**,** 9-22.https://doi.org/10.1016/j.jmbbm.2019.01.014

Falcinelli, C., Di Martino, A., Gizzi, A., Vairo, G. & Denaro, V. 2020. Fracture risk assessment in metastatic femurs: a patient-specific CT-based finite-element approach. *Meccanica,* 55**,** 861-881.https://doi.org/10.1007/s11012-019-01097-x

Fan, Y., Jalali, A., Chen, A., Zhao, X., Liu, S., Teli, M., Guo, Y., Li, F., Li, J., Siegel, A., Yang, L., Liu, J., Na, S., Agarwal, M., Robling, A. G., Nakshatri, H., Li, B. Y. & Yokota, H. 2020. Skeletal loading regulates breast cancer-associated osteolysis in a loading intensity-dependent fashion. *Bone Res,* 8**,** 9.https://doi.org/10.1038/s41413-020-0083-6

Farach-Carson, M. C., Lin, S.-H., Nalty, T. & Satcher, R. L. 2017. Sex differences and bone metastases of breast, lung, and prostate cancers: do bone homing cancers favor feminized bone marrow? *Frontiers in Oncology,* 7**,** 163.https://doi.org/10.3389/fonc.2017.00163

Fernández, M. P., Sasso, S. J., Mcphee, S., Black, C., Kanczler, J., Tozzi, G. & Wolfram, U. 2022. Nonlinear micro finite element models based on digital volume correlation measurements predict early microdamage in newly formed bone. *Journal of the Mechanical Behavior of Biomedical Materials***,** 105303.https://doi.org/10.1016/j.jmbbm.2022.105303

Fratzl, P. & Weinkamer, R. 2007. Nature's hierarchical materials. *Progress in Materials Science,* 52**,** 1263-1334.https://doi.org/10.1016/j.pmatsci.2007.06.001

Fritton, S. P. & Weinbaum, S. 2009. Fluid and solute transport in bone: flow-induced mechanotransduction. *Annual review of fluid mechanics,* 41**,** 347.https://doi.org/10.1146/annurev.fluid.010908.165136

Frost, H. M. 1964. Dynamics of bone remodeling. *Bone biodynamics***,** 315-334

Frost, H. M. 1987. Bone "mass" and the "mechanostat": a proposal. *The anatomical record,* 219**,** 1-9.https://doi.org/10.1002/ar.1092190104

Frost, H. M. 1991. A new direction for osteoporosis research: a review and proposal. *Bone,* 12**,** 429-437.https://doi.org/10.1016/8756-3282(91)90032-e

Frost, H. M. 1996. Perspectives: A proposed general model of the "mechanostat"(suggestions from a new skeletal-biologic paradigm). *The Anatomical Record: An Official Publication of the American Association of Anatomists,* 244**,** 139-147.https://doi.org/10.1002/(SICI)1097-0185(199602)244:2<139::AID-AR1>3.0.CO;2-X

Ganguly, S. S., Li, X. & Miranti, C. K. 2014. The Host Microenvironment Influences Prostate Cancer Invasion, Systemic Spread, Bone Colonization, and Osteoblastic Metastasis. 4.10.3389/fonc.2014.00364

Garcia-Aznar, J. M., Rüberg, T. & Doblare, M. 2005. A bone remodelling model coupling microdamage growth and repair by 3D BMU-activity. *Biomechanics and Modeling in Mechanobiology,* 4**,** 147-167.https://doi.org/10.1007/s10237-005-0067-x

Gatti, V., Azoulay, E. M. & Fritton, S. P. 2018. Microstructural changes associated with osteoporosis negatively affect loading-induced fluid flow around osteocytes in cortical bone. *Journal of Biomechanics,* 66**,** 127-136.https://doi.org/10.1016/j.jbiomech.2017.11.011

Geraldes, D. M. & Phillips, A. T. 2014. A comparative study of orthotropic and isotropic bone adaptation in the femur. *International Journal for Numerical Methods in Biomedical Engineering,* 30**,** 873-889.https://doi.org/10.1002/cnm.2633

Gimbrone Jr, M. A., Leapman, S. B., Cotran, R. S. & Folkman, J. 1972. Tumor dormancy in vivo by prevention of neovascularization. *The Journal of experimental medicine,* 136**,** 261-276.https://doi.org/10.1084/jem.136.2.261

Gourion-Arsiquaud, S., Faibish, D., Myers, E., Spevak, L., Compston, J., Hodsman, A., Shane, E., Recker, R. R., Boskey, E. R. & Boskey, A. L. 2009. Use of FTIR spectroscopic imaging to identify parameters associated with fragility fracture. *Journal of Bone and Mineral Research,* 24**,** 1565-1571.https://doi.org/10.1359/jbmr.090414

Guise, T. A. 2002. The vicious cycle of bone metastases. *Journal of Musculoskeletal & Neuronal Interactions,* 2**,** 570-2

Guise, T. A. & Mundy, G. R. 1998. Cancer and bone. *Endocrine Reviews,* 19**,** 18-54.https://doi.org/10.1210/edrv.19.1.0323

Hambli, R. 2014. Connecting mechanics and bone cell activities in the bone remodeling process: an integrated finite element modeling. *Frontiers in Bioengineering and Biotechnology,* 2**,** 6.https://doi.org/10.3389/fbioe.2014.00006

Hamed, E., Lee, Y. & Jasiuk, I. J. a. M. 2010. Multiscale modeling of elastic properties of cortical bone. 213**,** 131-154

Hay, J., Pharr, G. & Medlin, D. 2000. Mechanical testing and evaluation. *ASM INTERNATIONAL. Metals handbook. Materials Park,* 8**,** 231-242

He, F., Chiou, A. E., Loh, H. C., Lynch, M., Seo, B. R., Song, Y. H., Lee, M. J., Hoerth, R., Bortel, E. L. & Willie, B. M. 2017. Multiscale characterization of the mineral phase at skeletal sites of breast cancer metastasis. *Proceedings of the National Academy of Sciences,* 114**,** 10542-10547.https://doi.org/10.1073/pnas.1708161114

Hemmatian, H., Laurent, M. R., Bakker, A. D., Vanderschueren, D., Klein-Nulend, J. & Van Lenthe, G. H. 2018. Age-related changes in female mouse cortical bone microporosity. *Bone,* 113**,** 1-8

Hoffler, C. E., Guo, X. E., Zysset, P. K. & Goldstein, S. A. 2005. An application of nanoindentation technique to measure bone tissue lamellae properties. *Journal of Biomechanical Engineering,* 7**,** 1046-1053.https://doi.org/10.1115/1.2073671

Huiskes, R., Weinans, H., Grootenboer, H., Dalstra, M., Fudala, B. & Slooff, T. 1987. Adaptive bone-remodeling theory applied to prosthetic-design analysis. *Journal of Biomechanics,* 20**,** 1135-1150.https://doi.org/10.1016/0021-9290(87)90030-3

Hunter, G. K. & Goldberg, H. a. J. P. O. T. N. a. O. S. 1993. Nucleation of hydroxyapatite by bone sialoprotein. 90**,** 8562-8565

Isaksson, H., Gröngröft, I., Wilson, W., Van Donkelaar, C. C., Van Rietbergen, B., Tami, A., Huiskes, R. & Ito, K. 2009. Remodeling of fracture callus in mice is consistent with mechanical loading and bone remodeling theory. *Journal of Orthopaedic Research,* 27**,** 664-672.https://doi.org/10.1002/jor.20725

Iwamura, M., Hellman, J., Cockett, A. T., Lilja, H. & Gershagen, S. 1996. Alteration of the hormonal bioactivity of parathyroid hormone-related protein (PTHrP) as a result of limited proteolysis by prostate-specific antigen. *Urology,* 48**,** 317-325.https://doi.org/10.1016/s0090-4295(96)00182-3

Jain, R. K., Martin, J. D. & Stylianopoulos, T. 2014. The role of mechanical forces in tumor growth and therapy. *Annual Review of Biomedical Engineering,* 16**,** 321.https://doi.org/10.1146/annurev-bioeng-071813-105259

Janssen, L. M., Ramsay, E. E., Logsdon, C. D. & Overwijk, W. W. 2017. The immune system in cancer metastasis: friend or foe? *Journal for immunotherapy of cancer,* 5**,** 1-14.https://doi.org/10.1186/s40425-017-0283-9

Jiang, F., Liu, S., Chen, A., Li, B.-Y., Robling, A. G., Chen, J. & Yokota, H. J. I. J. O. O. 2018. Finite element analysis of the mouse distal femur with tumor burden in response to knee loading. 5**,** 863

Jie, S., Guo, X. & Ouyang, Z. 2019. Tumor ablation using novel photothermal NaxWO3 nanoparticles against breast cancer osteolytic bone metastasis. *International Journal of Nanomedicine,* 14**,** 7353.https://doi.org/10.2147/ijn.s217974

Jilka, R. L. 2013. The relevance of mouse models for investigating age-related bone loss in humans. *Journals of Gerontology. Series A: Biological Sciences and Medical Sciences,* 68**,** 1209-17.https://doi.org/10.1093/gerona/glt046

Jilka, R. L. J. J. O. G. S. a. B. S. & Sciences, M. 2013. The relevance of mouse models for investigating age-related bone loss in humans. 68**,** 1209-1217

Jinnah, A. H., Zacks, B. C., Gwam, C. U. & Kerr, B. A. 2018. Emerging and established models of bone metastasis. *Cancers,* 10**,** 176.https://doi.org/10.3390/cancers10060176

Jones, L. W., Viglianti, B. L., Tashjian, J. A., Kothadia, S. M., Keir, S. T., Freedland, S. J., Potter, M. Q., Jung Moon, E., Schroeder, T. & Herndon, J. E. 2010. Effect of aerobic exercise on tumor physiology in an animal model of human breast cancer. *Journal of Applied Physiology,* 108**,** 343-348.https://doi.org/10.1152/japplphysiol.00424.2009

Judex, S., Garman, R., Squire, M., Donahue, L. R. & Rubin, C. 2004. Genetically based influences on the site-specific regulation of trabecular and cortical bone morphology. *Journal of Bone and Mineral Research,* 19**,** 600-606.https://doi.org/10.1359/jbmr.040101

Kakinuma, T. & Hwang, S. T. 2006. Chemokines, chemokine receptors, and cancer metastasis. *Journal of Leukocyte Biology,* 79**,** 639-651.https://doi.org/10.1189/jlb.1105633

Kampschulte, M., Langheinirch, A., Sender, J., Litzlbauer, H., Althöhn, U., Schwab, J., Alejandre-Lafont, E., Martels, G. & Krombach, G. Nano-computed tomography: technique and applications. RöFo-Fortschritte auf dem Gebiet der Röntgenstrahlen und der bildgebenden Verfahren, 2016. © Georg Thieme Verlag KG, 146-154.

Kaneko, T. S., Bell, J. S., Pejcic, M. R., Tehranzadeh, J. & Keyak, J. H. 2004. Mechanical properties, density and quantitative CT scan data of trabecular bone with and without metastases. *Journal of Biomechanics,* 37**,** 523-530.https://doi.org/10.1016/j.jbiomech.2003.08.010

Kaneko, T. S., Pejcic, M. R., Tehranzadeh, J. & Keyak, J. H. 2003. Relationships between material properties and CT scan data of cortical bone with and without metastatic lesions. *J Medical engineering physics,* 25**,** 445-454.https://doi.org/10.1016/S1350-4533(03)00030-4

Keller, T. S. 1994. Predicting the compressive mechanical behavior of bone. *Journal of Biomechanics,* 27**,** 1159-1168.https://doi.org/10.1016/0021-9290(94)90056-6

Kenkre, J. S. & Bassett, J. 2018. The bone remodelling cycle. *Annals of Clinical Biochemistry,* 55**,** 308-327.https://doi.org/10.1177/0004563218759371

Keyak, J., Meagher, J., Skinner, H. & Mote Jr, C. 1990. Automated three-dimensional finite element modelling of bone: a new method. *Journal of biomedical engineering,* 12**,** 389-397

Keyak, J. H., Kaneko, T. S., Rossi, S. A., Pejcic, M. R., Tehranzadeh, J. & Skinner, H. B. 2005. Predicting the strength of femoral shafts with and without metastatic lesions. *Clinical orthopaedics related research,* 439**,** 161-170.https://doi.org/10.1097/01.blo.0000174736.50964.3b

Keyak, J. H., Kaneko, T. S., Skinner, H. B., Hoang, B. H. & Research, R. 2007. The effect of simulated metastatic lytic lesions on proximal femoral strength. *Clinical Orthopaedics,* 459**,** 139-145.https://doi.org/10.1097/BLO.0b013e3180514caa

Keysight Technologies Inc. 2017. Nano Indenter G200 – Data Sheet.

Kim, Y. & Othmer, H. G. 2015. Hybrid models of cell and tissue dynamics in tumor growth. *Math Biosci Eng,* 12**,** 1141-56.10.3934/mbe.2015.12.1141

Koenders, P., Beex, L., Langens, R., Kloppenborg, P., Smals, A. & Benraad, T. J. 1991. Steroid hormone receptor activity of primary human breast cancer and pattern of first metastasis. *Breast Cancer Research and Treatment,* 18**,** 27-32.https://doi.org/10.1007/bf01975440

Kohli, N., Ho, S., Brown, S. J., Sawadkar, P., Sharma, V., Snow, M. & García-Gareta, E. 2018. Bone remodelling in vitro: Where are we headed?:-A review on the current understanding of physiological bone remodelling and inflammation and the strategies for testing biomaterials in vitro. *Bone,* 110**,** 38-46.https://doi.org/10.1016/j.bone.2018.01.015

Kozlow, W. & Guise, T. A. 2005. Breast cancer metastasis to bone: mechanisms of osteolysis and implications for therapy. *Journal of Mammary Gland Biology and Neoplasia,* 10**,** 169-80.https://doi.org/10.1007/s10911-005-5399-8

Kretschmann, K. L. & Welm, A. L. 2012. Mouse models of breast cancer metastasis to bone. *Cancer and Metastasis Reviews,* 31**,** 579-83.https://doi.org/10.1007/s10555-012-9378-4

Kretschmann, K. L., Welm, A. L. J. C. & Reviews, M. 2012. Mouse models of breast cancer metastasis to bone. 31**,** 579-583

Kuhn, H., Medlin, D. 2000. ASM metals handbook: mechanical testing and evaluation. *ASM International,* 8**,** 462-476

Kumar, S. & Weaver, V. M. 2009. Mechanics, malignancy, and metastasis: the force journey of a tumor cell. *Cancer and Metastasis Reviews,* 28**,** 113-27.https://doi.org/10.1007/s10555-008-9173-4

Kumar, V., Naqvi, S. M., Verbruggen, A., Mcevoy, E. & Mcnamara, L. 2022. A novel mechanobiological model of bone metastasis reveals that mechanical stimulation inhibits the pro-osteoclastogenic effects of breast cancer cells. *bioRxiv*.https://doi.org/10.1101/2022.09.19.508588

Lane, N. E., Yao, W., Balooch, M., Nalla, R. K., Balooch, G., Habelitz, S., Kinney, J. H. & Bonewald, L. F. 2006. Glucocorticoid-treated mice have localized changes in trabecular bone material properties and osteocyte lacunar size that are not observed in placebo-treated or estrogen-deficient mice. *Journal of bone mineral research,* 21**,** 466-476.https://doi.org/10.1359/jbmr.051103

Langley, R. R. & Fidler, I. J. J. E. R. 2007. Tumor cell-organ microenvironment interactions in the pathogenesis of cancer metastasis. 28**,** 297-321

Lee, T., Staines, A. & Taylor, D. 2002. Bone adaptation to load: microdamage as a stimulus for bone remodelling. *Journal of Anatomy,* 201**,** 437-446.https://doi.org/10.1046/j.1469-7580.2002.00123.x

Lelekakis, M., Moseley, J. M., Martin, T. J., Hards, D., Williams, E., Ho, P., Lowen, D., Javni, J., Miller, F. R., Slavin, J. & Anderson, R. L. 1999. A novel orthotopic model of breast cancer metastasis to bone. *Clinical and Experimental Metastasis,* 17**,** 163-70.https://doi.org/10.1023/a:1006689719505

Lerner, U. H. Osteoblasts, osteoclasts, and osteocytes: unveiling their intimate-associated responses to applied orthodontic forces. Seminars in Orthodontics, 2012. Elsevier, 237-248.

Li, W. 2016. Damage models for soft tissues: a survey. *Journal of Medical and Biological Engineering,* 36**,** 285-307.https://doi.org/10.1007/s40846-016-0132-1

Li, X. F., Zanzonico, P., Ling, C. C. & O'donoghue, J. 2006. Visualization of experimental lung and bone metastases in live nude mice by X-ray micro-computed tomography. *Technology in Cancer Research & Treatment,* 5**,** 147-55

Licini, C., Vitale-Brovarone, C. & Mattioli-Belmonte, M. 2019. Collagen and non-collagenous proteins molecular crosstalk in the pathophysiology of osteoporosis. *Cytokine & Growth Factor Reviews,* 49**,** 59-69.https://doi.org/10.1016/j.cytogfr.2019.09.001

Liedert, A., Kaspar, D., Augat, P., Ignatius, A., Claes, L. & Tissues 2005. Mechanobiology of bone tissue and bone cells. *Mechanosensitivity in cells,* Logothetis, C. J. & Lin, S.-H. 2005. Osteoblasts in prostate cancer metastasis to bone. *Nature Reviews Cancer,* 5**,** 21-28.10.1038/nrc1528

Lu, Y., Zuo, D., Li, J. & He, Y. 2019. Stochastic analysis of a heterogeneous micro-finite element model of a mouse tibia. *Journal of Medical Engineering and Physics,* 63**,** 50-56.https://doi.org/10.1016/j.medengphy.2018.10.007

Lynch, M. E., Brooks, D., Mohanan, S., Lee, M. J., Polamraju, P., Dent, K., Bonassar, L. J., Van Der Meulen, M. C. & Fischbach, C. 2013. In vivo tibial compression decreases osteolysis and tumor formation in a human metastatic breast cancer model. *Journal of Bone and Mineral Research,* 28**,** 2357-67.https://doi.org/10.1002/jbmr.1966

Lynch, M. E., Neu, C. P., Seelbinder, B. & Mccreery, K. P. 2020. The Role of Mechanobiology in Cancer Metastasis. *Mechanobiology.* Elsevier.

Ma, Y. V., Lam, C., Dalmia, S., Gao, P., Young, J., Middleton, K., Liu, C., Xu, H. & You, L. 2018. Mechanical regulation of breast cancer migration and apoptosis via direct and indirect osteocyte signaling. *Journal of Cellular Biochemistry,* 119**,** 5665-5675.https://doi.org/10.1002/jcb.26745

Macedo, F., Ladeira, K., Pinho, F., Saraiva, N., Bonito, N., Pinto, L. & Gonçalves, F. J. O. R. 2017. Bone metastases: an overview. 11

Macneil, J. A. & Boyd, S. K. 2007. Accuracy of high-resolution peripheral quantitative computed tomography for measurement of bone quality. *Medical engineering & physics,* 29**,** 1096-1105

Mann, K. A., Lee, J., Arrington, S. A., Damron, T. A. & Allen, M. J. 2008. Predicting distal femur bone strength in a murine model of tumor osteolysis. *Clinical orthopaedics related research,* 466**,** 1271-1278.https://doi.org/10.1016/j.medengphy.2006.11.002

Margolis, D. S., Lien, Y.-H. H., Lai, L.-W. & Szivek, J. A. 2004. Bilateral symmetry of biomechanical properties in mouse femora. *Medical engineering physics,* 26**,** 349-353.https://doi.org/10.1016/j.medengphy.2003.11.002

Martín-Badosa, E., Amblard, D., Nuzzo, S., Elmoutaouakkil, A., Vico, L. & Peyrin, F. 2003. Excised bone structures in mice: imaging at three-dimensional synchrotron radiation micro CT. *Radiology,* 229**,** 921-928.https://doi.org/10.1148/radiol.2293020558

Mashiatulla, M., Ross, R. D. & Sumner, D. R. 2017. Validation of cortical bone mineral density distribution using micro-computed tomography. *Bone,* 99**,** 53-61.https://doi.org/10.1016/j.bone.2017.03.049

Masuda, H., Fukabori, Y., Nakano, K., Shimizu, N. & Yamanaka, H. 2004. Expression of bone morphogenetic protein-7 (BMP-7) in human prostate. *The Prostate,* 59**,** 101-106.10.1002/pros.20030

Mc Donnell, P., Harrison, N., Liebschner, M. & Mc Hugh, P. 2009. Simulation of vertebral trabecular bone loss using voxel finite element analysis. *Journal of Biomechanics,* 42**,** 2789-2796.https://doi.org/10.1016/j.jbiomech.2009.07.038

Mcnamara, L. J. J. O. T. R. S. I. 2010. Perspective on post-menopausal osteoporosis: establishing an interdisciplinary understanding of the sequence of events from the molecular level to whole bone fractures. 7**,** 353-372

Mcnamara, L. M. (ed.) 2011. *2.210 - Bone as a Biomaterial In: Deucheyne, P., Comprehensive Biomaterials*: Oxford: Elsevier.

Mcnamara, L. M. & Prendergast, P. J. 2007. Bone remodelling algorithms incorporating both strain and microdamage stimuli. *Journal of Biomechanics,* 40**,** 1381-1391.https://doi.org/10.1016/j.jbiomech.2006.05.007

Mei, X., Middleton, K., Shim, D., Wan, Q., Xu, L., Ma, Y.-H. V., Devadas, D., Walji, N., Wang, L. & Young, E. W. 2019. Microfluidic platform for studying osteocyte mechanoregulation of breast cancer bone metastasis. *Integrative Biology,* 11**,** 119-129.https://doi.org/10.1093/intbio/zyz008

Mellon, S. J. & Tanner, K. J. I. M. R. 2012. Bone and its adaptation to mechanical loading: a review. 57**,** 235-255

Miller, L. M., Little, W., Schirmer, A., Sheik, F., Busa, B. & Judex, S. 2007. Accretion of bone quantity and quality in the developing mouse skeleton. *Journal of Bone and Mineral Research,* 22**,** 1037-45.https://doi.org/10.1359/jbmr.070402

Minami, K., Liu, S., Liu, Y., Chen, A., Wan, Q., Na, S., Li, B.-Y., Matsuura, N., Koizumi, M. & Yin, Y. J. S. R. 2017. Inhibitory effects of dopamine receptor D 1 agonist on mammary tumor and bone metastasis. 7**,** 1-12

Mittra, E., Akella, S. & Qin, Y. X. 2006. The effects of embedding material, loading rate and magnitude, and penetration depth in nanoindentation of trabecular bone. *J Journal of Biomedical Materials Research Part A: An Official Journal of The Society for Biomaterials,* 79**,** 86-93.https://doi.org/10.1002/jbm.a.30742

Mow, V. C., Kuei, S., Lai, W. M. & Armstrong, C. G. 1980. Biphasic creep and stress relaxation of articular cartilage in compression: theory and experiments. *Journal of Biomechanical Engineering,* 102**,** 73-84.https://doi.org/10.1115/1.3138202

Mulvihill, B. M., Mcnamara, L. M. & Prendergast, P. J. 2008. Loss of trabeculae by mechano-biological means may explain rapid bone loss in osteoporosis. *Journal of the Royal Society Interface,* 5**,** 1243-1253.https://doi.org/10.1098/rsif.2007.1341

Mundy, G. R. 2002. Metastasis to bone: causes, consequences and therapeutic opportunities. *Nature Reviews: Cancer,* 2**,** 584-93.https://doi.org/10.1038/nrc867

Nazarian, A., Hermannsson, B. J., Muller, J., Zurakowski, D. & Snyder, B. D. 2009. Effects of tissue preservation on murine bone mechanical properties. *Journal of Biomechanics,* 42**,** 82-6.https://doi.org/10.1016/j.jbiomech.2008.09.037

Nazarian, A., Von Stechow, D., Zurakowski, D., Muller, R. & Snyder, B. D. 2008. Bone volume fraction explains the variation in strength and stiffness of cancellous bone affected by metastatic cancer and osteoporosis. *Calcified Tissue International,* 83**,** 368-79.https://doi.org/10.1007/s00223-008-9174-x

Nickerson, N. K., Mohammad, K. S., Gilmore, J. L., Crismore, E., Bruzzaniti, A., Guise, T. A. & Foley, J. 2012. Decreased autocrine EGFR signaling in metastatic breast cancer cells inhibits tumor growth in bone and mammary fat pad. *PloS One,* 7**,** e30255.https://doi.org/10.1371/journal.pone.0030255

Niyibizi, C. & Eyre, D. R. 1994. Structural Characteristics of Cross-Linking Sites in type V Collagen of Bone: Chain Specificities and Heterotypic Links to Type I Collagen. *European Journal of Biochemistry,* 224**,** 943-950.https://doi.org/10.1111/j.1432-1033.1994.00943.x

Nuzzo, S., Lafage-Proust, M., Martin-Badosa, E., Boivin, G., Thomas, T., Alexandre, C. & Peyrin, F. 2002. Synchrotron radiation microtomography allows the analysis of three-dimensional microarchitecture and degree of mineralization of human iliac crest biopsy specimens: effects of etidronate treatment. *Journal of Bone and Mineral Research,* 17**,** 1372-1382.https://doi.org/10.1359/jbmr.2002.17.8.1372

O'sullivan, L., Allison, H., Parle, E., Schiavi, J. & Mcnamara, L. 2020. Secondary alterations in bone mineralisation and trabecular thickening occur after long-term estrogen deficiency in ovariectomised rat tibiae, which do not coincide with initial rapid bone loss. *Osteoporosis International,* 31**,** 587-599.https://doi.org/10.1007/s00198-019-05239-5

Oliver, W. C. & Pharr, G. M. 1992. An improved technique for determining hardness and elastic modulus using load and displacement sensing indentation experiments. *Journal of materials research,* 7**,** 1564-1583

Oliviero, S., Roberts, M., Owen, R., Reilly, G., Bellantuono, I. & Dall'ara, E. 2021. Non-invasive prediction of the mouse tibia mechanical properties from microCT images: comparison between different finite element models. *Biomechanics and Modeling in Mechanobiology,* 20**,** 941-955.https://doi.org/10.1007/s10237-021-01422-y

Oumarou, N., Jehl, J.-P., Kouitat, R. & Stempfle, P. 2010. On the variation of mechanical parameters obtained from spherical depth sensing indentation. *International Journal of Surface Science and Engineering,* 4**,** 416-428.https://doi.org/10.1504/ijsurfse.2010.035144

Page, J. M., Merkel, A. R., Ruppender, N. S., Guo, R., Dadwal, U. C., Cannonier, S. A., Basu, S., Guelcher, S. A. & Sterling, J. a. J. B. 2015. Matrix rigidity regulates the transition of tumor cells to a bone-destructive phenotype through integrin β3 and TGF-β receptor type II. 64**,** 33-44

Paget, S. 1889. The distribution of secondary growths in cancer of the breast. *Lancet***,** 571-573.https://doi.org/10.1016/s0140-6736(00)49915-0

Palanca, M., Barbanti-Bròdano, G. & Cristofolini, L. 2018. The size of simulated lytic metastases affects the strain distribution on the anterior surface of the vertebra. *Journal of Biomechanical Engineering,* 140

Palanca, M., Barbanti-Brodano, G., Marras, D., Marciante, M., Serra, M., Gasbarrini, A., Dall'ara, E. & Cristofolini, L. 2021a. Type, size, and position of metastatic lesions explain the deformation of the vertebrae under complex loading conditions. *Bone,* 151**,** 116028.https://doi.org/10.1016/j.bone.2021.116028

Palanca, M., De Donno, G. & Dall'ara, E. 2021b. A novel approach to evaluate the effects of artificial bone focal lesion on the three-dimensional strain distributions within the vertebral body. *PloS One,* 16**,** e0251873.https://doi.org/10.1371/journal.pone.0251873

Palanca, M., Oliviero, S. & Dall'ara, E. 2022. MicroFE models of porcine vertebrae with induced bone focal lesions: Validation of predicted displacements with digital volume correlation. *Journal of the Mechanical Behavior of Biomedical Materials,* 125**,** 104872.https://doi.org/10.1016/j.jmbbm.2021.104872

Parr, W., Chamoli, U., Jones, A., Walsh, W. & Wroe, S. 2013. Finite element micro-modelling of a human ankle bone reveals the importance of the trabecular network to mechanical performance: new methods for the generation and comparison of 3D models. *Journal of Biomechanics,* 46**,** 200-205.https://doi.org/10.1016/j.jbiomech.2012.11.011

Paschalis, E., Tatakis, D., Robins, S., Fratzl, P., Manjubala, I., Zoehrer, R., Gamsjaeger, S., Buchinger, B., Roschger, A. & Phipps, R. 2011. Lathyrism-induced alterations in collagen cross-links influence the mechanical properties of bone material without affecting the mineral. *Bone,* 49**,** 1232-1241.https://doi.org/10.1016/j.bone.2011.08.027

Penninger, C. L., Patel, N. M., Niebur, G. L., Tovar, A. & Renaud, J. E. 2008. A fully anisotropic hierarchical hybrid cellular automaton algorithm to simulate bone remodeling. *Mechanics Research Communications,* 35**,** 32-42.https://doi.org/10.1016/j.mechrescom.2007.10.007

Pepe, V., Oliviero, S., Cristofolini, L. & Dall'ara, E. 2020. Regional nanoindentation properties in different locations on the mouse tibia from C57BL/6 and Balb/C female mice. *Frontiers in Bioengineering and Biotechnology,* 8**,** 478

Pereira, A. F., Javaheri, B., Pitsillides, A. & Shefelbine, S. 2015. Predicting cortical bone adaptation to axial loading in the mouse tibia. *Journal of the Royal Society Interface*, 12**,** 20150590.https://doi.org/10.1098/rsif.2015.0590

Pharr, G., Oliver, W. & Brotzen, F. 1992a. On the generality of the relationship among contact stiffness, contact area, and elastic modulus during indentation. *Journal of materials research,* 7**,** 613-617.https://doi.org/10.1557/jmr.1992.0613

Pharr, G., Oliver, W. & Brotzen, F. J. J. O. M. R. 1992b. On the generality of the relationship among contact stiffness, contact area, and elastic modulus during indentation. 7**,** 613-617

Phillips, A. T., Villette, C. C. & Modenese, L. 2015. Femoral bone mesoscale structural architecture prediction using musculoskeletal and finite element modelling. *International Biomechanics,* 2**,** 43-61.https://doi.org/10.1080/23335432.2015.1017609

Plunkett, T. A. & Rubens, R. D. 1999. The biology and management of bone metastases. *Critical Reviews in Oncology/Hematology,* 31**,** 89-96.https://doi.org/10.1016/s1040-8428(99)00008-6

Pollmann, D., Siepmann, S., Geppert, R., Wernecke, K.-D., Possinger, K. & Lüftner, D. J. a. R. 2007. The amino-terminal propeptide (PINP) of type I collagen is a clinically valid indicator of bone turnover and extent of metastatic spread in osseous metastatic breast cancer. 27**,** 1853-1862

Posner, A. S. & Betts, F. 1975. Synthetic amorphous calcium phosphate and its relation to bone mineral structure. *Accounts of Chemical Research,* 8**,** 273-281.https://doi.org/10.1021/ar50092a003

Poundarik, A. A., Boskey, A., Gundberg, C. & Vashishth, D. 2018. Biomolecular regulation, composition and nanoarchitecture of bone mineral. *Scientific Reports,* 8**,** 1-8.https://doi.org/10.1038/s41598-018-19253-w

Prendergast, P., Huiskes, R. & Søballe, K. 1997. Biophysical stimuli on cells during tissue differentiation at implant interfaces. *Journal of Biomechanics,* 30**,** 539-548.https://doi.org/10.1016/s0021-9290(96)00140-6

Pulaski, B. A., Terman, D. S., Khan, S., Muller, E. & Ostrand-Rosenberg, S. 2000. Cooperativity of Staphylococcal aureus enterotoxin B superantigen, major histocompatibility complex class II, and CD80 for immunotherapy of advanced spontaneous metastases in a clinically relevant postoperative mouse breast cancer model. *Cancer Research,* 60**,** 2710-2715

Quinn, C., Kopp, A. & Vaughan, T. J. 2022. A coupled computational framework for bone fracture healing and long-term remodelling: Investigating the role of internal fixation on bone fractures. *International Journal for Numerical Methods in Biomedical Engineering,* 38**,** e3609.https://doi.org/10.31224/osf.io/e36ba

Ramos, A. & Simoes, J. 2006. Tetrahedral versus hexahedral finite elements in numerical modelling of the proximal femur. *Medical Engineering & Physics,* 28**,** 916-924.https://doi.org/10.1016/j.medengphy.2005.12.006

Rankin, E. B., Nam, J.-M. & Giaccia, A. J. J. T. I. C. 2016. Hypoxia: signaling the metastatic cascade. 2**,** 295-304

Rathnayaka, K., Momot, K. I., Noser, H., Volp, A., Schuetz, M. A., Sahama, T. & Schmutz, B. 2012. Quantification of the accuracy of MRI generated 3D models of long bones compared to CT generated 3D models. *Medical engineering & physics,* 34**,** 357-363

Ravoori, M., Czaplinska, A. J., Sikes, C., Han, L., Johnson, E. M., Qiao, W., Ng, C., Cody, D. D., Murphy Jr, W. A. & Do, K.-A. 2010. Quantification of mineralized bone response to prostate cancer by noninvasive in vivo µCT and non-destructive ex vivo µCT and DXA in a mouse model. *PloS One,* 5**,** e9854.https://doi.org/10.1371/journal.pone.0009854

Razi, H., Birkhold, A. I., Weinkamer, R., Duda, G. N., Willie, B. M. & Checa, S. 2015. Aging leads to a dysregulation in mechanically driven bone formation and resorption. *Journal of Bone and Mineral Research,* 30**,** 1864-1873

Regmi, S., Fu, A. & Luo, K. Q. 2017. High shear stresses under exercise condition destroy circulating tumor cells in a microfluidic system. *Scientific Reports,* 7**,** 1-12.https://doi.org/10.1038/srep39975

Rejniak, K. A. & Anderson, A. R. 2011. Hybrid models of tumor growth. *Wiley Interdiscip Rev Syst Biol Med,* 3**,** 115-25.10.1002/wsbm.102

Renders, G., Mulder, L., Van Ruijven, L., Langenbach, G. & Van Eijden, T. 2011. Mineral heterogeneity affects predictions of intratrabecular stress and strain. *Journal of Biomechanics,* 44**,** 402-407

Rennick, J. A., Nazarian, A., Entezari, V., Kimbaris, J., Tseng, A., Masoudi, A., Nayeb-Hashemi, H., Vaziri, A. & Snyder, B. D. 2013. Finite element analysis and computed tomography based structural rigidity analysis of rat tibia with simulated lytic defects. *Journal of Biomechanics,* 46**,** 2701-9.https://doi.org/10.1016/j.jbiomech.2013.06.024

Rho, J.-Y., Tsui, T. Y. & Pharr, G. M. 1997. Elastic properties of human cortical and trabecular lamellar bone measured by nanoindentation. *Biomaterials,* 18**,** 1325-1330.https://doi.org/10.1016/s0142-9612(97)00073-2

Rho, J., Zioupos, P., Currey, J. & Pharr, G. 1999. Variations in the individual thick lamellar properties within osteons by nanoindentation. *Bone,* 25**,** 295-300.https://doi.org/10.1016/s8756-3282(99)00163-5

Richert, L., Keller, L., Wagner, Q., Bornert, F., Gros, C., Bahi, S., Clauss, F., Bacon, W., Clézardin, P., Benkirane-Jessel, N. & Fioretti, F. 2015. Nanoscale Stiffness Distribution in Bone Metastasis. *World Journal of Nano Science and Engineering,* 05**,** 219-228.https://doi.org/10.4236/wjnse.2015.54023

Robert, J. & Reinhold, W. C. 2015. Bisphosphonates as new anticancer agents? *Bulletin du Cancer,* 102**,** 297-299.https://doi.org/10.1016/j.bulcan.2015.02.010

Rodriguez-Florez, N., Oyen, M. L. & Shefelbine, S. J. 2013. Insight into differences in nanoindentation properties of bone. *Journal of the Mechanical Behavior of Biomedical Materials,* 18**,** 90-99.https://doi.org/10.1016/j.jmbbm.2012.11.005

Roohani, I., Cheong, S. & Wang, A. 2021. How to build a bone?-Hydroxyapatite or Posner's clusters as bone minerals. *Open Ceramics,* 6**,** 100092.https://doi.org/10.1016/j.oceram.2021.100092

Roschger, P., Gupta, H., Berzlanovich, A., Ittner, G., Dempster, D., Fratzl, P., Cosman, F., Parisien, M., Lindsay, R. & Nieves, J. 2003. Constant mineralization density distribution in cancellous human bone. *Bone,* 32**,** 316-323.https://doi.org/10.1016/s8756-3282(02)00973-0

Roschger, P., Paschalis, E. P., Fratzl, P. & Klaushofer, K. 2008. Bone mineralization density distribution in health and disease. *Bone,* 42**,** 456-66.https://doi.org/10.1016/j.bone.2007.10.021

Rosol, T. J., Tannehill-Gregg, S. H., Leroy, B. E., Mandl, S. & Contag, C. H. 2003. Animal models of bone metastasis. *Cancer: Interdisciplinary International Journal of the American Cancer Society,* 97**,** 748-757.https://doi.org/10.1002/cncr.11150

Rubin, M. A. & Jasiuk, I. 2005. The TEM characterization of the lamellar structure of osteoporotic human trabecular bone. *Micron,* 36**,** 653-664.https://doi.org/10.1016/j.micron.2005.07.010

Ruffoni, D., Fratzl, P., Roschger, P., Klaushofer, K. & Weinkamer, R. 2007. The bone mineralization density distribution as a fingerprint of the mineralization process. *Bone,* 40**,** 1308-1319

Saito, M. & Marumo, K. J. O. I. 2010. Collagen cross-links as a determinant of bone quality: a possible explanation for bone fragility in aging, osteoporosis, and diabetes mellitus. 21**,** 195-214

Salvatore, G., Berton, A., Giambini, H., Ciuffreda, M., Florio, P., Longo, U. G., Denaro, V., Thoreson, A. & An, K.-N. 2018. Biomechanical effects of metastasis in the osteoporotic lumbar spine: A Finite Element Analysis. *BMC Musculoskeletal Disorders,* 19**,** 1-8.https://doi.org/10.1186/s12891-018-1953-6

Sandino, C., Mcerlain, D. D., Schipilow, J. & Boyd, S. K. 2017. Mechanical stimuli of trabecular bone in osteoporosis: A numerical simulation by finite element analysis of microarchitecture. *Journal of the Mechanical Behavior of Biomedical Materials,* 66**,** 19-27.https://doi.org/10.1016/j.jmbbm.2016.10.005

Sarazin, B. A., Ihle, C. L., Owens, P. & Lynch, M. E. 2021. Mechanobiology of Bone Metastatic Cancer. *Current osteoporosis reports***,** 1-12.https://doi.org/10.1007/s11914-021-00704-9

Sas, A., Ohs, N., Tanck, E. & Van Lenthe, G. H. 2020. Nonlinear voxel-based finite element model for strength assessment of healthy and metastatic proximal femurs. *Bone Reports,* 12**,** 100263.https://doi.org/10.1016/j.bonr.2020.100263

Sas, A., Tanck, E., Wafa, H., Van Der Linden, Y., Sermon, A. & Van Lenthe, G. H. 2022. Fracture risk assessment and evaluation of femoroplasty in metastatic proximal femurs. An in vivo CT-based finite element study. *Journal of Orthopaedic Research*.https://doi.org/10.1002/jor.25331

Scannell, P. T. & Prendergast, P. J. 2009. Cortical and interfacial bone changes around a non-cemented hip implant: simulations using a combined strain/damage remodelling algorithm. *Medical Engineering & Physics,* 31**,** 477-488.https://doi.org/10.1016/j.medengphy.2008.11.007

Scheuren, A. C., Vallaster, P., Kuhn, G. A., Paul, G. R., Malhotra, A., Kameo, Y. & Müller, R. 2020. Mechano-regulation of trabecular bone adaptation is controlled by the local in vivo environment and logarithmically dependent on loading frequency. *Frontiers in Bioengineering and Biotechnology,* 8**,** 566346.https://doi.org/10.3389/fbioe.2020.566346

Schileo, E., Dall'ara, E., Taddei, F., Malandrino, A., Schotkamp, T., Baleani, M. & Viceconti, M. 2008. An accurate estimation of bone density improves the accuracy of subject-specific finite element models. *Journal of Biomechanics,* 41**,** 2483-2491.https://doi.org/10.1016/j.jbiomech.2008.05.017

Schulte, F. A., Lambers, F. M., Webster, D. J., Kuhn, G. & Müller, R. 2011. In vivo validation of a computational bone adaptation model using open-loop control and time-lapsed micro-computed tomography. *Bone,* 49**,** 1166-1172.https://doi.org/10.1016/j.bone.2011.08.018

Schulte, F. A., Zwahlen, A., Lambers, F. M., Kuhn, G., Ruffoni, D., Betts, D., Webster, D. J. & Müller, R. 2013. Strain-adaptive in silico modeling of bone adaptation—a computer simulation validated by in vivo micro-computed tomography data. *Bone,* 52**,** 485-492.https://doi.org/10.1016/j.bone.2012.09.008

Sekita, A., Matsugaki, A., Ishimoto, T. & Nakano, T. 2017. Synchronous disruption of anisotropic arrangement of the osteocyte network and collagen/apatite in melanoma bone metastasis. *Journal of Structural Biology,* 197**,** 260-270.https://doi.org/10.1016/j.jsb.2016.12.003

Selvaggi, G. & Scagliotti, G. V. 2005. Management of bone metastases in cancer: A review. *Critical Reviews in Oncology/Hematology,* 56**,** 365-378.https://doi.org/10.1016/j.critrevonc.2005.03.011

Shinoda, Y., Kobayashi, H., Kaneko, M., Ohashi, S., Bessho, M., Hayashi, N., Oka, H., Imanishi, J., Sawada, R. & Ogura, K. 2019. Prediction of the pathological fracture risk during stance and fall-loading configurations for metastases in the proximal femur, using a computed tomography-based finite element method. *Journal of Orthopaedic Science,* 24**,** 1074-1080.https://doi.org/10.1016/j.jos.2019.08.014

Siegel, R. L., Miller, K. D. & Jemal, A. 2019. Cancer statistics, 2019. *CA: A Cancer Journal for Clinicians,* 69**,** 7-34.https://doi.org/10.3322/caac.21551

Sikavitsas, V. I., Temenoff, J. S. & Mikos, A. G. 2001. Biomaterials and bone mechanotransduction. *Biomaterials,* 22**,** 2581-2593.https://doi.org/10.1016/s0142-9612(01)00002-3

Silva, M. J., Brodt, M. D., Fan, Z. & Rho, J. Y. 2004. Nanoindentation and whole-bone bending estimates of material properties in bones from the senescence accelerated mouse SAMP6. *Journal of Biomechanics,* 37**,** 1639-46.https://doi.org/10.1016/j.jbiomech.2004.02.018

Silva, M. J., Keaveny, T. M. & Hayes, W. C. 1998. Computed tomography-based finite element analysis predicts failure loads and fracture patterns for vertebral sections. *Journal of Orthopaedic Research,* 16**,** 300-308

Singhal, H., Bautista, D. S., Tonkin, K. S., O'malley, F. P., Tuck, A. B., Chambers, A. F. & Harris, J. F. J. C. C. R. 1997. Elevated plasma osteopontin in metastatic breast cancer associated with increased tumor burden and decreased survival. 3**,** 605-611

Smotrova, E., Li, S. & Silberschmidt, V. V. 2022. Mechanoregulated trabecular bone adaptation: progress report on in silico approaches. *Biomaterials Biosystems***,** 100058.https://doi.org/10.1016/j.bbiosy.2022.100058

Søballe, K. 1993. Hydroxyapatite ceramic coating for bone implant fixation: mechanical and histological studies in dogs. *Acta Orthopaedica Scandinavica,* 64**,** 1-58.https://doi.org/10.3109/17453679309155636

Sohail, A., Younas, M., Bhatti, Y., Li, Z., Tunç, S. & Abid, M. 2019. Analysis of trabecular bone mechanics using machine learning. *Evolutionary Bioinformatics,* 15**,** 1176934318825084.https://doi.org/10.1177/1176934318825084

Sottnik, J. L., Dai, J., Zhang, H., Campbell, B. & Keller, E. T. 2015. Tumor-induced pressure in the bone microenvironment causes osteocytes to promote the growth of prostate cancer bone metastases. *Cancer research,* 75**,** 2151-2158

Spruijt, S., Van Der Linden, J. C., Sander Dijkstra, P., Wiggers, T., Oudkerk, M., Snijders, C. J., Van Keulen, F., Verhaar, J. A., Weinans, H. & Swierstra, B. A. 2006. Prediction of torsional failure in 22 cadaver femora with and without simulated subtrochanteric metastatic defects: a CT scan-based finite element analysis. *Acta Orthopaedica,* 77**,** 474-481.https://doi.org/10.1080/17453670610046424

Stewart, S., Darwood, A., Masouros, S., Higgins, C. & Ramasamy, A. 2020. Mechanotransduction in osteogenesis. *Bone & Joint Research,* 9**,** 1-14.https://doi.org/10.1302/2046-3758.91.bjr-2019-0043.r2

Sullivan, J. & Anderson, S. 2000. Introduction to the Musculoskeletal System: Care of the young athlete. *Rosemont: American Academy of Orthopaedic Surgeons,* Suzuki, S., Nomizu, T., Nihei, M., Rokkaku, Y., Kimijima, I., Tsuchiya, A. & Abe, R. J. N. G. C. G. S. 1989. Clinical evaluation of serum osteocalcin in patients with bone metastasis of breast cancer. 24**,** 2386-2393

Szewczyk, K. A., Fuller, K. & Chambers, T. J. 2013. Distinctive subdomains in the resorbing surface of osteoclasts. *PloS One,* 8**,** e60285.https://doi.org/10.1371/journal.pone.0060285

Tang, B., Ngan, A. H. & Lu, W. W. 2007. An improved method for the measurement of mechanical properties of bone by nanoindentation. *Journal of Materials Science: Materials in Medicine,* 18**,** 1875-81.https://doi.org/10.1007/s10856-007-3031-8

Taube, T., Elomaa, I., Blomqvist, C., Beneton, M. N. C. & Kanis, J. A. 1994. Histomorphometric evidence for osteoclast-mediated bone resorption in metastatic breast cancer. *Bone,* 15**,** 161-166.https://doi.org/10.1016/8756-3282(94)90703-X

Thudium, C. S., Moscatelli, I., Flores, C., Thomsen, J. S., Brüel, A., Gudmann, N. S., Hauge, E.-M., Karsdal, M. A., Richter, J. & Henriksen, K. 2014. A comparison of osteoclast-rich and osteoclast-poor osteopetrosis in adult mice sheds light on the role of the osteoclast in coupling bone resorption and bone formation. *Calcified Tissue International,* 95**,** 83-93

Tracqui, P. 2009. Biophysical models of tumour growth. *Reports on Progress in Physics,* 72.Artn 056701

10.1088/0034-4885/72/5/056701

Tresguerres, F., Torres, J., López-Quiles, J., Hernández, G., Vega, J. & Tresguerres, I. 2020. The osteocyte: A multifunctional cell within the bone. *Annals of Anatomy-Anatomischer Anzeiger,* 227**,** 151422.https://doi.org/10.1016/j.aanat.2019.151422

Turner, C. H., Forwood, M., Rho, J. Y. & Yoshikawa, T. 1994. Mechanical loading thresholds for lamellar and woven bone formation. *Journal of Bone and Mineral Research,* 9**,** 87-97.https://doi.org/10.1002/jbmr.5650090113

Van Lenthe, G. H., Voide, R., Boyd, S. K. & Müller, R. 2008. Tissue modulus calculated from beam theory is biased by bone size and geometry: implications for the use of three-point bending tests to determine bone tissue modulus. *Bone,* 43**,** 717-723.https://doi.org/10.1016/j.bone.2008.06.008

Van Rietbergen, B., Huiskes, R., Eckstein, F. & Ruegsegger, P. 2003. Trabecular bone tissue strains in the healthy and osteoporotic human femur. *Journal of Bone and Mineral Research,* 18**,** 1781-8.https://doi.org/10.1359/jbmr.2003.18.10.1781

Van Rietbergen, B., Huiskes, R., Weinans, H., Sumner, D., Turner, T. & Galante, J. 1993. The mechanism of bone remodeling and resorption around press-fitted THA stems. *Journal of Biomechanics,* 26**,** 369-382.https://doi.org/10.1016/0021-9290(93)90001-u

Van Tol, A. F., Schemenz, V., Wagermaier, W., Roschger, A., Razi, H., Vitienes, I., Fratzl, P., Willie, B. M. & Weinkamer, R. 2020. The mechanoresponse of bone is closely related to the osteocyte lacunocanalicular network architecture. *Proceedings of the National Academy of Sciences,* 117**,** 32251-32259.https://doi.org/10.1073/pnas.2011504117

Vaughan, T. J., Mccarthy, C. T. & Mcnamara, L. M. 2012. A three-scale finite element investigation into the effects of tissue mineralisation and lamellar organisation in human cortical and trabecular bone. *Journal of the Mechanical*

Behavior of Biomedical Materials, 12**,** 50-62.https://doi.org/10.1016/j.jmbbm.2012.03.003

Verbruggen, A. S., Mccarthy, E. C., Dwyer, R. M. & Mcnamara, L. M. 2022. Temporal and spatial changes in bone mineral content and mechanical properties during breast-cancer bone metastases. *Bone Reports***,** 101597.https://doi.org/10.1016/j.bonr.2022.101597

Verbruggen, A. S. & Mcnamara, L. M. 2023. Mechanoregulation may drive osteolysis during bone metastasis: A finite element analysis of the mechanical environment within bone tissue during bone metastasis and osteolytic resorption. *Journal of the Mechanical Behavior of Biomedical Materials***,** 105662.https://doi.org/10.1016/j.jmbbm.2023.105662

Verbruggen, S. W., Thompson, C. L., Duffy, M. P., Lunetto, S., Nolan, J., Pearce, O. M., Jacobs, C. R. & Knight, M. M. 2021. Mechanical stimulation modulates osteocyte regulation of cancer cell phenotype. *Cancers,* 13**,** 2906.https://doi.org/10.3390/cancers13122906

Verbruggen, S. W., Vaughan, T. J. & Mcnamara, L. M. 2012. Strain amplification in bone mechanobiology: a computational investigation of the in vivo mechanics of osteocytes. *Journal of the Royal Society Interface,* 9**,** 2735-2744.https://doi.org/10.1098/rsif.2012.0286

Verhulp, E., Van Rietbergen, B. & Huiskes, R. 2008. Load distribution in the healthy and osteoporotic human proximal femur during a fall to the side. *Bone,* 42**,** 30-5.https://doi.org/10.1016/j.bone.2007.08.039

Vesper, E. O., Hammond, M. A., Allen, M. R. & Wallace, J. M. 2017. Even with rehydration, preservation in ethanol influences the mechanical properties of bone and how bone responds to experimental manipulation. *Bone,* 97**,** 49-53.https://doi.org/10.1016/j.bone.2017.01.001

Viceconti, M., Qasim, M., Bhattacharya, P. & Li, X. 2018. Are CT-based finite element model predictions of femoral bone strengthening clinically useful? *Current osteoporosis reports,* 16**,** 216-223

Viguet-Carrin, S., Roux, J., Arlot, M., Merabet, Z., Leeming, D., Byrjalsen, I., Delmas, P. & Bouxsein, M. 2006. Contribution of the advanced glycation end product pentosidine and of maturation of type I collagen to compressive biomechanical properties of human lumbar vertebrae. *Bone,* 39**,** 1073-1079.https://doi.org/10.1016/j.bone.2006.05.013

Voide, R., Van Lenthe, G. H. & Müller, R. 2008. Femoral stiffness and strength critically depend on loading angle: a parametric study in a mouse-inbred strain. *Biomed. Tech.*https://doi.org/10.1515/BMT.2008.019

Wang, J. H.-C. & Thampatty, B. P. 2006. An introductory review of cell mechanobiology. *Biomechanics modeling in mechanobiology,* 5**,** 1-16.https://doi.org/10.1007/s10237-005-0012-z

Wang, L., Wang, Y., Chen, A., Teli, M., Kondo, R., Jalali, A., Fan, Y., Liu, S., Zhao, X. & Siegel, A. J. T. F. J. 2019. Pitavastatin slows tumor progression and alters urine-derived volatile organic compounds through the mevalonate pathway. 33**,** 13710-13721

Wang, N., Reeves, K. J., Brown, H. K., Fowles, A. C., Docherty, F. E., Ottewell, P. D., Croucher, P. I., Holen, I. & Eaton, C. L. 2015. The frequency of osteolytic bone metastasis is determined by conditions of the soil, not the number of seeds; evidence from in vivo models of breast and prostate cancer. *Journal of experimental clinical cancer research,* 34**,** 1-12.https://doi.org/10.1186/s13046-015-0240-8

Wang, S., Pei, S., Wasi, M., Parajuli, A., Yee, A., You, L. & Wang, L. 2021. Moderate tibial loading and treadmill running, but not overloading, protect adult murine bone from destruction by metastasized breast cancer. *Bone,* 153**,** 116100.https://doi.org/10.1016/j.bone.2021.116100

Weatherholt, A. M., Fuchs, R. K. & Warden, S. J. 2013. Cortical and trabecular bone adaptation to incremental load magnitudes using the mouse tibial axial compression loading model. *Bone,* 52**,** 372-379.https://doi.org/10.1016/j.bone.2012.10.026

Webster, D., Schulte, F. A., Lambers, F. M., Kuhn, G. & Müller, R. 2015. Strain energy density gradients in bone marrow predict osteoblast and osteoclast activity: a finite element study. *Journal of Biomechanics,* 48**,** 866-874.https://doi.org/10.1016/j.jbiomech.2014.12.009

Webster, D. J., Morley, P. L., Van Lenthe, G. H. & Müller, R. 2008. A novel in vivo mouse model for mechanically stimulated bone adaptation–a combined experimental and computational validation study. *Computer Methods in Biomechanics and Biomedical Engineering,* 11**,** 435-441.https://doi.org/10.1080/10255840802078014

Weigelt, B., Peterse, J. L. & Van't Veer, L. J. J. N. R. C. 2005. Breast cancer metastasis: markers and models. 5**,** 591-602

Weinkamer, R., Eberl, C. & Fratzl, P. 2019. Mechanoregulation of bone remodeling and healing as inspiration for self-repair in materials. *Biomimetics,* 4**,** 46.https://doi.org/10.3390/biomimetics4030046

Wergedal, J. & Baylink, D. J. 1974. Electron microprobe measurements of bone mineralization rate in vivo. *American Journal of Physiology-Legacy Content,* 226**,** 345-352.https://doi.org/10.1152/ajplegacy.1974.226.2.345

Wernle, J. D., Damron, T. A., Allen, M. J. & Mann, K. A. 2010. Local irradiation alters bone morphology and increases bone fragility in a mouse model. *Journal of Biomechanics,* 43**,** 2738-2746.https://doi.org/10.1016/j.jbiomech.2010.06.017

Whyne, C. M., Hu, S. S. & Lotz, J. C. 2003. Burst fracture in the metastatically involved spine: development, validation, and parametric analysis of a three-dimensional poroelastic finite-element model. *Spine,* 28**,** 652-660.https://doi.org/10.1097/01.brs.0000051910.97211.ba

Willinghamm, M. D., Brodt, M. D., Lee, K. L., Stephens, A. L., Ye, J. & Silva, M. J. 2010. Age-related changes in bone structure and strength in female and male BALB/c mice. *Calcified Tissue International,* 86**,** 470-83.https://doi.org/10.1007/s00223-010-9359-y

Wolff, J. 1893. Das gesetz der transformation der knochen. *DMW-Deutsche Medizinische Wochenschrift,* 19**,** 1222-1224.https://doi.org/10.1055/s-0028-1144106

Woo, S.-B. & Solomon, D. H. 2007. Bisphosphonate therapy for cancer and prevalence of inflammatory jaw conditions. *Journal of the National Cancer Institute,* 99**,** 986-987.https://doi.org/10.1093/jnci/djm029

Wright, L. E., Ottewell, P. D., Rucci, N., Peyruchaud, O., Pagnotti, G. M., Chiechi, A., Buijs, J. T. & Sterling, J. A. 2016. Murine models of breast cancer bone metastasis. *BoneKEy reports,* 5.https://doi.org/10.1038/bonekey.2016.31

Wu, D., Isaksson, P., Ferguson, S. J. & Persson, C. 2018. Young's modulus of trabecular bone at the tissue level: A review. *Acta Biomaterialia,* 78**,** 1-12.https://doi.org/10.1016/j.actbio.2018.08.001

Wu, Z., Baker, T. A., Ovaert, T. C. & Niebur, G. L. 2011. The effect of holding time on nanoindentation measurements of creep in bone. *Journal of Biomechanics,* 44**,** 1066-1072.https://doi.org/10.1016/j.jbiomech.2011.01.039

Yao, Z., Murali, B., Ren, Q., Luo, X., Faget, D. V., Cole, T., Ricci, B., Thotala, D., Monahan, J. & Van Deursen, J. M. 2020. Therapy-induced senescence drives bone loss. *Cancer Research,* 80**,** 1171-1182.https://doi.org/10.1158/0008-5472.can-19-2348

Yavropoulou, M. P. & Yovos, J. 2016. The molecular basis of bone mechanotransduction. *Journal of musculoskeletal neuronal interactions,* 16**,** 221.PMID: 27609037

Yavropoulou, M. P. & Yovos, J. G. 2007. The role of the Wnt signaling pathway in osteoblast commitment and differentiation. *Hormones - Athens,* 6**,** 279.https://doi.org/10.14310/horm.2002.1111024

Yoneda, T., Michigami, T., Yi, B., Williams, P. J., Niewolna, M. & Hiraga, T. 2000. Actions of bisphosphonate on bone metastasis in animal models of breast carcinoma. *Cancer,* 88**,** 2979-88.https://doi.org/10.1002/1097-0142(20000615)88:12+<2979::aid-cncr13>3.0.co;2-u

Yoneda, T., Sasaki, A., Dunstan, C., Williams, P. J., Bauss, F., De Clerck, Y. A. & Mundy, G. R. 1997. Inhibition of osteolytic bone metastasis of breast cancer by combined treatment with the bisphosphonate ibandronate and tissue inhibitor of the matrix metalloproteinase-2. *The Journal of clinical investigation,* 99**,** 2509-2517.https://doi.org/10.1172/jci119435

Yoneda, T., Sasaki, A. & Mundy, G. R. 1994. Osteolytic bone metastasis in breast cancer. *Breast Cancer Research and Treatment,* 32**,** 73-84.https://doi.org/10.1007/BF00666208

Yosibash, Z., Mayo, R. P., Dahan, G., Trabelsi, N., Amir, G. & Milgrom, C. 2014. Predicting the stiffness and strength of human femurs with real metastatic tumors. *Bone,* 69**,** 180-190.https://doi.org/10.1016/j.bone.2014.09.022

You, J., Yellowley, C., Donahue, H., Zhang, Y., Chen, Q. & Jacobs, C. 2000. Substrate deformation levels associated with routine physical activity are less stimulatory to bone cells relative to loading-induced oscillatory fluid flow. *Journal of Biomechanical Engineering,* 122**,** 387-393.https://doi.org/10.1115/1.1287161

Zeitoun, D., Caliaperoumal, G., Bensidhoum, M., Constans, J. M., Anagnostou, F. & Bousson, V. J. E. R. E. 2019. Microcomputed tomography of the femur of diabetic rats: alterations of trabecular and cortical bone microarchitecture and vasculature—a feasibility study. 3**,** 1-9

Zheng, Y., Zhou, H., Dunstan, C. R., Sutherland, R. L. & Seibel, M. J. 2013. The role of the bone microenvironment in skeletal metastasis. *J Bone Oncol,* 2**,** 47-57.https://doi.org/10.1016/j.jbo.2012.11.002

Zhou, J. Z., Riquelme, M. A., Gu, S., Kar, R., Gao, X., Sun, L. & Jiang, J. X. 2016. Osteocytic connexin hemichannels suppress breast cancer growth and bone metastasis. *Oncogene,* 35**,** 5597-5607.https://doi.org/10.1038/onc.2016.101

Zhou, X. & Liu, J. 2014. A computational model to predict bone metastasis in breast cancer by integrating the dysregulated pathways. *BMC Cancer,* 14**,** 618.10.1186/1471-2407-14-618

Zysset, P. K., Guo, X. E., Hoffler, C. E., Moore, K. E. & Goldstein, S. A. 1999. Elastic modulus and hardness of cortical and trabecular bone lamellae measured by nanoindentation in the human femur. *Journal of Biomechanics,* 32**,** 1005-1012.https://doi.org/10.1016/S0021-9290(99)00111-6